Corso di Dottorato in Ingegneria Industriale (XXX ciclo)

Flow boiling in a circular channel and CHF in rectangular minichannels with low-GWP refrigerants

Supervisors
Prof. Rita Mastrullo
Prof. Alfonso William Mauro

PhD Coordinator
Prof. Michele Grassi

PhD Candidate
Luca Viscito

December 2017

Abstract

The correct design of evaporators and heat-spreader systems continuously requests flow boiling heat transfer and pressure drop data, especially for new low-GWP fluids that are about to replace HFC substances in different fields. More data are also required in operating conditions that promote flow asymmetry, for which the classical heat transfer prediction methods are not completely accurate. In addition, the progressive miniaturization of electronic devices and their performance evolution made the two-phase cooling an interesting option. For these systems, the determination of the critical heat flux (CHF) is extremely important to avoid possible overheating and physical burn-out.

In this context, the first part of the thesis provides new CHF data for five different refrigerants (R134a, R32, R1234yf, R1234ze and R1233zd) in an aluminum multi-minichannel heat sink in which seven rectangular minichannels are carved. A new operative definition of critical heat flux is firstly given. Then, the effect of geometry (represented by the L_h/D ratio, equal to 19, 27 and 44), mass flux (from 145 to 3000 kg/m^2 s) and saturation temperature (from 24.7 to 75.5 °C) is investigated and discussed. Finally, the experimental data are compared to the predicted values obtained from some of the most quoted CHF correlations available in scientific literature.

New flow boiling heat transfer and pressure drop data in a single, circular, horizontal smooth stainless steel channel of 6.0 mm internal diameter are instead provided in the second part of the thesis. Specifically, the heat transfer coefficients are measured at the top, bottom, left and right sides of the tube in order to have a more accurate estimation of the peripheral average heat transfer coefficient. Different operative conditions are chosen to promote stratification and to better understand the relative importance of the convective and nucleate boiling contributions on the two-phase heat transfer process. Propane (R290) and R134a are employed as working fluids. Mass flux goes from 150 to 500 kg/m^2 s, heat flux from 2.5 to 40 kW/m^2 and saturation temperature is set from 20 to 35 °C. The effect of all the operative parameters and also that of the working fluids on local heat transfer coefficients and pressure drop are discussed and the experimental data are compared with some of the available correlations taken from scientific literature.

Acknowledgments

During his lesson on the temperature scales, my chemistry teacher peeped out through the classroom desks, trying to realize where that shy voice was coming from. Eventually, he found a trembling forearm above the students bowed heads. A younger and skinner version of me was about to ask his silly question: "*If we assume the lowest limit of 0 K, why can't there be a similar upper threshold?*", I wondered.

I hope the reader might forgive the foolishness of that inquiry coming from a thirteen years old boy. The teacher, however, was indulgent, and had his own way to describe the molecular vibration intensity. "*Motion*", he replied with a smile. "*We can see stillness as a lack of motion, but there is not a limit to disorder*".

Those words, heard in my first high school year, answered a deeper question: I then realized why I have always liked *cold*, and anything related to it. I consider cold, somehow, as logical and more manageable and understandable, which reflects my meditative personality and the seeking of rationality and order in my life. Maybe it is only a good joke, but I like to believe that all of this has had its contribution for bringing me here, where I stand as a member of this *refrigeration* research group.

Apart from the unforgotten chemistry teacher Caputano, which unconsciously initiated me to this educational path, I wish at this point to express my sincere gratitude to everyone who, by any means, has helped me during my PhD studies.

First of all, I would like to thank my supervisors *Prof. Rita Mastrullo* and *Prof. William Mauro*, for giving me the opportunity to work in this group. Moreover, your encouragement and guidance in these three years made me grow in several aspects. With the help of your endless support, I could face all the difficulties encountered with a different and constructive spirit.

To all my former and current colleagues at the department, for making it such a pleasant place to stay. *Francesco Botticella*, *Marcello Tammaro*, *Claudia Vellucci*, it has been a pleasure to work with you all. Thank you very much for your friendship, our road trip is the

evidence that we were eager to spend more time together, apart from the regular work days. *Marcello Iasiello*, *Gianluca Lillo*, *Gerardo Mauro*, thank you for your radiant company and congeniality. Not a chance to get bored any time with your presence.

A special thank to *Aurelio*, *Federico*, *Marialuisa* and *Miriam*, who shared with me the everyday trips back and forward in this last year. Your company made our daily journeys briefer and more enjoyable.

Finally, I am truly indebted to *my whole family*, for their unconditional support in helping me get this far. Despite limited resources, you never impeded my education at any point. *Sharon*, my dearest, I understand I have been more distracted in this intense period. Thank you for your love and patience, I truly appreciate your efforts to make me feel closer.

<div align="right">

Luca Viscito

Napoli, 10/12/2017

</div>

Table of contents

1   Introduction

1.1   Motivations and background

T he research on flow boiling of refrigerants is of primary importance in several fields, such as air conditioning, refrigeration, nuclear systems and Organic Rankine Cycles (ORC). For these applications, the capability to determine the two-phase heat transfer and pressure drop within a wide range of saturation temperatures and other operative parameters is extremely important for the correct design of evaporators and heat spreaders systems. Indeed, the current predictive methods are not completely satisfactory, since most of them have been conceived for symmetric flow conditions with predominant convective contribution, which may not necessarily occur in some particular operating conditions. Furthermore, an accurate determination of the pressure drop in heat exchangers is fundamental for the environmental impact of systems, since it allows to minimize the energy losses connected to the fluid handling and, therefore, the indirect contribution to the emissions of pollutants in the atmosphere.

In other applications, as the cooling of electronic systems, the research on flow boiling is also of great interest, since air-cooling has reached its limit and phase change heat transfer in compact heat sinks is already a viable solution. In fact, the size of electronic devices has significantly decreased in recent years, leading to more compact and faster chips but at the same time to great chip power densities and dissipation of much higher heat fluxes than ever before. According to the International Technology Roadmap for Semiconductors [1], the heat flux from microchips is likely to keep on rising, especially for high power defense electronics, in which the dissipation of 1000 W/cm^2 is already a fact [2]. Also in case of new generation of photovoltaic cells, it is possible to concentrate the solar illumination in small operating spots (>500 suns), thus obtaining a substantial enhancement of the panel performance [3], but also the need of an active cell cooling in order to prevent undesired overheating and thermal failures. In this context, minichannel and multi-minichannel two-

phase cooling technology has attracted considerable attention in the last decades, thanks to several advantages such as light weight, reduced fluid charge and less material consumption [4]. Flow boiling refrigerants inside multi-minichannel heat sinks is a good option if compared to a single-phase flow, thanks to the enhanced heat transfer and a uniformity of the wall temperature, which is highly recommended in case of cooling of microchips or other electronic devices. Moreover, two-phase flows are preferable when high heat fluxes have to be dissipated, in order to avoid significant pressure drops related to water at high mass flow rates. With boiling refrigerants, instead, low fluid mass flow rates are possible by exploiting the latent heat, thus leading to a substantial reduction of the pumping power.

In designing a two-phase multi-minichannel heat sink working with an imposed heat flux to be dissipated, it is important to know the critical heat flux (CHF) value for any operating condition and working fluid adopted. The CHF, in fact, represents the cooling upper limit and the maximum heat flux that can be handled. Beyond this condition, the system is subjected to a steep reduction of the heat transfer efficiency with a consequent sudden rise of the temperatures and the possible physical burn-out of the device that has to be cooled. In this context, the collection of CHF data for multi-minichannel heat sinks with different fluids and operating conditions is of significant importance.

For all the mentioned applications, the choice of a suitable fluid is not of secondary concern. According to the Montreal Protocol, CFC refrigerants have been banned from the market in most developed countries of the world, due to the harmful effect of chlorine on the ozone layer. Nowadays, synthetic HFCs are widely used thanks to their lack of chlorine; their drawback, however, is a high global warming potential (GWP) that increases the greenhouse effect once they are released in atmosphere. According to the 2014 F-Gas European Regulation [5], a gradual removal of high-GWP substances is already planned for the next years. Interesting alternatives are represented by other synthetic refrigerants like R32 or hydro-fluoro-olefin fluids (HFO), such as R1234yf, R1234ze, R1233zd, or hydrocarbons (HC), as propane (R290).

Particularly, HFO refrigerants have the advantages of very low GWP values (<5), but their drawback may be a reduced cooling capacity which leads to higher mass flow rates for cooling systems and lower performances. As regards propane, it represents a valuable

alternative thanks to its very low GWP (<3), good material compatibility and excellent thermodynamic properties, that can even improve the system efficiency, thus reducing the indirect effect on global warming [6]. Despite its high flammability, with size reduction and a correct design of the heat exchangers, the fluid inventory can be conveniently reduced without affecting the system performance, with particular benefits on safety issues.

1.2   Objectives of the study

The present work aims to provide flow boiling heat transfer coefficients and two-phase pressure drops data in a circular, horizontal channel and critical heat flux (CHF) new data for a multi-minichannel heat sink. Working fluids, geometries and operating conditions are varied for the experiments and their effect is recorded and shown. Thus, the main objectives of this these may be summarized as follows:

- Set-up of the experimental apparatus for the CHF measurements in an aluminum multi-minichannel heat sink.
- Conceive a new operative CHF detection method.
- Collection of saturated CHF data using R134a, R1234yf, R1234ze, R1233zd and R32 over different ranges of mass fluxes and saturation temperature, and for three different geometries according to the heated length-on-equivalent diameter ratio (L_h/D) of the minichannels.
- Study the effect of mass velocity, saturation temperature, working fluid and L_h/D ratio on the recorded experimental CHF.
- Find out the applicability range of existing CHF correlations for conventional, single minichannels and multi-minichannel geometries using the present experimental data.
- Set-up of the same experimental apparatus by changing part of the measurement instrumentation and the test section, using a single horizontal channel of 6.0 mm internal diameter for the flow boiling experiments.
- Collect flow boiling heat transfer coefficient data in order to understand the effect of stratification at low mass velocities and the relative importance of the nucleative and convective contributions intervening in the heat transfer mechanism, so that more accurate heat transfer predictive methods may be realized.

- Compare the experimental two-phase heat transfer coefficient data to the prediction of some available correlations.

- Collect two-phase frictional pressure drops for refrigerants R134a and propane (R290) over different ranges of mass velocities and saturation temperature.

- Study the effect of operating parameters and working fluids on the experimental two-phase frictional pressure drop.

- Compare the experimental two-phase frictional pressure drop data to the values obtained by using some available prediction methods.

1.3 Layout of the thesis

The present thesis is divided in eight chapters, organized as follows:

- *Chapter 1* provides a background to the study, by motivating the work and stating the research objectives.

- *Chapter 2* provides the basic definitions of main parameters and non-dimensional numbers that intervene when describing the boiling phenomena. Also the fundamentals of boiling process are exposed in this section.

- In *Chapter 3*, an overview of the state of the art related to the existing studies in open literature on saturated CHF for different geometries and operating conditions is provided. The most quoted CHF prediction methods will also be shown in this section. The second part of the chapter deals with a literature review on flow boiling heat transfer and pressure drop in conventional and minichannels, illustrating the typical trends observed in the literature and some of the most quoted predictive methods developed by several authors.

- *Chapter 4* describes the experimental facility as well as the measurement instrumentation and the two test section arrangements used for the CHF measurements. In addition, the experimental methodology, data reduction process and evaluation of the experimental uncertainty of all the parameters of interest are also shown. The new CHF operative definition for all the experiments of this thesis is described in this section.

- The first part of *Chapter 5* presents the experimental conditions used for the saturated CHF experiments and the effect of an orifice insert at the inlet manifold of the multi-

minichannel test section on the stability of the main parameters controlled during the experiments. The second part of the chapter presents the results of the CHF experimental campaign in terms of boiling curves and CHF values, exposing also the effect of all the operative parameters on the experimental data. Finally, a critical assessment of some of the saturated CHF prediction methods available is performed at the end of the chapter.

- *Chapter 6* describes the new parts of the experimental facility used for the flow boiling experiments, paying particular attention to the stainless steel tube used as test section. The *in-situ* calibration procedure of the differential pressure transducer and the thermocouples for the wall temperature measurement is explained in this section. Data reduction, uncertainty analysis and the validation of both test section and measurement instrumentation for the flow boiling experiments are also shown.

- The first part of *Chapter 7* provides the experimental procedure adopted for the flow boiling experiments and the range of operative parameters investigated. In the second part, the heat transfer and pressure drop results are shown and the effect of working fluids and thermodynamic conditions as well as the comparisons with predictive methods are also discussed.

- Finally, *Chapter 8* summarizes the main outcomes of this work.

2 Fundamental definitions

This chapter presents the fundamentals of boiling and two-phase fluid mechanics and provides information on the primary parameters used throughout this thesis. The critical heat flux phenomenon occurring in two-phase boiling flows will also be briefly presented. For all the equations displayed, the subscripts "L" and "V" will be used to distinguish between vapor and liquid phase.

2.1 Basic definitions and dimensionless numbers

Dimensional and non-dimensional parameters generally employed for the description of two-phase flows are discussed here.

2.1.1 Vapor quality

The vapor quality x is defined as the vapor mass flow rate $\dot{m}_V$ divided by total mass flow rate of liquid and vapor phase

$$x = \frac{\dot{m}_V}{\dot{m}_V + \dot{m}_L} \tag{2.1}$$

When phase change does not take place in the tube, the vapor quality remains unchanged and it can be obtained by measuring the mass flow rate of each phase. In case the tube is heated and boiling takes place, instead, one should take into account the phase change and the increase of vapor quality along the tube with the following equation, being Δi_{LV} the latent heat, $\dot{m}$ the total mass flow rate and $\delta\dot{Q}$ the heat applied over an infinitesimal length.

$$dx = \frac{\delta\dot{Q}}{\dot{m} \cdot \Delta i_{LV}} \tag{2.2}$$

2.1.2 Cross sectional void fraction

In two-phase flow, the cross-sectional void fraction is one of the most important parameters to be determined, since it provides the mean velocities of the liquid and the vapor phases. It

defines the cross-sectional area occupied by each phase (see Figure 2.1) and it represents a fundamental parameter in the calculation of pressure drop, flow pattern transitions and heat transfer coefficients. The void fraction α is defined as:

$$\alpha = \frac{A_V}{A_V + A_L} \tag{2.3}$$

where A_V is the cross sectional area occupied by the vapor phase and A_L that occupied by the liquid phase. The void fraction may be rewritten by substituting the vapor and liquid mass flow rates obtaining a function of vapor quality, liquid and vapor velocities and densities.

$$\alpha = \frac{1}{1 + \left(\dfrac{u_V}{u_L} \cdot \dfrac{1-x}{x} \cdot \dfrac{\rho_V}{\rho_L} \right)} \tag{2.4}$$

In the above equation, the velocities ratio u_V/u_L is often referred as *slip ratio S,* and may be calculated with dedicated models that either conceive the same velocity for liquid and vapor phase ($S = 1$, *homogeneous model*), or having S > 1 (*separated flow models*).
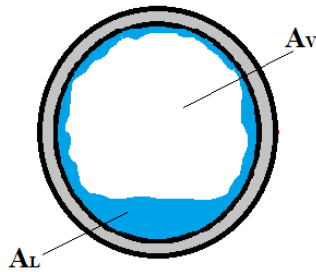
Figure 2.1 Cross sectional void fraction representation

2.1.3 *Mass velocity (mass flux)*

The mass velocity, also referred as mass flux, is defined as the mass flow rate divided by the cross sectional area:

$$G = \frac{\dot{m}}{A} \tag{2.5}$$

The principal unit of measurement for the mass velocity is [kg/m^2 s]. Considering the continuity law, the mass velocity is also the expression of the mean flow velocity multiplied by the mean density.

2.1.4 Reynolds number

The Reynolds number is conventionally defined as the ratio of the inertial forces over the viscous forces. For a single-phase flow inside a duct having an hydraulic diameter d_h, it can be expressed as:

$$Re = \frac{G \cdot d_h}{\mu} \tag{2.6}$$

where d_h is calculated with the ratio of the cross sectional area to over the wetted perimeter. For circular tubes, $d_h = d$.

In case of two-phase flows, the Reynolds number for the vapor and liquid phase is generally expressed, respectively, as:

$$Re_V = \frac{G \cdot x \cdot d_h}{\mu_V} \tag{2.7}$$

$$Re_L = \frac{G \cdot (1-x) \cdot d_h}{\mu_L} \tag{2.8}$$

In some correlations, the authors refer to the Reynolds number evaluated by considering each phase flowing alone in the whole cross section of the tube at the total mass velocity. In this case, the vapor-only and liquid-only Reynolds numbers are defined as:

$$Re_{VO} = \frac{G \cdot d_h}{\mu_V} \tag{2.9}$$

$$Re_{LO} = \frac{G \cdot d_h}{\mu_L} \tag{2.10}$$

2.1.5 Prandtl number

The Prandtl number refers to the ratio of the molecular diffusivity of momentum over the molecular diffusivity of heat. It can be expressed as a function of the fluid properties for both the vapor and the liquid phase.

$$Pr = \frac{\mu/\rho}{\lambda/\rho \cdot c} = \frac{\mu \cdot c}{\lambda} \tag{2.11}$$

$$Pr_V = \frac{\mu_V \cdot c_{p,V}}{\lambda_V} \tag{2.12}$$

$$Pr_L = \frac{\mu_L \cdot c_L}{\lambda_L} \tag{2.13}$$

2.1.6 Bond number

The Bond number is related to the ratio of the gravitational forces to the surface tension forces. In case of flow inside pipes, its characteristic length is the tube hydraulic diameter:

$$Bd = \frac{g \cdot (\rho_L - \rho_V) \cdot d_h^2}{\sigma} \tag{2.14}$$

2.1.7 Boiling number

The Boiling number is a dimensionless parameter that represents the stirring effect of the bubbles upon the flow. This number is often used in correlations for flow boiling heat transfer coefficient and critical heat flux and it is expressed as the ratio of the heat flux q over the mass flux G and the latent heat:

$$Bo = \frac{q}{G \cdot \Delta i_{LV}} \tag{2.15}$$

2.1.8 Froude number

The Froude number represents the ratio of the inertia forces over the gravitational forces. It is often used to correlate the stratification phenomena for two-phase flow inside tubes. It can be expressed as:

$$Fr = \frac{G^2}{g \cdot d_h \cdot \rho^2} \qquad (2.16)$$

The separated vapor and liquid Froude numbers inside a tube may be written as:

$$Fr_V = \frac{G^2}{g \cdot d_h \cdot \rho_V^2} \qquad (2.17)$$

$$Fr_L = \frac{G^2}{g \cdot d_h \cdot \rho_L^2} \qquad (2.18)$$

2.1.9 Weber number

The Weber number expresses the ratio of inertia forced over surface tension forces. Its characteristic length for flows confined into tubes is the inner diameter. However most of the times, for CHF prediction methods, it can be referred to the heated length of the channel. For the liquid phase it is evaluable as:

$$We_L = \frac{G^2 \cdot d_h}{\rho_L \cdot \sigma} \qquad (2.19)$$

2.1.10 Nusselt number

The Nusselt number is defined as the ratio of convection over conduction heat transfer. It can be seen as the dimensionless heat transfer coefficient h. In case of flows inside pipes, its characteristic length is the inner tube diameter:

$$Nu = \frac{h \cdot d_h}{\lambda} \qquad (2.20)$$

2.1.11 Lockart-Martinelli parameter

This parameter X was introduced by Lockart and Martinelli [7] and it is defined as the ratio between the theoretical pressure gradients which would occur if each phase would flow alone in the pipe with the original flow rate of each phase. It is expressed as:

$$X^2 = \frac{\left(\dfrac{dP}{dz}\right)_{LO}}{\left(\dfrac{dP}{dz}\right)_{VO}} \qquad (2.21)$$

This parameter is a measure of how much the two-phase mixture is close to be a liquid ($X>>1$) or to a vapor ($X<<1$). Modeling the pressure drop of each phase with the classical form:

$$f_V = C_V \cdot Re^{-n} \tag{2.22}$$

$$f_L = C_L \cdot Re^{-m} \tag{2.23}$$

and assuming the same friction model for both phases (e.g. both turbulent or both laminar), the exponents $m=n$ and $C_L=C_V$. Equation (2.21) therefore becomes:

$$X_{tt}^2 = \left(\frac{1-x}{x}\right)^{\frac{2-n}{2}} \cdot \left(\frac{\rho_V}{\rho_L}\right)^{0.5} \cdot \left(\frac{\mu_L}{\mu_V}\right)^{\frac{n}{2}} \tag{2.24}$$

The original authors and then Taitel and Dukler [8] used $n = 2$ as exponent:

$$X_{tt}^2 = \left(\frac{1-x}{x}\right)^{0.9} \cdot \left(\frac{\rho_V}{\rho_L}\right)^{0.5} \cdot \left(\frac{\mu_L}{\mu_V}\right)^{0.1} \tag{2.25}$$

The subscript tt means that both phases are considered turbulent. Anyway, several methods are employed in scientific literature to calculate the Lockart-Martinelli parameter for one of both fluids flowing in laminar regime (X_{tl}, X_{lt}, X_{ll}).

2.2   Brief outlines on boiling process

Boiling can be defined as a process in which a liquid substance turns into vapor; this is caused by heating that substance past its boiling point. As a matter of fact, boiling is identified as the heat transfer mechanism that leads to evaporation. Many researchers are intensely working on boiling heat transfer phenomena, because it is really hard to find a common single model which is able to describe the boiling process. Boiling can be divided into several categories, according to the geometric situation and also to the heat transfer contributions that occur. Thus, three different mechanisms of boiling are described:

a) *Nucleate boiling*. Heat transfer causes vapor bubble nucleation, usually at a solid surface. Bubbles then grow and finally detach from the surface.

b) *Convective boiling*. The heat is conducted through a film of liquid. There is no bubble nucleation, but the liquid evaporates at the vapor-liquid interface.

c) *Film Boiling*. Again there is no bubble nucleation and the liquid evaporates at the vapor-liquid interface, but this time there is a film of vapor between the solid heated surface and the liquid. The heat is then conducted through the vapor.

As regard the geometric situation, it is possible to have:

a) *Pool boiling*. The boiling in this case occurs at a heated surface in a pool of liquid which, without taking into account any convection (and therefore any motion) induced by the boiling phenomenon itself, is stagnant. That's to say that there is no flow imposed from the outside.

b) *Flow boiling*. The liquid does not form a pool. It has an imposed velocity relative to the heated surface. Typically, this boiling process shows up when the fluid flows inside a tube, thus pumped through a heated channel.

Another classification is needed: a standard boiling process, in which the fluid temperature is maintained at the saturation point, is so called *saturated boiling*. However, the bubble nucleation might appear even when the bulk fluid temperature is below the saturation point. In this case, the overall boiling mechanism is defined *sub-cooled boiling*.

It is fair to say that in pool boiling only nucleate boiling and film boiling might occur, whereas in flow boiling it is possible to observe all the boiling mechanisms above mentioned.

2.3 Pool boiling

A comprehensive discussion of pool boiling should start with Nukiyama's experiment [9], illustrated in Figure 2.2.
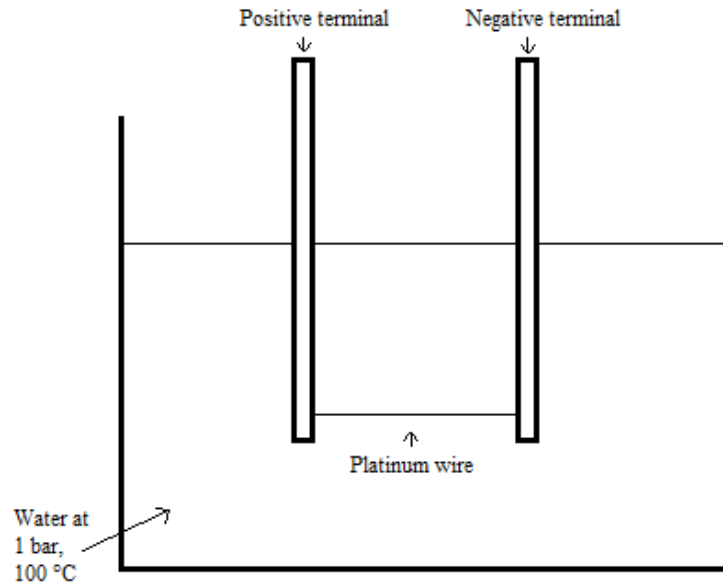
Figure 2.2 Pool boiling experiment with imposed heat flux

A platinum wire is immersed in water and it is electrically heated. The current and the voltage applied at the end of the wire enable the electrical power and therefore the heat flux, which is computable. Moreover, from the electrical resistance of the wire, it is possible to obtain its temperature. Results of this experiment are shown in the form of the *pool boiling curve*, displayed in Figure 2.3, as well as the types of vapor formation and the heat transfer mechanisms. The horizontal axis is made up of wall superheat ΔT_{sat} values (which is the wall temperature minus the liquid saturation temperature), whereas the heat flux q is represented on the vertical axis.
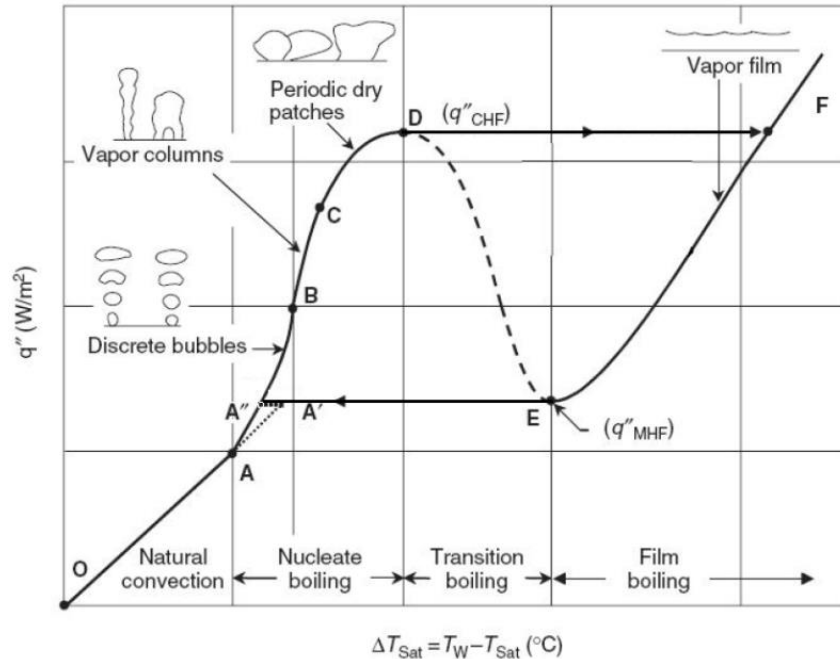
Figure 2.3 Boiling curve and heat transfer mechanisms in pool boiling. Imagine taken from Kandlikar and Chung [10]

It is clear that the pool boiling curve is divided into several regions. At the beginning (O-A) there is no bubble formation, the heat transfer mechanism is merely natural convection with single-phase liquid. At a certain value (A) of ΔT_{sat}, bubbles start to form from the cavities of the heated surface, due to its roughness. This point is known as *onset of nucleate boiling* (ONB). Initiation of boiling goes usually together with a wall superheat excursion (A'), caused by the delay in the first nucleation of bubble, which is much more significant for fluids with great wettability. For these liquids a sudden activation of a large number of cavities at an increased wall superheat leads to a reduction in the solid surface temperature, whereas the heat flux remains constant (A'-A''). After the onset of nucleate boiling, the slope in the boiling curve increases tremendously and the same happens to the heat transfer coefficient. It is still a nucleate boiling mechanism, but at the beginning there are discrete bubbles released from some active sites (A-B), while at higher heat fluxes the nucleating sites become more and more, leading to a strong augment of bubble releasing, with vapor columns rising up from the hot surface (B-C). This type of trend defines the transition from isolated bubbles to fully developed nucleate boiling. In this situation, the evaporation near

15

the bubbles becomes more and more intense, with dry spots on the hot surface which are normally replaced by "fresh" liquid. However, with increasing heat flux, liquid becomes more and more unable to rewet the heated surface and this behavior leads to a strong reduction in the slope of the curve (C-D). At a certain point there is no more macroscopic contact between liquid and heated surface, because the strong nucleation and growth of the bubbles forms a barrier to the incoming liquid; the heat flux corresponding to this condition (D) is so called *critical heat flux* (CHF) or *burnout point* and represents the upper limit of nucleate boiling. When the heat flux is higher than the CHF, there is no longer contact between solid surface and liquid; depending on the magnitude of the heat flux imposed, it might occur a partial or a complete drying of the heated surface. With the equipment shown in Figure 2.2, the boiling curve displays a hysteresis loop (A''-B-C-D-F-E-A''): for increasing heat flux, the process would follow the clockwise-oriented arrows, completely bypassing the dotted line (D-E), which was guessed by Nukiyama. To obtain the complete boiling curve, it is necessary to control the temperature rather than the heat flux and this procedure can be done, for instance, heating the surface with external hot liquid. In this other case, the boiling curve would show no hysteresis. Line E-F represents the stable film boiling, with the surface totally covered with vapor film. The vapor surface is unstable, and bubbles are released from it into the liquid. The E-F line has to be obtained by reducing the heat flux once point F has been reached. Condition E represents the situation when the vapor film can no longer be sustained and collapses; the heat flux associated with that is called *minimum heat flux* (MHF). The region between nucleate and film boiling, represented by the dotted line D-E, is known as the transition boiling region. It is a complex region where parts of the surface are in film boiling regime and parts in fully developed nucleate boiling regime (with slugs and columns).

As a summary, the pool boiling curve suggests three different boiling regimes, along with additional sub-regions: nucleate boiling, transition boiling and film boiling.

To better understand the pool boiling phenomenon, Figure 2.4 taken from [11] displays the various stages in the pool boiling curve.
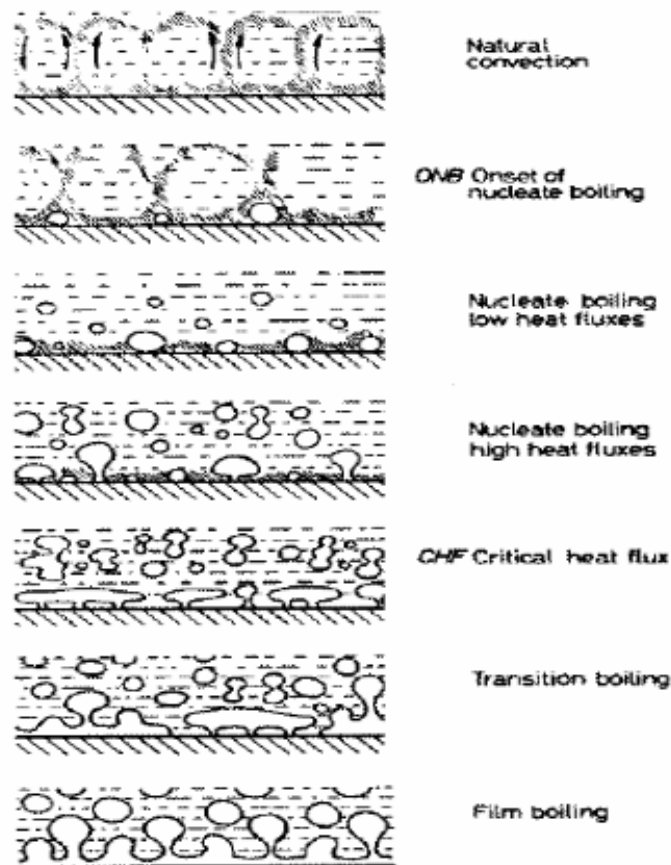
Figure 2.4 Various patterns in the pool boiling process at increasing heat flux [11]

Some parameters are important in a pool boiling process, since they are able to modify the pool boiling curve. First of all surface wettability, which shifts the nucleate boiling line toward the right; thus, for the same wall superheat $T_w - T_{sat}$, the heat flux is less than before and it leads to minor nucleate boiling heat transfer coefficients. The surface roughness is also an important parameter: it tends to move the nucleate and transition lines to the left, implying improvement in the nucleate boiling heat transfer characteristics [12]. Cracks and crevices do not, of themselves, constitute nucleation sites for the bubbles: they must also contain pockets of gas, probably air trapped when the vessel is filled with the liquid; it is from these pockets of trapped air that vapor bubbles begin to grow during nucleate boiling. Surface contamination (as depositions or dirt particles) has an effect similar to surface roughness.

The heat transfer coefficient in nucleate boiling is very high (typically above 10 kW/m^{2}K). As explained by Hsu and Graham [13], at least three heat transfer mechanisms controlling the nucleate pool boiling process can be identified:

Bubble agitation mechanism. During their growth, bubbles move from their original position, giving motion to surrounding liquid. This situation determines a sort of liquid forced flow which augments the heat transfer coefficient.

Vapor-liquid exchange mechanism. After the bubbles departure from the surface, some "fresh" liquid from on high comes to cool down the heated surface, taking away sensible heat.

Microlayer evaporation mechanism. While conventional evaporation takes place around the sides and top of the bubble, micro-evaporation is happening in the thin layer of liquid underneath the bubble which is trapped between a rapidly growing bubble and the hot surface.

The microlayer evaporation is an important phenomenon which deserves particular attention, since it is possible that the same mechanism happens in the thin film between the elongated bubbles and the heated wall in narrow tubes. This could explain the similarity in behavior between pool boiling and boiling in micro-channels.

In conclusion, pool boiling is an interesting type of heat transfer for many thermal cooling systems, since it can sustain large heat fluxes with low heated surface temperatures. One of its direct applications is in flooded evaporators, where the fluid that needs to be cooled is flowing into pipes, which are completely flooded by saturated liquid refrigerant.

2.4 Flow boiling

In flow boiling, the evaporating liquid has a certain velocity relative to the heated surface (the inside wall of a tube), and this leads to an increasing vapor quality along the channel. Unlike pool boiling, there is not a precise pattern once wall superheat and heat flux are determined: two-phase flow regimes in a boiling channel are "developing" along the heated channel itself. Thus, it is useful to introduce the various types of patterns which can occur in a flow boiling process, before dealing with heat transfer mechanisms.

2.4.1 Two-phase flow patterns in flow boiling

The two phases in a heated channel can adopt various geometric configurations, known as flow patterns, according to the special distribution of the vapor and liquid phases in the channel. To determine and predict a flow pattern, it is necessary to analyze at least three physical parameters:

a) Surface tension, which tends to maintain the channel wall always wet and to form small liquid drops and small spherical gas bubbles;

b) Gravity, which tends to pull the liquid to the bottom of the channel;

c) Deformability of the gas-liquid interface that often results in continuous coalescence and breakup processes.

Some common flow patterns for vertical upflow are shown in Figure 2.5:

| Bubbly | Slug | Churn | Annular/Dispersed |
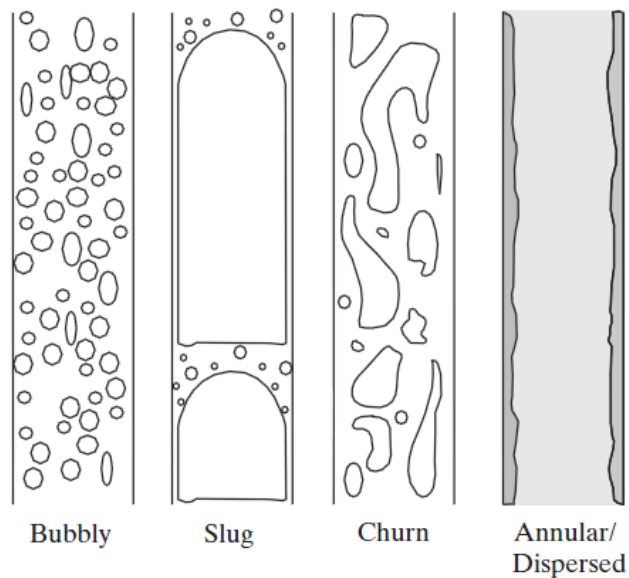
Figure 2.5 Some flow patterns occurring in vertical upflow in a tube

In bubbly flow, the vapor phase is present in form of bubbles dispersed in the continuous liquid phase. These bubbles may vary in size and shape, depending on the substance

properties and other parameters, but they are nearly spherical and smaller than the size of the tube. Bubbly flow ends when discrete little bubbles coalesce and produce very large bubbles, which reach the tube diameter size and eventually become elongated.

In plug flow (sometimes known as slug flow) the gas phase is present as large bullet-shaped bubbles, with hemispherical nose and irregular tail; there are also some small gas spots distributed throughout the liquid phase. The main bubbles are known as Taylor bubbles and they are surrounded by a thin liquid film between them and the tube wall and also separated one each other by plugs of liquid.

At higher vapor qualities, the disruption of the large Taylor bubbles leads to churn flow, where chaotic motion of the irregular-shaped gas pockets takes place. This flow pattern is highly unstable, due to its oscillatory nature: large waves are moving forth in the flow direction and the liquid near the tube wall continuously pulses up and down.

With increasing vapor quality, annular flow replaces churn flow. The liquid travels partly as an annular film on the walls of the tube and partly as small drops (entrainment) distributed in the gas, which flows in the center of the tube. Usually the interface is disturbed by high frequency waves. Eventually, the liquid film thickness at the wall completely evaporates or is torn due to the instabilities and the annular flow is replaced by mist flow, in which the remaining liquid remains dispersed in the vapor core.

The common flow patterns for horizontal tubes are illustrated in Figure 2.6. They are similar to those in vertical flows, but the distribution of the liquid is influenced by gravity that tends to stratify the liquid to the bottom of the tube and the gas to the top. Moreover, unlike vertical tubes, some patterns may occur or not, depending on the flow rate value and its effect on the gravity force.
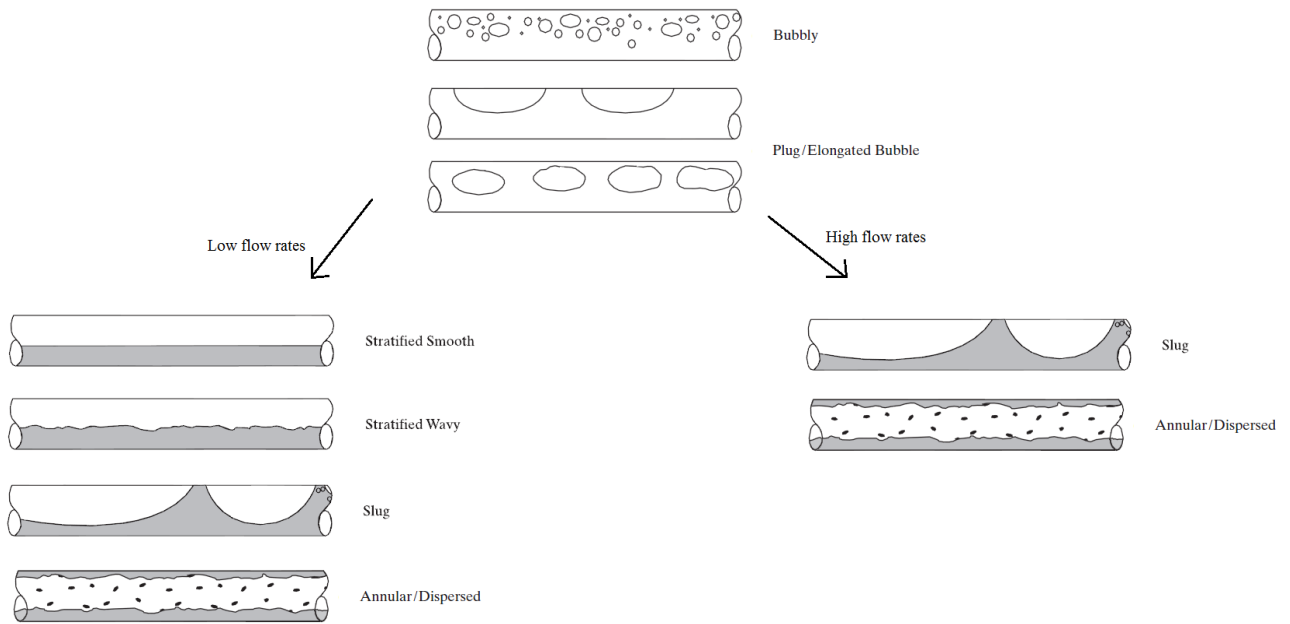
Figure 2.6 Flow patterns in horizontal flow in a tube occurring at low and high flow rates

Bubbly flow and plug flow are almost the same already seen in vertical upflows, except from the gas phase position, which is now considerably closer to the upper wall of the channel. The stratified smooth flow regime occurs at very low flow rates and it is characterized by a complete separation between the liquid and the gas phase, which occupies the upper part of the tube. Moreover the liquid-gas interface is smooth. Most frequently the interface is wavy, leading to the stratified wavy flow. For higher flow rates, instead, a complete stratified flow never shows up and the inner walls are wetted up to the top of the channel. At higher vapor qualities, the wave amplitude is so large that it is able to wet the entire channel cross section. This regime, known as slug flow, is thus different from the slug flow already defined for vertical pipes, since the gas phase is no longer contiguous: the liquid can contain entrained small droplets and the gas phase may contain entrain liquid droplets.

With increasing vapor quality, annular flow appears. This regime is very similar to vertical annular flow, except that the liquid film is ticker at the bottom of the tube than at the top, because of the gravity effect.

Different writers have defined other flow patterns, creating almost 100 different names. Many of these are merely alternative names, while others delineate minor differences in the

main flow patterns already presented. These ones probably represent the minimum number which can sensibly be defined.

2.4.2 Heat transfer in flow boiling

Figure 2.7 displays a picture of forced flow boiling process for a circular vertical tube with uniform heat flux imposed and a qualitative temperature profile. In this case liquid enters the tube in sub-cooled conditions.
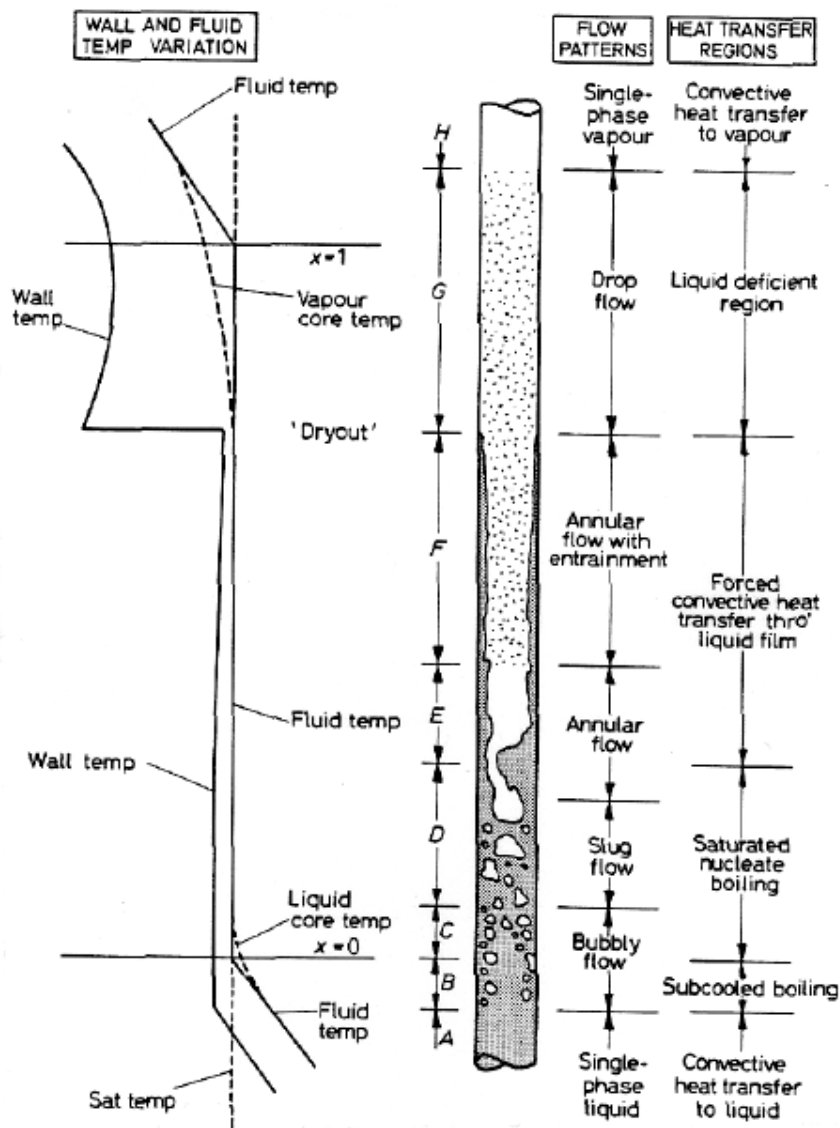
Figure 2.7 Flow boiling in a vertical tube, with wall and fluid temperature. Image taken from Collier and Thome [11]

The overall boiling process can be seen as the composition of three different contributions: nucleate boiling, with the formation of bubbles occurring at the solid surface; convective evaporation, which takes place at the interface between liquid and gas phases; film boiling, which may appear in case of flow instabilities, with internal walls not completely covered by the liquid phase. Particularly, referring to Figure 2.7, several distinct areas can be observed:

Zone A: The fluid enters the tube in sub-cooled conditions. Heat transfer mechanism is merely convective heat transfer to liquid. Both wall temperature and fluid temperature are increasing, thus the heat transfer coefficient is almost constant.

Zone B: Wall temperature might exceed the saturation temperature, but the bulk fluid temperature is still below this limit. This situation leads to an overall vapor quality less than 0, but bubble nucleation may appear close to the channel walls. Bubbly flow is the actual flow pattern. The bubbles just formed grow and reach out into the relative cool liquid, thus the vapor begins to condense and in doing so causes the liquid temperature to rise slightly, therefore approaching the saturation temperature. For this reason, the heat transfer coefficient increases rapidly. This primary formation of bubbles is known as onset of nucleate boiling, ONB.

Zone C: Bulk fluid has approached the saturation temperature, thus the average vapor quality is greater than 0 and saturated nucleate boiling can start. Fluid and wall temperatures remain the same, thus the heat transfer coefficient is almost constant. In this region more nucleation sites are activated, then the contribution to heat transfer from convective single-phase mechanism becomes negligible.

Zone D: Individual gas small bubbles coalesce, forming bullet-shape vapor bubbles. Nothing has changed for the heat transfer region, since the leading mechanism is saturated nucleate boiling, and still the heat transfer coefficient is almost constant.

Zone E: Further downstream, the heat transfer mechanism changes, because of the addition of vapor in the flow. Liquid plugs tear and a thin film of liquid is attached to the channel walls, forming the annular flow. While nucleate boiling is predominant in the bubbly and slug flow regimes, the annular flow pattern brings to a convective boiling mechanism. The thickness of the thin liquid film in annular flow is such that the thermal conductivity is able

to prevent the liquid from being superheated enough to sustain bubble nucleation. Heat is therefore transferred from the wall by forced convection to the liquid-vapor interface, where evaporation occurs.

Zone F: As the flow rate ought to be constant, the liquid evaporation makes the vapor velocity increase, and this leads to two consequences. First of all, the liquid-vapor interface is no longer smooth, but it becomes wavy, with some liquid droplets torn from the liquid (annular flow with entrainment). The most important consequence, however, is that the rapid vapor pushes the liquid film against the wall, dragging it towards the end of the channel and improving the convective heat transfer mechanism. The difference between the wall and the fluid temperature gets smaller, thus the heat transfer coefficient increases slowly.

Zone G: In the annular flow the liquid film gets thinner and thinner, until it dries out. This phenomenon is then known as dry-out (or burnout, even if this last definition implies that the physical solid surface is destroyed, which does not always occur). From this point on, the wall is completely dry, but some liquid droplets may occupy the central part of the channel (entailing a drop flow). Because of the lack of liquid film in the channel, the wall temperature suddenly rises, while the fluid temperature remains almost constant (equal to saturation temperature), at least until the vapor quality is lower than 1. In fact, vapor temperature slowly rises, but it is cooled down thanks to the evaporation of the droplets present in the middle of the channel. This situation leads to a tremendous decrease of the heat transfer coefficient, and the heat transfer regime might be defined as "liquid deficient region".

Zone H: Further downstream, eventually the entrained droplets will completely evaporate, leading to a pure vapor single-phase flow and to a single-phase vapor forced convection heat transfer regime. The fluid temperature rises together with the wall temperature, and the heat transfer coefficient remains low.

From this description, it could be noticed that bubble nucleation begins when the thermodynamic quality x is lower than 0 and liquid drops persist when the vapor quality is greater than 1. This leads to the assumption that there is no thermodynamic equilibrium in these areas: both liquid and vapor are not saturated and so not in equilibrium with each other.

The evolution of flow boiling inside a horizontal circular tube is shown in Figure 2.8.
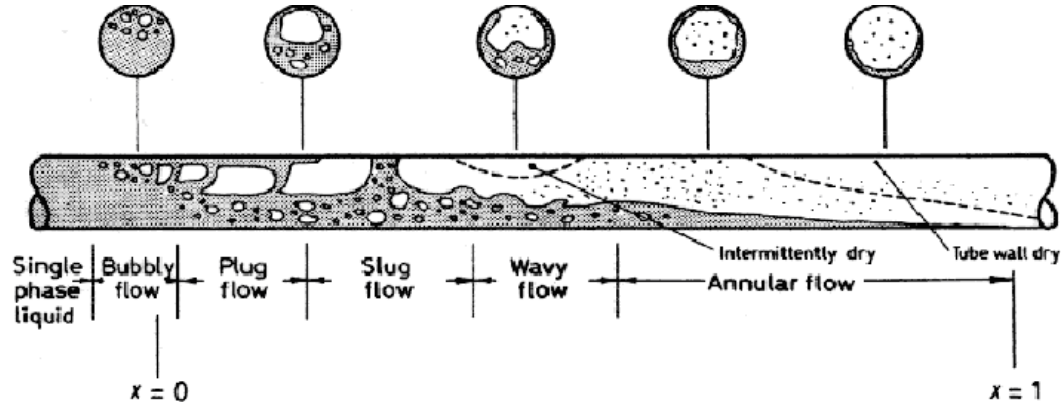
Figure 2.8 Flow boiling in a horizontal circular tube. Image taken from Collier and Thome [11]

Although there are no great differences between what happens in horizontal and vertical pipes, gravity force tends to push the liquid phase to the bottom of the channel. The annular flow is therefore slightly asymmetric and eventually the top part of the channel might be intermittently dry. This means that the dry-out tends to begin at the top and progressively to increase around the perimeter of the tube in the direction of the flow. Actually the annular flow pattern is typical for high flow rates (when the vapor phase, with its velocity, is able to sustain the liquid phase on the top, prevailing over the gravity force), whereas for low flow rates the two phases might be completely separated in a wavy flow. In this case the top of the tube may be intermittently dry if the waves wash the top of the tube or completely dry otherwise.

2.4.3 Critical heat flux

Finally, the study of flow boiling cannot overlook the critical heat flux (CHF) phenomenon, that refers to the value of heat flux at which the local heat transfer coefficient decreases sharply due to the replacement of liquid by vapor phase adjacent to the heat transfer surface [11] [14]. There exist other terminologies for this condition in the literature such as DNB (departure from nucleate boiling), dry-out, boiling crisis and burn-out, with the last one used to point out the consequent sharp rise of the wall temperature and the physical irreversible damage caused to the device that has to be cooled. However, none of these terms are fully satisfactory and due to the complexity of the phenomenon itself, most of researchers have

their own CHF definition and detecting method used for their experiments. A summary of the CHF operative definitions encountered in scientific literature will be given in the next chapter. Generally, the CHF condition can be of different nature:

Sub-cooled CHF

In this case, the phenomenon is also known as DNB (departure from nucleate boiling) the bulk fluid temperature is below the saturation temperature when CHF occurs. This condition may be reached in case of large mass velocities, high inlet sub-cooling and channels with a small heated length-to-diameter ratio [14]. At the channel outlet, the bulk fluid remains mostly in the liquid state and a large number of small vapor bubbles cover the heated wall behaving as a vapor film layer. Some theories for the sub-cooled CHF are:

- Intense boiling, bubble-liquid boundary separates from the heated wall, resulting in a stagnant liquid to evaporate.
- Bubble crowding, that prevents liquid flow rewetting the surface and therefore causing vapor layer.
- Dry-out of liquid sub-layer beneath large vapor bubbles that causes the rise of local wall temperature.

Saturated CHF

This type of CHF is instead caused by a gradual depletion of the liquid film on the heated wall and it is more related to a dry-out phenomenon [14]. In this case, the flow pattern is mostly annular. As shown in Figure 2.9, the crisis occurs when the flow rate of the liquid film reduces and eventually goes to zero. Saturated CHF may be generally encountered in case of small mass velocities, a low inlet sub-cooling degree and geometries with high values for the heated length-to-diameter ratio.
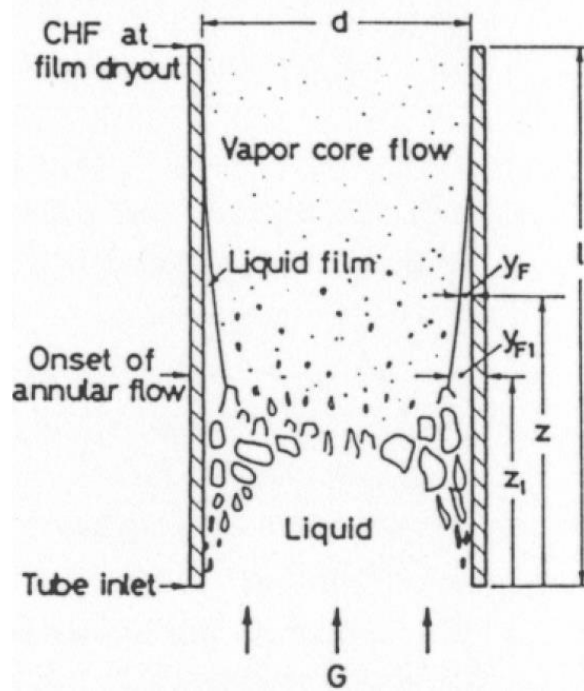
Figure 2.9 Schematic representation of saturated CHF in a vertical heated tube. Image taken from Katto [15]

3   Literature review

This chapter presents a state of the art review of in-tube flow boiling and critical heat flux in minichannels and multi-minichannels heat sink. Following the same order of the following experimental chapters, the literature review will be firstly focused on the critical heat flux topic and then to the flow boiling heat transfer and pressure drop studies.

3.1   Critical heat flux review

The CHF detection methods used by different researchers will be discussed in the first sub-section. Then, recent studies on saturated CHF conducted with minichannels or multi-minichannel systems are reviewed. Finally, empirical correlations and CHF predictive methods are summarized in the last section.

3.1.1   Critical heat flux definition in literature

Despite the differences between sub-cooled CHF and saturated CHF phenomena explained in the previous chapter, critical heat flux is usually referred in literature as the condition in which the cooling mechanism cannot be sustained any longer due to a sudden deterioration of the wall heat transfer coefficient.

Actually, the terms critical heat flux (CHF) and dry-out are often indifferently used in scientific papers to describe the situation where the heated surface lacks its contact with the liquid phase, leading to a sharp rise of the wall temperature. Some researchers [16] [17] [11] state that the difference between the two terms are due to the way in which the mentioned situation occurs. Kim and Mudawar [16], for instance, link the term CHF to an abrupt phenomenon, more similar to the departure of nucleate boiling (DNB) occurring in case of high sub-cooling and when the amount of liquid in the channel is still considerable. The authors also stated that CHF is mainly a function of the inlet sub-cooling and the working fluid, identifying also several triggering mechanisms. On the other hand, they define dry-out as a gentler phenomenon occurring in case of saturated conditions and only when the flow

regime is annular. Maqbool et al. [18], instead, define differently CHF and dry-out as two different mechanisms occurring in saturated conditions. They stated that that critical heat flux might appear at any vapor quality, representing the upper limit of the wall heat flux at which the liquid is intensely torn from the heated surface. Dry-out, instead, should appear always at a higher vapor quality, independently on the wall heat flux imposed, when the liquid film thickness is no longer sufficient to wet the channel wall. Moreover, they distinguish the *dry-out incipience* (also known in other works as *intermittent dry-out*, *onset of dry-out*), that is the case in which the liquid film is still present but vanishingly, having intermittent dry patches caused by an uneven evaporation and/or a lack of symmetry in the liquid film. *Dry-out completion*, instead, was described to occur at higher vapor qualities, when the liquid film is completely evaporated. The approach of Maqbool et al. [18] is further shown in Figure 3.1, in which both the dry-out incipience and dry-out completion are highlighted in the boiling curve of propane flowing at a mass flux of 100 kg/m^2 s and a saturation temperature of 23 °C.
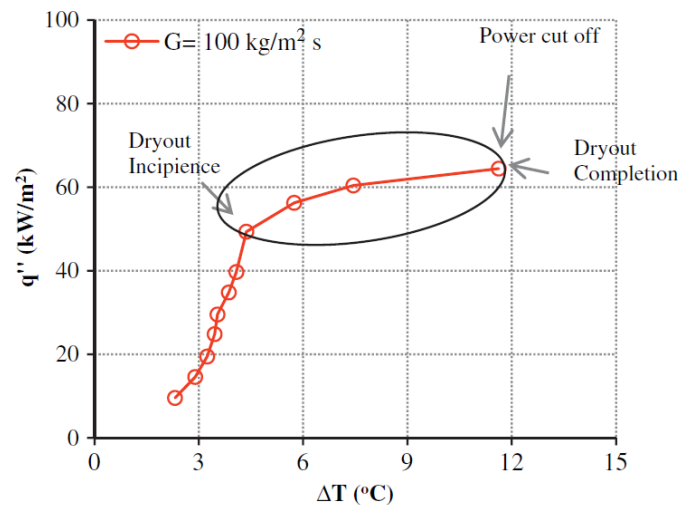
Figure 3.1 Boiling curve of propane with highlighted dry-out incipience and completion according to the definition of Maqbool et al. [18]

Callizo et al. [19] and Ali and Palm [20] identify in the dry-out incipience the situation in which the heat transfer coefficient decreases appreciably, leading to an evident shift in the

slope of the boiling curve and therefore to sharp increases in the wall superheat with small increments of the wall heat flux.

A considerable amount of parameters, together with the working fluid itself, may influence the CHF mechanism. The boiling curve is in fact highly dependent on the working fluid, mass velocity, heat sink geometry, heated surface material, roughness and so on. For the CHF experiments of Qu and Mudawar [21] with water in rectangular microchannels, a sudden rise of the wall superheat was detected, with a narrow dry-out region and almost no difference between the dry-out incipience and completion. Thus, the phenomenon could be closely linked to critical heat flux. Other experiments carried out by Lee and Mudawar [22] with refrigerant R134a show instead a wider dry-out region, with a boiling curve that gently changes its slope. Figure 3.2 shows the mentioned experiments taken from different studies and the difference in the extent of the dry-out regions. Kim and Mudawar [16] suggest that the sharp change in the boiling curve slope is typical of fluids carrying a high latent heat (as water and ammonia), whereas the broader dry-out region might be linked to refrigerants and other dielectric fluids having a relatively low latent heat and lower CHF values.
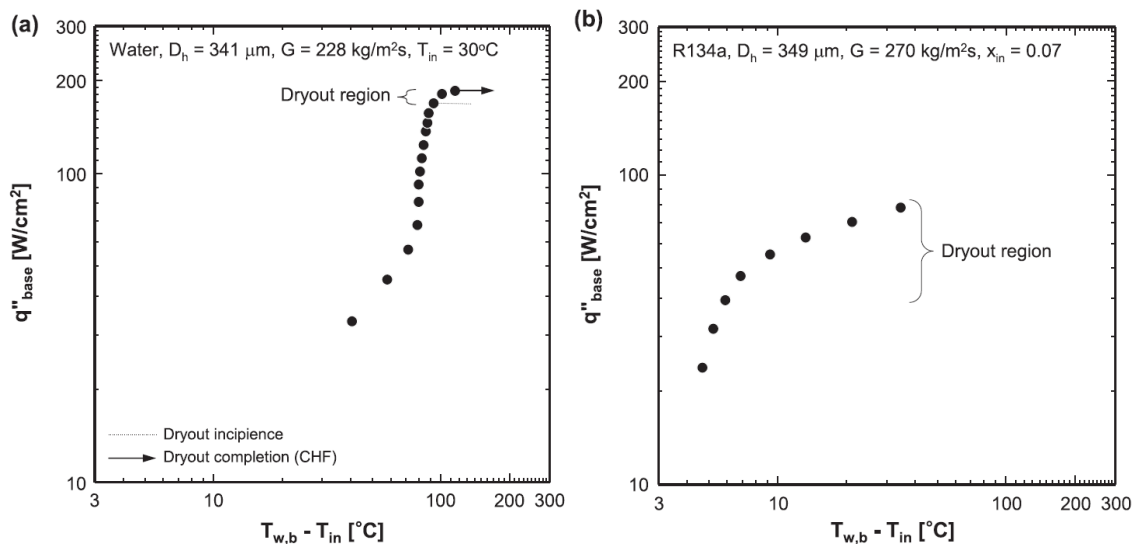
Figure 3.2 Differences in dry-out regions extent observable in boiling curves of different refrigerants at similar operating conditions and geometry [16]. (a) Boiling curve of water (high latent heat). (b) Boiling curve of R134a (low latent heat)

However, sudden excursion of the wall temperature are also found in literature for refrigerants, especially in case of single ducts [23] [24]. Other authors have instead found a different behavior with flow boiling of refrigerants inside multi-minichannel systems [25] [26] [27]. The presence of the solid heat sink substrate and its non-negligible thickness may in fact lead to heat redistribution aided by conduction phenomena, causing therefore a mitigating effect on the critical condition and a gentler boiling curve nature. This effect was found to be more evident when increasing the thickness of the metal substrate and/or the number of minichannels in the work of Saenen and Thome [28]. Finally, the mass velocity is also recognized as a key factor to determine the boiling curve shape [25] [29].

As shown, for saturated flow boiling the distinction between dry-out incipience and dry-out completion and CHF is often indistinct in open literature and some works use different terms and detection methods to refer to the same phenomenon.

Different authors opted for different CHF detection methods, according to their experimental results. For instance, Lazarek and Black [30], Katto and Ohno [31], Qu and Mudawar [21], Wojtan et al. [23] identified CHF as a sudden excursion of the wall temperature by almost keeping constant the imposed heat flux. Other studies pointed out instabilities when approaching critical heat flux: Lezzi et al. [32], Kim et al. [33] and Kuan [34] identified CHF when the wall temperature was exposed to a sharp temperature excursion in a short span of time. Mauro et al. [26] and Mastrullo et al. [29] located CHF when the slope of the boiling curve was found to be inferior to a chosen threshold of 1.0 W/cm^2 K. Finally, among other researchers, Ong and Thome [24], Ali and Palm [20], Tibiriçá et al. [35], Anwar et al. [36], Agostini et al. [37] identified CHF as the wall heat flux corresponding to a chosen threshold for the wall superheat, regardless the boiling curve shape. From a practical point of view, this last method succeeds to preserve the device that has to be cooled from overheating and burn-out in real applications, without looking at the stability of the boiling process.

It is important to highlight that different CHF detection methods lead to different CHF values for the same experiments. For this reason, large discrepancies are found in literature for critical heat flux tests taken in similar conditions and prediction methods may be substantially different from one another. In this thesis, a new different method [38] to detect the thermal crisis is employed. Further details will be given in section 4.3.3.

3.1.2   Critical heat flux studies for minichannels and multi-minichannel heat sinks

Recent studies on saturated CHF performed with mini or microchannels are here briefly reviewed.

Bowers and Mudawar [39] performed saturated CHF experiments for flow in an array of circular tubes inserted in a test block. Refrigerant R113 was used as working fluid with mass velocities from 31 to 150 kg/m^2 s for minichannels of 2.54 mm diameter and from 120 to 480 kg/m^2 s for microchannels of 0.51 mm diameter. The system pressure was 1.38 bar, with inlet sub-cooling ranging from 10 to 32 K. The authors observed a lack of inlet sub-cooling effect on CHF.

Yun and Kim [40] investigated the dry-out of carbon dioxide for flow boiling in tubes of 2.0 and 0.98 mm internal diameter. The authors noted that the critical vapor quality (i.e. the vapor quality at the critical condition) was lower for larger heat flux but increased slightly with increasing mass flux.

Qu and Mudawar [21] studied saturated CHF for water in a microchannel copper heat sink made up of an array of 21 rectangular channels (215 μm wide and 821 μm high). Experiments were conducted for 18 different operative conditions over a mass flux range of 86-368 kg/m^2 s and a pressure close to the ambient, with inlet sub-cooling of 40 and 70 °C. They observed that the CHF was independent on the inlet temperature but it increased slightly with increasing mass flux.

Kuan and Kandlikar [41] experimentally investigated the critical heat flux of water in six parallel microchannels in different operative conditions. Their results showed that the CHF increased with mass flux but decreased with increasing exit vapor fraction.

Roday et al. [42] performed critical heat flux experiments in a single tube with internal diameter of 0.427 mm, showing that CHF increased with an increase in mass flux and exit pressure. In case of saturated conditions, the CHF was also found to have an increasing trend with quality.

Agostini et al. [37] obtained CHF values for refrigerant R236fa in a silicon multi-microchannel heat sink made up of 67 parallel channels, each of them 223 μm wide and 680 μm high, with a length of 20 mm. The wall CHF was seen to increase with increasing mass

velocity (from 276 to 992 kg/m^2 s), whereas the inlet saturation temperature (from 20.31 to 34.27 °C) and the inlet sub-cooling (from 0.4 to 15.3 K) were found to have a negligible influence on the saturated CHF.

Park and Thome [25] measured CHF of R134a, R236fa, R245fa in two different multi-microchannels copper heat sinks, made up of 20 and 29 channels, respectively. With increasing mass velocity (from 100 to 4000 kg/m^2 s) the CHF was observed to be higher, but the increase rate was slower for higher mass fluxes. CHF was instead seen to decrease with increasing inlet saturation temperature (a range of 10-50 °C was investigated). These trends were found to be dependent both on the flow condition and the channel size.

Mauro et al. [26] studied saturated CHF of R134a, R236fa and R245fa in a multi-microchannel heat sink, made up of 29 copper parallel channels that were 199 μm wide and 756 μm high. The different effects regarding mass velocity, saturation temperature and inlet sub-cooling were investigated. It was found that CHF enhancement was possible with a split flow system (that is one inlet and two outlets), providing also a much lower pressure drop.

Ali and Palm [20] obtained saturated CHF measurements with refrigerant R134a in vertical single tubes with two different internal diameters (1.224 mm and 1.70 mm) and a heated length of 220 mm. The saturation temperatures investigated were of 27 and 32 °C, whilst the mass flux was kept within the range 50-600 kg/m^2 s. The authors found that the CHF was almost not affected by a change in the saturation temperature, whereas it increased with increasing mass flux and decreased with reducing the tube diameter.

Ong and Thome [24] published CHF results with refrigerants R134a, R236fa and R245fa in 1.03 mm, 2.2 mm and 3.04 mm diameter horizontal circular tubes. The authors observed no influence of the sub-cooling degree, while CHF increased with increasing mass flux and decreased at higher saturation temperatures. Finally, CHF was seen to rise with decreasing the tube diameter until a threshold value of 0.79 mm, in which the trend was reversed.

Maqbool et al. [18] performed dry-out tests of propane in a single vertical round minichannel with internal diameters of 1.22 mm and 1.70 mm, using the same experimental facility of [20]. They found a higher CHF with reducing the inlet vapor quality, whereas the thermal crisis was significantly delayed by increasing the mass velocity from 200 to 400 kg/m^2 s.

Finally, the authors observed that the influence of the saturation temperature (23 °C to 43 °C) was negligible.

Tibiriçá et al. [35] obtained CHF data in circular tubes using R134a and R245fa and compared the results with experimental data obtained with flattened tubes having the same equivalent internal diameter of 2.2 mm, but different aspect ratios of 1/4, 1/2, 2 and 4. The saturation temperature was fixed to 31 °C. The CHF data were found to be independent on the tube aspect ratio when the same heated length was kept.

Mikielewicz et al. [43] presented CHF results for four fluids (SES 36, R134a, ethanol and R123) in two small diameter silver tubes with inner diameter of 1.15 mm and 2.3 mm, at a wide range of saturation temperatures and mass fluxes. Similarly to other authors [10, 11, 12], they found the CHF being enhanced (more than 200 %) when increasing the inner diameter tube from 1.15 mm to 2.30 mm.

Diani et al. [44] investigated on flow boiling of R1234yf and R1234ze inside a 3.4 mm internal diameter microfin tube. The authors obtained CHF values by keeping constant the saturation temperature to 30 °C. The inlet vapor quality was instead varied from 0.10 up to 0.99. For both fluids, they found that the vapor quality in critical condition was increasing from 0.85 to 1.0 when the mass flux ranged from 200 to 900 kg/m^2 s.

Anwar et al. [45] performed several tests with R1234yf in a vertical stainless steel test section (1.60 mm inside diameter and 245 mm heated length) under upward flow conditions. They found that signs of dry-out first appeared at vapor qualities of 85%, with the values generally increasing with increasing mass flux.

Different authors also tried to examine the effect of the heated length-on-diameter ratio on the saturated CHF. Lezzi et al. [32] studied critical heat flux of water in a single circular channel with a fixed internal diameter of 1.0 mm. By changing the heated length from 502 to 975 mm, they found that CHF changed from 1.6 to 0.9 MW/m^2, with a reduction of 44%.

Wojtan et al. [23] used different heated length (from 20 to 70 mm) for their single circular channel of 0.50 and 0.80 mm ID, finding out that the CHF dropped more than 65% when increasing the L_h/D ratio from 25 to 87.5.

Del Col et al. [46] investigated the dry-out during flow boiling of R134a and R22 inside a 0.96 mm single circular microchannel heated with a secondary fluid. The authors reported that the average critical heat flux increased with mass velocity and decreased with increasing the heated length. At critical condition, the vapor quality ranged from 0.65 to 0.85 in case of R134a and from 0.4 and 0.7 in case of R22.

Roday and Jensen [47] obtained experimental CHF data for water and R123 in a single horizontal channel, by changing the heated length and the inner diameter. In case of water with the tube of 0.286 mm, the authors found a significant CHF drop (approximately -52%) when increasing the heated length from 21.66 to 57.62 mm, both for low (315 kg/(m^2 s)) and high (1570 kg/(m^2 s)) mass fluxes.

Tanaka et al. [48], by collecting different CHF data from existing study, stated that critical heat flux was greatly affected by the L_h/D ratio, especially at low mass velocities, where CHF dropped more than 100% by augmenting L_h/D from 50 to 179.

Wu and Li [49] examined the effect of the L_h/D ratio on the critical Boiling number *Bo*, obtaining that at a threshold of $L_h/D = 150$, its influence on the critical phenomenon was negligible. For lower values, the Boiling number was seen to steeply decrease with the heated length.

3.1.3   Existing correlations for critical heat flux

Most of CHF prediction correlations rely on empirical models since the physics behind the controlling mechanism is not fully understood yet. Here, some well-known existing correlations that could be used to predict saturated flow boiling CHF are presented.

The correlation of Lazarek and Black [30] was developed to predict critical conditions under low reduced pressures, taking also into account the effects of the sub-cooling:

$$CHF_{Lazarek-Black} = G \cdot D^{0.25} \cdot \left(\frac{D}{L_h}\right)^{0.59} \cdot \left(1 + 3.11 \cdot \frac{\Delta i_{sub}}{\Delta i_{LV}}\right) \qquad (3.1)$$

Being an empirical correlation, the tube diameter has to be expressed in [cm] and the CHF in [W/cm^2].

Katto and Ohno [31] improved their original generalized CHF correlation of forced convective boiling in uniformly heated tube, developed for large tubes and a wide range of experimental conditions and working fluids. Their correlation considered the critical boiling number as a function of the sub-cooling as well as the densities ratio, the liquid Weber number and the heated length-to-internal diameter ratio:

$$CHF_{Katto-Ohno} = \dot{q}_{co} \cdot \left(1 + K \cdot \frac{\Delta i_{sub}}{\Delta i_{LV}}\right) \tag{3.2}$$

$$\dot{q}_{co} = f\left(\frac{\rho_V}{\rho_L}; \frac{\sigma \rho_L}{G^2 L_h}; \frac{L_h}{D}; \frac{\Delta i_{sub}}{\Delta i_{LV}}\right) \tag{3.3}$$

Due to the correlation complexity and length, the reader may find more details and the whole prediction method in the reference mentioned.

Qu and Mudawar [21] developed the following correlation based on their CHF data for water in a microchannel heat sink. The authors found no influence of the sub-cooling, which was not included in their prediction method.

$$CHF_{Qu-Mudawar} = 33.43 \cdot G \cdot \Delta i_{LV} \cdot \left(\frac{\rho_V}{\rho_L}\right)^{1.11} \cdot We_L^{-0.21} \cdot \left(\frac{L_h}{D}\right)^{-0.36} \tag{3.4}$$

Zhang et al. [50] developed a correlation based on the Weber number evaluated with the channel diameter and the heated length-to-diameter ratio. This predictive method was obtained with a large database concerning flow boiling of water in tubes with different diameters and heated lengths. The investigated system pressures varied from 1.01 up to 190 bar and the mass fluxes ranged from 5.33 up to 134000 kg/m^2 s. Also the inlet vapor quality was taken into account:

$$CHF_{Zhang} = 0.0352 \cdot G \cdot \Delta i_{LV} \cdot \left[We_D + 0.0119 \cdot \left(\frac{L_h}{D}\right)^{2.31} \cdot \left(\frac{\rho_V}{\rho_L}\right)^{0.361}\right]^{-0.295} \cdot \left(\frac{L_h}{D}\right)^{-0.311} \cdot \left[2.05 \cdot \left(\frac{\rho_V}{\rho_L}\right)^{0.17} - x_{in}\right] \tag{3.5}$$

Wojtan et al. [23] proposed the following correlation that well fitted their data for saturated CHF of R134a and R245fa in their minichannel:

$$CHF_{Wojtan} = 0.437 \cdot G \cdot \Delta i_{LV} \cdot \left(\frac{\rho_V}{\rho_L} \right)^{0.073} \cdot We_L^{-0.24} \cdot \left(\frac{L_h}{D} \right)^{-0.72} \qquad (3.6)$$

Kuan [34] developed a correlation for saturated CHF of water and R123 flowing into a multi-minichannel heat sink, with mass fluxes ranging from 50.4 to 533.8 kg/m^2 s and inlet vapor qualities from 0.39 to 0.93. The empirical formula considers a linear dependence of the CHF on the mass velocity and does not take into account the sub-cooling effect:

$$CHF_{Kuan} = 0.2305 \cdot G \cdot \Delta i_{LV} \cdot \left(\frac{L_h}{D} \right)^{-0.9056} \qquad (3.7)$$

Callizo [51] modified Katto and Ohno correlation based on his experimental data with R134a, R22 and R245fa in a 0.640 mm tube and a uniformly heated length of 213 mm. As claimed by the author, since the channel diameter and heated length remained unchanged in the experimental investigation, their effect on the CHF represented by the Weber number and length-to-diameter ratio may not have been captured in the following correlation.

$$CHF_{Callizo} = 0.3216 \cdot G \cdot \Delta i_{LV} \cdot \left(\frac{\rho_V}{\rho_L} \right)^{0.084} \cdot We_L^{-0.034} \cdot \left(\frac{L_h}{D} \right)^{-0.942} \qquad (3.8)$$

Kosar and Peles [27] suggested a new CHF correlation for multichannel saturated CHF based on their R123 tests. Since no existing correlation followed their CHF trend with the system pressure, they developed a new CHF correlation as a function of the outlet pressure.

$$CHF_{Kosar-Peles} = G \cdot \Delta i_{LV} \cdot \left(\left[0.0934 \cdot \frac{P_{out}}{P_{cr}} - 0.34 \cdot \left(\frac{P_{out}}{P_{cr}} \right)^2 - 0.00013 \right] \cdot x_{out}^{0.59} \right)^{\frac{1}{1.08}} \qquad (3.9)$$

Ong and Thome [24] experimentally investigated the effect of heat flux, flow pattern, saturation temperature, sub-cooling and working fluid properties on saturated CHF in minichannels. The authors proposed a new CHF correlation effective for circular channels

and rectangular multi-minichannels, involving the confinement number *Co* and a diameter based non-dimensional group related to the macro-to micro scale transition.

$$CHF_{Ong} = 0.12 \cdot G \cdot \Delta i_{LV} \cdot \left(\frac{\mu_L}{\mu_V}\right)^{0.183} \cdot \left(\frac{\rho_V}{\rho_L}\right)^{0.062} \cdot We_L^{-0.141} \cdot \left(\frac{L_h}{D}\right)^{-0.72} \cdot \left(\frac{D}{D_{th}}\right)^{0.11} \tag{3.10}$$

$$D_{th} = \frac{1}{Co}\sqrt{\frac{\sigma}{g \cdot (\rho_L - \rho_V)}} \tag{3.11}$$

Mikielewicz et al. [43] studied dry-out for four fluids in two small diameter silver tubes, varying mass flux and heat flux. Based on their data, the authors proposed their own CHF prediction method, in which the Weber number was constructed by using the diameter as characteristic length.

$$CHF_{Mikielewicz} = 0.62 \cdot \left(\frac{\rho_V}{\rho_L}\right)^{-0.02} \cdot We_D^{-0.05} \cdot \left(\frac{L_h}{D}\right)^{-1.17} \tag{3.12}$$

Tanaka et al. [48] collected CHF data for thin rectangular channels from previous studies and examined the effect of the heated length in detail. The authors also proposed a new saturated CHF correlation applicable for a wide range of operative conditions and heated lengths.

$$CHF_{Tanaka} = q^* \cdot \Delta i_{LV} \cdot \sqrt{\lambda \rho_V g (\rho_L - \rho_V)} \tag{3.13}$$

$$q^* = \frac{\left[(0.71)^2 \cdot A_c \cdot \sqrt{\frac{D}{\lambda}}\right]}{S_h \cdot \left[1 + \left(\frac{\rho_V}{\rho_L}\right)^{0.25}\right]^2} + 0.0047 \cdot G^* \cdot \left(\frac{L_h}{D}\right)^{-0.31} \tag{3.14}$$

$$\lambda = \sqrt{\frac{\sigma}{g \cdot (\rho_L - \rho_V)}} \tag{3.15}$$

$$G^* = \frac{G}{\sqrt{\lambda \rho_V g (\rho_L - \rho_V)}} \tag{3.16}$$

Anwar et al. [36] found that a very simple correlation was able to fit all their CHF data obtained with seven refrigerants in a vertical minitube. The prediction method does not take into account the effect of the Weber number and the densities and viscosities ratio.

$$CHF_{Anwar} = 0.27 \cdot G \cdot \Delta i_{LV} \cdot \left(\frac{D}{L_h} \right)$$

(3.17)

3.2 Flow boiling heat transfer review

Hundreds of works on flow boiling heat transfer of different refrigerants, geometries and operative conditions. The objective of this section is therefore not to describe all the papers published on this topic, but to illustrate only those sufficient to illustrate typical trends observed in the literature. In the second part, the main correlations available in literature will be shown.

3.2.1 Experimental studies on flow boiling heat transfer

Starting from conventional channels, Hambraeus [52] reported a heat transfer investigation of flow boiling of R134a in a 12 mm inner diameter tube. The heat transfer coefficient was seen to be dependent on mass velocity and heat flux, suggesting that both nucleate boiling and convective boiling were present.

Wang et al. [53] studied two-phase heat transfer coefficient for R22 and R410A inside a smooth tube with 6.54 mm inner diameter. The authors noticed that for both fluids, at low mass velocity, the heat transfer coefficient was only dependent on heat flux, but not on vapor quality. In case of $G = 400$ kg/m^2 s, the heat transfer performance increased with increasing vapor quality.

Kattan et al. [54] presented an experimental study on flow boiling heat transfer for five refrigerants (R134a, R123, R402A, R404A and R502) evaporating inside two horizontal smooth tubes of 12.0 mm and 10.92 mm internal diameter. The authors defined three different trends according to the vapor quality: up to $x = 0.15$, they observed a maximum in heat transfer coefficient which could be related to a change in the flow pattern. Then, for intermediate vapor qualities, the heat transfer coefficient decreased monotonically with increasing vapor quality, at least in case of low mass velocities. Finally, at higher vapor

qualities, the authors observed a decrease of the heat transfer coefficient that was explained as a transition from annular to annular with partial dry-out flow regime.

Park and Hrnjak [55] obtained experimental data of heat transfer coefficient for carbon dioxide and R410A in a 6.1 mm inner diameter horizontal tube. In case of R410A, the authors found the influence of all the operative parameters (heat flux, mass flux and vapor quality), while only heat flux determined a significant heat transfer coefficient enhancement in case of carbon dioxide, revealing the predominance of nucleate boiling for this refrigerant.

Lazarek and Black [30] found in their experiments with R113 in a vertical channel of 3.1 mm inner diameter that the flow boiling heat transfer coefficient was not dependent on vapor quality but strongly influenced by heat flux, concluding that the nucleate boiling mechanism was dominant during their tests.

Bortolin et al. [56] studied flow boiling of R245fa in a 0.96 mm minichannel at 31 °C. Also in this case, the heat transfer coefficient increased only with heat flux, while mass velocity and vapor quality had no significant influence.

Kew and Cornwell [57] conducted experiments in two sets of parallel minichannels. The authors found that nucleate boiling was dominant in the isolated bubble region at lower qualities, whereas for annular flow region, convective effects were accentuated.

Ong and Thome [58] performed flow boiling heat transfer experiments with R134a, R236fa and R245fa in a 1.03 mm inner diameter circular channel. The local heat transfer coefficients displayed a heat flux and mass flux dependency. The same authors [24] completed their study with two other diameters of 2.20 mm and 3.04 mm and the same refrigerants and observed that the heat transfer coefficient was monotonically increasing with vapor quality, suggesting that convective boiling was the dominant heat transfer mechanism.

Mastrullo et al. [59] provided experimental data for flow boiling of carbon dioxide in a 6.0 mm inner diameter smooth tube at different operative conditions. The authors found that the heat transfer coefficient was almost independent on mass flux and, for low evaporating temperatures, also on vapor quality. The influence of saturation temperature was remarkable only for at low vapor qualities, whereas a high influence of heat flux was always observed. The authors measured local heat transfer coefficient at the top, bottom, left and right side of

the tube and found that at low vapor qualities the top of the tube showed the highest local heat transfer coefficient, probably due to the occurrence of slug flow regime and a larger contribution of nucleate boiling. At higher vapor qualities, they found no significant variations of circumferential heat transfer coefficients in case of high mass fluxes, indicating a symmetric annular flow regime. For low mass velocities, instead, the difference in the local heat transfer coefficients was explained as the occurrence of a stratified-wavy flow pattern.

Del Col [60] examined the effect of saturation temperature (from 25 to 45 °C) on flow boiling of halogenated refrigerants. The heat transfer coefficient was seen to increase with vapor quality in case of R134a, it was instead roughly constant for R22 and R125 and even decreased with vapor quality in case of R410A. Moreover, at low vapor quality, the heat transfer coefficient increased with saturation temperature, whereas this effect was not observed at higher vapor qualities.

Tibiriçá and Ribatski [61] provided experimental data on flow boiling of R134a and R245fa in a 2.30 mm tube, with a saturation temperature of 22, 31 and 41 °C. They found that the heat transfer coefficient was a strong function of heat flux, mass velocity and vapor quality. The effect of saturation temperature was restricted to low vapor qualities.

Grauso et al. [62] presented experimental heat transfer coefficients of refrigerant R1234ze and R134a in a 6.0 mm inner diameter tube. The authors found the same trend with vapor quality for both fluids, with the only difference for the earlier dry-out inception in case of R1234ze and the heat transfer coefficient of R134a being about 15% higher than those of R1234ze at low vapor qualities. For both refrigerants, the effect of the saturation temperature was found negligible, whereas a strong effect of mass flux and a slight influence of heat flux (mostly at medium-low vapor qualities) was recorded.

The same authors [63] [64] performed experiments with R410A, carbon dioxide and propane blends in a 6.0 mm inner diameter horizontal smooth tube. The authors observed that the heat transfer coefficient measured at the top and bottom side of the tube preserved the same trend with vapor quality also varying considerably the reduced pressure. In case of slug, intermittent and annular flow regimes at low reduced pressure, low heat fluxes and high mass fluxes, the top heat transfer coefficient was generally higher than the bottom heat transfer coefficient. With increasing heat flux, they observed that the bottom heat transfer coefficient

became higher than the top one in the intermittent region; whereas increasing the reduced pressure or reducing the mass velocity, the bottom heat transfer coefficient could overcome the top heat transfer coefficient in the annular flow regime.

3.2.2   Flow boiling heat transfer prediction methods

The boiling heat transfer coefficient may be written as prescribed in the Newton formula, being q the heat flux, T_{wall} the tube wall temperature and T_f the fluid temperature, which corresponds also to its saturation temperature.

$$h = \frac{q}{T_{wall} - T_f} \qquad (3.18)$$

As explained in the previous chapter, two mechanisms are assumed to govern flow boiling heat transfer in tubes: nucleate boiling, related to the formation of bubbles at the tube wall, and convective boiling, related to the conduction and convection through a thin liquid film with evaporation at the liquid-vapor interface. Although, for simplicity purposes, these mechanisms were often assumed to be independent one from the other, it is well documented [11] that these phenomena can coexist and also interfere during a boiling process. As the quality increases, convective boiling gradually replaces nucleate boiling. Cooper [65] and Jung et al. [66] stated that in conventional channels nucleate boiling could be considered suppressed at vapor qualities $x > 0.20$, letting the flow boiling process be dominated by the convective mechanism. Generally, when flow boiling is controlled by nucleate boiling mechanism, the heat transfer coefficient is expected to increase with increasing heat flux and saturation temperature, while the effect of mass velocity and vapor quality should be negligible. The increase of heat transfer coefficient with saturation temperature can be explained by the decrease in surface tension which may result in the reduction of bubble departure diameter and hence may enhance the nucleate boiling contribution. On the other hand, when convective boiling dominates the flow boiling process, the heat transfer coefficient seems to be independent on heat flux and system pressure, while increases with increasing mass flux and vapor quality.

Several correlations have been developed to calculate the heat transfer coefficient during flow boiling, trying to match the contributions of these two mechanisms, but their combined

effects are not fully understood yet. In forced boiling in tubes, models for heat transfer coefficient can be divided into three different groups [67]:

Enhancement approach

In this kind of models, the two-phase heat transfer coefficient is evaluated as a liquid single-phase heat transfer coefficient, multiplied by an enhancement factor E

$$h = E \cdot h_L \tag{3.19}$$

Superposition approach

In this case, the two-phase heat transfer coefficient is a sum of the nucleate boiling term and a convective boiling term. S is the nucleate boiling suppression factor, reflecting that in flow boiling the average superheat is lower than that in pool boiling, due to the thinner thermal boundary layer. E is the enhancement factor or multiplier ($E > 1$), introduced because the velocities are much higher due to the presence of the vapor phase which pushes the liquid downstream. Hence forced convection heat transfer is higher in a two-phase flow, compared to the liquid single-phase situation.

$$h = S \cdot h_{pb} + E \cdot h_L \tag{3.20}$$

Asymptotic approach

In this case, the models are very similar to the superposition approach, but a power function is added, in which the exponent n is always $n > 1$.

$$h = \left(\left(S \cdot h_{pb} \right)^n + \left(E \cdot h_L \right)^n \right)^{\frac{1}{n}} \tag{3.21}$$

Chen [68] proposed the first superposition model for evaporation in vertical tubes. The nucleate pool boiling correlation of Forster and Zuber [69] was proposed to evaluate the h_{pb}, whereas the single-phase heat transfer h_L was evaluated with the correlation of Dittus and Boelter [70]. The parameters ΔT_{sat} and ΔP_{sat} are referred to the wall superheat and to the corresponding difference in saturation pressure.

$$h_{Chen} = S \cdot h_{pb} + E \cdot h_L \tag{3.22}$$

$$h_{pb} = 0.00122 \cdot \left[\frac{\lambda_L^{0.79} \cdot c_L^{0.45} \cdot \rho_L^{0.49}}{\sigma^{0.5} \cdot \mu_L^{0.29} \cdot \Delta i_{LV}^{0.24} \cdot \rho_V^{0.24}} \right] \cdot \Delta T_{sat}^{0.24} \cdot \Delta P_{sat}^{0.75} \tag{3.23}$$

$$h_L = 0.023 \cdot \mathrm{Re}_L^{0.8} \cdot \mathrm{Pr}_L^{0.4} \cdot \left(\frac{\lambda_L}{d} \right) \tag{3.24}$$

The author developed graphical functions for the evaluation of the suppression factor S and the enhancement factor E, but did not suggest any parametric equation for the best-fit curves [71], even if many parametric equations were instead proposed by others. The expressions of the enhancement and suppression factor that best fit Chen graphical function are:

$$\begin{aligned} 1/X_{tt} \leq 0.1 &\to E = 1 \\ 1/X_{tt} > 0.1 &\to E = 2.35(1/X_{tt} + 0.213)^{0.736} \end{aligned} \tag{3.25}$$

$$\begin{aligned} \mathrm{Re}_{tp} < 32.5 &\to S = \frac{1}{1 + 0.12 \cdot \left(\mathrm{Re}_{tp} \right)^{1.14}} \\ 32.5 \leq \mathrm{Re}_{tp} \leq 70 &\to S = \frac{1}{1 + 0.42 \cdot \left(\mathrm{Re}_{tp} \right)^{0.78}} \\ \mathrm{Re}_{tp} > 70 &\to S = 0.0797 \cdot e^{1 - \mathrm{Re}_{tp}/70} \end{aligned} \tag{3.26}$$

$$\mathrm{Re}_{tp} = \mathrm{Re}_L \cdot E^{1.25} \cdot 10^{-4} \tag{3.27}$$

A modified form of the Chen method was introduced by Gungor and Winterton [72] from a large database of 3693 experimental points taken from literature and including R11, R12, R22, R113, R114 and water. The authors used the correlation of Cooper [73] for the nucleate pool boiling term and a different function for the suppression and enhancement parameters, with the last one expressed as a function of the boiling number.

$$h_{pb} = h_{Cooper} = 55 \cdot P_{red}^{0.12} \cdot \left(\log_{10} \left(P_{red} \right) \right)^{-0.55} \cdot M^{-0.5} \cdot q^{0.67} \tag{3.28}$$

$$E = 1 + 24000 \cdot Bo^{1.16} + 1.37 \cdot \left(1/X_{tt} \right)^{0.86} \tag{3.29}$$

$$S = \frac{1}{1+1.15 \cdot 10^{-6} \cdot E^2 \cdot Re_L^{1.17}} \tag{3.30}$$

In case the tube is horizontal and the Froude number is less than 0.05, the parameters E and S should be multiplied by E_2 and S_2, respectively:

$$E_2 = Fr^{(0.1-2 \cdot Fr)} \tag{3.31}$$

$$S_2 = \sqrt{Fr} \tag{3.32}$$

From the previous model, Del Col [60] proposed a simple modification to match his database obtained for flow boiling of halogenated refrigerants at high saturation temperatures in a horizontal smooth tube:

$$h_{DelCol} = 1.2 \cdot h_{Gung-Wint} \tag{3.33}$$

Kandlikar [74] expressed the two-phase flow boiling heat transfer coefficient as the larger value of the convective and the nucleate boiling contributions, which are evaluable as follows, where F_f is a fluid-dependent parameter and Fr_{LO} is the Froude number considering the liquid phase flowing alone in the whole cross section of the tube. Finally, C_v is the convective number and the liquid single-phase heat transfer coefficient h_{LO} is computable from the Gnielinski [75] correlation:

$$h_{nb} = \left(0.6683 \cdot Cv^{-0.2} \cdot (1-x)^{0.8} \cdot f_2 \cdot Fr_{LO} + 1058 \cdot Bo^{0.7} \cdot (1-x)^{0.8} \cdot F_f \right) \cdot h_{LO} \tag{3.34}$$

$$h_{cb} = \left(1.136 \cdot Cv^{-0.9} \cdot (1-x)^{0.8} \cdot f_2 \cdot Fr_{LO} + 667.2 \cdot Bo^{0.7} \cdot (1-x)^{0.8} \cdot F_f \right) \cdot h_{LO} \tag{3.35}$$

$$Cv = \left(\frac{1-x}{x} \right)^{0.8} \cdot \left(\frac{\rho_V}{\rho_L} \right)^{0.5} \tag{3.36}$$

$$h_{LO} = \frac{(f/8) \cdot (Re_{LO} - 1000) \cdot Pr_L}{1+12.7 \cdot (f/8)^{0.5} \cdot (Pr_L^{2/3} - 1)} \cdot \frac{\lambda_L}{d} \tag{3.37}$$

Bertsch et al. [76] proposed a heat transfer model for saturated flow boiling in small channels, fitted to a database of 3899 experimental points from 14 independent studies. The

two-phase heat transfer coefficient was obtained as a function of the vapor quality and the confinement number.:

$$h_{Bertsch} = h_{pb} \cdot (1-x) + h_{cb,tp} \cdot \left[1 + 80 \cdot (x^2 - x^6) \cdot e^{-0.6 \cdot Co}\right]$$ (3.38)

The pool boiling heat transfer coefficient was taken from Cooper [73] equation, while the two-phase convective heat transfer coefficient was expressed as a function of the vapor quality and the vapor and liquid single-phase heat transfer coefficients computed with the correlation of Hausen [77].

$$h_{cb,tp} = h_{conv,L} \cdot (1-x) + h_{conv,V} \cdot x$$ (3.39)

$$h_{conv} = \left(3.66 + \frac{0.0668 \cdot \dfrac{d}{L} \cdot Re \cdot Pr}{1 + 0.04 \cdot \left[\dfrac{d}{L} \cdot Re \cdot Pr\right]^{2/3}} \right) \cdot \frac{\lambda}{d}$$ (3.40)

Liu and Winterton [78] developed an asymptotic model adopting $n = 2$ as empowering coefficient (see Equation (3.21)). The nucleate pool boiling correlation was taken from Cooper [73] (see Equation (3.28)) and the liquid heat transfer coefficient from Dittus and Boelter [70] (see Equation (3.24)), by using the only-liquid Reynolds number Re_{LO}. The enhancement E and suppression S factors were instead expressed as:

$$E = \left[1 + x \cdot Pr_L \cdot \left(\frac{\rho_L}{\rho_V} - 1\right)\right]^{0.35}$$ (3.41)

$$S = \left(1 + 0.055 \cdot E^{0.1} \cdot Re_{LO}^{0.16}\right)^{-1}$$ (3.42)

Lazarek and Black [30] developed an empirical correlation for the heat transfer coefficient during flow boiling inside minichannels. The prediction method was a Nusselt-type correlation, having only a dependency on the Reynolds number and the boiling number. The authors correlated their 728 measurements to the following formula:

$$h_{Laz-Black} = 30 \cdot Re_{LO}^{0.857} \cdot Bo^{0.714} \cdot \left(\frac{\lambda_L}{d}\right)$$ (3.43)

The same approach was used also by Tran et al. [79], who replaced the Reynolds number with the Weber number to eliminate viscous effects in favor of surface tension as:

$$h_{Tran} = 840000 \cdot \left(Bo^2 \cdot We_L \right)^{0.3} \cdot \left(\frac{\rho_L}{\rho_V} \right)^{-0.4} \tag{3.44}$$

Similarly, Yu et al. [80] obtained a new equation by changing the constants.

$$h_{Yu} = 640000 \cdot \left(Bo^2 \cdot We_{LO} \right)^{0.27} \cdot \left(\frac{\rho_L}{\rho_V} \right)^{-0.2} \tag{3.45}$$

Kew and Cornwell [57] also modified the Lazarek and Black correlation [30] to fit their database where convective boiling was the dominant heat transfer mechanism. The authors therefore introduced the effect of the vapor quality:

$$h_{Kew-Corn} = 30 \cdot \mathrm{Re}_{LO}^{0.857} \cdot Bo^{0.714} \cdot \left(\frac{1}{1-x} \right)^{0.143} \cdot \left(\frac{\lambda_L}{d} \right) \tag{3.46}$$

Sun and Mishima [81] found that their data were not dependent on the effect of vapor quality. Their correlation was based on the effect of Reynolds number, boiling number and Weber number:

$$h_{Sun-Mish} = \frac{6 \cdot \mathrm{Re}_{LO}^{1.05} \cdot Bo^{0.54}}{We_{LO}^{0.191} \cdot \left(\rho_V / \rho_L \right)^{0.142}} \cdot \frac{\lambda_L}{d} \tag{3.47}$$

Other researchers developed phenomenological models based on the two-phase flow structure occurring during evaporation. Kattan et al. [54] proposed a series of correlations to be used according to the flow pattern, which had to be determined using their own two-phase flow pattern map [82]. The model covers fully stratified flows, intermittent flows, annular flows and annular flows with partial dry-out, whereas slug and plug flows are identified as intermittent flow regimes and mist flow and bubbly flow are instead not considered. The heat transfer coefficients are obtained from the evaluation of the wet and dry perimeters, which are geometrically related to the flow structure. Particularly, the heat transfer coefficient is seen as a weighted average of two heat transfer coefficients: one for the dry area of the tube and one for the wetted area, as shown in Figure 3.3:

48

$$h_{Kattan} = \frac{\vartheta_{dry} \cdot h_V + (2\pi - \vartheta_{dry}) \cdot h_{wet}}{2\pi}$$ (3.48)
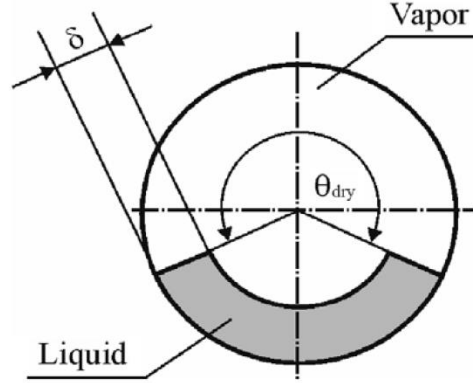
Figure 3.3 Schematic diagram of the liquid distribution. Image taken from Thome-El Hajal [83]

In this prediction method, the dry angle ϑ_{dry} assumes different values according to the flow pattern. In case of annular and intermittent flows, the tube perimeter is always wet and the dry angle is 0. Dedicated equations are instead proposed for the stratified flow before and after the dry-out inception. The vapor heat transfer coefficient h_V is calculated with the Dittus and Boelter correlation [70], whereas h_{wet} is obtained with an asymptotic expression which combines nucleate and convective boiling contributions.

$$h_{wet} = \left(h_{pb}^3 + h_{cb}^3 \right)^{1/3}$$ (3.49)

Cooper correlation [73] was used for the nucleate boiling contribution, whereas the convective boiling contribution was assumed to be a function of the liquid film Reynolds number:

$$h_{cb} = 0.0133 \cdot \left[\frac{4 \cdot G \cdot (1-x) \cdot \delta}{(1-\alpha) \cdot \mu_L} \right]^{0.69} \cdot \left[\frac{c_L \cdot \mu_L}{\lambda_L} \right]^{0.4} \cdot \frac{\lambda_L}{\delta}$$ (3.50)

In the above equation, α is the cross sectional void fraction predicted by the drift flux model of Rouhani and Axelsson [84] and modified by Steiner [85] for horizontal tubes, whereas δ represents the liquid film thickness.

Thome and El Hajal [83] proposed a modification to this method according to their data of flow boiling of carbon dioxide in horizontal tubes. Wojtan et al. [86], instead, extended the model of Kattan et al. [54] to their database and their flow pattern map. They divided the stratified wavy region into three different sub-zones: slug, slug/stratified-wavy and stratified-wavy, proposing dedicated equations to calculate the dry angle for these three sub-regions.

Thome et al. [87] proposed a three-zones model for the flow boiling heat transfer coefficient, suggesting that in the intermittent region the evaporation proceeds as follows:

a) A liquid slug flows;
b) An elongated bubble passes in evaporation;
c) A vapor slug passes in case the thin evaporating liquid film dries out before a new liquid slug arrives.

The model and the three zones described above are schematized in Figure 3.4.
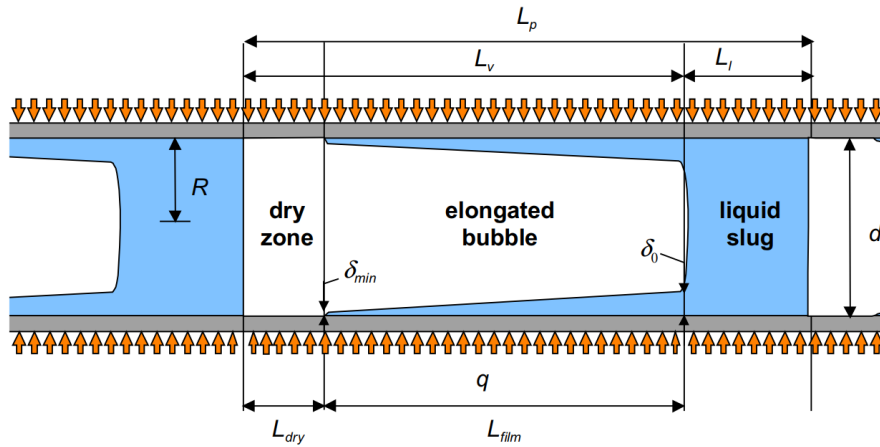
Figure 3.4 Three-zone model of Thome et al. [87] for intermittent flows in minichannels.

The heat transfer coefficient is evaluated as a time-average of the successive heat transfer coefficients for the three zones

$$h_{Thome} = \frac{t_L}{\tau} \cdot h_L + \frac{t_{film}}{\tau} \cdot h_{film} + \frac{t_V}{\tau} \cdot h_V \qquad (3.51)$$

The heat transfer coefficient of the liquid and vapor phases are taken from the asymptotic method (with $n = 4$) of Churchill and Usagi [88]. Three adjustable parameters (the minimum thickness of the liquid film at dry-out δ_{min}, a correction factor for the prediction of the initial film thickness δ_0 and the pair frequency $1/\tau$) are conceived and difficult to predict theoretically.

Mauro et al. [89] presented the modeling of the liquid film distribution and heat transfer during convective boiling in horizontal tubes in the annular flow region. The authors used the existing symmetrical annular flow models [90] [91] [92] [93] and a tool to predict the threshold between symmetric and asymmetric annular flow [94] to develop a series of correlations able to evaluate the annular film thickness and the heat transfer coefficients around the perimeter of horizontal tubes. Particularly, the mean, top and bottom heat transfer coefficients were obtained as a function of the same Nusselt number and using the corresponding film thickness as characteristic lengths:

$$h_{Mauro,ave} = Nu \cdot \frac{\lambda_L}{\delta_{ave}} \tag{3.52}$$

$$h_{Mauro,top} = Nu \cdot \frac{\lambda_L}{\delta_{top}} \tag{3.53}$$

$$h_{Mauro,bot} = Nu \cdot \frac{\lambda_L}{\delta_{bot}} \tag{3.54}$$

$$Nu = 0.0776 \cdot \delta_+^{0.90} \cdot Pr_L^{0.52} \tag{3.55}$$

The construction of the Nusselt number is based on the non-dimensional film thickness which can be in turn evaluated as a function of the liquid film Reynolds number. Further details on the complete prediction method can be found in the reference mentioned [89].

3.3 Two-phase pressure drop review

The total pressure drop occurring in a two-phase flow inside a tube can be considered as a sum of three different contributions: the variation of the fluid gravitational potential energy ΔP_{grav}, the acceleration term ΔP_{acc}, which considers the variation of the fluid kinetic energy,

and the frictional pressure drop ΔP_{fr} that considers the energy dissipation due to friction on the channel walls or between the two phases.

$$\Delta P_{tot} = \Delta P_{grav} + \Delta P_{acc} + \Delta P_{fr} \tag{3.56}$$

The static pressure drop is a function of the tube height and the acceleration of gravity. In case of horizontal tubes, there is no change in the static head and therefore $\Delta P_{grav} = 0$. The acceleration term corresponds to the change in the kinetic energy of the flow due to the change in the vapor and liquid velocities in the tube. This term reflects a pressure drop in case of evaporating flow and a pressure gain in case of condensing flow, and it is a function of the inlet and outlet vapor qualities and cross sectional void fractions. In case of adiabatic flows, there is no acceleration or deceleration of the fluid ($\Delta P_{acc} = 0$).

$$\Delta P_{acc} = G^2 \cdot \left\{ \left[\frac{(1-x)^2}{\rho_L \cdot (1-\alpha)} + \frac{x^2}{\rho_V \cdot \alpha} \right]_{outlet} - \left[\frac{(1-x)^2}{\rho_L \cdot (1-\alpha)} + \frac{x^2}{\rho_V \cdot \alpha} \right]_{inlet} \right\} \tag{3.57}$$

The shear stress between the flowing fluid and the channel wall is represented by the frictional pressure drop. During experiments, this term is evaluated by subtracting the acceleration and (in case of vertical tubes) the gravitational terms.

3.3.1 Experimental studies on two-phase frictional pressure drop

Frictional two-phase pressure drops in tubes has been largely studied over the last four decades for different fluids, geometries and operating conditions. A concise summary of the recent studies on this topic is presented here.

Zhang and Webb [95] obtained two-phase pressure drop data for refrigerants R134a, R22 and R404A in a multiport extruded aluminum tube with an hydraulic diameter of 2.13 mm and in two copper tubes of 6.25 and 3.25 mm internal diameter, respectively. The authors observed that the pressure drop increased significantly with increasing mass velocity and vapor quality. Particularly, regarding the vapor quality dependence, the pressure drop reached a maximum and then it decreased. These trends were also observed in all the studies quoted in this section. According to the scientific literature, the maximum of the frictional pressure gradient may occur at the inception of dry-out or mist flow regime, or even before the dry-

out occurrence [96]. The disappearance of the liquid film may be an explanation of the peak location at the inception of dry-out or mist flow regime, due to two different phenomena:

- The decrease of the tube surface apparent roughness seen by the vapor phase, as suggested by Ducoulombier [97].
- The decrease of the friction factor due to the vapor phase in contact with the wall, whose viscosity is considerably lower to that of the liquid.

Kuo and Wang [98] performed diabatic and adiabatic experiments of pressure drop with refrigerants R22 and R407C in a microfin tube of 9.52 mm internal diameter. The authors found that the pressure gradients of R407C were approximately 50-80% lower than those of R22 obtained with the same operative conditions. They attributed this reduction to the difference in flow pattern for the pure refrigerants and the mixture.

Quiben and Thome [96] provided experimental data on two-phase flow pressure drop of R134a, R22 and R410A in horizontal channels with two different diameters of 8.0 mm and 13.8 mm. The authors observed that a smaller diameter tube led to higher frictional pressure gradients and that the pressure drops of R134a were higher than those of R22 and R410A. They also observed that the effect of evaporation heat flux was only of minor importance at vapor qualities before the peak value. However, the location of the peak changed by shifting to lower vapor qualities when increasing the heat flux, representing the most important influence of heat flux during observations. They also observed two distinct configurations: in the first one, the pressure drop peak was located near or before the onset of dry-out occurring at the top of the tube. In the second configuration, they associated the appearance of this peak with the damping out of the interfacial waves to explain the phenomenon. Finally, they compared their database to the correlations of Müller-Steinhagen and Heck [99] and Grönnerud [100], where 50% and 40% of the data, respectively, were included in an error band of ±20%.

Grauso et al. [62] presented experimental pressure drop data for refrigerants R134a and R1234ze in a smooth horizontal tube of 6.0 mm inner diameter. The authors found that the adiabatic pressure gradient increased strongly with vapor quality reaching a maximum and then decreasing for both refrigerants at the same operative conditions. Experimental data for R1234ze resulted slightly higher than those of R134a obtained at the same conditions,

whereas similar variations were found with each operative parameter: slight decrease with increasing saturation temperature and strong increase with mass flux.

The same authors [101] studied adiabatic frictional pressure gradients for refrigerants R410A and carbon dioxide analyzing the effect of the reduced pressure (from 0.19 to 0.52 for R410A and from 0.57 to 0.64 for carbon dioxide) and mass flux. They found that at similar operative conditions (reduced pressure higher than 0.50) the experimental data of both fluids resulted very similar, whereas the frictional pressure gradient started to increase significantly when reducing the saturation temperature in case of R410A. Finally, they compared their database to the correlations of Müller-Steinhagen and Heck [99] and Friedel [102], with the first prediction method giving a very good agreement (75.4% of the experimental data in an error bandwidth of ±30%).

Mauro et al. [103] compared their database obtained for a 6.00 mm inner diameter horizontal smooth tube and for different refrigerants (R22, R507, R404A, R407C, R410A, R417A and R507A) and different experimental conditions (saturation temperature ranging from -18.4 °C to 46.2 °C) to different correlations. They showed that the prediction methods of Grönnerud [100] and Quiben and Thome [104] were equally accurate for their experimental data.

Del Col et al. [105] measured adiabatic pressure drop of refrigerant R1234yf in a single circular channel of 0.96 mm internal diameter at different mass fluxes, at a saturation temperature of 40 °C and compared the data to those obtained by Cavallini et al. [106] with the same channel and refrigerant R134a. The total pressure drop measured with R1234yf was slightly lower (10-12%) as compared to R134a at the same operating conditions. The authors explained that this was due to the reduced pressure of R1234yf, which is greater by 20% than that of R134a at 40 °C saturation temperature.

Park and Hrnjak [55] measured two-phase flow pressure drop in a 6.1 mm internal diameter horizontal smooth tube for carbon dioxide, R410A and R22. Two different saturation temperature of -15 and -30 °C were chosen. The authors found that the measured pressure drop of carbon dioxide was much lower than that of R22 and R410A at identical conditions. Among different correlations, they found that the prediction method of Müller-Steinhagen and Heck [99] was the best at fitting their data.

Padilla et al. [107] measured two-phase pressure drop for refrigerants R134a, R410A and R1234yf in horizontal straight tubes of different diameters (from 7.90 to 10.85 mm), with several mass fluxes (from 187 to 1702 kg/m^2 s) and saturation temperatures (from 4.8 to 20.7 °C). They found that the pressure drop of R134a was higher than that of R1234yf and that of R410A, suggesting a significant influence of the physical properties of refrigerants. Furthermore, the peak in the pressure drop occurred at vapor qualities from 0.77 to 0.92. The authors stated that even if the prediction methods of Müller-Steinhagen and Heck [99] and Revellin and Haberschill [108] were able to fairly predict the data within a ±10% error band, the trend of the vapor quality corresponding to the maximum pressure gradient was not well captured by both correlations.

Cavallini et al. [109] provided two-phase pressure drop data for three refrigerants (R236ea, R134a and R410A) in a multi-port minichannel tube having an hydraulic diameter of 1.4 mm, by setting the saturation temperature to 40 °C. They found that R236ea, carrying the lowest reduced pressure, showed the highest pressure drop, whereas the lowest pressure gradient was obtained with refrigerant R410A, which had the highest reduced pressure. The authors compared their database to several prediction methods, observing that none of them was able to fairly fit the R410A data. On the other hand, pressure drops of R134a and R236ea were fairly predicted by the correlation of Müller-Steinhagen and Heck [99].

Revellin and Thome [110] measured two-phase pressure drop in microchannels of two different diameters (0.509 and 0.790 mm) in a wide range of experimental conditions for refrigerants R134a and R245fa. They found for both refrigerants that with higher saturation temperatures (from 26 to 35 °C) the pressure drop was lower. As regards the effect of vapor quality, they observed a change in the increasing trend (i.e. a sudden reduction of pressure drop at $x = 0.35$) in case of high mass fluxes (1000 and 1200 kg/m^2 s). This behavior was explained as a change in the flow patterns with the transition from wavy annular to smooth annular.

Tibiriçá et al. [111] and Tibiriçá and Ribatski [112] presented experimental flow boiling pressure drop data for refrigerant R134a and R245fa in a horizontal smooth tube with an internal diameter of 2.32 mm at saturation temperatures of 31°c and 41 °C. The experimental trends with vapor quality, mass flux and saturation temperature already shown were also

confirmed with these studies. The authors also compared their data to several prediction methods, obtaining that Cioncolini et al. [90] model worked the best to fit their experiments.

3.3.2 Two-phase frictional pressure drop prediction methods

When modeling two-phase pressure drop, empirical correlations are often used, because they provide a good accuracy in the range of operating conditions in which they were developed and also because they are particularly easy to implement. Homogeneous flow and separated flow models are the two main approaches for the construction of the empirical models.

Homogeneous flow models

This technique is probably the simplest way to analyze two-phase flow behavior. For these models, the two-phase mixture is treated as a single-phase fluid with average properties of the liquid and the vapor phases, which are assumed to flow at the same velocity. The frictional pressure drop is estimated as if the flow is only liquid or vapor single-phase flowing alone, by suitably averaging the thermodynamic properties (density and viscosity):

$$\left.\frac{dP}{dz}\right|_{fr} = \frac{2 \cdot f_{tp} \cdot G^2}{d \cdot \rho_{tp}}$$

(3.58)

The two-phase mixture density ρ_{tp} is obtained as:

$$\rho_{tp} = \left(\frac{x}{\rho_V} + \frac{1-x}{\rho_L}\right)^{-1}$$

(3.59)

The two-phase friction factor f_{tp} is instead differently defined according to the two-phase Reynolds number

$$f_{tp} = \frac{16}{\mathrm{Re}_{tp}} \text{for } \mathrm{Re}_{tp} < 2000$$

(3.60)

$$f_{tp} = \frac{0.079}{\mathrm{Re}_{tp}^{0.25}} \text{for } \mathrm{Re}_{tp} > 2000$$

(3.61)

$$\mathrm{Re}_{tp} = \frac{G \cdot d}{\mu_{tp}}$$

(3.62)

Different definitions of the two-phase mixture viscosity μ_{tp} have been proposed by several authors. Among these, the expressions of Cicchitti et al. [113], McAdams et al. [114] and Dukler et al. [115] are shown in the equations below:

$$\mu_{tp,Cicch.} = x \cdot \mu_V + (1-x) \cdot \mu_L \qquad (3.63)$$

$$\mu_{tp,McAdams} = \left(\frac{x}{\mu_V} + \frac{1-x}{\mu_L} \right)^{-1} \qquad (3.64)$$

$$\mu_{tp,Dukler} = \rho_{tp} \cdot \left(x \cdot \frac{\mu_V}{\rho_V} + (1-x) \cdot \frac{\mu_L}{\rho_L} \right) \qquad (3.65)$$

Separated flow models

With this different approach, the phases are assumed to be separated into two streams, liquid and vapor, each flowing at its own constant velocity, thus leading to independent laminar or turbulent flows. In this regard, Lockhart and Martinelli [7] assessed four flow regimes during two-phase flows: liquid and vapor both turbulent (**tt**), liquid laminar and vapor turbulent (**lt**), liquid turbulent and vapor laminar (**tl**) and liquid and vapor both laminar (**ll**). For this technique, the total volume occupied by the liquid and the vapor phase should remain constant at any time and equal to the volume of the pipe. This implies that the flow pattern cannot change along the tube, thus eliminating the plug/slug flows (where the flow pattern is intermittent) from the analysis.

The two-phase frictional pressure gradient is in this case obtained with a two-phase multiplier for the liquid (or the vapor) phase pressure drops:

$$\left. \frac{dP}{dz} \right|_{fr} = \left. \frac{dP}{dz} \right|_V \cdot \Phi_V^2 \qquad (3.66)$$

$$\left. \frac{dP}{dz} \right|_{fr} = \left. \frac{dP}{dz} \right|_L \cdot \Phi_L^2 \qquad (3.67)$$

where:

$$\frac{dP}{dz}\bigg|_V = \frac{2 \cdot f_V \cdot G^2 \cdot x^2}{d \cdot \rho_V} \tag{3.68}$$

$$\frac{dP}{dz}\bigg|_L = \frac{2 \cdot f_L \cdot G^2 \cdot (1-x)^2}{d \cdot \rho_L} \tag{3.69}$$

and the single-phase friction factors of the liquid and the vapor phases, together with their Reynolds numbers, are evaluated using the classical definitions (see Equations (3.60)-(3.62)). The multipliers are instead related to the Martinelli parameter (see Equation (2.25)):

$$\Phi_V^2 = 1 + C \cdot X + X^2 \tag{3.70}$$

$$\Phi_L^2 = 1 + \frac{C}{X} + \frac{1}{X^2} \tag{3.71}$$

The parameter C was firstly estimated by Chisholm [116] to best fit the empirical curves given by Lockhart and Martinelli in their original paper [7]. Particularly, $C=20$ in case of turbulent-turbulent flows (**tt**), $C=12$ for laminar-turbulent flows (**lt**), $C=10$ for turbulent-laminar flows (**tl**) and $C=5$ for laminar-laminar flows (**ll**).

Other authors tried to modify the parameter C to best fit their own database. For instance, Mishima and Hibiki [117] measured frictional pressure gradients for air and water flowing in minichannels of 1-4 mm, obtaining C as an empirical function of the tube diameter, expressed in [m]:

$$C = 21 \cdot \left(1 - e^{-0.319 \cdot d}\right) \tag{3.72}$$

Pamitran et al. [118] obtained frictional pressure drop data for five refrigerants (R22, R134a, R290, R744 and R410A) in horizontal tubes up to 3.0 mm internal diameter and within a range of mass fluxes from 50 to 600 kg/m^2 s. The authors developed a correlation for the C factor depending on the two-phase Weber number, in which the two-phase mixture density is a function of the void fraction, and the two-phase Reynolds number (see Equation (3.62)), in which the two-phase mixture viscosity is a obtained with the model of Beattie and Whalley [119]:

$$C = 0.003 \cdot We_{tp}^{-0.433} \cdot \mathrm{Re}_{tp}^{1.23} \tag{3.73}$$

$$We_{tp} = \frac{G^2 \cdot d}{\rho_{tp} \cdot \sigma} \tag{3.74}$$

$$\rho_{tp} = \alpha \cdot \rho_V + (1 - \alpha) \cdot \rho_L \tag{3.75}$$

With a different approach the frictional pressure drop is calculated using a two-phase multiplier with the frictional pressure gradient of the single phases, by considering the liquid and the vapor flowing alone in the channel with the total mass flow rate. Martinelli and Nelson [120] proposed the following expression:

$$\left.\frac{dP}{dz}\right|_{fr} = \left.\frac{dP}{dz}\right|_{LO} \cdot \Phi_{LO}^2 \tag{3.76}$$

$$\left.\frac{dP}{dz}\right|_{LO} = f_{LO} \cdot \frac{2 \cdot G^2}{d \cdot \rho_L} \tag{3.77}$$

where the liquid-only friction factor is evaluated as usual:

$$f_{LO} = \frac{16}{\mathrm{Re}_{LO}} \text{for } \mathrm{Re}_{LO} = \frac{G \cdot d}{\mu_L} < 2000 \tag{3.78}$$

$$f_{LO} = \frac{0.079}{\mathrm{Re}_{LO}^{0.25}} \text{for } \mathrm{Re}_{LO} = \frac{G \cdot d}{\mu_L} > 2000 \tag{3.79}$$

The authors correlated the liquid-only two-phase multiplier to the original liquid two-phase multiplier defined in Equation (3.71):

$$\Phi_{LO}^2 = \Phi_L^2 \cdot (1 - x)^{1.8} \tag{3.80}$$

Other researchers extended the model of Martinelli and Nelson [120] for different experimental conditions and fluids, by implementing a dedicated function for the liquid-only two-phase multiplier Φ_{LO}. Friedel [102] proposed the following correlation:

$$\Phi_{LO}^2 = E + \frac{3.24 \cdot F \cdot H}{Fr^{0.045} \cdot We^{0.035}} \tag{3.81}$$

In the above equation, the factors H, F and E are a function of the thermophysical properties and the liquid-only and vapor-only friction factors, evaluated with the corresponding

properties. The Froude and Weber number are instead defined with the help of the homogenous two-phase density (see Equation (3.59)):

$$Fr = \frac{G^2}{g \cdot d \cdot \rho_{tp}^2} \tag{3.82}$$

$$We = \frac{G^2 \cdot d}{\sigma \cdot \rho_{tp}} \tag{3.83}$$

$$H = \left(\frac{\rho_L}{\rho_V}\right)^{0.91} \cdot \left(\frac{\mu_V}{\mu_L}\right)^{0.19} \cdot \left(1 - \frac{\mu_V}{\mu_L}\right)^{0.7} \tag{3.84}$$

$$F = x^{0.78} \cdot (1-x)^{0.224} \tag{3.85}$$

$$E = (1-x)^2 + x^2 \cdot \frac{\rho_L \cdot f_{VO}}{\rho_V \cdot f_{LO}} \tag{3.86}$$

Zhang and Webb [95] modified the correlation of Friedel [102] to predict two-phase pressure drop of 134a, R22 and R404A in a multi-port aluminum tube with an hydraulic diameter of 2.13 mm and two copper tubes with internal diameters of 6.25 and 3.25 mm. The authors used the reduced pressure to take into account the effect of the fluid properties, without using the Weber and Froude numbers:

$$\Phi_{LO}^2 = (1-x)^2 + 2.87 \cdot x^2 \cdot P_{red}^{-1} + 1.68 \cdot x^{0.8} \cdot (1-x)^{0.25} \cdot P_{red}^{-1.64} \tag{3.87}$$

Grönnerud [100] developed its own liquid-only two-phase multiplier using around 1000 data points for R12 and ammonia in a horizontal macrotube of 26.2 mm internal diameter:

$$\Phi_{LO}^2 = 1 + \frac{dP}{dz}\bigg|_{fr} \cdot \left[\left(\frac{\rho_L}{\rho_V}\right) \cdot \left(\frac{\mu_L}{\mu_V}\right)^{-0.25} - 1\right] \tag{3.88}$$

The frictional pressure gradient was imposed as a function of the Froude number and the friction factor f_{Fr} should be fixed at 1.0 in case $Fr_L \geq 1$.

$$\frac{dP}{dz}\bigg|_{fr} = f_{Fr} \cdot \left[x + 4 \cdot \left(x^{1.8} - x^{10} \cdot f_{Fr}^{0.5}\right)\right] \tag{3.89}$$

$$f_{Fr} = Fr_L^{0.3} + 0.0055 \cdot \left(\ln \frac{1}{Fr_L} \right)^2 \qquad (3.90)$$

$$Fr_L = \frac{G^2}{g \cdot d \cdot \rho_L^2} \qquad (3.91)$$

Finally, Müller-Steinhagen and Heck [99] proposed a method developed from 7851 frictional pressure drop data points obtained for two-phase flow in horizontal pipes of several mixtures (air-water, steam-water, hydrocarbons-air, oils-air, R11, R12, R22, neon and nitrogen) and from 1462 data points in vertical channels including air-water, steam-water, R12 and Argon. Their database included internal diameters from 4 to 392 mm. This method was seen to work surprisingly well for different independent database and it is also particularly easy to implement, since it considers the two-phase pressure drop as a sort geometrical average on the vapor quality of the all-liquid and all-vapor frictional pressure drops:

$$\frac{dP}{dz}\bigg|_{fr} = F \cdot (1-x)^{1/3} + \frac{dP}{dz}\bigg|_{VO} \cdot x^3 \qquad (3.92)$$

$$F = \frac{dP}{dz}\bigg|_{LO} + 2 \cdot \left(\frac{dP}{dz}\bigg|_{VO} - \frac{dP}{dz}\bigg|_{LO} \right) \cdot x \qquad (3.93)$$

$$\frac{dP}{dz}\bigg|_{LO} = f_{LO} \cdot \frac{2 \cdot G^2}{d \cdot \rho_L} \qquad (3.94)$$

$$\frac{dP}{dz}\bigg|_{VO} = f_{vo} \cdot \frac{2 \cdot G^2}{d \cdot \rho_V} \qquad (3.95)$$

4 CHF experimental facility and method

The CHF experiments were performed in a test facility conceived and built in the Refrigeration Laboratory at the Università di Napoli "Federico II". This chapter begins with a detailed description of the experimental apparatus, giving particular attention to the test sections employed and the measurement equipment. The experimental procedure and the data reduction processes are then described and the uncertainty of measured and derived parameters are also discussed and computed. Finally, the energy balance between the electric heater and the single-phase sub-cooled liquid flow is shown to determine the amount of heat losses to the surrounding environment.

4.1 Test facility description

The experimental test rig consists in a closed main loop in which the refrigerant conditions in terms of mass flow rate, pressure and temperature were independently set and controlled. A secondary loop for the cooling medium (demineralized water) was also provided. A photograph and a schematic of the whole experimental set-up are shown in Figure 4.1 and Figure 4.2, respectively.

4.1.1 Main and secondary loops

The refrigerant flow path is portrayed in Figure 4.2 with a black line. The working fluid in sub-cooled liquid condition is driven into the Coriolis mass flow meter and then into the test section for the CHF measurements by means of a two-gear magnetic pump (GC–M23 JF5S6, series 220, from Techma gpm s.r.l). It was designed to elaborate from 1.3 up to 2.5 dm³/min by changing its rotating speed from 1650 to 3400 rpm thanks to a 0.34 kW electric motor (Cantoni Sh-71-2a) and a 0.40 kW inverter (ABB ACS310). At the inlet of the test section a ceramic PT100 RTD and an absolute pressure transducer placed on the stainless steel tube were able to define the thermodynamic properties of the working fluid, whereas a differential pressure transducer provided the pressure drop across the multi-minichannel heat sink.

Another Pt100 RTD was finally placed to read the refrigerant test section outlet temperature. The fluid in saturated condition passes through a manually controlled throttling valve, which allows a fine regulation of both mass flow rate and system pressure, and then into a plate heat exchanger, in which the working fluid condenses thanks to the cold water in the secondary loop. A liquid receiver (Italest of 1.1 dm^3 capacity) was then placed in order to compensate for the changes of required fluid charge during the experiments with a varying thermal load. The loop is finally closed with a double pipe heat exchanger that provides a slight sub-cooling to the refrigerant before entering the pump. In this heat exchanger, the demineralized water flows in the inside tube and the liquid refrigerant in the annulus between the two tubes. For tests requiring very low mass fluxes, a manually-controlled by-pass valve is able to recirculate a portion of the liquid refrigerant from the pump outlet to the liquid receiver, avoiding the test section. The main loop is also equipped with a filter-dryer (Castel 4308-M12S) placed after the Coriolis flow meter, preventing the presence of small solid particles flowing through the plant. Finally a liquid indicator between the liquid receiver and the sub-cooler warns the users about potential lack of fluid charge into the experimental plant.

Demineralized water flows into the secondary loop, which is portrayed as a blue line in Figure 4.2, feeding both the sub-cooler and the plate condenser in order to manage the thermal load applied to the test section, thus guaranteeing a desired system pressure. The water temperature is remotely set and controlled by means of a thermostatic bath (Lauda RP 855), carrying a 8 dm^3 pool that can be brought from -55 to 200 °C, thanks to a dedicated R134a chiller and a electric resistance working with Joule effect. The water pump (Wilo TOP-S 25-10) draws the demineralized water directly from the thermostatic bath into the double pipe sub-cooler and then into the plate condenser. Two ball cock valves allow for excluding, when needed, each heat exchanger, thanks to two separate by-pass circuits. A stainless steel expansion vessel (Elbi HX-2F) with a capacity of 2 dm^3 restricts the variation of the liquid water specific volume with the varying temperature.

Different transducers (ceramic Pt100 RTDs and an absolute pressure transducer) are placed throughout the main and secondary loops in order to monitor and control the correct functioning of the experimental facility. The overall specifics of each transducer and their accuracy will be given in the measurement instrumentation section.

Figure 4.1 Photograph of the experimental set-up
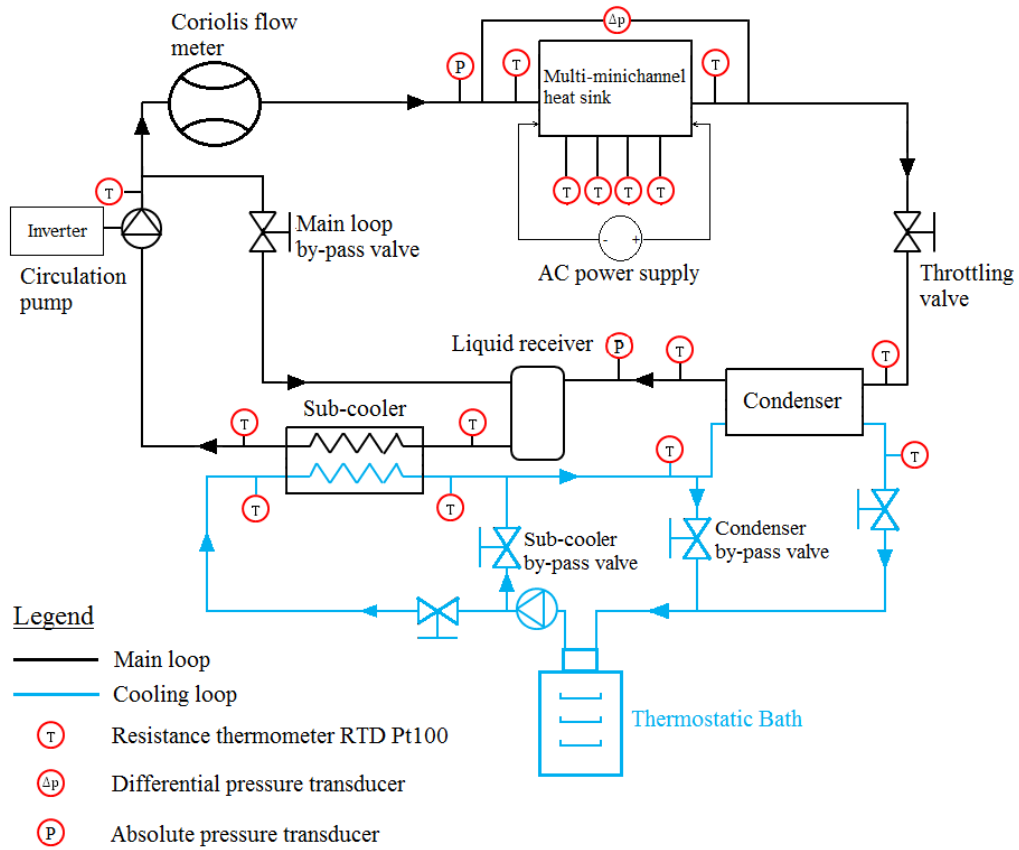
Figure 4.2 Schematic representation of the CHF test rig

4.1.2 Test section

The CHF experimental campaign was carried out by employing an aluminum multi-minichannel heat exchanger as test section, placed horizontally in the test facility. A photograph of the heat sink is shown in Figure 4.3. Six fins provide seven rectangular minichannels, each of them 2 mm wide and 35 mm long. The channels height could be set to 1 mm and 0.5 mm giving equivalent diameters of 1.3 mm and 0.8 mm, respectively. The height was regulated by using two different aluminum cogged covers (see Figure 4.4) placed above the main aluminum block and sealed with a rubber gasket. Two manifolds at the extremities of the test section, with the inlet and the outlet sections perpendicular to the minichannels stream, were designed to guarantee a better balance of the flow distribution.

The inlet manifold was free from orifices and flow stabilizers. Such devices are able to soften the flow instabilities approaching the thermal crisis and prevent possible back-flows, which could be responsible for a partial rewetting of the heated surface and therefore a delayed critical heat flux. The choice of avoiding inlet restrictions and orifices for this experimental campaign entails the drawback of an unstable mass flow rate when close to the thermal crisis and also the need to operatively define the CHF. However, in this way the effective operative conditions encountered in real applications are preserved.
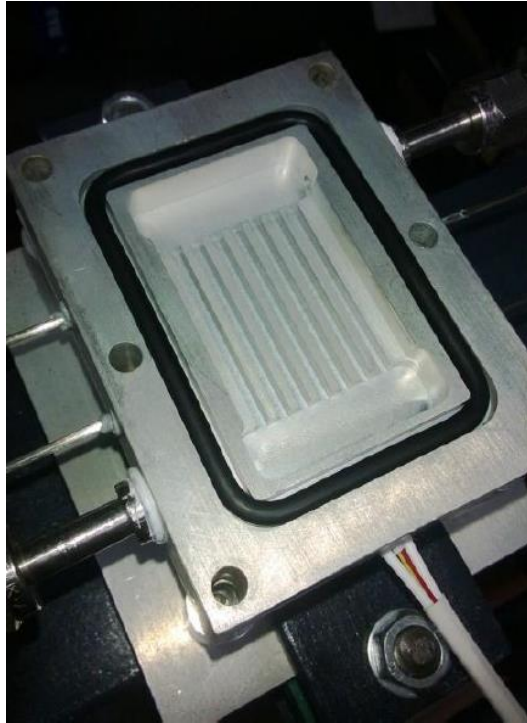
Figure 4.3 Aluminum multi-minichannel heat sink used as test section for the CHF experiments
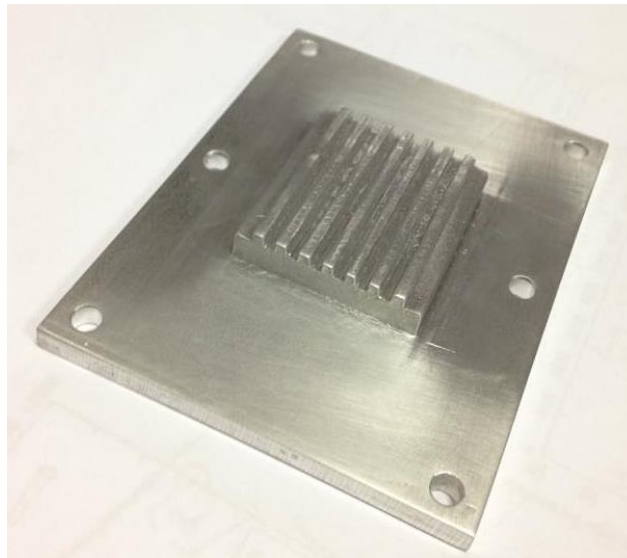
Figure 4.4 Aluminum cogged cover used for a channel height of 0.5 mm

Two different test section arrangements were used in the experimental campaign for this PhD thesis. In both cases, the heat dissipated by the boiling fluid was supplied from the bottom

thanks to a dedicated slot carved underneath the aluminum main block. In the first set of experiments, the heated length was 25 mm and the heat was provided by means of a ceramic square element (25 x 25 mm^2 and 2 mm thick, see Figure 4.5), which was able to supply up to 697 W (at 25 °C and 240 V). In this case the minichannels height was fixed to 1 mm, having an equivalent diameter of 1.3 mm and a heated length-on-equivalent diameter ratio (L_h/D) equal to 19. The thermal contact between the ceramic square heater and the aluminum test section was ensured with a special nano-aluminum thermal compound, presenting a thermal conductivity of 11.2 W/m K, as declared by the manufacturer.
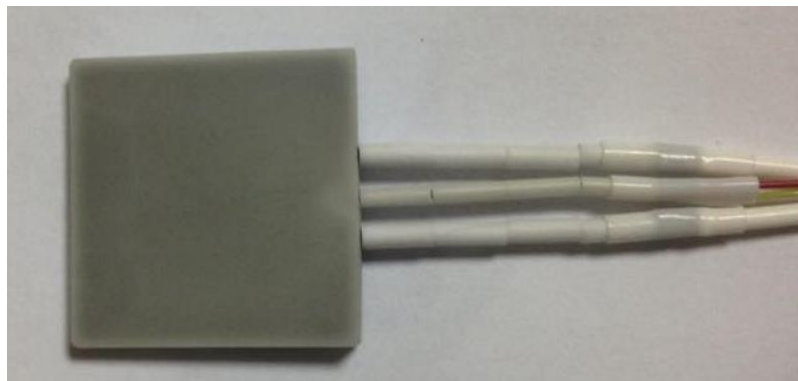
Figure 4.5 Watlow Ultramic ceramic square heater used for the first set of experiments with a L_h/D ratio of 19

The second set of experiments was carried out by lengthening the slot underneath the test section and thus having a heated section of 35 mm, equal to the minichannel length. The heat was provided thanks to a silicon nitride ceramic cartridge heater (Bach HPT100072, see Figure 4.6) accommodated in a copper block, whose pyramidal edge was put in the slot underneath the aluminum test section. According to the manufacturer, the cartridge heater is able to provide up to 3000 W (at 600 °C and 400 V). In this case, both minichannels heights of 1 mm and 0.5 mm were used, thus having two different equivalent diameters of 1.3 mm and 0.8 mm and therefore two heated-length-on-equivalent diameter ratios of 27 and 44, respectively. The peculiar copper pyramidal geometry was chosen to preserve the perpendicular direction of the heat flux referring to the minichannel cross section. Different simulations were also run to appreciate the heat flux direction and to estimate the maximum temperatures reached in the solid structure at different operating conditions and thermal

loads. The thermal contacts between the cartridge heater and the copper block and between the copper structure and the aluminum test section were ensured with a high temperature thermal compound (Timtronics RedIce 611HT), able to work up to a maximum operating temperature of 360 °C with a thermal conductivity of 3.2 W/m K. The compound was carefully placed avoiding possible air sacks and ensuring the uniformity of heat flux. A 3D drawing and a picture of the second test section arrangement are shown in Figure 4.7, while the main geometrical features are summarized in Figure 4.8.

For both the test section arrangements, the heat was provided thanks to Joule effect by using AC power supply and a solid state relay (Gavazzi RM-1E-40-AA-25), able to vary the electrical load up to 400 V and 25 A. The relay desired output was set using 4-20 mA current provided by Arduino One controller. The channels wall temperature was estimated thanks to four cylindrical Pt100 RTDs placed alongside the test section (two for each side) at a distance of 2.5 mm from the channels wall.

In order to minimize the heat losses, the whole test facility was covered with an appropriate layer of synthetic rubber, provided by Armacell. According to the manufacturer, its thermal conductivity is 0.042 W/m K. The same insulating material was also used to cover the aluminum heat sink in the first test section arrangement. For the second test section arrangement, instead, the presence of the bulky copper structure and the higher temperatures reached during the experiments led to the use of a first layer of mineral wool (carrying a thermal conductivity of 0.07 W/m K) and then a second layer of synthetic rubber.

Figure 4.6 Bach silicon nitride cartridge heater used for the experiments with a L_h/D ratio of 27 and 44
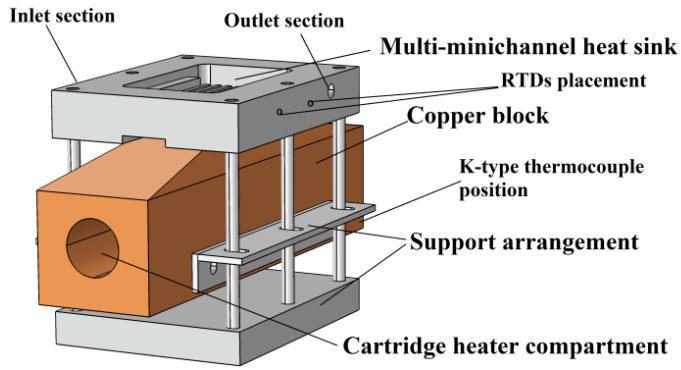
Figure 4.7 3D drawing and a picture of the aluminum heat sink in its second arrangement

Feature	Value	Symbol
Number of channels	7	N
Channels width	2 mm	W_{ch}
Channels height	1/0.5 mm	H_{ch}
Channels length	35 mm	L
Equivalent diameter: $\frac{4 \cdot W_{ch} H_{ch}}{2 \cdot (W_{ch} + H_{ch})}$	1.3/0.8 mm	D
Heated width	25 mm	W_h
Heated lengths	25/35 mm	$L_{h,}$
L_h/D ratio	19/27/44	L_h/D
Distance RTD-wall	2.5 mm	s
Distance between RTDs	10 mm	W_{RTD}
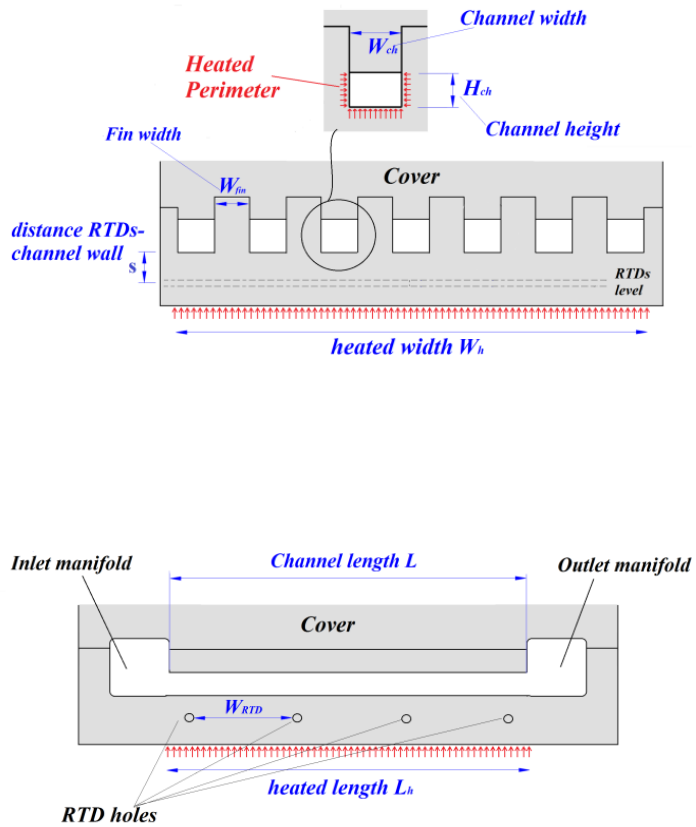
Figure 4.8 Aluminum heat sink cross and longitudinal section, with the main geometrical information

4.2   Measurement instrumentation

The main features of the measuring instruments and the user interface used for the CHF experiments are given in this section. All the instrument specifications in terms of measurement range, output range and their accuracy is discussed here, while the related uncertainty analysis of the measured and derived parameters will be shown in detail in section 4.4.

4.2.1   Absolute pressure measurements

Two absolute pressure transducers (CTE8-050-AY4N, provided by Tersid) measured the refrigerant absolute pressure at the inlet of the test section and at the inlet of the liquid receiver (i.e. plate condenser outlet), respectively. Their range of effectiveness is 0-50 bar, with a current output signal of 4-20 mA. The accuracy of ±0.3%, according to the manufacturer, includes the non-linearity, repeatability and hysteresis effects.

4.2.2   Differential pressure measurements

The pressure drop across the multi-minichannel heat sink was measured thanks to a differential pressure transducer (1151 Smart, provided by Rosemount) connected to the inlet and outlet parts of the test section. The high and low sides of the transducers are connected to the experimental facility by a 2 mm internal diameter copper tubes. The operating range is 0-60 kPa with an output current signal of 4-20 mA and the overall instrument accuracy, including the non- linearity, hysteresis and repeatability effects, is ±0.45 kPa.

4.2.3   Mass flow rate measurement

The mass flow rate in the test section was monitored thanks to a Coriolis mass flow meter (MicroMotion S12S, provided by Emerson) placed after the pump, powered with AC current and 230V with an output signal of 4-20 mA, having an operative range of 0-115.7 g/s. The instrument was calibrated up to 2% of the full scale (at 2.3 g/s), giving a maximum uncertainty of ±1% of the reading. For precautionary purposes, this value was used for the whole experimental campaign.

4.2.4   Temperature measurements

Different ceramic RTDs were placed throughout the experimental plant in order to monitor the refrigerant and demineralized water conditions during the experiments. The sensors were

all fastened at the external part of the stainless steel tubes, with the thermal contact ensured by the use of a nano-aluminum thermal compound. The Pt100 RTDs were calibrated by the manufacturer using three points of measurements (-25 °C, 0 °C and +25 °C) with an overall declared uncertainty of ±0.18 °C. The provided calibration curve was then used in the whole sensor range of -80 - +250 °C. The four cylindrical Pt100 RTDs placed inside the aluminum heat sink were also calibrated by the manufacturer exposing an overall declared uncertainty of ±0.154°C.

4.2.5 Electrical heat input measurements

As explained in the previous sections, the heat was provided thanks to Joule effect by using AC power supply and a solid state relay able to modulate the voltage applied to the ceramic heater in a range 0–230 V for the square ceramic element and 0–380 V for the cartridge silicon nitride ceramic heater. The imposed heat rate was then measured by means of a digital wattmeter (HM8115-2, provided by Rohde & Schwarz), which uses true rms (root mean square value) converters for measuring voltage and current separately, within a range of 0.1– 500 V and 0.001–16 A, respectively. The real-time power was then measured using an analog multiplier, while the active power is derived by integrating the instantaneous power for the period of the sinusoidal wave. The declared uncertainty of the instrument is ±1% of the reading. All values were remotely read and controlled via serial interface RS232.

4.2.6 Data acquisition system and user interface

The different output signals coming from the transducers were read by a series of FieldPoint modules, provided by National Instrument, and all the data were finally transferred to a pc desktop and monitored in Labview [121] environment. Specifically, the FP-RTD-124 modules collected data from all the Pt100 RTDs placed in the experimental plant, then translating the electrical resistance into a temperature using the calibration lines provided by the manufacturer. The 4-20 mA current output signals coming from the absolute and differential pressure transducers and from the Coriolis mass flow meter were instead recorded by two FP-AI-110 modules and translated into the desired parameters using the linear calibration curve of each transducer. The bath temperature and the imposed heat power were instead recorded with their own dedicated hardware and then transferred to the pc desktop and monitored in Labview [121] environment. The remote controls for the variation

of the pump frequency and the imposed heat load were given in Labview [121] software with two dedicated 4-20 mA circuits commanded by Arduino One controller.

The user interface in Labview [121] is shown in Figure 4.9. All the parameters of interests were read in real-time and their overall uncertainty in the recording time was estimated, to let the user be aware of the goodness and stability of each experiment. The thermodynamic conditions at the test section inlet and outlet were visible with a green and an orange dot on a p-h diagram, whereas the expected critical value was computed with one of the correlations available in literature and placed as a red dot on the p-h diagram. In this way, the user was warned when the estimated critical condition was about to be approached. Automatic controls were also able to shut-off the electric load applied to the test section in case of the occurrence of dangerous situations (either system pressure and temperature over a chosen limit or undesired low refrigerant mass flow rates)..
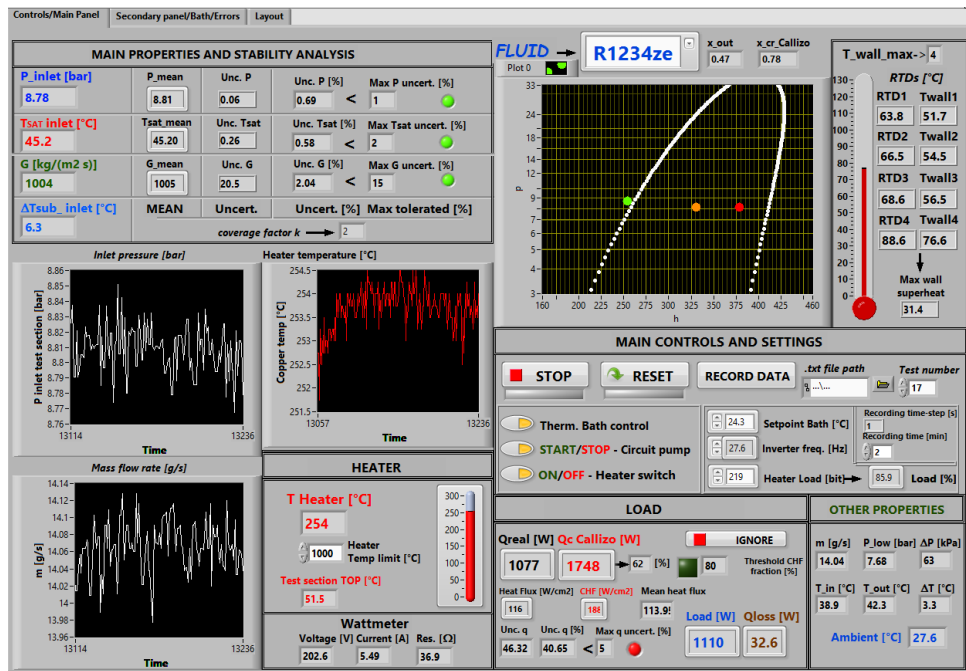
Figure 4.9 Labview [121] interface for the CHF experiments

4.3 Method

The description of the experimental procedure, together with the data reduction process and the operative definition of critical heat flux used for the experiments shown in this thesis are discussed in this section.

4.3.1 Experimental procedure

The purpose of each test was to describe a complete boiling curve from the onset of boiling region up to the critical condition. For each boiling curve, the desired parameters in terms of mass flux, inlet sub-cooling and inlet saturation temperature (i.e. system pressure) were imposed and monitored throughout the experiment. Specifically, the refrigerant mass flow rate was obtained by setting a specific inverter frequency of the circulation pump. The saturation temperature was instead fixed by imposing the desired temperature of the thermostatic bath. Further adjustments of both mass flow rate and system pressure were possible thanks to the manually-controlled by-pass valve and the micrometric throttling valve. Small variations of the inlet sub-cooling were obtained by manipulating the ball cock valve controlling the secondary fluid mass flow rate inside the double pipe sub-cooler. However, the limited working fluid charge in the experimental facility (2.0 kg for all the fluids tested) allowed only reduced sub-coolings (0-20 °C) for all the operating conditions.

Once all the desired parameters were fixed, for both the test sections the heat was supplied in steps (roughly 20-40 W) for the first part of the boiling curve and in smaller increments when the critical condition was approached, in order to be more accurate in the CHF detection. K-type thermocouples were able to monitor the heaters temperature. For safety reason and to avoid the test section burnout, the power supply was shut-off at the threshold of 150 °C for the square ceramic heater and at 350 °C for the silicon cartridge heater in the second test section arrangement. During the tests, the operating parameters were subjected to small deviations from the set values caused by the increasing heat power applied. These divergences were accordingly corrected by manipulating the throttling and by-pass valves at disposal.

The system was considered stabilized when the relative uncertainties of heat imposed, saturation temperature and mass flux were inferior to 3%, 2% and 10%, respectively in the

recording time of 2 minutes with a recording frequency of 1 Hz. For each point of the boiling curve, the nominal value was assigned to the sample average value.

4.3.2   Data reduction

The data reduction process was implemented with Matlab [122] software and the calculation of all thermodynamic properties was carried out with the software REFPROP 9.0, developed by NIST [123].

For a given test point, the mass flux inside the test section was evaluated as follows:

$$G = \frac{\dot{m}}{N \cdot W_{ch} \cdot H_{ch}}$$
(4.1)

where $\dot{m}$ is the measured mass flow rate, whereas N represents the number of minichannels (always equal to 7 for this experimental campaign), W_{ch} is the minichannels width (equal to 2 mm) and H_{ch} is the minichannels height (which was set to 1.0 and 0.5 mm).

The inlet saturation temperature was instead directly evaluated thanks to the measured inlet absolute pressure by means of the software REFPROP 9.0 [123]. The same approach was used to evaluate the inlet saturated liquid and vapor enthalpies and also the effective inlet enthalpy:

$$i_{in} = f(T_{in}, P_{in})$$
(4.2)

The inlet sub-cooling was computed by subtracting the inlet measured temperature to the inlet saturation temperature:

$$\Delta T_{sub,in} = T_{sat} - T_{in}$$
(4.3)

For the evaluation of the wall temperature, four cylindrical Pt100 resistance thermometers were positioned below the channels wall at a distance of 2.0 mm from the ceramic heater (or the copper block in the second test section arrangement) and at 2.5 mm from the minichannels inferior wall (see Figure 4.8 for further details). The real wall temperature was evaluated by assuming 1-D heat conduction in the perpendicular direction with respect to the channel cross section and fluid flow. A preliminary numerical analysis with dedicated

software confirmed that the axial conduction in the aluminum block was negligible when compared to the main flux in the vertical direction.

$$T_{w,i} = T_{RTD,i} - \frac{\dot{q}_b \cdot s}{\lambda_{al}} \tag{4.4}$$

In the above equation, the subscript i refers to the ith resistance thermometer. T_{RTD} is the measured temperature and T_w is the estimated wall temperature. The aluminum thermal conductivity is λ_{al} (considered constant and equal to 240 W/m K), the distance wall-RTD is indicated as s. The parameter $\dot{q}_b$ is the base heat flux, obtained with the ratio of the heat power divided by the base heated surfaces beneath the aluminum test section (which are 25 x 25 mm^2 and 25 x 35 mm^2 for the first and second test section arrangements, respectively).

$$\dot{q}_b = \frac{\dot{Q}}{W_h \cdot L_h} \tag{4.5}$$

The actual wall heat flux q_w, used for the CHF detection and for the boiling curves exposed in the results section, takes into account the effective heat transfer surface provided by the multi-minichannel heat sink. Specifically, the heated perimeter (also shown in the enlargement in Figure 4.8) is the sum of the channels bottom walls and the two lateral fin surfaces, multiplied by a fin efficiency. The top side was instead ignored and considered adiabatic. The same approach was also used by Park and Thome [25] for their copper multi-minichannel test section.

$$\dot{q}_w = \frac{\dot{Q}}{N \cdot L_h \cdot \left(W_{ch} + 2H_{ch} \cdot \eta\right)} \tag{4.6}$$

In the above equation η is the fin efficiency, whereas the heated length is indicated as L_h (equal to 25 and 35 mm for the first and second test section arrangements). The fin efficiency and therefore the wall heat flux were found with an iterative calculation explained with the following algorithm:

a) A first value of 0.90 for the fin efficiency was guessed.
b) The wall heat flux was evaluated with Equation (4.6)
c) The heat transfer coefficient HTC was then evaluated with the following equation:

$$HTC = \frac{\dot{q}_w}{T_{w,\max} - T_{sat,in}} \tag{4.7}$$

Where $T_{w,max}$ is the maximum wall temperature estimated among the four cylindrical RTDs with Equation (4.4).

d) Using 1-D conduction theory, the fin efficiency could be recalculated as suggested by Baher and Stephan [124]:

$$m^2 = \frac{HTC \cdot 2\left(W_{fin} + L_h\right)}{\lambda_{al} \cdot W_{fin} \cdot L_h} \tag{4.8}$$

$$\eta = \frac{\tanh\left(m \cdot H_{ch}\right)}{m \cdot H_{ch}} \tag{4.9}$$

e) The calculation was then repeated from point b) up to the variation of the fin efficiency between two consecutive iterations was inferior to 0.001.

The outlet fluid enthalpy was estimated with an energy balance applied to the test section, by assuming the aluminum block adiabatic through the surroundings:

$$i_{out} = i_{in} + \frac{\dot{Q}}{\dot{m}} \tag{4.10}$$

Finally, the test section outlet vapor quality was computed as a function of the outlet enthalpy and of the outlet refrigerant pressure, which was in turn deduced from the measured inlet fluid pressure and total pressure drop ΔP_{drop}:

$$x_{out} = f\left(P_{out}, i_{out}\right) \tag{4.11}$$

$$P_{out} = P_{in} - \Delta P_{drop} \tag{4.12}$$

4.3.3 CHF operative definition

As known, the boiling curves exhibit a high slope during evaporation due to the very high heat transfer coefficient reached in case of stable boiling. As soon as the critical region is approached, the slope becomes lesser and lesser with a moderate or sharp increase of the wall

superheat with small heat flux increments. Rigorously, the CHF should be identified when the boiling curve becomes almost horizontal, exposing a nearly 0 value for its slope.

However, the experimental results presented in this thesis have shown that the boiling curves, especially when increasing the mass velocity, did not provide an abrupt decrease in their slope, but only a gentle drop was detected. Yet, this behavior is not unique and other similar cases were published by different researchers in scientific literature [25] [26] [27], especially when working with multi-minichannels test sections without inlet restrictions and orifices.

As an example, Figure 4.10 shows two boiling curves of refrigerant R1234yf at a saturation temperature of 45 °C and with two different mass velocities of 148 and 348 kg/m^2 s. It is evident that, for the highest mass flux, the thermal crisis is not marked as a sudden flat deviation from the boiling curve's trend. This behavior is instead seen for the curve obtained with the lowest mass velocity. The reason to these discrepancies has to be probably found in the mal-distribution problems occurring in multi-channels systems.
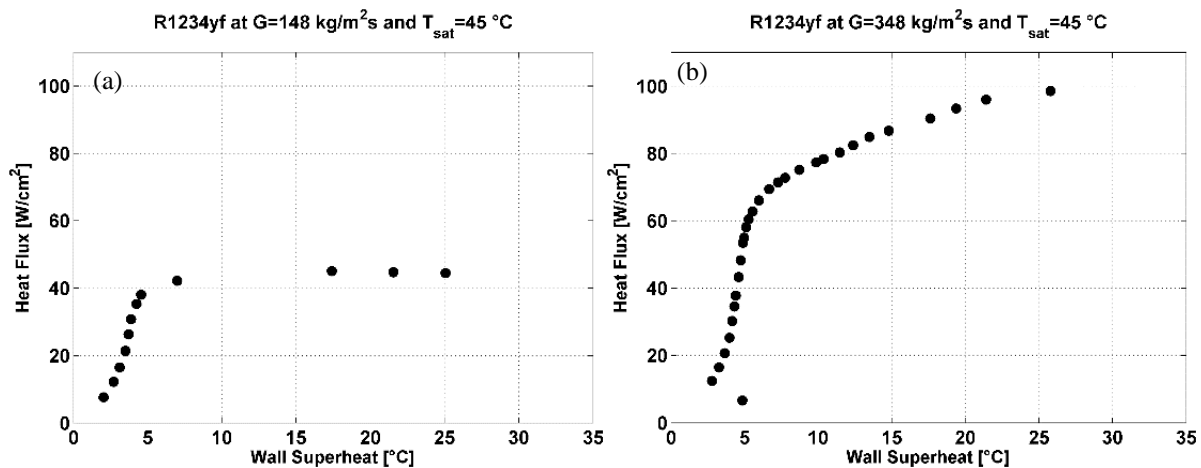
Figure 4.10 Difference in experimental boiling curves slope when approaching the critical condition with two different mass velocities of: (a) 148 kg/m^2 s and (b) 348 kg/m^2 s. In both cases the working fluid is R1234yf at a saturation temperature of 45 °C.

This behavior made necessary the use of an objective method to identify the thermal crisis. Additionally, as explained in the literature review section, the definition of critical heat flux

is often unclear and different authors use different terminology and detection methods to refer to the same phenomenon.

Figure 4.11 shows some experimental CHF values defined with different methods as a function of the mass velocity G for the refrigerant R134a, a heated length-on-equivalent diameter ratio $L_h/D = 27$ at a saturation temperature of 45 °C. The blue and red curves are constructed by using as CHF definition the wall heat flux corresponding to a chosen threshold for the wall superheat of 25 and 45 °C, respectively. The green line is instead constructed by defining the CHF as the wall heat flux in which the slope of the boiling curve is inferior to the limit value of 1.0 W/cm^2 K. In case of mass velocities of $G > 700$ kg/m^2 s, the boiling curve never reached the threshold slope and the CHF could not be defined with this method. Finally, the black dashed line refers to the CHF values evaluated with the predictive method of Callizo [51].
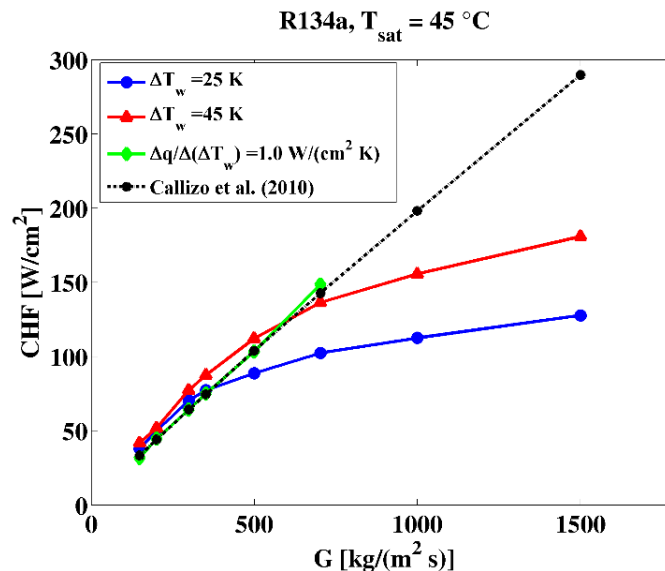
Figure 4.11 Effect of a different CHF detection method on the experimental results [38]

Even if referring to the same experiment, Figure 4.11 shows that the CHF values are strongly dependent on the detection method used, especially for high mass fluxes. In case of $G < 500$ kg/m^2 s, all the mentioned criteria give approximately the same results, thus indicating that the boiling curve is subjected to a steep wall superheat when approaching the thermal crisis

only for low mass velocities. The slope threshold criterion seems to be in good agreement with the correlation used at any mass flux, but the CHF is found at very high wall superheats, which cannot be realistically sustained in real cooling applications.

In this thesis, a new method [38] to detect the critical heat flux during experiments was implemented, by considering both the boiling curve minimum slope threshold and the maximum wall superheat that might be tolerated during realistic cooling applications. Specifically, when the wall superheat (defined with the inlet saturation temperature and the maximum wall temperature among the four RTDs) was inferior to 25 °C, the critical heat flux was defined as the wall heat flux occurring when the boiling curve slope decreased below a chosen limit of 1.0 W/cm^2 K, the same value used also in [26] and [29]. Practically, the analytical slope of the boiling curve was found with a cubic spline interpolation from the experimental data and the search of CHF only began when the slope was always below a threshold value of 1.5 W/cm^2 K. As an example, Figure 4.12 shows the slope of the boiling curve found with refrigerant R134a at a saturation temperature of 65 °C and an average mass flux of 300 kg/m^2 s. From the green line, the slope will be always inferior to 1.5 W/cm^2 K and the research of CHF may start. The actual CHF (plotted as a red star in Figure 4.12) is then found when the curve first reach the imposed limit of 1.0 W/cm^2 K,
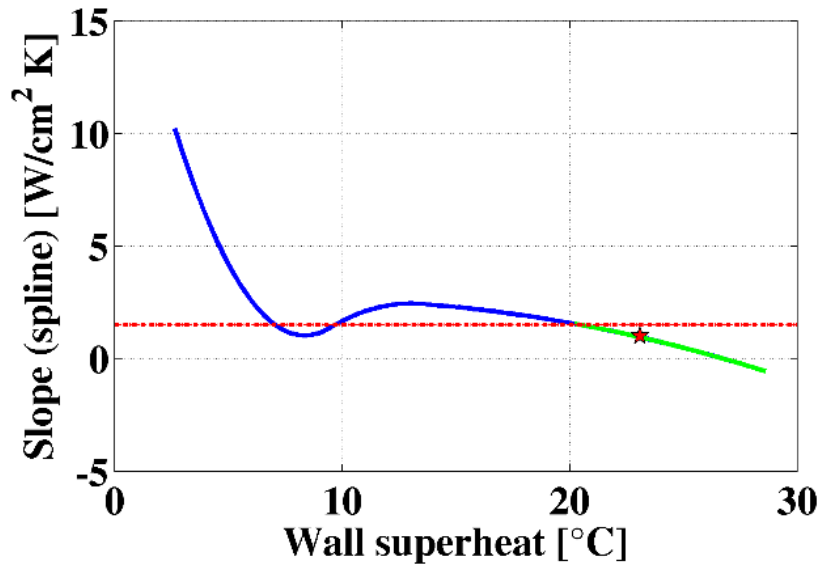
Figure 4.12 CHF detection method in case of refrigerant R134a at $L_h/D = 27$, G=301 kg/m^2 s and T_{sat}=65 °C [38]. The red dashed line provides the search threshold of 1.5 W/cm^2 K and the real CHF value is found at a slope of 1.0 W/cm^2 K, displayed as a red star.

Either in case the abovementioned method was not able to detect the CHF or the wall superheat at the critical condition was higher than 25 °C, the CHF values was defined as the wall heat flux corresponding to a wall superheat of 25 °C. For a better comprehension of the method, the complete algorithm for the CHF detection is shown in Figure 4.13.

As a summary, since at high mass fluxes it was not possible to reach an almost horizontal line in the boiling curve, the wall superheat detection method was implemented in order to look at the practical point of view, so that excessive wall temperature and overheating were prevented in the device that has to be cooled. For low mass velocities, instead, in which the boiling curves did expose a sudden change of slope up to very low values, it was preferred to keep the slope threshold method for the CHF detection.

The effect of a different threshold for the boiling curve slope when detecting the critical heat flux was also studied for this thesis. Figure 4.14 shows the CHF obtained with the only slope method as a function of the chosen threshold, for refrigerant R1234ze at different mass velocities and saturation temperatures. It was seen that at low mass velocities, the thermal crisis corresponded to a sharp change of the boiling curve slope and thus the choice of a specific threshold (from 1.0 to 2.5 W/cm^2 K) was non-influential. Anyway, the CHF values

would be also similar to those obtained employing the wall superheat detection method. For higher mass velocities (from 300-350 kg/m^{2}s up to 1500 kg/m^2 s), the CHF was always detected with the 25 °C wall superheat limit and the choice of a different slope limit was not significant any longer.

Boiling curve plot

Evaluation of the boiling curve slope

Are the last intervals below the research threshold? — **NO**

YES

Search the CHF with the operative threshold value

Is the CHF found? — **NO** → $\Delta T_w \geq \Delta T_{w,lim}$? — **NO** → CHF not found

YES

YES

Check: $\Delta T_{w,cr} < \Delta T_{w,lim}$? — **NO** → $CHF = \dot{q}_w(\Delta T_{w,lim})$

YES

CHF found with the interpolating spline method
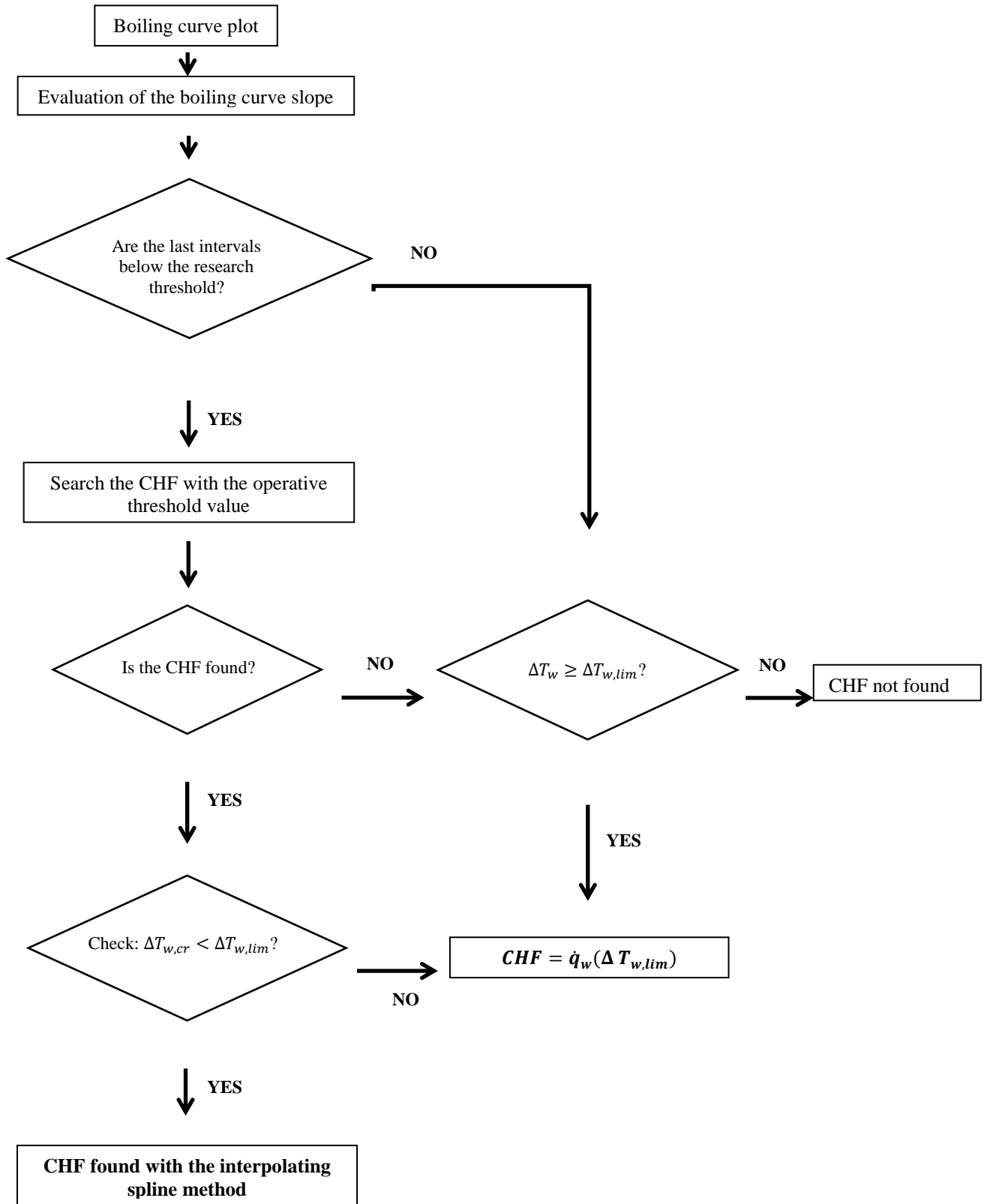
Figure 4.13 Algorithm for the CHF detection method [38]
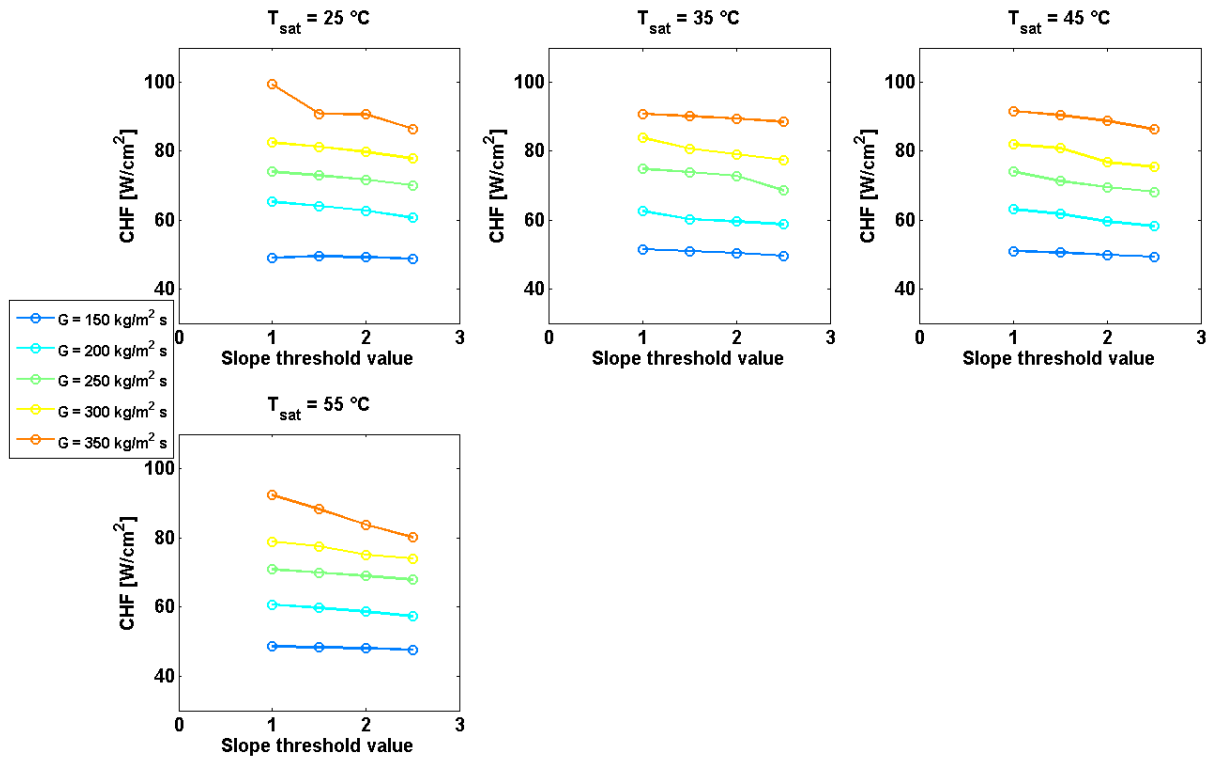
Figure 4.14 Effect of a different slope threshold value on the CHF if detected only with the slope method

4.4 Uncertainty analysis

Unfortunately, when treating experimental data, the true values of measured quantities are always unknown. The best practice is to estimate the uncertainty of a measured or derived quantity, which defines a band or a range where the actual or correct value is most likely to lie. The experimental results must therefore be expressed together with an uncertainty limit, otherwise they will not be meaningful as one will not know how far a measured or derived parameter is from the correct value.

Many references on uncertainty treatment have been available through the decades, such as Moffat [125] [126], Kline and McClintock [127], Coleman and Steele [128] and Taylor [129]

[130]. In this thesis, the uncertainty of measurements and their propagation in the results are discussed according to the ISO [131] standard.

First of all, the uncertainty of the result of a measurement is due to several error sources, that can be categorized as random or precision (Type A uncertainty) and systematic or bias (Type B uncertainty), whether the error changes during the experimental time or it remains steady.

Type A uncertainty is statistical in nature and can be estimated by the standard deviation of the mean value for a quantity which has been measured for a sufficiently large number of times (typically more than 10-20 times). The standard deviation of a mean value is defined as:

$$s_{\bar{x}} = \frac{s_x}{\sqrt{n}} = \sqrt{\frac{1}{n \cdot (n-1)} \cdot \sum_{i=1}^{n} (x_i - \bar{x})^2}$$
(4.13)

where s_x is the standard deviation computed from a sample of the population, n is the number of measurements, x_i (i=1, 2, …, n) are the sample measurements and $\bar{x}$ the mean value given by:

$$\bar{x} = \frac{1}{n} \cdot \sum_{i=1}^{n} x_i$$
(4.14)

Type B uncertainty $w_{\bar{x}}$ is not statistical in nature and most of the times is constant and must be estimated from the previous available measurement data, documents and calibration certificates provided by the manufacturers and personal knowledge of the operator regarding the behavior of the instruments. The several mentioned sources of type B error are often independent and can be combined using the root-sum-square (RSS) method to evaluate the total uncertainty of type B.

According to BIPM/ISO standards [131], components of uncertainties of type A and type B may be considered to be independent and the combined uncertainty $u_{\bar{x}}$ can be evaluated with the root-sum-square (RSS) of the standard deviations:

$$u_{\bar{x}} = \sqrt{s_{\bar{x}}^2 + w_{\bar{x}}^2}$$
(4.15)

The combined uncertainty obtained with the relation above mentioned lies within 68% (σ) confidence level for a normal distribution of variables. To be more confident of the interval within which the measured value is believed to lie, an expanded uncertainty is usually used and it can be obtained by multiplying the combined uncertainty with the coverage factor z as:

$$U_{\bar{x}} = z \cdot u_{\bar{x}} \tag{4.16}$$

Typically, z is chosen in the range from 2 to 3 [132]. When the normal distribution is applied, z=2 defines an interval with a level of confidence of 95,45%, whereas z=3 leads to an interval with a level of confidence higher than 99%. Finally, the result of a measurement should be expressed in this form:

$$X = \left(\bar{x} \pm U_{\bar{x}}\right)\vartheta \tag{4.17}$$

where ϑ is the measure unity of the measured value.

Unfortunately, in many cases a value y is not measured directly, but it is a function of m several variables (for instance the heat flux seen in data reduction equations, whose value is dependent on the measured voltage and current):

$$y = f\left(x_1; x_2; \ldots; x_m\right) \tag{4.18}$$

where x_1 up to x_m are the input variables. The combined uncertainty of the function y is therefore influenced by a change in each variable and it can be estimated from this relation:

$$u_y^2 = \sum_{i=1}^{m} \left(\frac{\partial f}{\partial x_i}\right)^2 \cdot u_{\bar{x}_i}^2 + 2 \cdot \sum_{i=1}^{m-1} \sum_{j=i+1}^{m} \frac{\partial f}{\partial x_i} \cdot \frac{\partial f}{\partial x_j} \cdot u_{\bar{x}_i, \bar{x}_j} \tag{4.19}$$

The Equation (4.19) is based on a first order Taylor series approximation and it is conveniently referred to as the law of propagation of uncertainty. The partial derivatives $\frac{\partial f}{\partial \bar{x}_i}$ are the sensitivity coefficients, $u_{\bar{x}_i}$ is the standard uncertainty associated with the input estimate x_i and $u_{\bar{x}_i, \bar{x}_j}$ is the estimated covariance associated with x_i and x_j. It is possible to state that the combined uncertainty is the root-sum-square (RSS) of the standard deviations:

$$u_y = \sqrt{s_y^2 + w_y^2} \tag{4.20}$$

With the uncertainties in y function for type A and type B errors are, respectively:

$$s_y^2 = \sum_{i=1}^{m}\left(\left(\frac{\partial f}{\partial \overline{x_i}}\right)^2 \cdot s_{\overline{x_i}}^2\right) + 2\cdot\sum_{i=1}^{m-1}\sum_{j=i+1}^{m}\frac{\partial f}{\partial \overline{x_i}}\cdot\frac{\partial f}{\partial \overline{x_j}}\cdot s_{\overline{x_i},\overline{x_j}} \tag{4.21}$$

$$w_y^2 = \sum_{i=1}^{m}\left(\left(\frac{\partial f}{\partial \overline{x_i}}\right)^2 \cdot w_{\overline{x_i}}^2\right) + 2\cdot\sum_{i=1}^{m-1}\sum_{j=i+1}^{m}\frac{\partial f}{\partial \overline{x_i}}\cdot\frac{\partial f}{\partial \overline{x_j}}\cdot w_{\overline{x_i},\overline{x_j}} \tag{4.22}$$

With the hypothesis of x_i all independent variables, the covariance associated with x_i and x_j is not anymore computable and it is permitted to state:

$$s_y^2 = \sum_{i=1}^{m}\left(\left(\frac{\partial f}{\partial \overline{x_i}}\right)^2 \cdot s_{\overline{x_i}}^2\right) \tag{4.23}$$

$$w_y^2 = \sum_{i=1}^{m}\left(\left(\frac{\partial f}{\partial \overline{x_i}}\right)^2 \cdot w_{\overline{x_i}}^2\right) \tag{4.24}$$

And to gain higher confidence level, the combined uncertainty for the function y, u_y, is multiplied by the coverage factor z, with its value chosen from the same range already discussed:

$$U_y = z\cdot u_y \tag{4.25}$$

4.4.1   *Uncertainty of measured parameters*

Most of the instrument specification has already been discussed in section 4.2. Table 4.1 provides a summary of the measurement range and the systematic uncertainty for each sensor. The combined uncertainty of each measured parameters was then evaluated with the law of propagation of error (see Equation (4.15)) adding the standard deviation of each sample s_x to the systematic uncertainty. Finally, the expanded uncertainty of the measured quantities was calculated (see Equation (4.16)) by using a coverage factor $z=2$, thus ensuring a confidence level of 95.45%.

Table 4.1 Summary of the instrument specification

Measurement	Range	B-type uncertainty (systematic) w_x
Temperature (4-wire Pt100 RTD)	-80/250 °C	±0.180 °C
Temperature (4-wire Pt100 cylindrical RTD)	-80/250 °C	±0.154 °C
Absolute pressure	0/50 bar	±0.3 % measurement
Differential pressure	0/60 kPa	±0.45 kPa
Flow meter	0.00/115.7 g/s	±1 % measurement
Electrical power	0/8 kW	±1 % measurement

4.4.2 Uncertainty of derived parameters

The evaluation of the expanded uncertainty of all the derived parameters of interest is shown here in detail.

Mass flux

Since the uncertainty of the geometrical characteristics of the channels were not available, the uncertainty of the mass flux is only a function of that of the mass flow rate.

$$u_c(G) = \sqrt{\left(\frac{\partial G}{\partial \dot{m}}\right)^2 \cdot u_c(\dot{m})^2} = \frac{u_c(\dot{m})}{N \cdot W_{ch} \cdot H_{ch}} \tag{4.26}$$

Due to the fluctuations of the mass flow rate in the test section when approaching the thermal crisis, the expanded uncertainty recorded during the tests could reach 15-25% in some cases. However, 90% of the experiments were obtained with a mass flux error band of ±10% and 80% of the experimental campaign carried out mass flux uncertainty inferior to ±5%.

Wall temperature

88

The channels inner wall temperature was estimated with the RTDs measurements in the aluminum block and the base wall heat flux, according to the hypothesis of 1-D heat conduction. The wall temperature expanded uncertainty was therefore evaluated by deriving the Equation (4.6):

$$u_c(T_{wall}) = \sqrt{u_c(T_{RTD})^2 + \left(\frac{s}{k_{al}} \cdot u_c(\dot{q}_b) \right)^2} \qquad (4.27)$$

In the above equation, the expanded equation of the base heat flux was instead computed as:

$$u_c(\dot{q}_b) = \frac{u_c(\dot{Q})}{W_h \cdot L_h} \qquad (4.28)$$

Inlet saturation temperature

The uncertainty of the inlet saturation temperature evaluated with the software REFPROP 9.0 [123] is dependent on the uncertainty of the measured inlet pressure. Thus, it could be written as:

$$u_c(T_{sat}) = dT_{sat} = \frac{\partial T_{sat}}{\partial P_{in}} \cdot dP_{in} \qquad (4.29)$$

By assuming a linear variation of the saturation temperature with pressure in the range of the inlet pressure uncertainty, the above expression may be re-expressed as:

$$u_c(T_{sat}) = \frac{T_{sat}(P_{in} + u_c(P_{in})) - T_{sat}(P_{in} - u_c(P_{in}))}{2 \cdot u_c(P_{in})} \cdot u_c(P_{in}) \qquad (4.30)$$

and therefore:

$$u_c(T_{sat}) = \frac{T_{sat}(P_{in} + u_c(P_{in})) - T_{sat}(P_{in} - u_c(P_{in}))}{2} \qquad (4.31)$$

For this experimental campaign, 90% of the database was obtained with an expanded uncertainty of the inlet saturation temperature at the critical condition inferior to ±0.5 °C. The maximum recorded uncertainty was instead roughly ±3.0 °C, occurred when testing refrigerant R1233zd. As a matter of fact, this fluid presents a very low slope of the p-T

saturation curve, meaning that even with low inlet pressure uncertainty, the related saturation temperature uncertainty is rather substantial.

Saturated and inlet enthalpies

Following the same approach used for the inlet saturation temperature, the uncertainty of the saturated liquid and vapor enthalpies were evaluated as:

$$u_c(i_L) = \frac{i_L(P + u_c(P)) - i_L(P - u_c(P))}{2} \tag{4.32}$$

$$u_c(i_V) = \frac{i_V(P + u_c(P)) - i_V(P - u_c(P))}{2} \tag{4.33}$$

The inlet enthalpy refers to a sub-cooled liquid and therefore it is a function of both inlet pressure and inlet temperature:

$$u_c(i_{in}) = di_{in} = \frac{\partial i_{in}}{\partial P_{in}} \cdot dP_{in} + \frac{\partial i_{in}}{\partial T_{in}} \cdot dT_{in} \tag{4.34}$$

$$u_c(i_{in}) = \frac{i_{in}(T_{in}, P_{in} + u_c(P_{in})) - i_{in}(T_{in}, P_{in} - u_c(P_{in}))}{2} + \frac{i_{in}(P_{in}, T_{in} + u_c(T_{in})) - i_{in}(P_{in}, T_{in} - u_c(T_{in}))}{2}$$

$$\tag{4.35}$$

Also in this case, the variation of the liquid enthalpy with temperature and pressure was considered linear in the range of the measured parameters uncertainty.

Inlet sub-cooling

The inlet sub-cooling uncertainty is a function of the uncertainty of the inlet saturation temperature and of the measured inlet temperature:

$$u_c(\Delta T_{sub}) = \sqrt{u_c(T_{sat})^2 + u_c(T_{in})^2} \tag{4.36}$$

Most of the experimental results (about 90%) were taken with an uncertainty of the inlet sub-cooling inferior to ±0.6 °C, whereas the maximum recorded uncertainty in the experimental database is ±3.0 °C, obtained with refrigerant R1233zd.

Wall superheat

Once the wall temperature uncertainty was evaluated, the wall superheat uncertainty could be calculated as:

$$u_c(\Delta T_{wall}) = \sqrt{(u_c(T_{wall}))^2 + u_c(T_{sat})^2}$$ (4.37)

Outlet enthalpy

The outlet enthalpy was computed with an energy balance performed on the test section (see Equation (4.10). The related uncertainty took therefore into account the uncertainty of the inlet enthalpy, the mass flow rate and the imposed heat:

$$u_c(i_{out}) = \sqrt{u_c(i_{in})^2 + \left(\frac{1}{\dot{m}} u_c(\dot{Q})\right)^2 + \left(\dot{Q} \cdot \frac{1}{\dot{m}^2} \cdot u_c(\dot{m})\right)^2}$$ (4.38)

Wall heat flux (CHF)

Neglecting the uncertainty of the geometrical parameters, the overall expanded uncertainty of the wall heat flux and therefore of the detected critical heat flux was computed as:

$$u_c(\dot{q}_w) = \frac{u_c(\dot{Q})}{N \cdot L_h \cdot (W_{ch} + 2 \cdot H_{ch} \cdot \eta)}$$ (4.39)

The overall wall CHF uncertainty should consider the uncertainty related to the boiling curve slope, which is affected by the wall superheat excursion. However, since the CHF phenomenon is obtained with sharp increases of the wall temperature for small heat flux variations, the uncertainty of the measured temperature is not of primary importance and the CHF expanded uncertainty was calculated by only taking into account the electrical measurement. For these reasons, the uncertainty of CHF in any test performed was always inferior to ±10%, and most of the experimental database (90% of the tests) falls into a CHF expanded error band of ±2.5%

Outlet vapor quality

Following the definition of vapor quality, its uncertainty was calculated as a function of the saturated outlet enthalpies and the outlet enthalpy:

$$u_c(x_{out}) = \sqrt{\left(\frac{1}{i_{V,out}-i_{L,out}} \cdot u_c(i_{out})\right)^2 + \left(\frac{i_{out}-i_{V,out}}{\left(i_{V,out}-i_{L,out}\right)^2} \cdot u_c(i_{L,out})\right)^2 + \left(\frac{i_{L,out}-i_{out}}{\left(i_{V,out}-i_{L,out}\right)^2} \cdot u_c(i_{V,out})\right)^2}$$

(4.40)

Most of the experimental database (about 90%) provided outlet vapor quality at the critical condition with an expanded uncertainty of ±0.10. Few points carried higher uncertainty, reaching a maximum of ±0.27.

Table 4.2 provides a summary of the expanded uncertainty of both experimental CHF and operating parameters set for the tests.

Table 4.2 Summary of CHF and operating parameters typical and maximum recorded uncertainties found during the experiments

Parameter	Maximum uncertainty for 90% of the database	Maximum recorded uncertainty
Saturation temperature T_{sat}	±0.5 °C	±3.0 °C
Mass flux G	±10%	±27%
Inlet sub-cooling ΔT_{sub}	±0.6 °C	±3.0 °C
Outlet vapor quality	±0.10	±0.27
CHF	±2.5%	±6.0%

4.5 Test section validation

Before the CHF experiments, the test facility was checked for potential heat losses needed to be taken into account in the data reduction process. This paragraph therefore shows the liquid single-phase experiments performed with refrigerant R134a for both the test section arrangements, that also helped to check the correct functioning of the whole measurement instrumentation. In order to get a satisfactory inlet sub-cooling and thus to maintain

compressed liquid across the test section, the fluid inventory was temporarily increased up to 4.0 kg.

4.5.1 *Single-phase tests for the first test section arrangement*

More than 40 single-phase tests with R134a were performed for the first test section arrangement. The mass flow rate was varied from 14 to 27 g/s, the inlet temperature was set from 27 to 37 °C, having a maximum temperature difference with the surrounding environment of 18 °C. The electrical heat rate imposed to the square ceramic element was varied from 0 to 420 W and compared to the heat absorbed by the liquid refrigerant flowing into the test section, which was calculated by neglecting the pressure drop contribution in the enthalpy variation:

$$\dot{Q}_{eff} = \dot{m} \cdot \overline{c} \cdot (T_{out} - T_{in}) \tag{4.41}$$

The liquid specific heat capacity was evaluated with the software REFPROP 9.0 [123] as a function of the arithmetical average of the inlet and outlet fluid temperatures. The results of the adiabaticity tests are shown in Figure 4.15: at any heat rate imposed, all the data are very close to the bisector. Quantitatively, the heat loss was significant (>4%) for heat powers applied inferior to 100 W, whereas they could be neglected (<4%) at higher heat rates, which were the real operating conditions for the CHF recorded for this thesis. For this reason, the useful heat was considered equal to the electrical measurement.
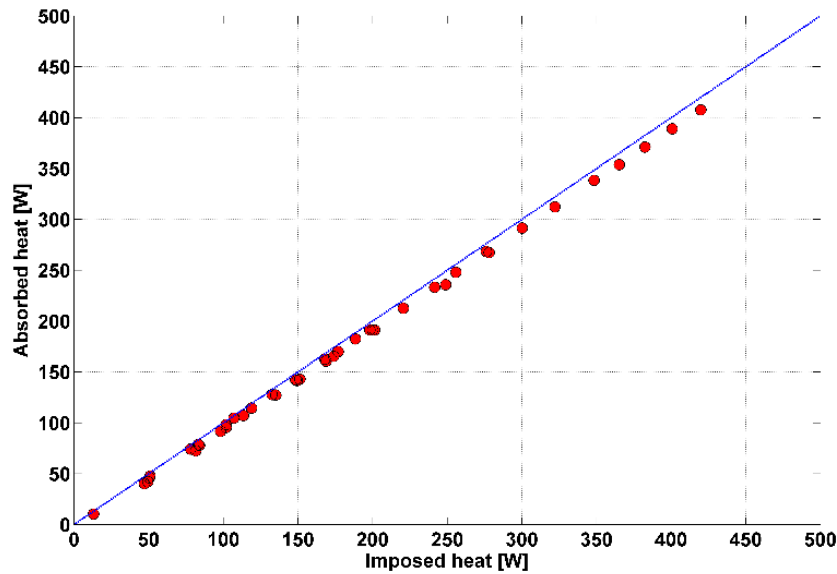
Figure 4.15 Absorbed versus injected heat for the first test section arrangement [29]

4.5.2   Single phase tests for the second test section arrangement

The energy balance was also performed for the second test section arrangement and 83 experiments in liquid single phase were carried out. The heat rate applied ranged from 0 to 720 W and the points in which the test section outlet sub-cooling were inferior to their own uncertainty were excluded from this analysis in order to avoid an undesired boiling process inside the test section. The wall temperatures obtained with the cylindrical RTDs and the heater temperature monitored with a K-type thermocouple, representing high potential for heat transfer towards the ambient, were similar to those reached during the CHF experiments. Particularly, the wall temperatures reached in some cases 90 °C and the copper block in which the cartridge heater was located reached up to 250 °C. The temperature of the environment, evaluated with a ceramic RTD, varied from 20 to 26 °C.

The energy balance performed with the second test section arrangement is shown in Figure 4.16. The absorbed heat is quite similar to the imposed electrical power, with heat losses always below 10% for an applied heat greater than 400 W, even if the presence of the bulky copper structure inevitably led to higher heat losses, when compared to the first test section arrangement. It was also found that the heat losses in this case could be set as a simple function of the difference between the copper temperature and the ambient temperature:

94

$$\dot{Q}_{loss} = 0.815 \cdot (T_{copper} - T_{amb})^{0.682} \tag{4.42}$$

The above equation was implemented in the data reduction process to obtain the effective heat rate.
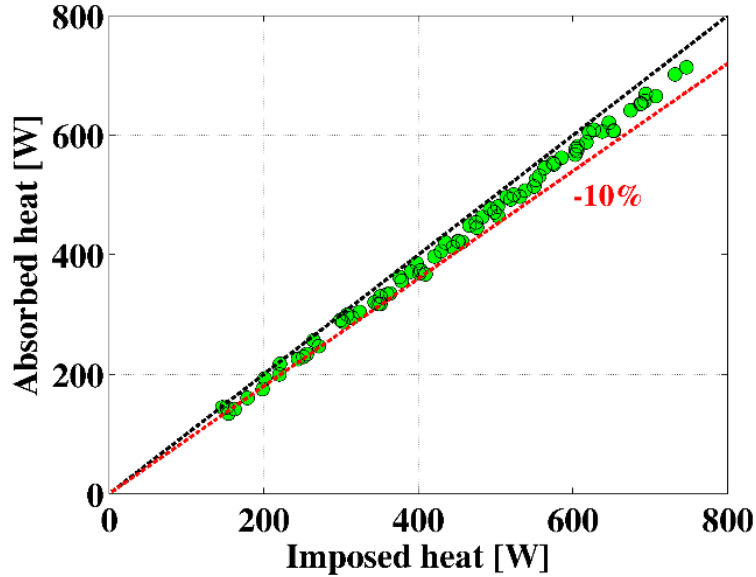
Figure 4.16 Absorbed versus injected heat for the second test section arrangement [38]

For a deeper validation, the liquid single phase heat transfer coefficient was also estimated and compared to the well-known predictive methods of Gnielinski [75] and Dittus-Boelter [70]. Specifically, the single phase heat transfer coefficient h_{sp} and the related Nusselt number were evaluated as:

$$h_{sp} = \frac{\dot{q}}{T_{wall} - T_f} \tag{4.43}$$

$$Nu_{sp} = h_{sp} \cdot \frac{D}{\lambda_f} \tag{4.44}$$

The wall temperature T_{wall} was calculated with the same expression used in two-phase experiments (see Equation (4.4)). D refers to the minichannels equivalent diameter and the fluid thermal conductivity λ_f was evaluated at the fluid temperature T_f., which was computed for each RTD position as:

$$T_{f,i} = T_{in} + \frac{L_{RTD,i}}{L_h} \cdot \frac{\dot{Q}}{\dot{m} \cdot c} \qquad (4.45)$$

where $L_{RTD,i}$ is the ith RTD distance from the beginning of the heated section and the specific heat c was evaluated at the average temperature between the inlet and outlet sections. The comparison between experimental and expected liquid phase heat transfer coefficient is shown in Figure 4.17. Most of the experimental points fall into the area defined by the two correlations prediction lines.
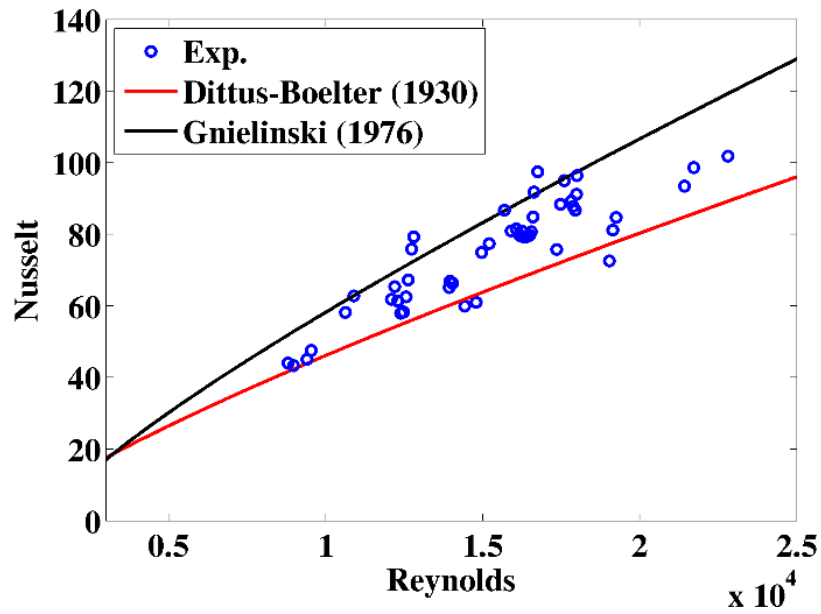
Figure 4.17 Experimental versus predicted values for the liquid single phase heat transfer coefficient for the second test section arrangement [38]

5 CHF results

This chapter presents experimental data concerning critical heat flux in the aluminum multi-minichannel heat sink illustrated in the previous chapter. The entire database is composed of 288 tests carried out with different working fluids, geometrical test section characteristics and operating parameters. The whole chapter is organized in five different sections: the first paragraph shows the chosen operating parameters set and monitored during the experiments, while the second section discusses about the instability analysis performed on the operating parameters. Then, the effect of mass flux, saturation temperature, working fluid and heated length-on-diameter ratio (L_h/D) on the boiling curves behavior is presented. In the third paragraph, the experimental CHF values are shown and the effect of the different operating conditions is discussed. Finally, the CHF results are compared against some of the correlations conceived for both single tubes and multi-minichannel geometries.

5.1 Experimental conditions

In this thesis, the main objective was to investigate on the effect of multiple parameters on the CHF detected with the procedure shown in 4.3.3. As regards the working fluids, R134a and low-GWP refrigerants R32, R1234yf, R1234ze and R1233zd were employed in the experimental facility. The minichannels geometry was changed by varying their height, using 1.0 and 0.5 mm, whereas their width of 2.0 mm remained unchanged. The resulting equivalent diameters were 1.3 and 0.8 mm, evaluated as:

$$D_{eq} = \frac{4 \cdot W_{ch} \cdot H_{ch}}{2 \cdot \left(W_{ch} + H_{ch}\right)} \tag{5.1}$$

The heated length was also varied, by using 25 mm and 35 mm (equal to the total length of any channel). With the heated length of 25 mm, only the equivalent diameter of 1.3 mm was used, whereas with L_h = 35 mm, both channels heights of 1.0 and 0.5 mm were employed. The resulting heated length-on-equivalent diameter ratios used in this thesis are 19, 27 and

44. Mass velocity G was also one of the main operating parameters and was subjected to a wide span of variation, being set from approximately 145 kg/m^2 s up to 3000 kg/m^2 s. The saturation temperature was changed from 24.7 °C up to 75.5 °C for any fluid except R32 (since it entailed system pressures higher than 30 bar, the safety operating limit for the plate heat exchanger). The resulting reduced pressure was within the range 0.036-0.677. The regulation of the ball cock valve in the double pipe heat exchanger allowed only a weak control of the inlet sub-cooling and the experiments were performed within the range 0.2-18.4 °C. Anyway, in the present thesis, its effect on boiling curves and CHF values was not taken into consideration for the parametric analysis, since other researchers [25] [26] observed that within low values (<20 °C) it had a negligible influence on the CHF mechanism. A summary of the range of all the operating conditions and CHF values is shown in Table 5.1.

Table 5.1 Summary of the operating conditions range and CHF results

Parameter	Range
Fluid	R134a, R1234ze, R1234yf, R1233zd, R32
L_h/D ratio	19; 27; 44
Saturation temperature T_{sat} [°C]	24.7-75.5
Mass flux G [kg/m^2 s]	145-3000
Inlet sub-cooling ΔT_{sub} [°C]	0.2-18.4
Critical heat flux CHF [W/cm^2]	19.8-223.7

It is important to declare that all the operating parameters shown in the following diagrams and tables such as the mass flux G, the inlet saturation temperature T_{sat} and the inlet sub-cooling ΔT_{sub} are meant to be evaluated at the critical condition (with a linear interpolation in the interval of experimental points in which the actual CHF was recorded) and not averaged over the points that compose the boiling curves.

98

As regards the wall superheat shown in the boiling curves and used for the critical heat flux detection, the choice for its evaluation could be made among the wall temperature measured by the four cylindrical RTDs placed along the test section, at a distance (W_{RTD}, see Figure 4.7 and Figure 4.8 for further details) of 10 mm one another. The temperature recorded from the four resistance thermometers during the tests was not the same, with greater differences approaching the thermal crisis. Figure 5.1 shows the RTDs measurement versus the outlet vapor quality in a complete boiling curve. The diagram refers to the fluid R134a at a saturation temperature of 75 °C and a mass flux of 700 kg/m^2 s, with the second test section arrangement ($L_h/D = 27$). It can be noted that at low vapor quality (i.e. during stable boiling), all the RTDs measured approximately the same temperature, and little variations were probably due to an increasing vapor quality along the minichannels and thus a possible different heat transfer coefficient. By approaching the critical heat flux, instead, the last thermocouple (RTD 4, placed closely to the outlet manifold) diverged from the other measurements, implying that the thermal crisis first appeared at the end of the channels and then spread upwards. In this thesis, this RTD measuring the maximum wall temperature was used for the construction of the boiling curves and for the CHF detection process, being interested to catch the onset of the thermal crisis. This choice, by a practical point of view, gives the chance to control the highest temperature reached by the cooling system, avoiding possible non-isothermal operations.
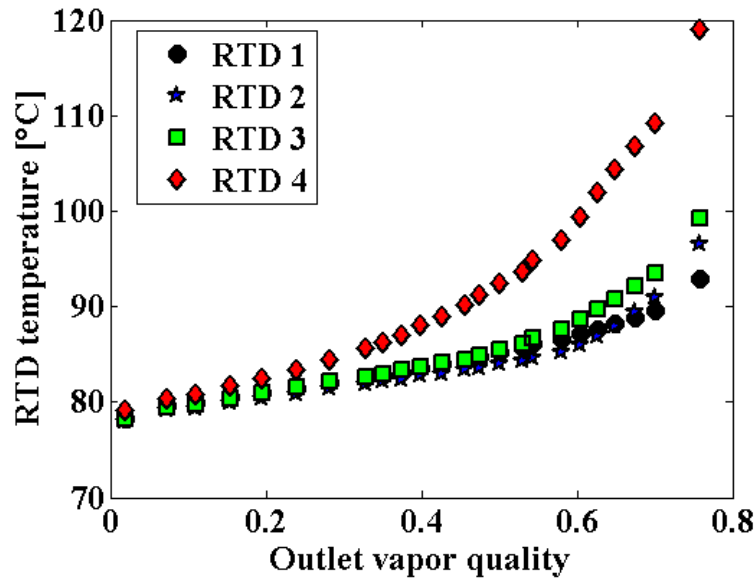
Figure 5.1 Typical trend of the cylindrical RTD measurement for the wall temperature. RTD 4 was chosen for the boiling curves construction and for the CHF detection process

5.2 Instability analysis

As already stated in the previous chapter, all the CHF results shown in this thesis were obtained without the use of flow stabilizers, preserving a design that may easily constructed in the industrial sector. However, being one objective of this research the development of a configuration that did not suffer of mal distribution, an aluminum slit-orifice was conceived to be placed in the inlet manifold to check for possible instabilities before the real CHF tests. The orifices dimensions were approximately 0.5×0.5 mm^2, and used with an equivalent diameter of 0.8 mm, thus reducing the channels inlet to a 25% of their original size. Some pictures of the slit-orifice insert and its positioning inside the test section are provided in Figure 5.2.

Figure 5.2 Photograph of the slit orifice used for the instability analysis and its positioning in the inlet manifold of the aluminum heat sink

Firstly, the boiling curves obtained with and without the slit orifice were compared. Figure 5.3 shows two experiments with refrigerant R1234yf, at a mass flux of 300 kg/m² s and a saturation temperature of 65 °C, with an L_h/D equal to 44. Apart from small differences in the first part of the evaporation process, the boiling curves almost overlapped, verifying that their behavior was almost identical with and without the slit-orifices insert. The same could be stated for the CHF experimental values.
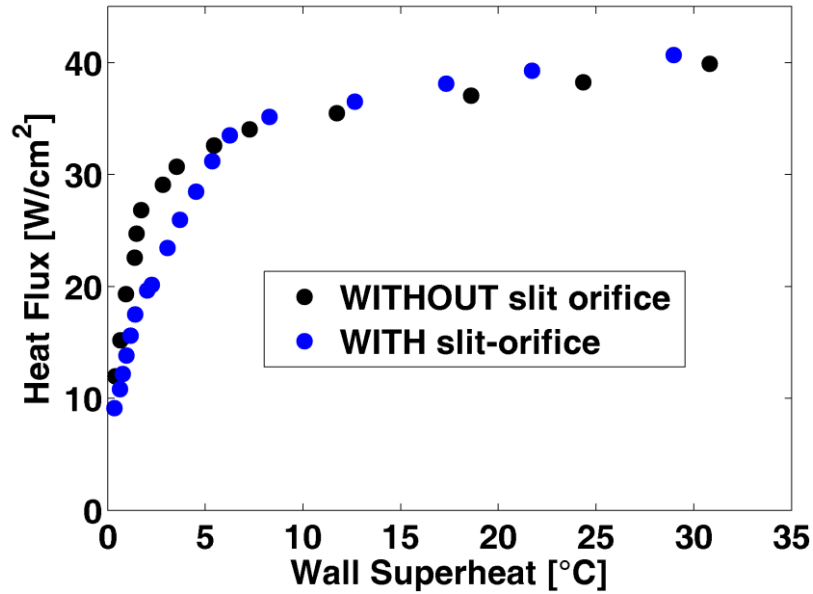
Figure 5.3 Boiling curves of R1234yf at $G = 300$ kg/m^2 s, $T_{sat} = 65$ °C and $L_h/D = 44$. Effect of the slit orifice insertion on the boiling curve behavior

Secondly, the fluctuation of operating parameters were analyzed in the same operating conditions as Figure 5.3, with and without the slit orifice. Three points have been chosen from the boiling curve at different locations (stable boiling, in the middle and during thermal crisis) and the fluctuations of the inlet pressure, inlet temperature and mass flow rate were plotted as a function of the recording time. Table 5.2 shows the graphical results of this analysis.

Table 5.2 Analysis of the operating parameters fluctuation with and without slit orifice. Experiments performed with refrigerant R1234yf at $G = 300$ kg/m^2 s, $T_{sat} = 65$ °C and $L_h/D = 44$.

WITHOUT SLIT-ORIFICE INSERT	WITH SLIT-ORIFICE INSERT
Boiling curve with the analyzed tests exposed	

Fluctuation of the inlet pressure	

Fluctuation of the inlet temperature	

Fluctuation of the mass flow rate	
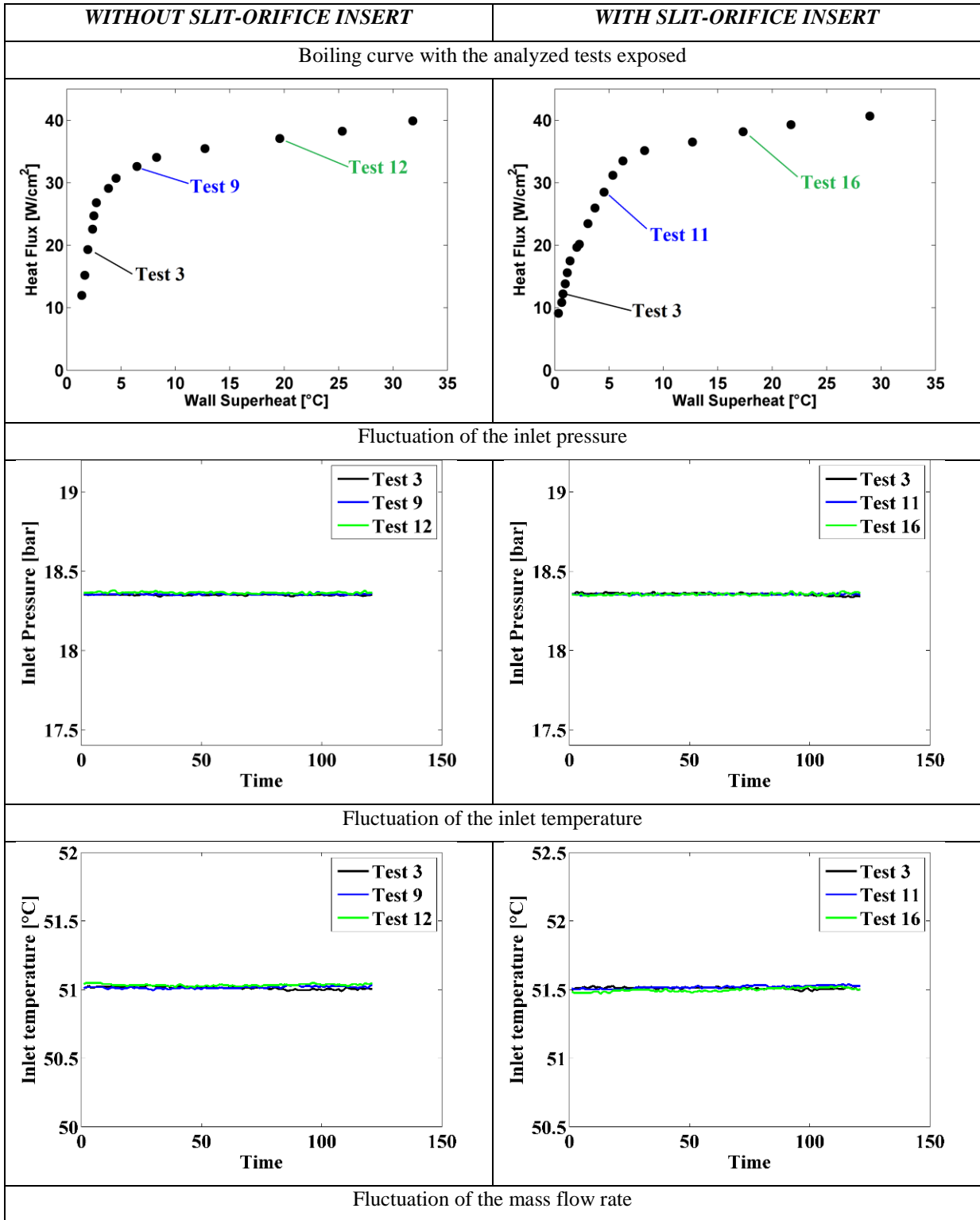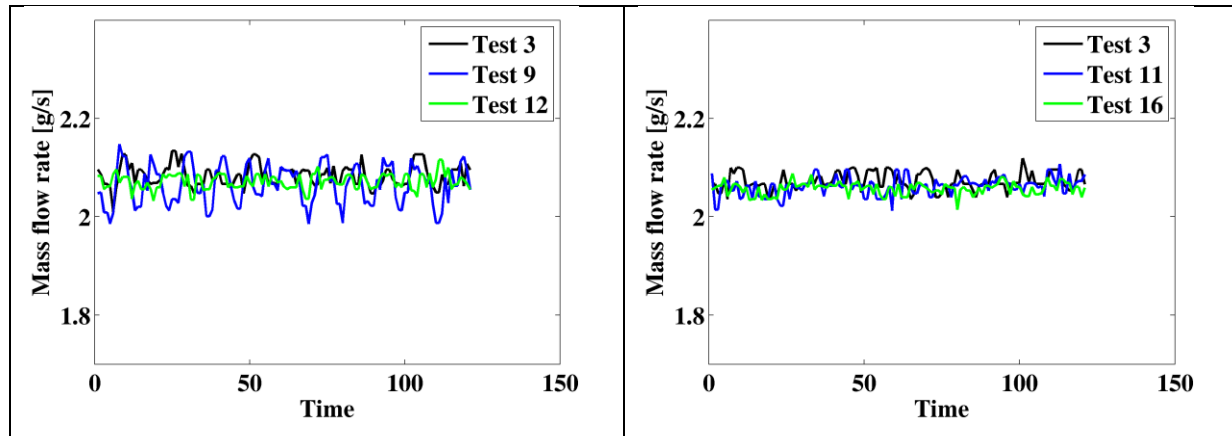
In both case, the inlet pressure fluctuations were plotted with the y-axis ranging in a ±5% band of the average value, the inlet temperature fluctuations ranging in a ±1 °C band of the average value and the mass flow rate fluctuations were plotted with the y-axis ranging in a ±15% band of the average value. It can be observed that no particular fluctuations were recorded for the inlet pressure, temperature and mass flow rate in both cases throughout the boiling curve (inlet pressure fluctuations within ±1%, inlet temperature fluctuations negligible and mass flow rate fluctuations within ±4.5%). Similar results were also obtained for different operating conditions and different fluids.

As a final check, the instability analysis for other two independent tests without the inlet slit orifice at low and high mass velocities was performed. Specifically, the fluctuations of the inlet pressure, inlet temperature and RTD measured wall temperatures at different locations of the boiling curve were analyzed for refrigerant R134a at $G = 300$ kg/m^2 s, $T_{sat} = 65$ °C and for refrigerant R1234ze at $G = 1000$ kg/m^2 s and $T_{sat} = 45$ °C (see Figure 5.4 and Figure 5.5 from (a) to (d)). It can be noticed that for both inlet pressure and inlet temperature, no significant fluctuations were detected, even for the last test approaching the thermal crisis, in which the oscillations of inlet pressure were more intense but always limited in a ±2% uncertainty band. The RTDs plotted for the 12th test at occurring CHF showed that the maximum temperature fluctuation was not severe and included in a ±0.5 °C range.
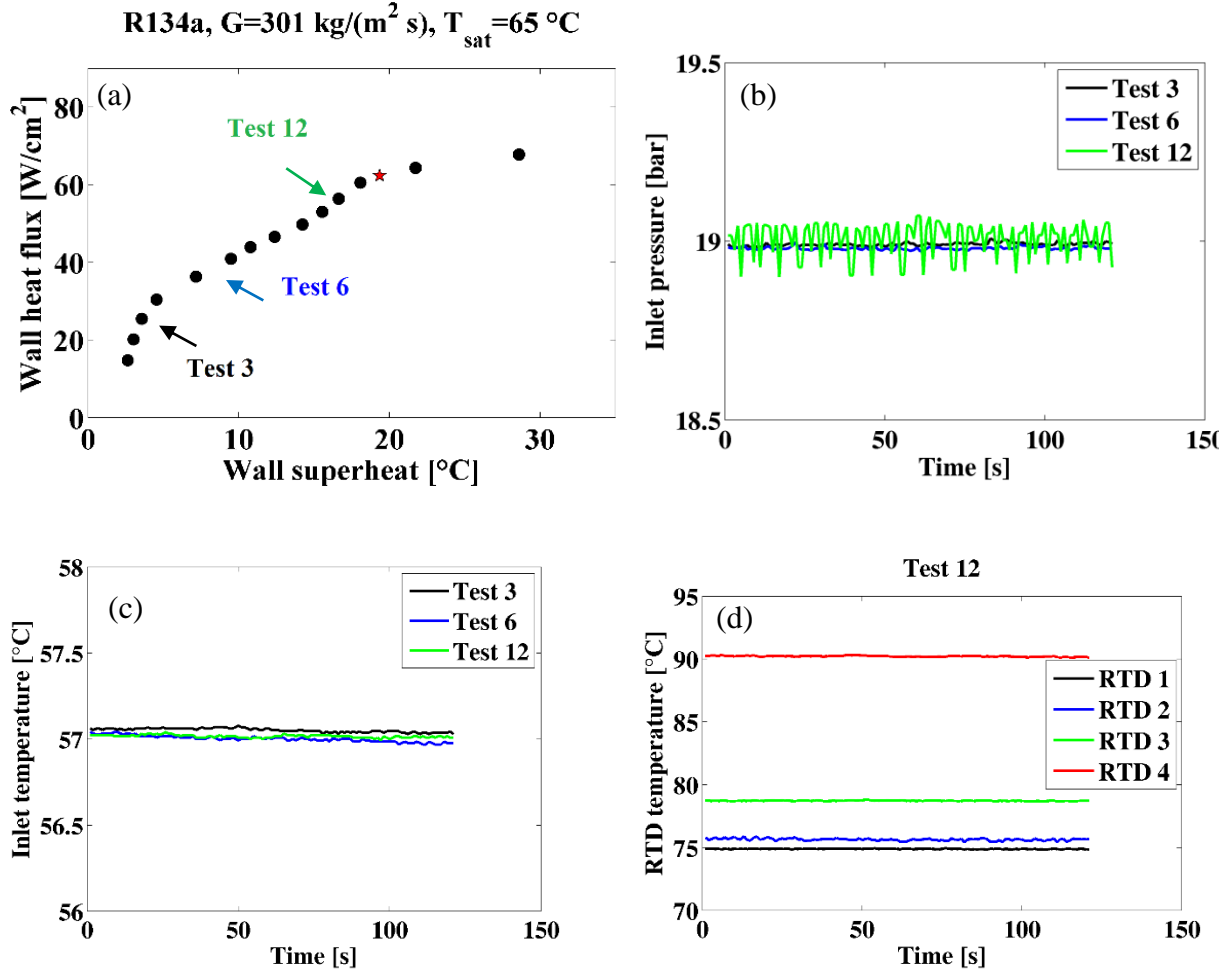
Figure 5.4 Instability analysis performed without inlet orifices for refrigerant R134a at G = 301 kg/m²
s, T_{sat} = 65 °C and L_h/D = 27. (a) Boiling curve; (b) inlet pressure fluctuations for tests 3, 6 and 12; (c)
inlet temperature fluctuations for tests 3, 6 and 12; (d) RTD wall temperature measurements for test
12 [38].
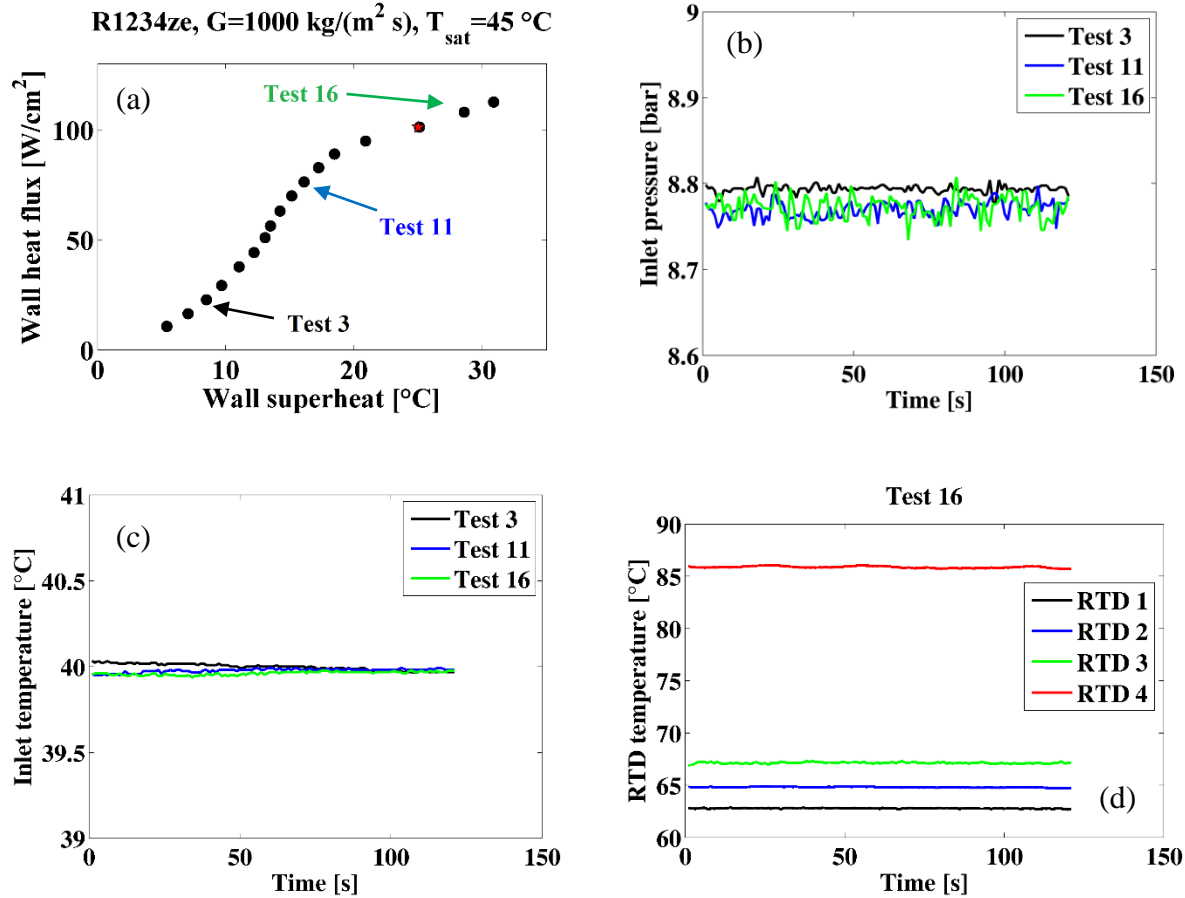
Figure 5.5 Instability analysis performed without inlet orifices for refrigerant R1234ze at $G = 1000$ kg/m^{2}s, $T_{sat} = 45$ °C and $L_h/D = 27$. (a) Boiling curve; (b) inlet pressure fluctuations for tests 3, 11 and 16; (c) inlet temperature fluctuations for tests 3, 11 and 16; (d) RTD wall temperature measurements for test 16 [38].

Based on these preliminary checks, it was possible to state that in the investigated range of mass velocities, the recorded CHF did not occur due to severe flow instabilities or back-flows, but more likely to dry-out incipience and its related "mild" instabilities, as also explained in [133].

5.3   Boiling curves

The effect of the main operative parameters on the experimental boiling curves is shown in this section.

5.3.1   Effect of the saturation temperature on the boiling curves

Figure 5.6 (a), (b) and (c) show boiling curves of refrigerants R134a, R1234yf and R1234ze, respectively. The tests were obtained with saturation temperatures from 25 °C up to 75 °C, with a fixed L_h/D equal to 18. The mass flux of 250 kg/m^2 s is an average of all the critical mass velocities of the boiling curves depicted. The first part of the boiling curves tends to slightly shift towards left with increasing saturation temperature, at any mass velocity and fluid tested. This particular trend suggests that the average flow boiling heat transfer coefficient (evaluated as the ratio of the wall heat flux over the wall superheat) is enhanced when increasing the saturation temperature. As an example, for refrigerant R134a (Figure 5.6 (a)), the heat transfer coefficient passing from 25 °C to 75 °C increases of almost 100% (from 99 kW/m^2 K to 198 kW/m^2 K). In case of refrigerant R1234yf (Figure 5.6 (b)), this effect is even more noticeable, with a heat transfer coefficient that goes from 83 to 218 kW/m^2 K. Finally, with refrigerant R1234ze (Figure 5.6 (c)), the increase of the heat transfer coefficient with saturation temperature in stable boiling is less emphasized (from 71 to 142 kW/m^2 K). Other independent studies [20] [45] [134] [44] with different geometries and fluids are consistent with these observed trends. As regards the second part of the boiling curve, the thermal crisis seems not to be strongly influenced by saturation temperature, for any fluid investigated, anticipating a weak effect of T_{sat} on the experimental CHF.
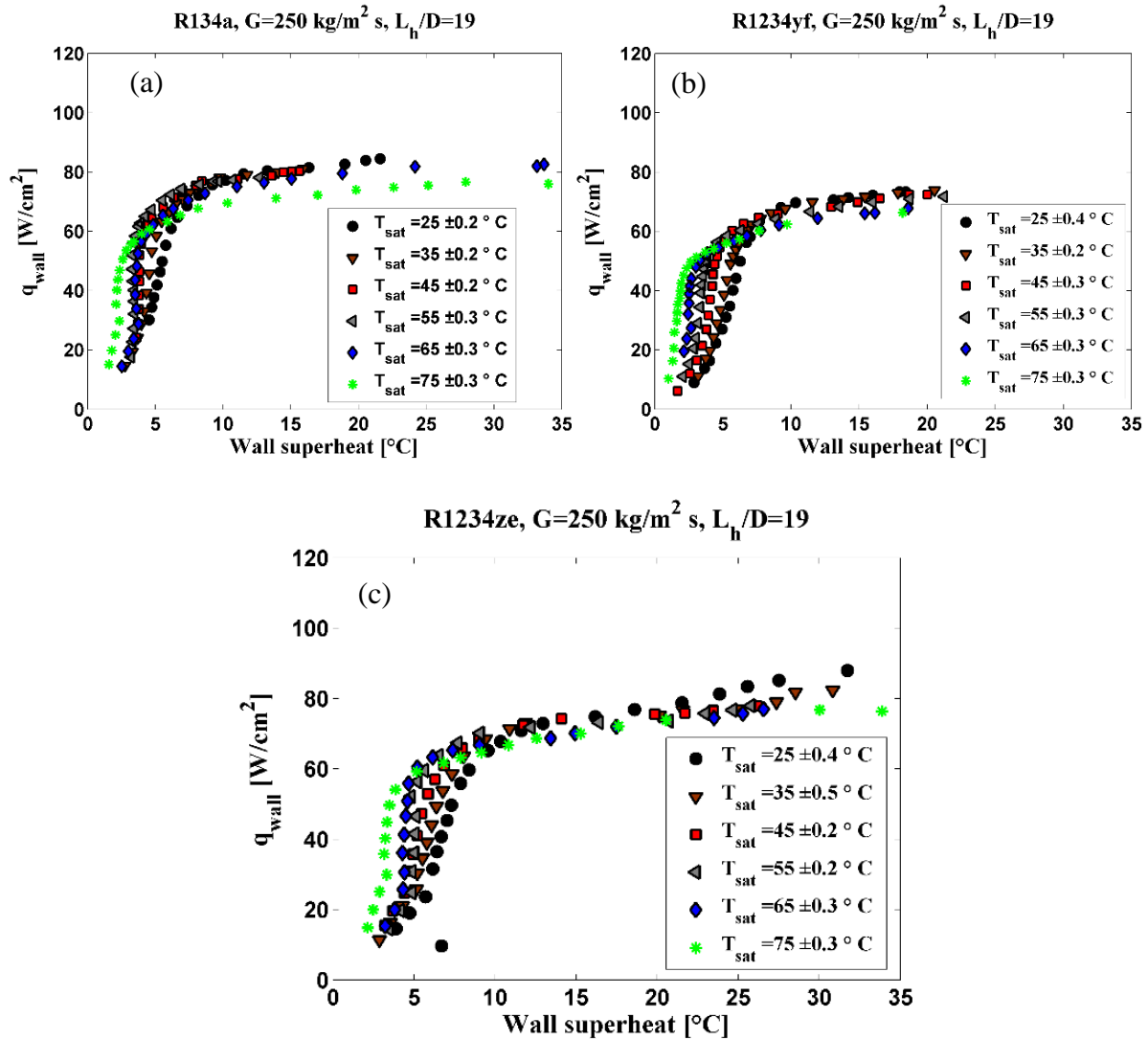
Figure 5.6 Experimental boiling curves obtained with an average mass flux at critical condition of 250 kg/m² s, L_h/D=19 and saturation temperatures from 25 to 75 °C. (a) R134a, (b) R1234yf, (c) R1234ze.

Similar results were obtained with a different heat sink geometry (L_h/D=27) and higher mass fluxes. Figure 5.7 shows the boiling curves of refrigerants R134a at G = 500 kg/m² s (a) and R1234ze at G = 1000 kg/m² s (b), with saturation temperatures ranging from 25 to 75 °C. Also in this case, the thermal crisis appears at approximately the same wall heat flux with increasing saturation temperature by having fixed the other operating parameters. Again, the system pressure shifts the first part of the boiling curves towards lesser wall superheats,

indicating a substantial increase of the average heat transfer coefficient with higher saturation temperatures.
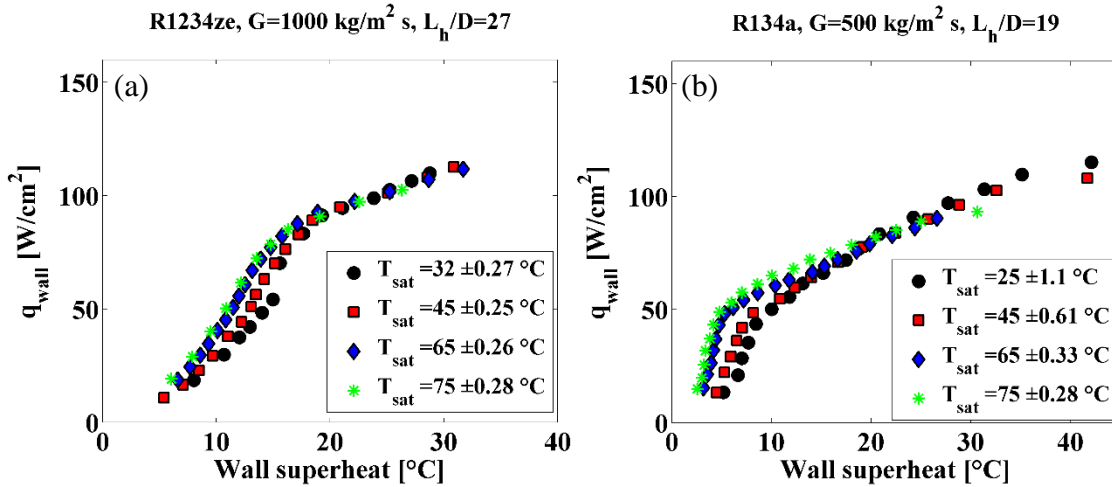
Figure 5.7 Experimental boiling curves obtained at saturation temperatures from 25 to 75 °C, with L_h/D=19 and (a) R134a at 500 kg/m² s, (b) R1234ze at 1000 kg/m² s, (c) R1234ze.

5.3.2   *Effect of mass velocity on the boiling curves*

The effect of mass flux on the experimental boiling curve is explained in Figure 5.8, for different working fluids and heat sink geometries. Figure 5.8 (a), (b) and (c) refer to refrigerants R134a, R1234yf and R1234ze, respectively, for a saturation temperature of 65 °C and L_h/D = 19. As illustrated in the CHF operative definition, the change of the boiling curves slope at approaching the thermal crisis becomes gentler at increasing mass velocity. The first part of the boiling curves (during stable boiling) are merging together with increasing mass flux, suggesting that its effect on the average heat transfer coefficient is almost negligible. On the other hand, the critical region seems to be delayed at higher mass fluxes, forewarning a substantial effect of the mass velocity on the experimental CHF.
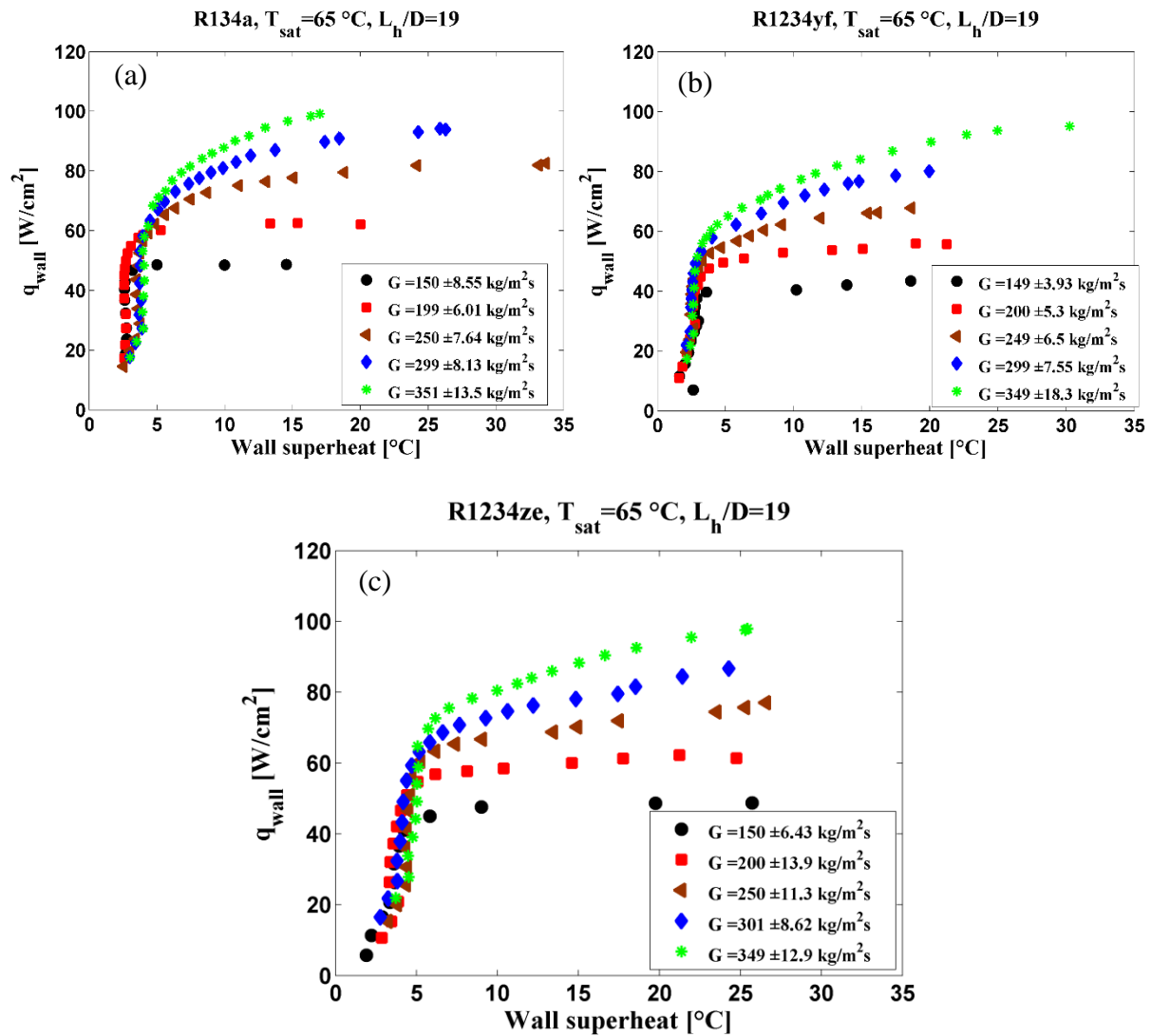
Figure 5.8 Experimental boiling curves with different mass velocities, at a saturation temperature of 65 °C and L_h/D = 19. Refrigerants: (a) R134a, (b) R1234yf, (c) R1234ze.

The same considerations are effective for refrigerant R32, at a lower saturation temperature of 25 °C, a different multi-minichannel heat sink geometry (L_h/D = 44) and a wider span of mass velocities investigated (152 up to 1504 kg/m² s, see Figure 5.9).
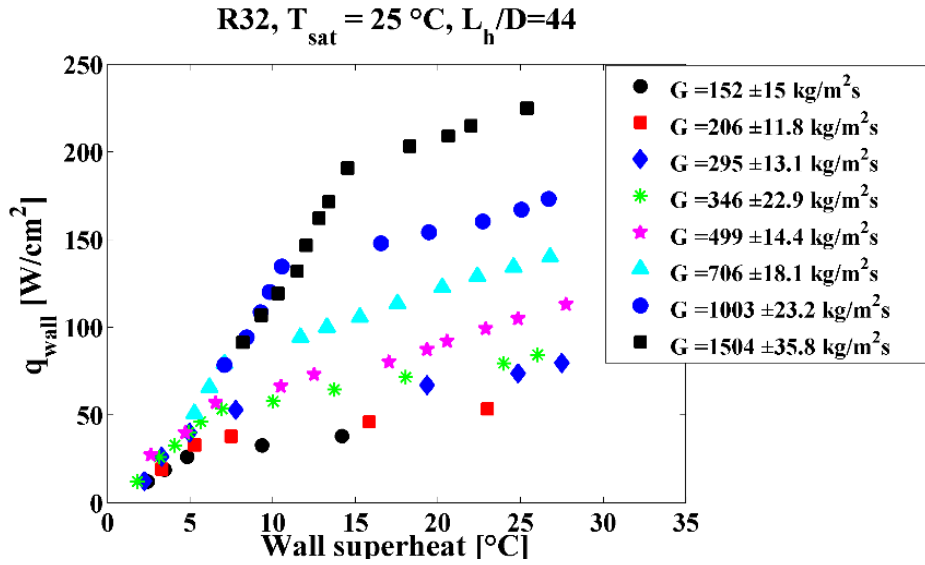
Figure 5.9 Experimental boiling curves of refrigerant R32 at a saturation temperature of 25 °C and $L_h/D = 44$, with increasing mass velocity.

5.3.3 Effect of the working fluids on the boiling curves

The different boiling curve behavior of refrigerants R134a, R1234yf and R1234ze is shown in Figure 5.10, in which $L_h/D = 19$, and the saturation temperature and mass velocity are fixed to 75 °C and 149 kg/m² s (a) and 25 °C and 300 kg/m² s (b), respectively. In the stable boiling region, for a fixed heat flux, R134a and R1234yf exhibit lower values for the wall superheat, suggesting a better heat transfer performance if compared to that of refrigerant R1234ze. In case of a higher mass velocity (see Figure 5.10 (a)), the average deduced heat transfer coefficients of R1234yf even overcomes those of R134a. The boiling curve slope begins to decrease at similar heat fluxes for all the three fluids shown when working at the same thermodynamic conditions, with a CHF only expected to be slightly lower for refrigerant R1234yf.
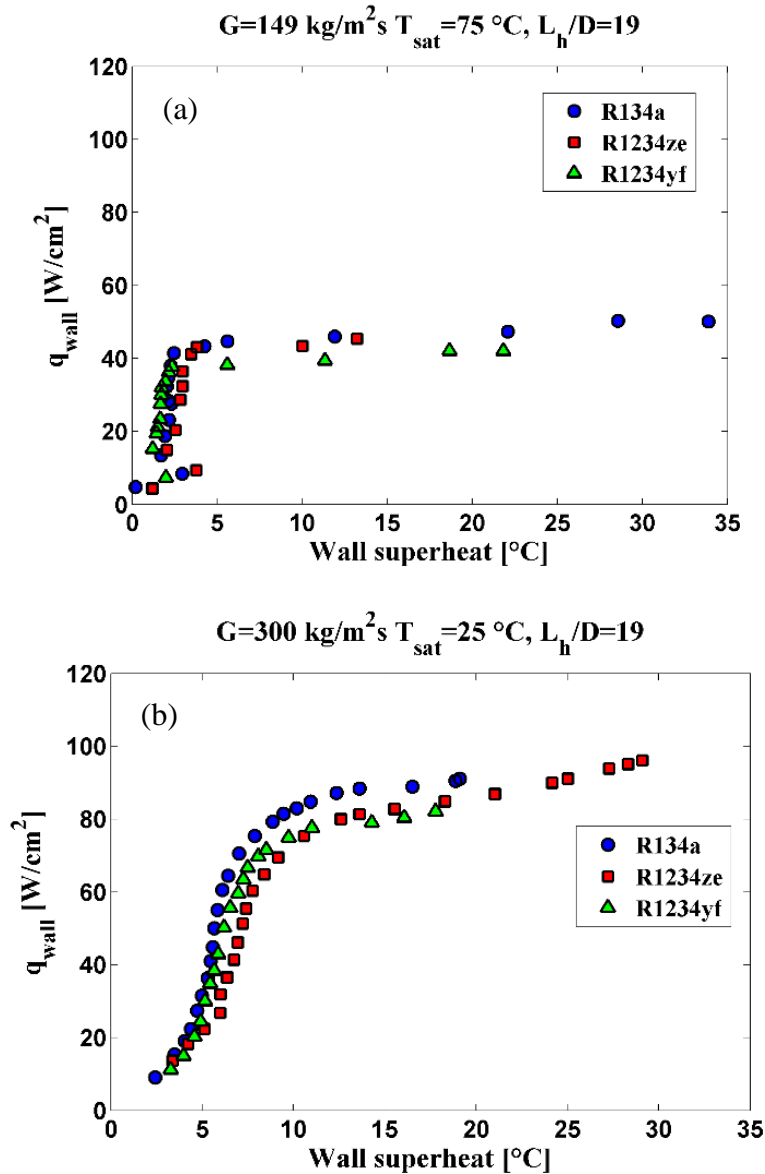
Figure 5.10 Experimental boiling curves with refrigerants R134a, R1234yf and R1234ze obtained at L_h/D = 19, with: (a) G = 149 kg/m² s and T_{sat} = 75 °C; (b) G = 300 kg/m² s and T_{sat} = 25 °C.

5.4   CHF values and parametric analysis

The experimental CHF values and the influence of all the operating conditions is shown in this section.

5.4.1 *Effect of saturation temperature and mass velocity on CHF*

The combined effect of the mass flux and saturation temperature on the experimental values of CHF is exposed in Figure 5.11, for different refrigerants and L_h/D ratios. The expanded CHF uncertainties are also displayed with an error band on the y-axis, whereas the critical mass velocities in legend are calculated by averaging all the critical mass fluxes of the corresponding curves. Figure 5.11 (a), (b) and (c) refer to refrigerants R1234yf, R134a and R1233zd, respectively, and to L_h/D ratios equal to 19, 27 and 44, respectively.

R134a, $L_h/D = 27$

Legend:
- G = 151 ±14.0 kg/m²s
- G = 201 ±18.1 kg/m²s
- G = 300 ±19.4 kg/m²s
- G = 351 ±15.9 kg/m²s
- G = 500 ±13.9 kg/m²s
- G = 701 ±15 kg/m²s
- G = 1000 ±21.2 kg/m²s
- G = 1500 ±30.8 kg/m²s

R1233zd, $L_h/D=44$

Legend:
- G=149±14 kg/m² s
- G=197±23 kg/m² s
- G=301±20 kg/m² s
- G=350±21 kg/m² s
- G=498±24 kg/m² s
- G=700±34 kg/m² s
- G=1000±31 kg/m² s
- G=1501±32 kg/m² s
- G=2002±28 kg/m² s
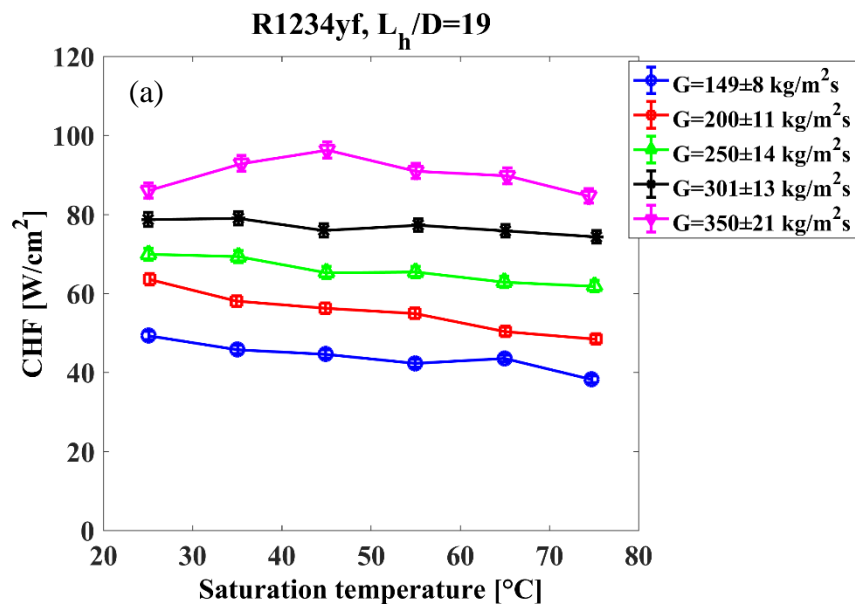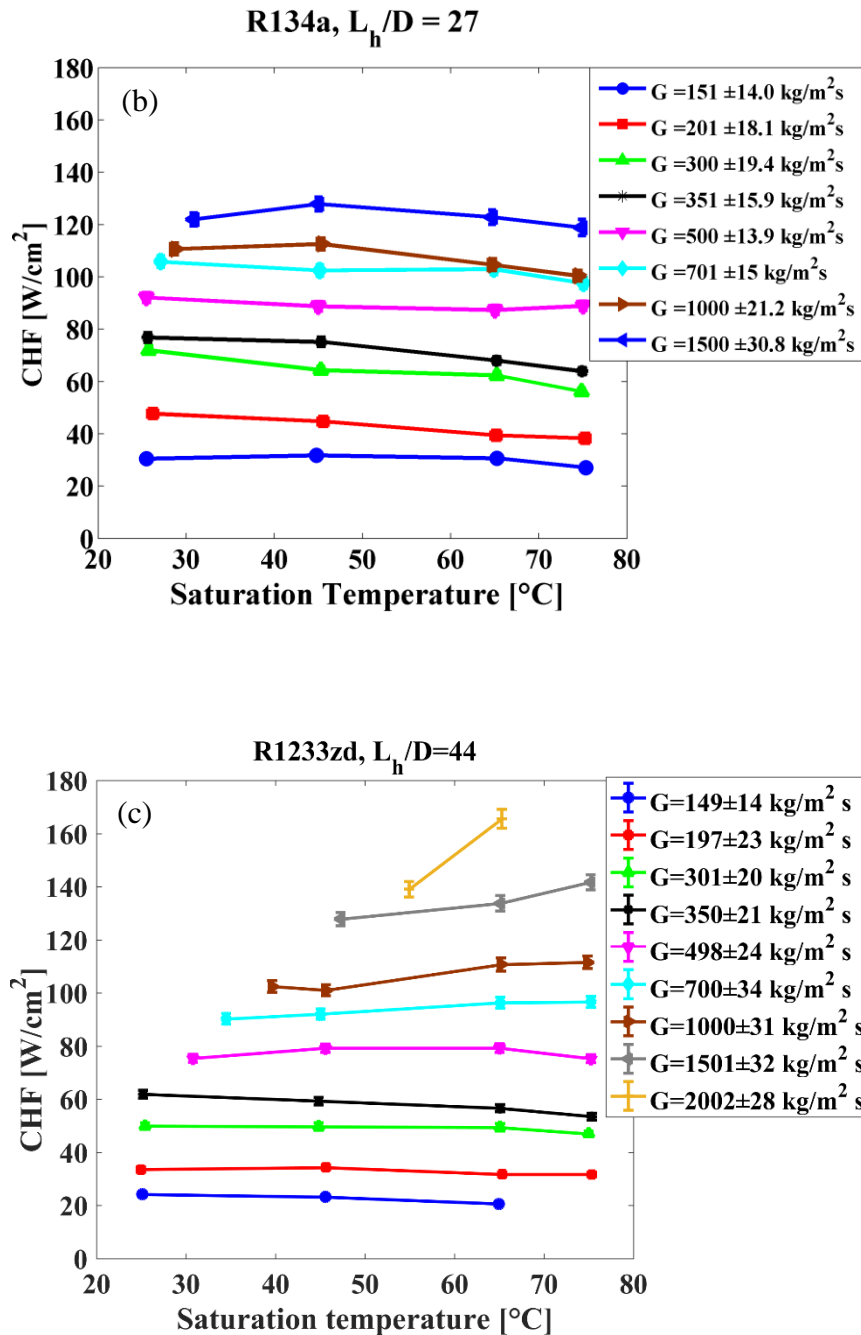
Figure 5.11 Experimental CHF values with their expanded uncertainty as a function of the saturation temperature and the average critical mass velocity. Tests performed with: (a) R1234yf and $L_h/D = 19$; (b) R134a and $L_h/D = 27$; (c) R1233zd and $L_h/D = 44$.

The CHF values are not greatly influenced by the saturation temperature, and the general trends for most of refrigerants suggest that a weak decrease of CHF is expected for an increasing saturation temperature. In case of R134a and $L_h/D = 27$ (see Figure 5.11 (b)), the

greatest fall of CHF is recorded at an average mass flux of 300 kg/m^2 s, where it passes from 72.0 to 56.2 W/cm^2, with a variation of -21.1%. For R1234yf, at $G = 200$ kg/m^2 s and $L_h/D =$ 19 (see Figure 5.11 (a)), the reduction with saturation temperature is about -25%, passing from 64 W/cm^2 to a CHF of 48 W/cm^2. A similar behavior is also recorded at low mass velocities for refrigerant R1233zd and $L_h/D = 44$ (see Figure 5.11 (c)). When the mass flux is higher than 500 kg/m^2 s, instead, the effect of the saturation temperature changes, leading to an enhancement of CHF values, which is higher at higher mass velocities. For instance, at G =2002 kg/m^2 s, the CHF increase is +19%, passing from 139 to 164 W/cm^2, when the saturation temperature is increased from 55 to 65 °C. The effect of the saturation temperature on thermodynamic properties that influence the boiling process and the CHF phenomenon has already been discussed by different authors [135] [51] [29]. With ongoing evaporation and annular flow, the instability of the liquid film thickness at the wall is a key element for the occurrence of critical heat flux. When flow instabilities are promoted, the liquid-vapor interfacial shear waves' amplitude may become large enough to overcome the liquid film thickness itself, leaving the heated wall in contact with the vapor phase, with the occurrence of a local intermittent dry-out. With a change of the saturation temperature, two different parameters intervene in the shape and amplitude of interfacial shear waves. First, the vapor-to-liquid density ratio increases with increased reduced pressure and leads to a lesser velocity difference between the two phases. The size of interfacial waves is then reduced, with a lower production of liquid entrained droplets in the vapor core, thus augmenting the flow stability and the expected thermal crisis. On the other hand, the surface tension of the fluid is in general substantially decreased when increasing the saturation temperature, leading to a more breakable contact between the liquid film and the heated wall, then promoting the CHF phenomenon. Moreover, also the latent heat is reduced with the increase of the reduced pressure, thus having a lower cooling capacity.

Table 5.3 shows the variation of the three abovementioned properties when changing the saturation temperature from 25 up to 75 °C for the refrigerants shown in Figure 5.11. The fall in the surface tension and latent heat is substantially inferior in case of R1233zd, so that the increase of the densities ratio. R1234yf presents instead the lowest values of the surface tension and the highest relative fall (83%) in its value when passing from 25 °C to 75 °C. The vapor-to-liquid density ratio is instead comparable to that of R134a and R1234ze, being

significantly higher than that of R1233zd, which present the lowest reduced pressure for the rage of saturation temperatures investigated. Finally, the latent heat decreases similarly for each fluid (with the exception of R1233zd), with a relative reduction of 35%, 39% and 30% for R134a, R1234yf and R1234ze, respectively.

The effect of mass flux on CHF is also evident in Figure 5.11. For any working fluid, the experimental critical heat flux substantially increases when increasing the mass velocity. For instance, with refrigerant R134a at a saturation temperature of 45 °C and $L_h/D = 27$, the CHF passes from 31.8 up to 127.9 W/cm^2, with a variation of +302%. The gap is higher for refrigerant R1233zd and $L_h/D = 44$ when changing mass velocity from 149 to 2002 kg/m^2 s. In this case, the CHF values for a saturation temperature of 65 °C go from 20.6 up to 165.5 W/cm^2, having an increment of +704%.

The experimental trends shown are in line with those reported using different fluids and geometries in the researches of Ali and Palm [20], Tibiriçá et al. [35], Anwar et al. [45] and Callizo et al. [19].

Table 5.3 Variation of the vapor-to-liquid density ratio, liquid surface tension and latent heat for refrigerants R134a, R1234yf, R1234ze and R1233zd evaluated in the whole range of saturation temperatures tested.

Properties modification from 25 °C to 75 °C	ρ_V/ρ_L $[-]$			σ $[mN/m]$			Δi_{LV} $[kJ/kg]$		
	25 °C	75 °C	$\Delta_\%$	25 °C	75 °C	$\Delta_\%$	25 °C	75 °C	$\Delta_\%$
R134a	0.027	0.138	**411%**	8.03	2.13	**-73%**	178	116	**-35%**
R1234yf	0.035	0.181	**420%**	6.17	1.06	**-83%**	145	88	**-39%**
R1234ze	0.022	0.109	**390%**	8.85	2.93	**-67%**	167	117	**-30%**
R1233zd	0.006	0.027	**350%**	14.5	8.30	**-43%**	192	161	**-16%**

5.4.2 Effect of working fluid and L_h/D ratio on CHF

The effect of the working fluid on CHF is shown in Figure 5.12 for two different saturation temperatures and L_h/D ratios. Specifically, Figure 5.12 (a) presents the critical heat flux values with their expanded uncertainty as a function of the mass flux for refrigerants R134a, R1234ze, R1234yf and R32, with an average saturation temperature of 25.6 °C and a L_h/D ratio of 27. Figure 5.12 (b) shows instead the experimental CHF values for R134a, R1234yf

and R1233zd at an average saturation temperature of 45 °C and a L_h/D ratio of 44. By having fixed the geometry and the operating conditions, the lower CHF values are found for refrigerants R1234yf and R1234ze, probably due to their lower surface tension and latent heat at disposal. The highest recorded CHFs are instead found with R32, which presents the greatest latent heat (271 kJ/kg at 25 °C) and a similar surface tension to that of other refrigerants. As regards R1233zd, its very high surface tension bestows a stable liquid film thickness with gentler interfacial instabilities and therefore delayed thermal crises, overcoming the effect of a small densities ratio, at least in case of low mass fluxes (see Figure 5.12 (b)). However, for $G > 700$ kg/m^2 s, the CHF values become smaller than those of R134a and R1234yf. It is likely that at higher mass velocities, the inertia effects come to be significant and the contribution of a low densities ratio on the film thickness instability may overcome the surface tension stabilizing effect.
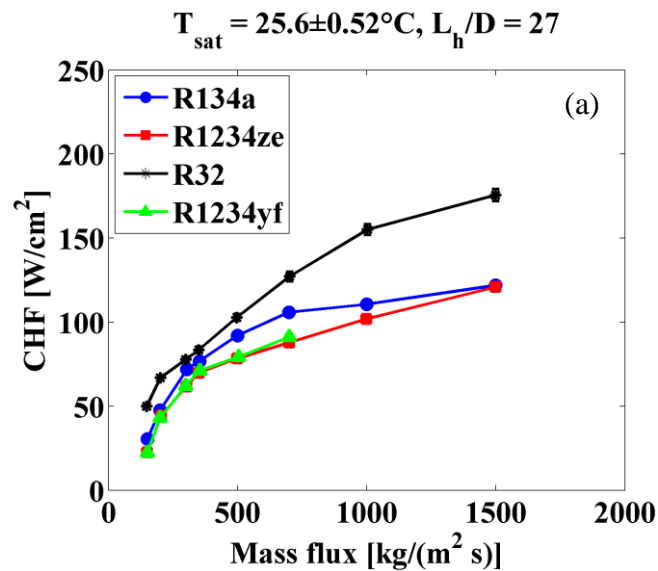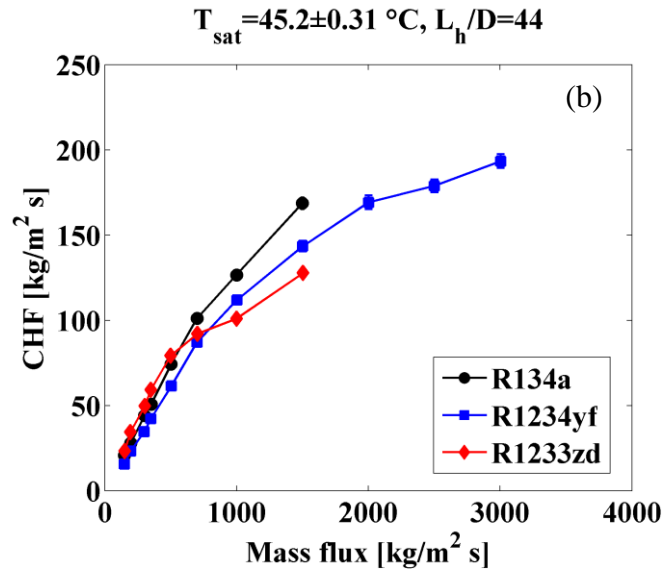
Figure 5.12 Experimental CHF values with their expanded uncertainty as a function of the mass flux, for different tested fluids. (a) $T_{sat} = 25.6$ °C and $L_h/D = 27$; (b) $T_{sat} = 45.2$ °C and $L_h/D = 44$.

As regards the effect of a different geometry, Figure 5.13 (a) shows experimental R134a CHF values obtained at low mass fluxes (up to 351 kg/m^2 s) as a function of the different L_h/D ratios of 19, 27 and 44 employed in this experimental campaign. As also recorded in other works published on this issue [48] [49], it is evident a general reduction of CHF with increasing L_h/D ratios, which is more accentuated for lower mass velocities. For instance, CHF drops from 65.4 to 28.0 W/cm^2 (-57%) at an average critical mass flux of 201 kg/m^2 s. The quadratic polynomial curves that fit the experimental data are indicating that the CHF reduction with L_h/D will probably be less significant at higher L_h/D ratios.

However, in case of higher mass velocities ($G > 500$ kg/m^2 s) the experimental trend is reversed. The CHF values for refrigerant R134a at 25 °C for all the mass fluxes tested are displayed in Figure 5.13 (b). For a mass velocity of 1500 kg/m^2 s, the CHF is higher when increasing L_h/D from 27 to 44, passing from 122 to 175 W/cm^2. The same considerations are effective for refrigerant R32 at 25 °C, for which the CHF increase with L_h/D is also recorded beginning from $G = 498$ kg/m^2 s.

R134a, T$_{sat}$ = 45±0.23 °C

(a)

Legend:
- G =151 ±14.0 kg/m^{2}s
- G =201 ±18 kg/m^{2}s
- G =299 ±14.2 kg/m^{2}s
- G =351 ±12.6 kg/m^{2}s

Y-axis: CHF [W/cm^2]
X-axis: L$_h$/D

R134a, T$_{sat}$ = 25±0.32 °C

(b)

Legend:
- G =149 ±8.22 kg/m^{2}s
- G =199 ±15.2 kg/m^{2}s
- G =301 ±9.26 kg/m^{2}s
- G =352 ±10.9 kg/m^{2}s
- G =499 ±14.6 kg/m^{2}s
- G =698 ±17 kg/m^{2}s
- G =1000 ±21.7 kg/m^{2}s
- G =1500 ±31.3 kg/m^{2}s

Y-axis: CHF [W/cm^2]
X-axis: L$_h$/D
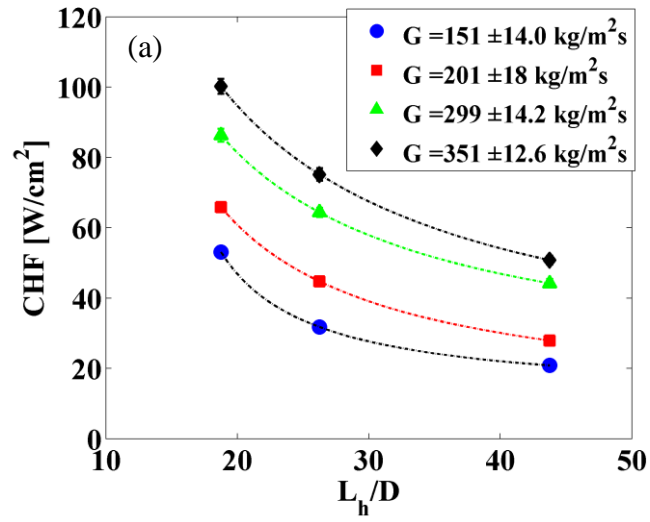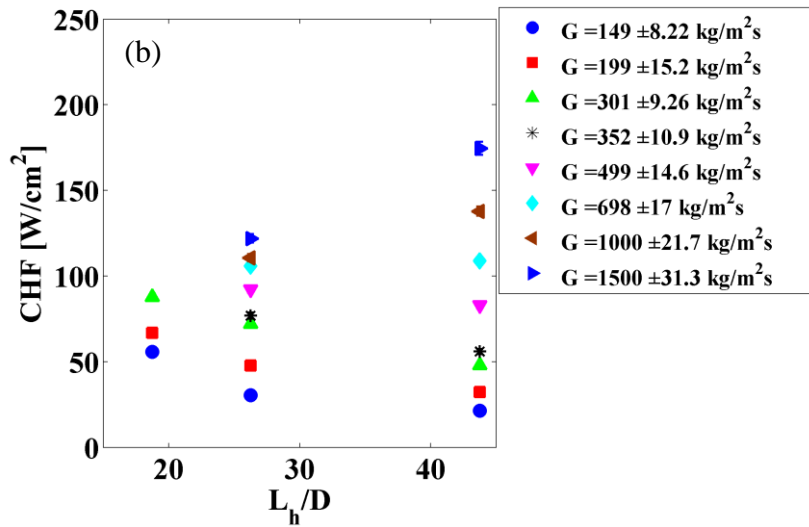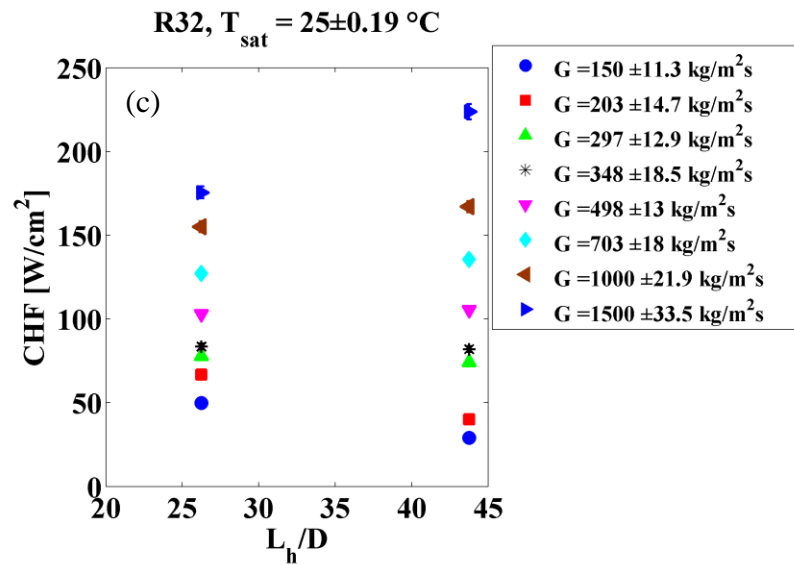
Figure 5.13 Experimental CHF values as a function of the L_h/D ratio and mass flux, obtained with: (a) R134a and $T_{sat} = 45$ °C; (b) R134a and $T_{sat} = 25$ °C; (c) R32 and $T_{sat} = 25$ °C.

Finally, the combined effect of mass flux, fluid and L_h/D ratio is shown in Figure 5.14, where the evolution of the experimental CHF as a function of the mass velocity for refrigerants R134a and R32 with two different L_h/D ratios of 27 and 44, and at a saturation temperature of 25 °C is displayed. Full lines refer to $L_h/D = 27$ and dashed lines to L_h/D ratio of 44. For both refrigerants, two zones can be observed: at low mass velocities ($G < 500$ kg/m² s), CHF is higher for the greatest value of the L_h/D ratio, whereas for higher mass fluxes, the critical values of $L_h/D = 44$ overcome those obtained at the same conditions with $L_h/D = 27$. As observed before, CHF is always higher for refrigerant R32. The same trends were also found at different saturation temperatures.
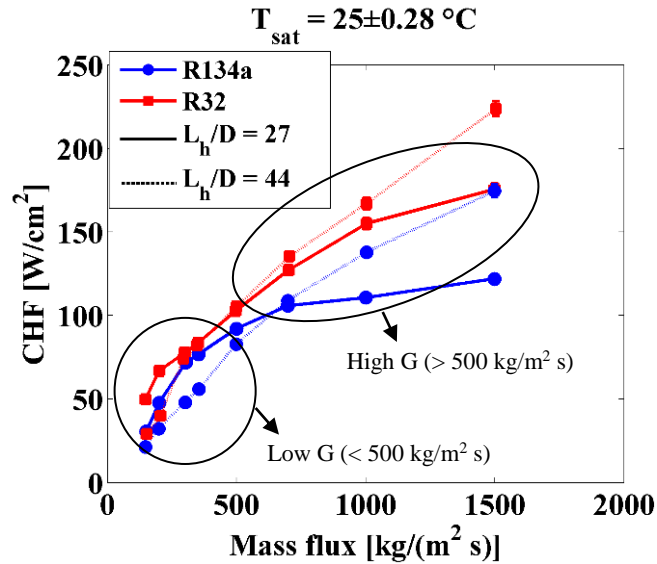
Figure 5.14 Experimental CHF at a saturation temperature of 25 °C as a function of the mass flux, for R134a and R32, with L_h/D ratios of 27 and 44.

5.5   Assessment of existing correlations

The experimental CHF are compared in this section against some of the most quoted correlations taken from scientific literature. Particularly, the correlations of Lazarek and Black [30], Qu and Mudawar [21], Zhang et al. [50], Wojtan et al. [23], Kuan [34], Ong and Thome [24], Mikielewicz et al. [43], Callizo [51], Anwar et al. [36], Tanaka et al. [48] and Katto and Ohno [31] were tested on the CHF experimental database.

5.5.1   A brief note on the use of CHF correlations

As shown in the literature review, the CHF empirical or semi-empirical correlations rely on the use of L_h/D ratio and the Weber number, which also contains the channel length or diameter as characteristic dimension. The difference between heated length and channel length and between heated diameter and channel diameter is omitted or not always clear, since most of the studies are related to circular channels, uniformly electrically heated on their perimeter for all their length.

In this thesis, when not expressly indicated by the authors, the L_h/D ratio is computed by using the heated length L_h (25 and 35 mm for the two test section arrangements) and the

121

heated equivalent diameter D_h, as already defined by Ong and Thome [24] in their CHF prediction methods for rectangular channels:

$$D_h = \frac{4 \cdot W_{ch} \cdot H_{ch}}{W_{ch} + 2H_{ch}} \tag{5.2}$$

Being the Weber number related to hydrodynamic phenomena, instead, it was evaluated by using the channels length L or the equivalent diameter D, unless different dispositions given by the authors.

5.5.2 Statistical analysis

The statistical parameters *MAE*, *MRE* and *SD* were used for this analysis. The Mean Absolute Error (MAE) and Mean Relative Error (MRE) are defined as follows:

$$MAE = \frac{1}{n} \sum_{i=1}^{n} |ER_i| \tag{5.3}$$

$$MRE = \frac{1}{n} \sum_{i=1}^{n} (ER_i) \tag{5.4}$$

In the equations, ER_i is the percentage variance of the experimental CHF_i value from the predicted one and n is the number of data points:

$$ER_i = \frac{CHF_{pred} - CHF_{exp}}{CHF_{exp}} \cdot 100 \tag{5.5}$$

Finally, the standard deviation *SD* is evaluated as:

$$SD = \sqrt{\frac{1}{n} \cdot \sum_{i=1}^{n} (ER_i - MRE)^2} \tag{5.6}$$

For a fair comparison, the experimental data in which the expanded uncertainty in the saturation temperature exceeded ±1 °C, or that of the mass flux or CHF exceeded ±6%, were excluded from this analysis.

The assessment summary is presented in Table 5.4 and some results of the statistical analysis are graphically shown in Figure 5.15. The experimental points have different markers and colors, in order to investigate on the validity of the correlations for high values of the mass

velocities and for different values of the L_h/D ratio. In particular, circular and square markers refers to $G < 500$ kg/m^2 s and $G > 500$ kg/m^2 s data, respectively, while the blue, red and green colors are related to L_h/D ratios of 19, 27 and 44, respectively.
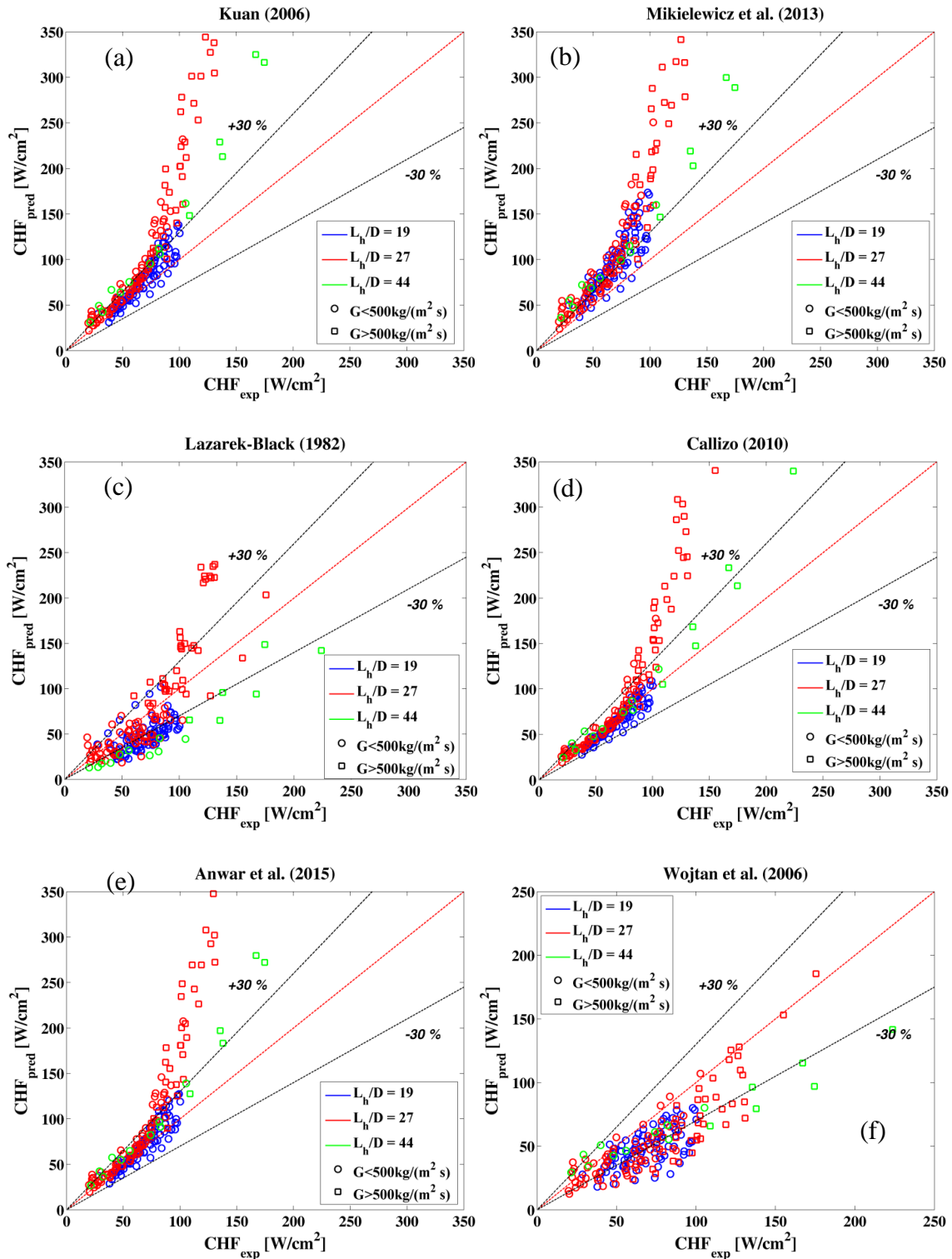
Figure 5.15 Experimental versus predicted CHF values obtained with different correlations [38]. Colors and markers refer to different L_h/D ratios and mass flux ranges, respectively. a) Kuan [34]; b) Mikielewicz et al. [43]; c) Callizo [51]; d) Anwar et al. [36]; e) Lazarek and Black [30]; f) Wojtan et al. [23].

124

Table 5.4 Summary of comparisons with the chosen correlations [38]. Each parameter has been evaluated for the whole database and also separately for the experimental points with mass velocities lower and higher than 500 kg/m² s. The best statistical results related to each parameter are highlighted in bold.

Authors	MAE			MRE			SD		
	G < 500 kg/(m² s)	G > 500 kg/(m² s)	whole	G < 500 kg/(m² s)	G > 500 kg/(m² s)	whole	G < 500 kg/(m² s)	G > 500 kg/(m² s)	whole
Wojtan et al. (2006)	27.9	***30.8***	***28.5***	-23.5	***-30.3***	***-25.0***	472.4	333.7	450.3
Zhang et al. (2006)	52.3	56.3	53.2	-52.2	-56.3	-53.1	225.7	90.5	199.4
Lazarek-Black (1982)	32.5	***37.5***	33.6	-24.3	***24.2***	***-13.8***	771.0	1503.6	1327.8
Ong-Thome (2011)	42.4	***36.8***	39.0	-41.6	***-31.5***	-37.3	335.9	499.5	440.3
Kuan (2006)	24.5	116.2	44.3	23.1	116.2	43.3	506.7	4758.3	2894.2
Qu-Mudawar (2004)	961.7	1040.0	978.7	961.7	1040.0	978.7	272094	196328	256742
Callizo (2010)	***11.1***	58.7	***21.4***	***-0.2***	58.1	***12.4***	243.7	2118.3	1225.2
Katto-Ohno (1984)	39.9	55.5	43.3	-38.6	-55.5	-42.2	389.7	141.0	384.8
Anwar et al. (2015)	***15.6***	92.5	32.2	***11.5***	92.5	29.1	373.4	3858.9	2237.9
Mikielewicz et al. (2013)	46.0	112.7	60.4	45.7	112.7	60.2	715.3	4612.8	2321.3
Tanaka et al. (2009)	85.7	76.5	83.7	-85.7	-76.5	-83.7	***14.3***	***43.6***	***35.0***

The comparison results of the correlations of Kuan [34], Mikielewicz et al. [43], Callizo [51] and Anwar et al. [36] are presented Figure 5.15 (a)-(d). The predictive methods of Kuan and Mikielewicz et al. show a good agreement for low mass velocities at any L_h/D ratio, slightly overpredicting the experimental points, while they largely fail for $G > 500$ kg/m² s. The same considerations are effective for the predictive methods of Callizo and Anwar et al., that work even better when $G < 500$ kg/m² s. It is important to state that almost all the previous correlations, with the exception of that of Mikielewicz et al., are conceived and developed for low mass velocities.

Lazarek and Black [30] and Wojtan et al. [23] correlations agreement is instead shown in Figure 5.15 (e)-(f). Lazarek and Black predictive method slightly underpredicts the experimental CHFs at low mass velocities, while it worsens for $G > 500$ kg/m² s. Also in this

case, the correlation was conceived with low G data (< 750 kg/m^2 s). The predictive methods of Wojtan et al. works instead relatively better at low and high mass fluxes. Most of the experimental CHFs are underestimated, but the method does not fail completely when increasing the mass velocities and this is probably due to the fact that the authors database contains experimental points up to $G = 1600$ kg/m^2 s. Different values of L$_h$/D are also fairly fit with this correlation. Similar results and considerations can be made with the correlation of Ong and Thome [24], which is not included in Figure 5.15.

The remaining predictive methods of Tanaka et al. [48], Zhang et al. [50] and Qu and Mudawar [21] largely fail to predict the present experimental database: they were then excluded from the graphical analysis but left in Table 5.4. The parameters *MAE*, *MRE* and SD were calculated both for the entire database and then separated for low and high mass velocities. The correlation of Callizo [51] works best in the whole database (*MAE* = 21.4%), followed by the predictive methods of Wojtan et al. [23]and Anwar et al. [36], with a *MAE* of 28.5% and 32.2%, respectively. Particularly, the best agreement is found for low mass velocities (*MAE$_{low G}$* of 11.1% and 15.6%, respectively) for Callizo and Anwar et al. These two correlations, however, largely fail when $G > 500$ kg/m^2 s.

Katto-Ohno [31] prediction method underestimates most of the experimental database, with a MAE equal to 43.3% and a MRE of -42.2%. A better agreement is instead found at low mass fluxes, in which the calculated MAE$_{low G}$ is 39.9%.

The correlation of Ong and Thome [24] better works with the experimental CHF for higher mass velocities with a *MAE$_{high G}$* of 26.8%. It is followed by the predictive methods of Wojtan et al. [23] and Lazarek and Black [30] (*MAE$_{high G}$* = 30.8% and 37.5%, respectively). These equations are actually more balanced, since the absolute deviations are relatively low also for mass fluxes inferior to 500 kg/m^2 s.

5.5.3   *Considerations on the CHF correlations structure*

The comparison between predicted and experimental CHF values has shown that a considerable amount of correlations works quite well for all the *L$_h$/D* ratios and as far as the mass velocity is kept below 500 kg/m^2 s. In most cases, this is due to the authors' original database, which lacked of high G experimental data.

By considering a typical CHF correlation structure (see Equation (5.7)), the effects of L_h/D and that of the mass flux G are included in the exponents δ and γ of the Weber number, respectively.

$$CHF = \alpha \cdot G \cdot \Delta h_{LV} \cdot \left(\frac{\rho_v}{\rho_l}\right)^{\beta} \cdot We_L^{-\gamma} \cdot \left(\frac{L_h}{D_h}\right)^{-\delta} \qquad (5.7)$$

By including the thermodynamic properties influence in the saturation temperature (i.e. reduced pressure), and observing that the mass flux is contained with the power of two in the definition of the Weber number, the general CHF dependences may be summarized as:

$$CHF = f\left(G^{1-2\gamma}, \frac{L_h}{D}^{-\delta}, P_{red}\right) \qquad (5.8)$$

Figure 5.16 (a) compares the experimental CHF trend of R134a at 25 °C with the mass velocity against that obtained with some of the mentioned correlations. As expected, the Lazarek and Black [30] correlation produces a linear increase of CHF with the mass flux, since the Weber number is not considered ($\gamma = 0$). Similar curves are also found with the correlations of Callizo [51] and Mikielewicz et al. [43], which have a very low exponent of the Weber number ($\gamma = 0.034$ and 0.05, respectively). Only the predictive method of Wojtan et al. [23], having a γ exponent not negligible and equal to 0.24, escapes from the linear trend, thus fairly representing the experimental data in all their range of mass velocities. Figure 5.16 (b) shows the CHF values for R134a at $T_{sat} = 25$ °C as a function of the L_h/D ratio for different mass fluxes. The experimental points are compared to the correlation of Callizo [51], which is represented by the colored full lines. The decreasing trend with L_h/D is well caught in case of low mass velocities, suggesting that the exponent $\delta = 0.942$ is a good option of the experimental data. At higher mass fluxes, instead, the correlation keeps on exposing the same behavior, failing to represent the experimental CHF values for $G = 1000$ and 1500 kg/m^2 s
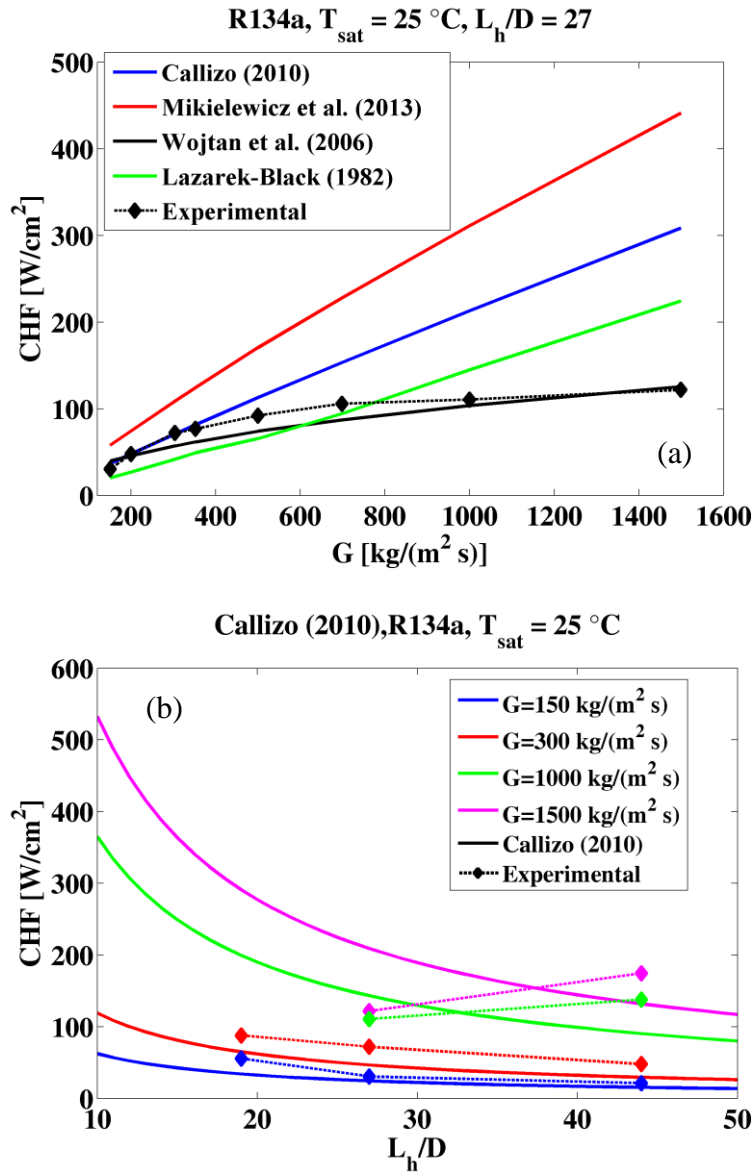
Figure 5.16 Experimental and predicted CHF evolution with mass velocity G and the L_h/D ratio [38]. (a) CHF as a function of the mass flux, for R134a at $T_{sat} = 25$ °C and $L_h/D = 27$. The full lines refer to the expected trend provided by the mentioned correlations; the dashed line refers to the present experimental database. (b) CHF for R134a at $T_{sat} = 25$ °C as a function of the L_h/D ratio for different mass fluxes. The dashed lines refer to the present experimental database, the full lines refer to values obtained with the prediction method of Callizo [51].

6 Flow boiling experimental facility and method

This chapter presents the results from the experimental investigation on saturated flow boiling heat transfer of refrigerants R134a and R32 in a stainless steel horizontal tube of 6.0 mm internal diameter. Tests were performed by measuring the heat transfer coefficient in four different positions along the tube perimeter in order to focus the attention on the flow symmetry and in particular on the influence of the operative parameters on the asymmetric annular flow structure.

The test facility used for the flow boiling tests is the same employed for the CHF experiments. Some necessary changes were made on the apparatus itself and on the measurement instrumentation in order to match with the new experimental campaign. All the specifications that remained unchanged are not described in this chapter and the reader is instead referenced to Chapter 4.

6.1 Flow boiling test facility

6.1.1 Apparatus description

Figure 6.1 is a schematic representation of the test facility used for the flow boiling experiments. The main fluid loop portrayed as a black line consisted of a throttling valve, a preheater section and a diabatic test section. The magnetic gear pump, the brazed plate condenser, Coriolis flow meter, double-pipe sub-cooler, liquid receiver and other accessories were the same used for the CHF experiments.

The sub-cooled refrigerant passed through the magnetic gear pump, where a throttling valve on the liquid line was employed during the experiments to adjust the system pressure and the mass flow rate to the desired values. The liquid then went into the preheater section, in which the heat was supplied by four fiberglass heating tapes (each of them with a nominal heat power of approximately 900 W at 230 V and 25 °C, as indicated by the manufacturer). The same solid state relay used to vary the applied voltage in the CHF experiments was here

employed to impose a desired preheater electrical load. The fluid then passed through an adiabatic, smooth, horizontal part, whose length of 40 cm (>60 tube internal diameter) was able to obtain a fully developed flow at the inlet of the tube section. A diabatic test section of 193.7 ±0.79 mm allowed the heat transfer coefficient and pressure drop measurements. Another micrometric throttling valve at the test section outlet was used for the single-phase tests to adjust the system pressure and mass flow rate. The liquid/vapor refrigerant mixture was condensed with the plate heat exchanger and then flowed into the liquid receiver. The working fluid was then sub-cooled thanks to the double pipe heat exchanger before the pump suction head that closed the loop. When very low mass fluxes were needed, the by-pass circuit was also activated with a manually controlled by-pass valve. The demineralized water flowing in the light blue line in Figure 6.1and feeding the condenser and the sub-cooler was controlled in temperature by setting a thermostatic bath, whose specifics are given in section 4.1.1.

Pressure transducers and resistance Pt100 thermometers placed throughout the apparatus were the same used for the CHF experiments. Details of the new sensors and transducers employed will be given in the measurement instrumentation section.
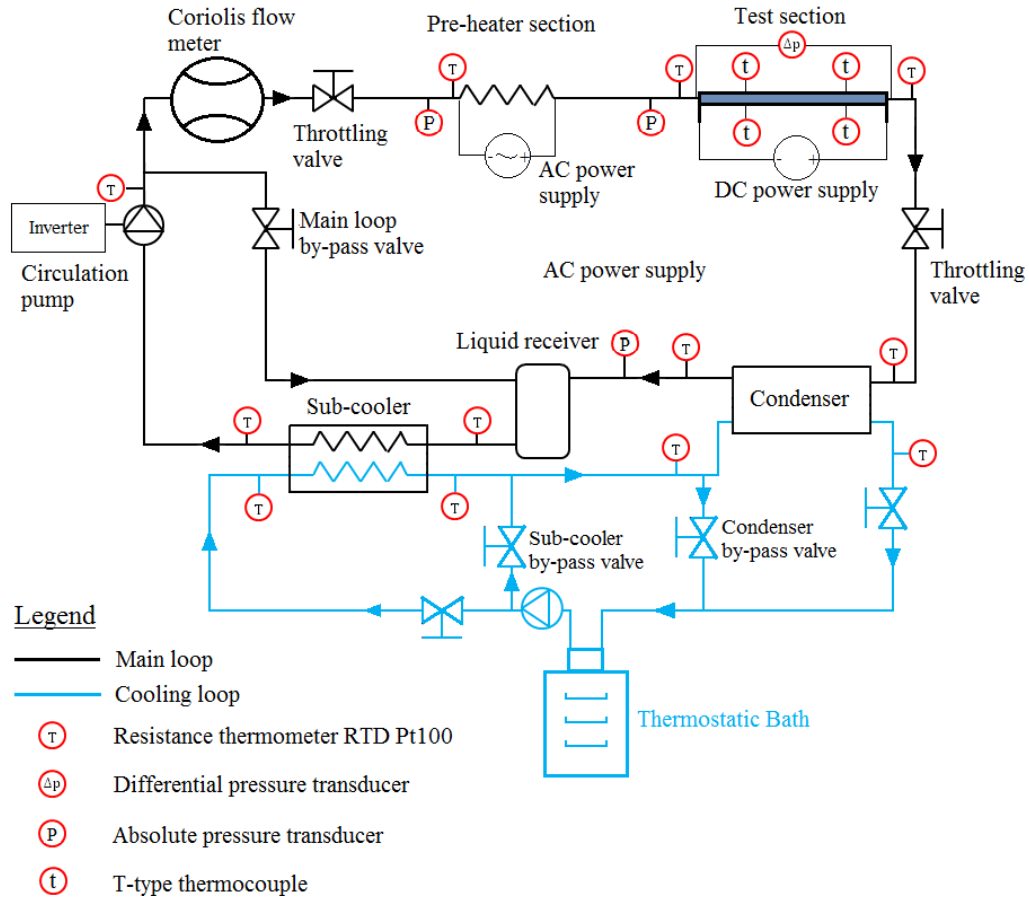
Figure 6.1 Schematic representation of the flow boiling experimental apparatus

6.1.2 *Flow boiling test section*

The test section employed in this work is a smooth, horizontal, circular stainless steel (type 316) tube with an internal diameter of 6.00 ±0.05 mm and an outer diameter of 8.00 ±0.05 mm. Figure 6.2 displays a picture and a schematic view of the test section with its geometrical characteristics. The heat is applied to the fluid by Joule effect, by means of a DC power supply unit (TDK-Lambda GEN 8-300, able to give up to 8 V and 300 A) and two copper electrodes welded on the external tube surface (see points A and E in Figure 6.2), placed at a distance of 193.7 ±0.79 mm one another. The electric connection between the DC power supply unit and the copper electrodes on the test tube was made with two short (<1.0 m) copper wires having a cross section of 70 mm^2. Two pressure taps for the pressure drop measurements were placed at a distance of 237.5 ±0.91 mm and included the diabatic test section.

The heat transfer coefficient measurements were taken at a distance of 146.7 ±0.64 mm far from the diabatic inlet section (see point C in Figure 6.2). In this position, four T-type thermocouples were placed on the top, bottom, left and right sides of the tube surface for the measurement of the outer wall temperature. A high temperature epoxy resin and a Kapton adhesive layer guaranteed the sensors fastening and their electrical insulation from the heated tube. The measurement points for the DC voltage was not located on the copper electrodes, since they could suffer of locally concentrated tension drop. Two measurement wires were instead clamped at a certain distance (see points B and D in Figure 6.2) to guarantee the heat flux uniformity. The SS316 test tube was supplied with DC current, and its electrical resistance is estimated to be 5.1 ±0.084 mΩ. A suitable amount of synthetic rubber (λ = 0.040 W/m K at 40 °C) covered the test section and the whole experimental facility in order to minimize the heat losses. The preheater section, due its higher temperatures reached during operation, was firstly covered by a high-temperature insulation wool (λ = 0.050 W/m K at 200 °C, as indicated by the manufacturer) and then covered by another layer of synthetic rubber.
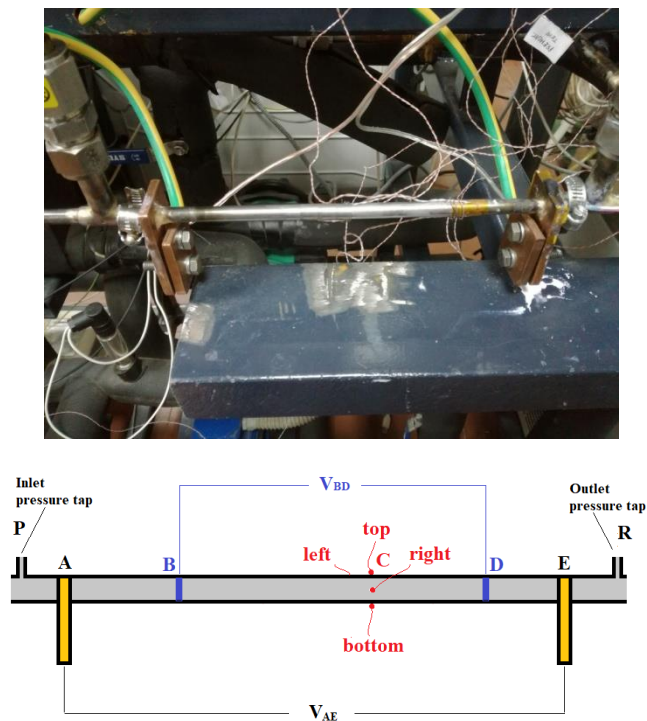
Geometrical features	
A, E	copper electrodes
B, D	voltage measurement points
C	temperature measurement point
AE	193.7 ±0.79 mm
BD	101.6 ±0.41 mm
AC	146.7 ±0.64 mm
d	6.00 ±0.05 mm (internal diameter)
d_o	8.00 ±0.05 mm (outer diameter)
PR	237.5 ±0.91 mm (pressure taps distance)
PC	166.9 ±0.91 mm

Figure 6.2 Photograph of the stainless steel tube and its main geometrical characteristics

6.2 Measurement instrumentation for flow boiling experiments

Some transducers already employed for the CHF experimental campaign were also used for the flow boiling experiments. Specifically, the same Pt100 thermometers shown in 4.1.1 were used in these tests to monitor the correct functioning of the apparatus. Moreover, the refrigerant mass flow rate and the preheater electrical loads were measured with the Coriolis flow meter and the digital wattmeter already described in 4.2.3 and 4.2.5, respectively. The inlet pressure, wall temperatures and heat power to the test tube were instead obtained with new transducers, described in detail in this section. The pressure drop was still measured with the same differential pressure transducer (1151 Smart, provided by Rosemount), but it was calibrated *in-situ* and the calibration procedure is described in the following section.

6.2.1   Absolute pressure measurements

The absolute pressure at the tube test section inlet was measured with a high accuracy absolute pressure transducer (Wika PE8154), with a range of measurement 0-25 bar, giving a current output signal of 4-20 mA. The transducer was calibrated by the manufacturer, providing an overall accuracy of ±0.1%. The refrigerant absolute pressure was also measured at the preheater inlet and at the liquid receiver inlet, with the same transducers used for the CHF experiments (see section 4.2.1), having a range of 0-50 bar and an accuracy of ±0.3%.

6.2.2   Pressure drop measurements and calibration procedure

The pressure drop across the test section was measured with the 1151 Smart differential pressure transducer provided by Rosemount. Before being assembled into the test facility, it was calibrated *in-situ* by measuring the height of a liquid column used to impose the physical pressure drop to the transducer.

The calibration procedure followed the following steps:

a) The low pressure tap of the transducer was left open and unconnected, in contact with the surrounding ambient atmospheric pressure. The high pressure tap was instead connected to a U-shape glass tube, which was vertically fixed on the wall beside a yardstick used for the height measurement.

b) Demineralized water was poured into the glass tube from the top, flooding the U-shape glass tube up to the same level of the pressure taps. In this case, the physical *zero* level was imposed and then electrically set on the transducer.

c) More water was poured in the glass tube up to a total height difference from the *zero* level of 1.485 ±0.004 m. The distance was measured by looking 20 times at the same level by different operators and the standard deviation of the measurement was taken as uncertainty. The *span* level was then electrically set on the transducer. The corresponding full scale of 14.513 ±0.005 kPa was calculated by using an acceleration of gravity of 9.806 m/s^2 and a liquid water density of 996.66 kg/m^3, related to a measured temperature of 26.5 °C taken during the calibration procedure.

d) Other liquid level measurements were taken at different heights (12.5%, 25% and 50% of the full scale) to verify the linear trend of the measured pressure drop with the output signal of 4-20 mA.

e) The calibration curve was finally obtained fitting the five measurements with a line. The corresponding equation, with the output current I expressed in [mA] and the resulting pressure drop ΔP in [kPa] is displayed below. The graphical results of the calibration procedure are shown in Figure 6.3, in which both the calibration points and the residual errors of the linear equation are displayed. The overall accuracy, obtained by taking into account both the uncertainty in the measured pressure drop and the residuals of the calibration curve was estimated to be ±0.06 kPa

$$\Delta P = 0.9054 \cdot I - 3.5827 \tag{6.1}$$
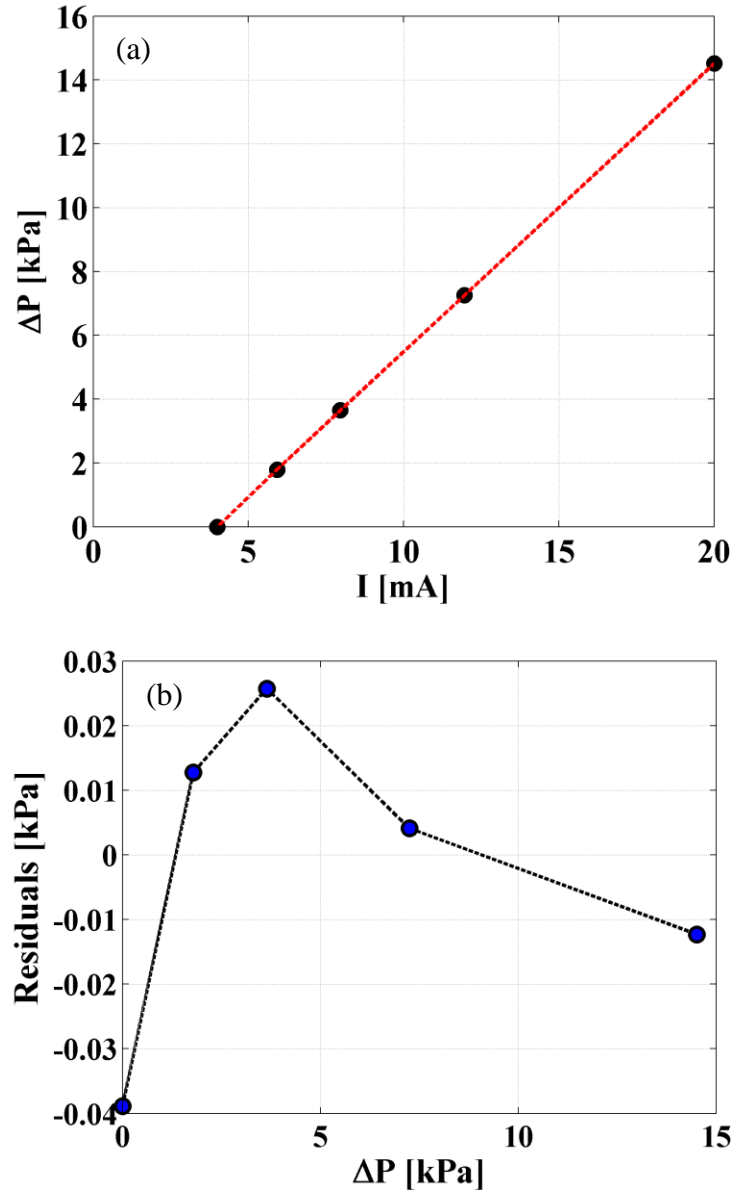
Figure 6.3 Calibration of the differential pressure transducer. (a) Calibration points and curve. Equation (6.1) reflects the linear trend. (b) Residual errors from the linear trend

6.2.3 Wall temperature measurements and thermocouples calibration procedure

Four T-type thermocouples were chosen for the estimation of the outer wall tube temperature. A good accuracy of these measurements was necessary for the goodness of the heat transfer coefficient results. For this reason, the four sensors were calibrated *in-situ* before being positioned on the tube surface.

The calibration procedure was carried out with the thermostatic bath by using two calibrated RTDs having an overall uncertainty of ±0.10 °C. The schematic set-up facility for the calibration process in shown in Figure 6.4. Specifically, each thermocouple to be calibrated was laid down in the thermostatic bath in close contact with one of the RTDs. Another thermocouple with the second calibrated RTD was instead placed in the environment. Two copper blocks (approximately 2x2x5 cm^3) were used to keep RTDs and thermocouples together and to provide a higher heat capacity during the calibration process, avoiding small possible temperature fluctuations. The thermocouple terminal wires were connected to the same module (NI 9212 provided by National Instruments), which could measure the thermocouples output voltage with a resolution of 0.85·10^{-9} V.
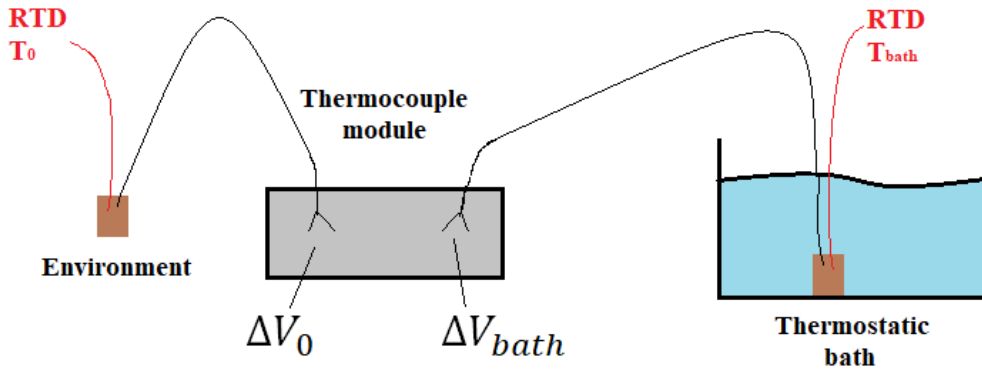
Figure 6.4 Schematic of the thermocouple calibration arrangement

Being ΔV_0 the voltage measured from the thermocouple in the environment and ΔV_{bath} the voltage of the thermocouple in the bath, the functional relations may be written as:

$$T_{bath} - T_{module} = f'(\Delta V_{bath}) \qquad (6.2)$$

$$T_0 - T_{module} = f''(\Delta V_0) \qquad (6.3)$$

Subtracting (6.3) from (6.2), it is possible to eliminate the influence of the unknown module temperature T_{module}:

$$T_{bath} - T_0 = f'''(\Delta V_{bath} - \Delta V_0) \qquad (6.4)$$

With the use of the RTDs in the thermostatic bath and in the environment, the calibration function f''' could be easily found. The four thermocouples (for the top, bottom, left and right sides of the tube) were calibrated using this procedure, using bath temperature from 5 to 85 °C. thus covering the whole range of possible operative conditions during the experiments. The maximum tolerated fluctuations for the RTDs temperature and for the recorded voltages during the calibration process was comparable to the measurement resolutions (0.032 °C and $7 \cdot 10^{-7}$ V, respectively). The accuracy for each thermocouple measurement was then set to ±0.10 °C, equal to that of the RTDs. As an example, the equation below represents the calibration function f''' of one of the four thermocouples positioned on the test tube (on the top) and Figure 6.5 shows its calibration curve obtained with the abovementioned procedure, together with the residual errors of the cubic equation.

$$T_{th} = T_0 + 0.042991 \cdot X^3 - 0.77924 \cdot X^2 + 24.358 \cdot X - 0.0038764 \qquad (6.5)$$

where $X = \Delta V_{th} - \Delta V_0$.
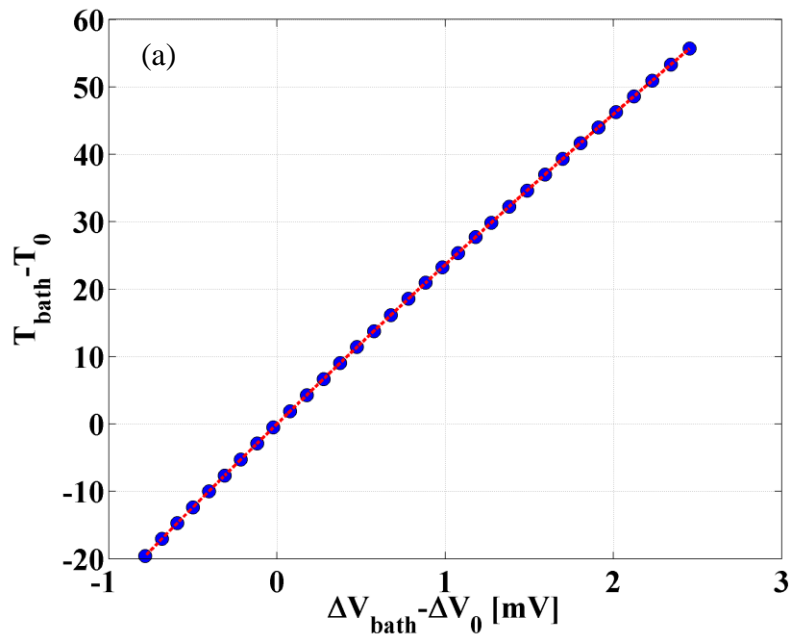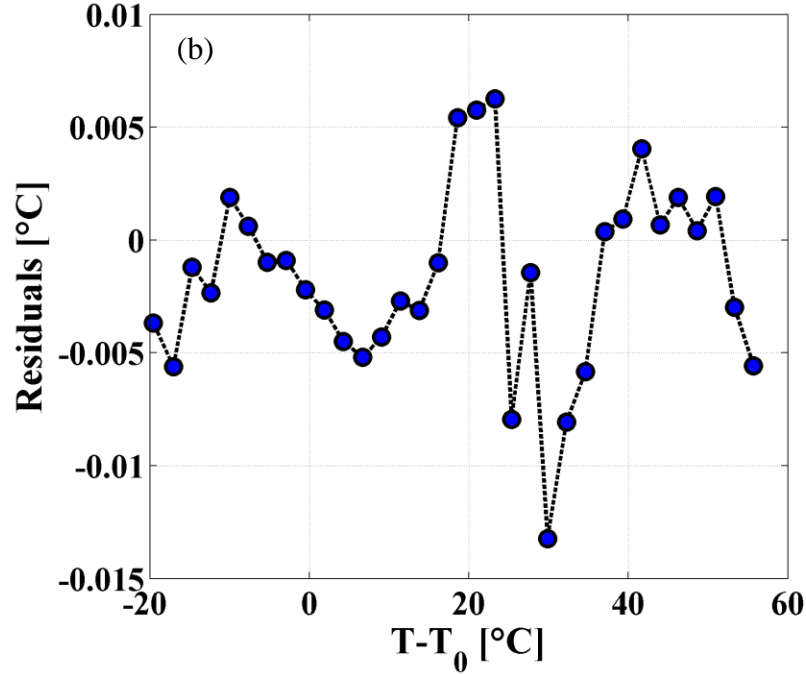
Figure 6.5 Calibration of the thermocouple positioned at the top side of the tube. (a) Calibration points and curve. Equation (6.5) reflects the cubic trend. (b) Residual errors from the linear trend

6.2.4 Electrical input to the test section

The heat power applied to the test tube by Joule effect for the wall heat flux estimation was calculated by independently measuring the DC voltage and current applied. Specifically, the voltage applied was obtained by using an analogic input module (FieldPoint FP AI-110, provided by National Instruments) and two wires fixed on the tube outer surface (see points BD in Figure 6.2). The FP module had a range of 0-5 V, carrying an uncertainty of $\pm 0.03\%$ of the reading. The DC current was instead directly measured with the DC power supply unit (0-300 A). The manufacturer guaranteed an overall accuracy of $\pm 1.0\%$ of the reading.

6.2.5 Data acquisition system and user interface

Similarly to the CHF experiments, the different output signals coming from the transducers were read by the FieldPoint modules and transferred to a pc Ddesktop and monitored in Labview [121] environment. Further specifications can be found in section 4.2.6.

The user interface in Labview [121] for the flow boiling experiments is shown in Figure 6.6. All the parameters of interests were read in real-time and their overall uncertainty in the

recording time was estimated, to let the user be aware of the goodness and stability of each experiment. The thermodynamic conditions at the preheater inlet, test section inlet and test section outlet were visible with a green, orange and red dots on a p-h diagram, respectively. Automatic controls were also able to shut-off the electric load applied both to the test section and the preheater in case of the following dangerous situations:

a) Preheater fiberglass heating tapes temperatures (monitored with two T-type thermocouples placed between tube and tapes) over 150 °C.
b) System pressure above 25 bar
c) Mass flux when heat load is applied below 50 kg/m^2 s
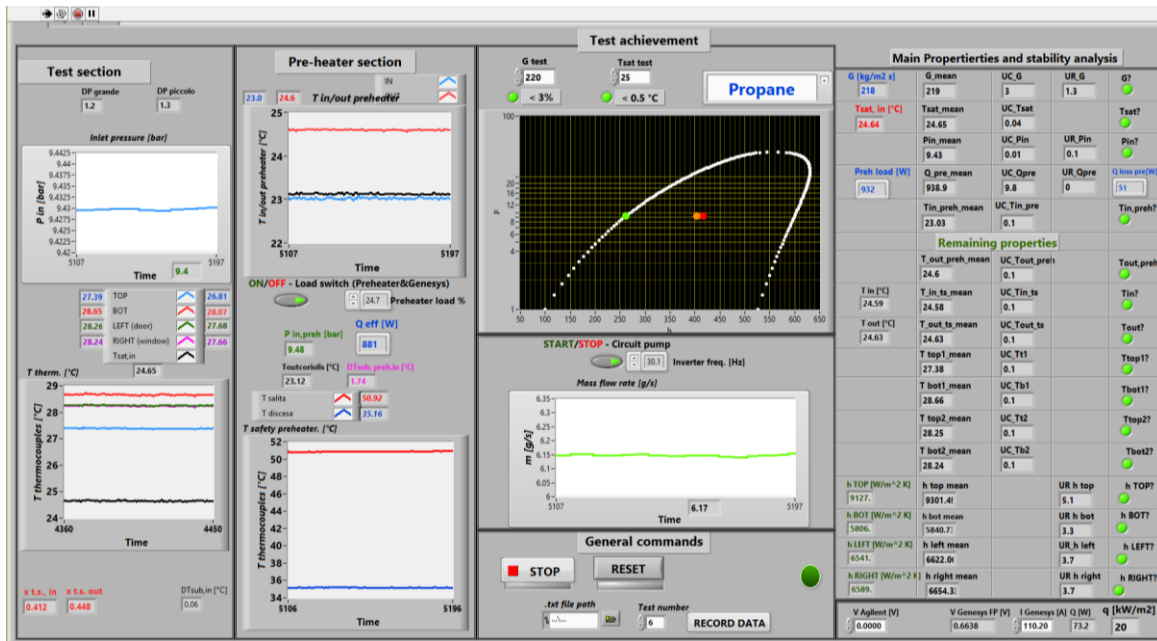
Figure 6.6 Labview [121] interface for the flow boiling experiments

6.3 Method for flow boiling experiments

The data reduction process for the flow boiling experiments is explained in this section.

6.3.1 Data reduction for the flow boiling experiments

At each thermocouple position (top, bottom, left and right side of the tube surface), the local heat transfer coefficient was evaluated by using the Newton equation:

$$h = \frac{q}{T_{wall} - T_{fluid}} \tag{6.6}$$

The mean heat flux presented in the result section was instead calculated by considering the arithmetical average of the four heat transfer coefficients obtained around the tube perimeter:

$$h_{mean} = \frac{h_{top} + h_{bot} + h_{left} + h_{right}}{4} \tag{6.7}$$

The heat flux on the test tube, as explained in the previous paragraph (see section 6.1.2), was calculated with the measured voltage V_{BD} between the positions B and D and the current I_{tube} flowing in the stainless steel tube:

$$q = \frac{V_{BD} \cdot I_{tube}}{\pi d \overline{BD}} \tag{6.8}$$

The inner wall temperature T_{wall} was evaluated by the measured outer wall temperature T_{th} and considering 1-D heat transfer and uniform generation in the metal tube:

$$T_{wall} = T_{th} + \frac{V_{BD} \cdot I_{tube}}{4\pi \lambda_{tube} \overline{BD}} \cdot \frac{\left(\frac{d_o}{d}\right)^2 \cdot \left(1 - \log\left(\left(\frac{d_o}{d}\right)^2\right)\right) - 1}{\left(\frac{d_o}{d}\right)^2 - 1} \tag{6.9}$$

In the above equation, d and d_0 represent the inner and outer diameter of the tube, respectively. λ_{tube} is the tube thermal conductivity, considered equal to 16.26 W/m K for all the experiments performed. The fluid saturation temperature T_{fluid} at the measurement point C (see Figure 6.2) is evaluated by considering a linear pressure drop from the tube inlet:

$$P_C = P_{in} - \Delta P \cdot \frac{\overline{PC}}{\overline{PR}} \tag{6.10}$$

$$T_{fluid} = T_{sat,C} = T_{sat}(P_C) \tag{6.11}$$

The local vapor quality at the measurement point C is:

$$x_C = \frac{i_C - i_{L,C}}{\Delta i_{LV,C}}$$

(6.12)

in which $i_{L,C}$ and $\Delta i_{LV,C}$ refer to the local liquid saturation enthalpy and latent heat and i_C is the local enthalpy at the measurement point, that was calculated using an energy balance on the preheater section:

$$i_C = i_{in} + \frac{4 \cdot \overline{AC} \cdot q}{G \cdot d}$$

(6.13)

The test section inlet enthalpy i_{in} was computed with an energy balance applied to the preheater section:

$$i_{in} = i_{in,preh} + \frac{\dot{Q}_{preh}}{\dot{m}}$$

(6.14)

$$i_{in,preh} = f(T_{in,preh}, P_{in,preh})$$

(6.15)

In the above equations, $\dot{Q}_{preh}$ is the preheater load directly measured by the digital wattmeter and $i_{in,preh}$ is the preheater inlet enthalpy (in sub-cooled liquid condition, obtained with measured temperature and pressure).

As regards the two-phase pressure drop across the test section, the frictional contribution was evaluated by subtracting the momentum contribution to the total measured pressure drop ΔP. The gravitational contribution was neglected due to the horizontal disposition of the tube:

$$\Delta P_{fr} = \Delta P - \Delta P_{acc}$$

(6.16)

The momentum pressure drop due to the ongoing evaporation inside the test section was calculated as follows:

$$\Delta P_{acc} = G^2 \cdot \left\{ \left[\frac{(1-x)^2}{\rho_L \cdot (1-\alpha)} + \frac{x^2}{\rho_V \cdot \alpha} \right]_{outlet} - \left[\frac{(1-x)^2}{\rho_L \cdot (1-\alpha)} + \frac{x^2}{\rho_V \cdot \alpha} \right]_{inlet} \right\}$$

(6.17)

The void fraction α was obtained with the Steiner [85] version of the drift flux model of Rouhani and Axelsson [136]:

$$\alpha = \frac{x}{\rho_V} \cdot \left[\left(1 + 0.12 \cdot (1-x)\right) \cdot \left(\frac{x}{\rho_V} + \frac{1-x}{\rho_L}\right) + 1.18 \cdot \frac{1-x}{G} \cdot \left(\frac{g \cdot \sigma \cdot (\rho_L - \rho_V)}{\rho_L^2}\right)^{0.25} \right]^{-1} \quad (6.18)$$

The vapor quality x and all the saturated thermodynamic properties in the void fraction expression were computed as an arithmetical average of the inlet and outlet vapor refrigerant properties. Finally, the frictional pressure gradient presented in the results section could be found as:

$$\left.\frac{\Delta P}{\Delta z}\right|_{fr} = \frac{\overline{\Delta P_{fr}}}{\overline{PR}} \quad (6.19)$$

All refrigerant thermodynamic properties are evaluated with the software REFPROP 9.0 [123], developed by NIST. The whole data reduction is instead carried out with MATLAB software [122].

6.4   Uncertainty analysis in flow boiling experiments

In this section, the uncertainty analysis of measured and derived quantities for the two-phase heat transfer and pressure drop experiments is shown. The uncertainty theory and calculation method is already discussed in section 0 and it is omitted in this part.

6.4.1   Uncertainty of measured quantities

Table 6.1 provides a summary of the measurement range and the systematic uncertainty for all the measurement instrumentation. Some sensors and transducers were already presented in Table 4.1 for the CHF experiments. The law of propagation of error was then used to evaluate the combined uncertainty of the measured parameters, by adding the standard deviation of each sample. The expanded uncertainty was finally calculated using a coverage factor $z = 2$, guaranteeing a confidence level of 95.45%.

Table 6.1 Summary of the measurement instrumentation for the flow boiling experiments with their operative range and accuracy

Measurement	Range	B-type uncertainty w_x
Temperature (4-wire Pt100 RTD)	-80/250 °C	±0.180 °C
Wall temperature (4 T-type thermocouples)	5/85 °C	±0.10 °C (calibrated *in-situ*)
Inlet absolute pressure	0/25 bar	±0.1 % reading
Absolute pressure	0/50 bar	±0.3 % reading
Differential pressure	0/14.51 kPa	±0.06 kPa
Flow meter	0.00/115.7 g/s	±1 % measurement
Electrical power (preheater)	0/8 kW	±1 % measurement
Voltage (test section)	0/5 V	±0.03 % measurement
Current (test section)	0/300 A	±1 % measurement

6.4.2   *Uncertainty of derived quantities*

The evaluation of the expanded uncertainty of all the derived parameters of interest is shown here in detail. The law of propagation of error was implemented for all the calculated quantities.

Mass flux

The uncertainty of the mass velocity takes into account that of the measured mass flow rate and of the internal diameter:

$$u_c(G) = \sqrt{\left(\frac{4 \cdot u_c(\dot{m})}{\pi \cdot d^2} \right)^2 + \left(\frac{8 \cdot \dot{m}}{\pi \cdot d^3} \cdot u_c(\mathrm{d}) \right)^2} \qquad (6.20)$$

Excluding the experiments performed during dry-out, in which the fluctuation of the mass flow rate was substantial, all the tests were recorded with an expanded uncertainty of the mass flow rate included in a ±3%.

Heat flux

The expanded uncertainty of the heat flux is dependent on the current and voltage applied to the test section and to the measured inner tube diameter and the distance BD where the voltage was taken (see Figure 6.2):

$$u_c(q) = \sqrt{\left(\frac{V_{BD} \cdot u_c(I)}{\pi \cdot d \cdot \overline{\overline{BD}}}\right)^2 + \left(\frac{I \cdot u_c(V_{BD})}{\pi \cdot d \cdot \overline{\overline{BD}}}\right)^2 + \left(\frac{V_{BD} \cdot I}{\pi \cdot d^2 \cdot \overline{\overline{BD}}} \cdot u_c(d)\right)^2 + \left(\frac{V_{BD} \cdot I}{\pi \cdot d \cdot \overline{\overline{BD}}^2} \cdot u_c(\overline{BD})\right)^2} \qquad (6.21)$$

The heat flux was kept stable during the experiments and its maximum expanded uncertainty was found to be ±1.8%.

Saturation temperature

The uncertainty of the saturation temperature at the test section inlet was evaluated by considering the influence of the measured inlet pressure, according to Equation (4.29) already used for the CHF experiments. The uncertainty of the saturation temperature at the measurement point C was instead also dependent on the uncertainty of the measured lengths and pressure drop (see Figure 6.2):

$$u_c(T_{sat,C}) = \frac{\partial T}{\partial P} \cdot dP = \frac{\partial T}{\partial P} \cdot u_c(P_C) \qquad (6.22)$$

$$u_c(P_C) = \sqrt{u_c(P_{in})^2 + \left(\frac{\overline{PC} \cdot u_c(\Delta P)}{\overline{PR}}\right)^2 + \left(\frac{\Delta P \cdot u_c(\overline{PC})}{\overline{PR}}\right)^2 + \left(\frac{\overline{PC} \cdot \Delta P \cdot u_c(\overline{PR})}{\overline{PR}^2}\right)^2} \qquad (6.23)$$

In the flow boiling experimental campaign, the maximum uncertainty in the saturation temperature in the experimental points far from the occurrence of dry-out was found to be ±0.07 °C.

Preheater inlet, test section inlet and saturated enthalpies

The enthalpy at the test section inlet was computed with an energy balance performed on the preheater. Its related uncertainty is:

$$u_c(i_{in}) = \sqrt{u_c(i_{in,preh})^2 + \left(\frac{1}{\dot{m}} u_c(\dot{Q}_{preh})\right)^2 + \left(\dot{Q}_{preh} \cdot \frac{1}{\dot{m}^2} \cdot u_c(\dot{m})\right)^2} \qquad (6.24)$$

In the above equation, the preheater inlet enthalpy was calculated with the measured preheater inlet temperature and pressure. Its uncertainty $u_c(i_{in,preh})$ then followed the same expression as Equation (4.34). The uncertainty of the enthalpy at the measurement point C was instead obtained by deriving Equation (6.13):

$$u_c(i_C) = \sqrt{u_c(i_{in})^2 + \left(\frac{4 \cdot q}{G \cdot d} \cdot u_c(\overline{AC})\right)^2 + \left(\frac{4 \cdot \overline{AC}}{G \cdot d} \cdot u_c(q)\right)^2 + \left(\frac{4 \cdot \overline{AC} \cdot q}{G^2 \cdot d} \cdot u_c(G)\right)^2 + \left(\frac{4 \cdot \overline{AC} \cdot q}{G \cdot d^2} \cdot u_c(d)\right)^2}$$

$$(6.25)$$

Vapor quality

The uncertainty of the vapor quality at the measurement point C is a function of the uncertainty of the inlet enthalpy and the measurement point enthalpy, respectively, and of the saturated liquid and vapor enthalpies. Its expression is written below:

$$u_c(x_C) = \sqrt{\left(\frac{1}{i_{V,C} - i_{L,C}} \cdot u_c(i_C)\right)^2 + \left(\frac{i_C - i_{V,C}}{(i_{V,C} - i_{L,C})^2} \cdot u_c(i_{L,C})\right)^2 + \left(\frac{i_{L,C} - i_C}{(i_{V,C} - i_{L,C})^2} \cdot u_c(i_{V,C})\right)^2} \quad (6.26)$$

The uncertainty of the saturated enthalpies was found by using the same expressions indicated in Equation (4.32) and Equation (4.33), by using the uncertainty of the pressure in the measurement point (see Equation (6.23)).

During experiments, the uncertainty of the vapor quality at the measurement point was always inferior to ±0.12 for the tests far from the dry-out occurrence.

Wall temperature

The uncertainty of the inner wall temperature was estimated by deriving Equation (6.9):

$$u_c(T_{wall}) = \sqrt{ u_c(T_{th})^2 + \left(\frac{u_c(V_{BD}) \cdot I \cdot \gamma}{4 \cdot \pi \cdot \lambda_{tube} \cdot \overline{BD}} \right)^2 + \left(\frac{u_c(I) \cdot V_{BD} \cdot \gamma}{4 \cdot \pi \cdot \lambda_{tube} \cdot \overline{BD}} \right)^2 + \left(\frac{u_c(\gamma) \cdot V_{BD} \cdot I}{4 \cdot \pi \cdot \lambda_{tube} \cdot \overline{BD}} \right)^2 + \left(\frac{V_{BD} \cdot I \cdot \gamma \cdot u_c(\overline{BD})}{4 \cdot \pi \cdot \lambda_{tube} \cdot \overline{BD}^2} \right)^2 }$$

<div align="right">(6.27)</div>

In the above equation, the parameter γ and its uncertainty are defined as:

$$\gamma = \frac{\varepsilon \cdot \left(1 - \log(\varepsilon) \right) - 1}{\varepsilon - 1}$$

<div align="right">(6.28)</div>

$$\varepsilon = \left(\frac{d_o}{d} \right)^2$$

<div align="right">(6.29)</div>

$$u_c(\gamma) = \frac{-\varepsilon + \log(\varepsilon) + 1}{\left(\varepsilon - 1 \right)^2} \cdot u_c(\varepsilon)$$

<div align="right">(6.30)</div>

$$u_c(\varepsilon) = \sqrt{ \left(\frac{2 \cdot d_o \cdot u_c(d_o)}{d^2} \right)^2 + \left(\frac{2 \cdot d_o^2 \cdot u_c(d)}{d^3} \right)^2 }$$

<div align="right">(6.31)</div>

The uncertainty of the outer wall temperatures $u_c(T_{th})$ measured by the thermocouples was instead computed by taking into account the calibration process uncertainty (± 0.10 °C) and the fluctuations in the measured voltages during operation.

Heat transfer coefficient

The heat transfer coefficient uncertainty at any measurement point was:

$$u_c(h) = \sqrt{ \left(\frac{u_c(q)}{T_{wall} - T_{sat,C}} \right)^2 + \left(\frac{q \cdot u_c(T_{wall})}{(T_{wall} - T_{sat,C})^2} \right)^2 + \left(\frac{q \cdot u_c(T_{sat,C})}{(T_{wall} - T_{sat,C})^2} \right)^2 }$$

<div align="right">(6.32)</div>

The uncertainty of the mean heat transfer coefficient, averaged along the tube perimeter, was:

$$u_c(h_{mean}) = 0.25 \cdot \sqrt{ u_c(h_{top})^2 + u_c(h_{bot})^2 + u_c(h_{left})^2 + u_c(h_{right})^2 }$$

<div align="right">(6.33)</div>

Most of the database provided heat transfer coefficient values with an overall uncertainty below $\pm 20\%$. Exceptions ($>40\%$) were found at the occurrence of dry-out, due to the more

significant fluctuations of the wall temperatures, mass flow rate and system pressure in such condition.

Pressure gradient

The pressure gradient uncertainty was calculated by taking into account both the measured pressure drop uncertainty and the uncertainty of the measured length $\overline{PR}$:

$$u_c\left(\frac{\Delta P}{\Delta z}\right) = \sqrt{\left(\frac{u_c(\Delta P)}{\overline{PR}}\right)^2 + \left(\frac{\Delta P \cdot u_c(\overline{PR})}{\overline{PR}^2}\right)^2} \qquad (6.34)$$

In most of the experiments, the frictional pressure gradient uncertainty was kept below ±2.0 kPa. Significant higher values were instead reached in case of dry-out occurrence.

The maximum expanded uncertainties found for the mean heat transfer coefficient, pressure drop and main operative parameters is shown in Table 6.2.

Table 6.2 Summary of heat transfer coefficient, pressure gradient and operating parameters typical and maximum recorded uncertainties found during the experiments

Parameter	Maximum uncertainty for 90% of the database	Maximum recorded uncertainty (dry-out conditions)
Saturation temperature T_{sat}	±0.07 °C	±0.15 °C
Mass flux G	±3%	±5%
Heat flux q	±0.70%	±1.8%
Vapor quality x	±0.12	±0.55
Heat transfer coefficient h	±20%	±45%
Pressure gradient $\frac{\Delta P}{\Delta z}$	±2.0 kPa	±2.9 kPa

6.5 Test section and preheater validation

Before the two-phase flow boiling experiments, the correct insulation of the preheater and the test section were verified with the help of liquid single-phase tests performed with refrigerant R134a. These tests were also able to check the correct functioning of the measurement instrumentation. The fluid charge in the apparatus, generally equal to 2.8 kg, was temporarily increased to 4.5 kg in order to get sufficient sub-cooling at the inlet of preheater and test sections, thus maintaining the compressed liquid condition.

6.5.1 Preheater adiabaticity tests

The correct insulation of the preheater section was verified with 16 dedicated liquid single phase tests. The mass flow rate was varied from 18 to 53 g/s, the preheater inlet temperature was set from 26 to 28 °C and the sub-cooling at the preheater outlet was always kept high (from 5 to 25 °C) in order to avoid possible two-phase flow. The electrical heat power imposed to the fiberglass heating tapes was varied from 220 up to 1460 W and compared to the heat absorbed by the liquid refrigerant flowing into the preheater section, which was calculated by neglecting the pressure drop contribution to the enthalpy variation:

$$\dot{Q}_{preh} = \dot{m} \cdot \overline{c} \cdot (T_{out,preh} - T_{in,preh}) \tag{6.35}$$

The liquid specific heat capacity was evaluated with the software REFPROP 9.0 [123] as a function of the arithmetical average of the preheater inlet and outlet fluid temperatures. The results of the adiabaticity tests (see Figure 6.7) showed that the heat losses were approximately 10% of the imposed heat rate, at any condition. In a further analysis, it was found that the heat losses at the preheater could be fairly fitted with a linear equation depending on the temperature difference between the fiberglass heating tapes and the surrounding environment, which ranged from 5 to 60 °C:

$$\dot{Q}_{loss,preh} = 2.025 \cdot (T_{preh,tape} - T_{amb}) - 2.376 \tag{6.36}$$
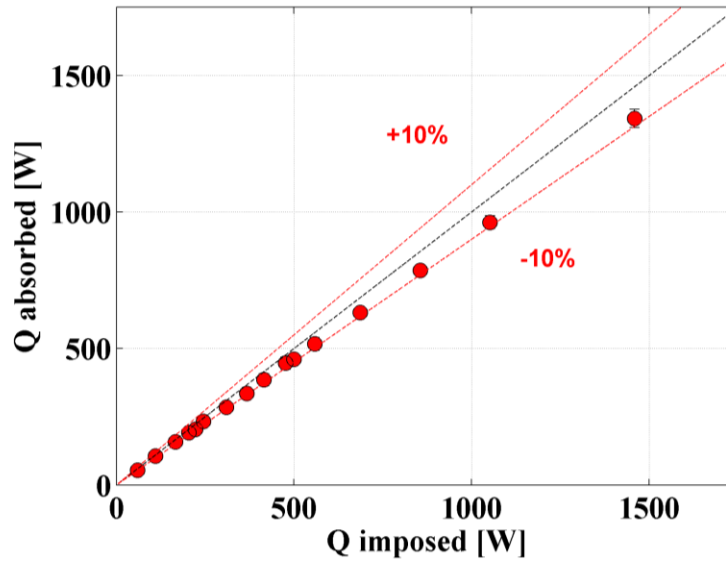
Figure 6.7 Adiabaticity tests performed for the preheater section

6.5.2 *Test section adiabaticity tests*

The correct insulation of the test section was instead verified with 34 tests performed in liquid single-phase. For these experiments, the mass flow rate was varied from 16 to 44 g/s, the test section inlet temperature from 28 to 31 °C and a considerable inlet sub-cooling (from 10 to 21 °C) was provided to ensure single-phase flow. The DC electrical power applied to the test section was varied from 40 to 175 W, covering the whole range of heat fluxes imposed during the flow boiling experiments. By neglecting the pressure drop contribution, the energy balance was performed as indicated in Equation (6.35) and the absorbed heat was compared to the electrical power.

The heat dispersed was found to be around 10%. Actually, the highest losses were obtained only in case of very high heat fluxes (more than 50 kW/m^2) and high tube temperatures (more than 40 °C), which were not operative conditions encountered in the present experimental campaign. The remaining points show heat losses below 4%, that were neglected in the data reduction process.

149
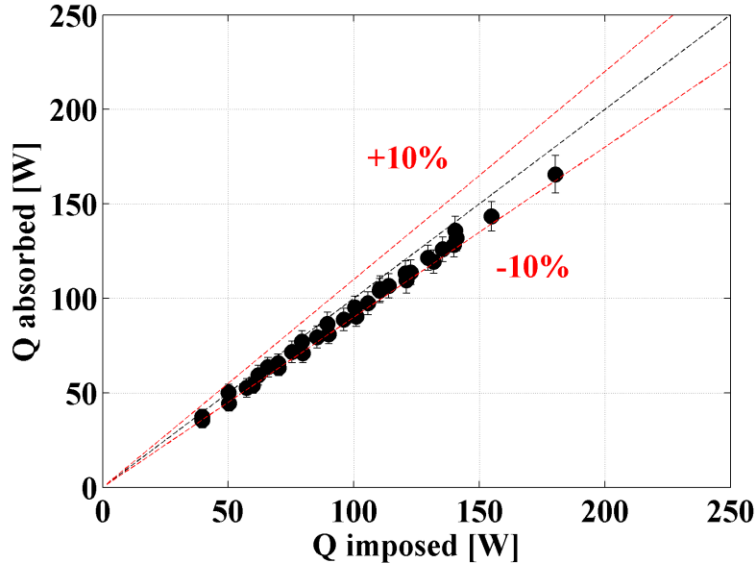
Figure 6.8 Adiabaticity tests performed for the flow boiling test section

The liquid single phase heat transfer coefficient was also estimated for the four thermocouple measurement and compared to the predictive methods of Dittus-Boelter [70]. Specifically, the single phase heat transfer coefficient h_{sp} was evaluated according to the equation below, already used for the CHF validation tests.

$$h_{sp} = \frac{\dot{q}}{T_{wall} - T_f} \qquad (6.37)$$

The wall temperature T_{wall} was calculated with the same expression used in two-phase experiments (see Equation (6.9)). The fluid temperature T_f at the thermocouple position was obtained from:

$$T_f = T_{in} + \frac{\overline{AD}}{\overline{AE}} \cdot \frac{\dot{Q}}{\dot{m} \cdot c} \qquad (6.38)$$

where the specific heat c was evaluated at the average temperature between the inlet and outlet sections. The comparison between experimental and expected liquid phase heat transfer coefficient is shown in Figure 6.9. Most of the experimental points fall into the an error band of ±20% from the Dittus-Boelter correlation,

150
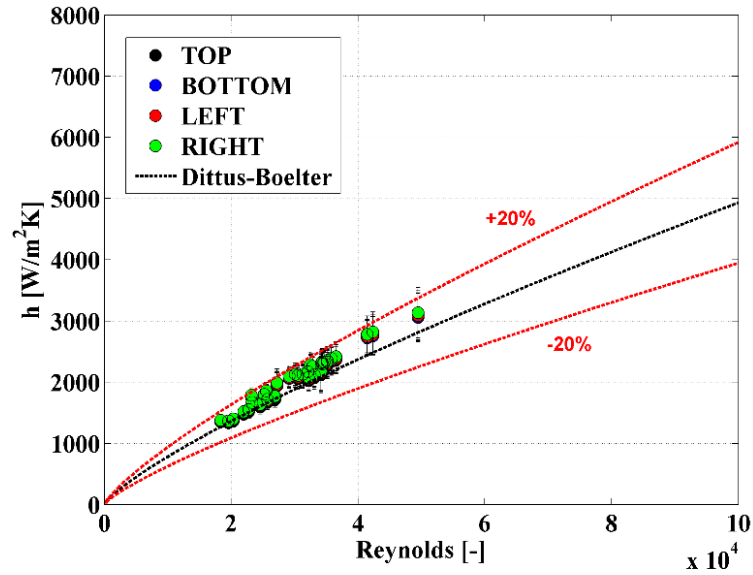
Figure 6.9 Experimental and predicted single-phase heat transfer coefficient against Reynolds number

6.5.3 Comparison with previous studies

Fur a further validation, some two-phase heat transfer coefficient tests were compared to other data taken from scientific literature and obtained in similar working conditions. Figure 6.10 shows the R134a two-phase heat transfer coefficient as a function of the vapor quality for an average mass flux of 200 kg/m^2 s, an imposed heat flux of 5.0 kW/m^2, and a saturation temperature of 20 °C. Values from this study were compared to those of Grauso et al. [62], obtained for a single circular tube of the same inner diameter of 6.0 mm and at similar operating conditions. The agreement between the two independent studies was satisfactory, with points that blend one another especially in case of vapor qualities higher than 0.40. For lower vapor qualities the heat transfer coefficient of Grauso et al. [62] was lower, probably due to the lower saturation temperature (7 °C) used by the authors.

Another comparison was performed in Figure 6.11, in which the experimental heat transfer coefficient as a function of the vapor quality was compared to other two independent studies of da Silva Lima et al. [137] and Dorao et al. [138] with the same refrigerant and similar operative conditions, but with a higher (13.84 mm) and lower (5.0 mm) internal diameter, respectively. Specifically, all the experiments in Figure 6.11 represent flow boiling of R134a at an average mass flux of 300 kg/m^2 s and an average saturation temperature of 20 °C. As

151

expected, the experimental heat transfer coefficient from this study was higher when compared to the results of da Silva Lima et al. [137], whereas similar values were obtained with the work of Dorao et al. [138].
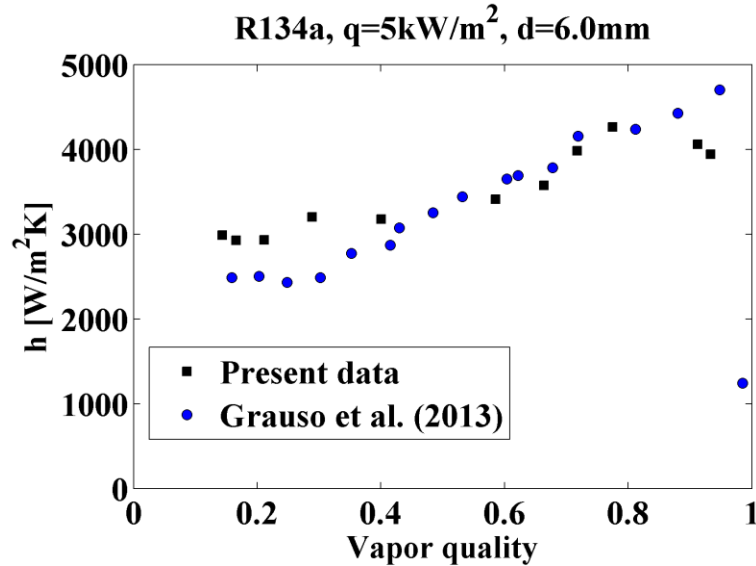
Figure 6.10 Heat transfer coefficient comparison: present data against work of Grauso et al. [62] obtained at similar operative condition and same inner diameter
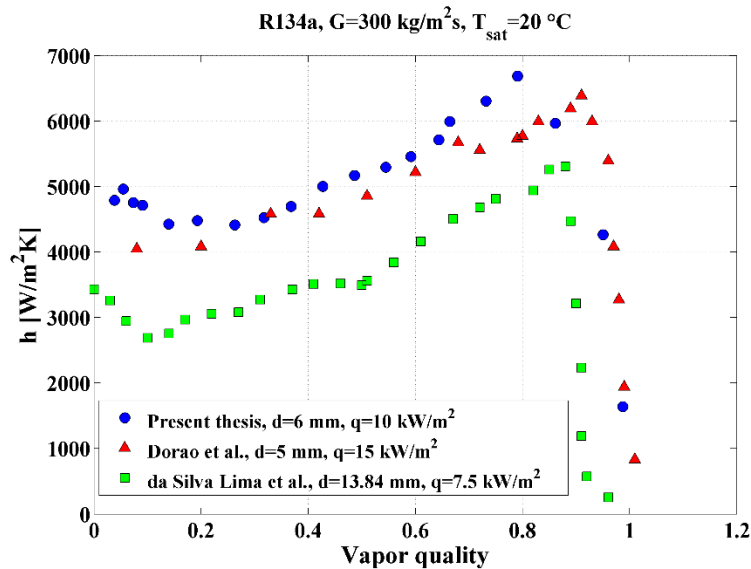
Figure 6.11 Heat transfer coefficient comparison with higher (13.84 mm) and lower (5.0 mm) internal diameters, at similar operative conditions (R134a, G = 300 kg/m^2 s, T_{sat} = 20 °C, q = 7.5-15.7 kW/m^2).

7 Flow boiling results

This chapter presents experimental data concerning two-phase flow boiling heat transfer coefficient and pressure drop in the stainless steel test tube of 6.0 mm inner diameter shown in the previous chapter. The experimental campaign consisted of more than 500 points carried out with refrigerants R134a and propane (R290), at different operative conditions in terms of mass velocity, heat flux, saturation temperature, vapor quality and working fluid. The description of the experimental procedure and a digression of the fluctuations of the main parameters during experiments is shown in the first paragraph. Then, the chosen operating parameters set and monitored during the experiments are presented. The effect of mass flux, heat flux, saturation temperature and working fluid on the heat transfer coefficient are shown in the third paragraph, together with the assessment of some chosen correlations. The effect of operating parameters and the comparisons between experimental and predicted data for frictional pressure drop is finally performed in the fourth and last paragraph.

7.1 Description of the experiments

For each flow boiling test, the purpose was to record the heat transfer coefficients at the top, bottom, left and right sides of the tube as a function of the local vapor quality, starting from the onset of boiling ($x = 0$) up to the dry-out condition ($x \approx 1.0$). The saturation temperature T_{sat}, mass flux G and heat flux q were set and kept constant for each experiment.

Specifically, the desired saturation temperature was obtained by setting the demineralized water temperature in the thermostatic bath. The mass flux was instead controlled by changing the inverter frequency of the electric motor matched with the magnetic gear pump. The mass flow rate and the system pressure (i.e. saturation temperature) could be adjusted during the experiments by manipulating the micrometric throttling valve and the main circuit by-pass valve. A small sub-cooling after the pump was always desired to avoid saturated flow at the preheater inlet and therefore a poor estimation of the vapor quality in the test section.

Preheater inlet sub-cooling degrees of approximately 2.0 °C were obtained by using the ball cock valves in the by-pass circuits present in the secondary loop. The heat flux applied to the test section was set by remotely changing the voltage from the DC power supply unit, covering a range of voltages of 0-1.0 V and high currents (0-190 A). Finally, the desired vapor quality at the inlet of the test section was obtained by varying the applied AC voltage to the four fiberglass heating tapes using a TRIAC electronic unit (up to 230 V) remotely commanded by Arduino One controller (4-20 mA).

Particular attention was given to the uncertainty of each operating parameter during the experiments. As an example, Figure 7.1 shows the time variation of the different temperatures that intervene for the evaluation of the heat transfer coefficient. The diagram refers to the experimental test of propane, at a mass velocity of 297 kg/m^2 s, an imposed heat flux of 40 kW/m^2 and a saturation temperature of 35 °C. The test displayed corresponds to a vapor quality of 0.27. In this case, the boiling process was very stable, with the A-type uncertainty of the different temperatures (calculated as a standard deviation of the sample of 90 points) very low and comparable to the resolution of the data acquisition system. The B-type uncertainty related to the absolute pressure transducer and the calibrated thermocouples accuracy was relatively higher. Thus, the overall uncertainty of the heat transfer coefficients for this type of points that are far from the occurrence of dry-out is mostly due to the systematic uncertainty of the measurement instrumentation.

A different situation is depicted in Figure 7.2, in which the operating conditions remained the same, but the vapor quality was fixed to 0.86, after the dry-out incipience point. In this case, larger fluctuations were obtained for both the saturation and the wall temperatures. Specifically, the A-type uncertainty of the saturation temperature was 5 times the one obtained during stable boiling, whereas the wall temperature fluctuations caused by the intermittent rewetting of the heated surface led to standard deviations of almost two order of magnitude higher than those calculated in case of lower vapor quality. These severe fluctuations are therefore the main responsible for the high heat transfer coefficient uncertainties calculated after the dry-out occurrence.
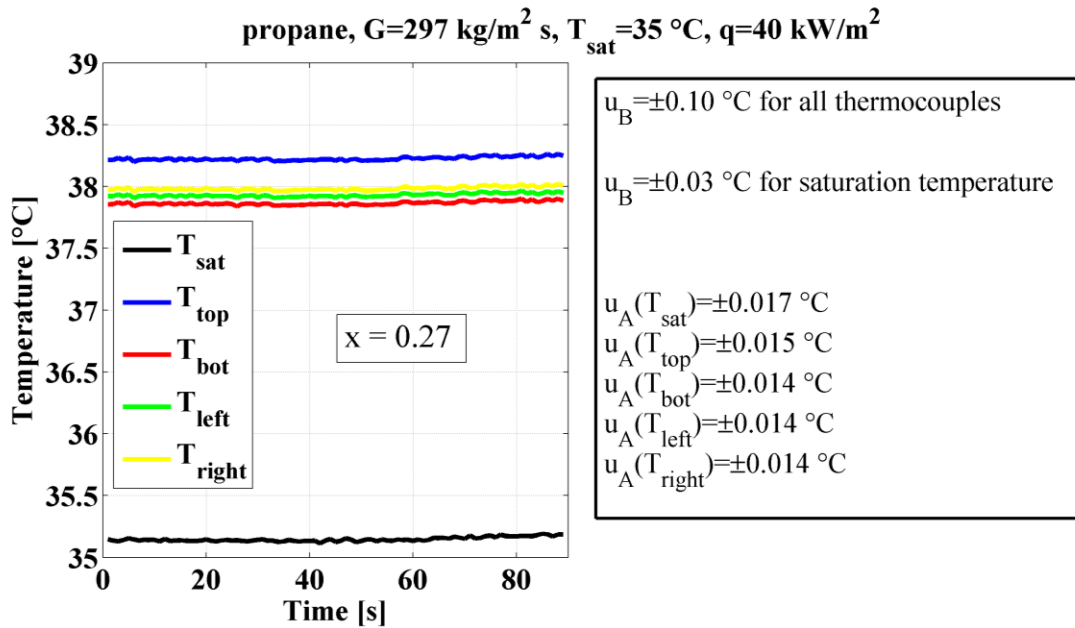
Figure 7.1 Stability analysis performed on the saturation and wall temperatures during stable boiling, at a vapor quality of 0.27. The experiment refers to propane at $G = 297$ kg/m^2 s, $q = 40$ kW/m^2 and $T_{sat} = 35$ °C. Instruments accuracy (B-type uncertainty) and observed fluctuations during the experiments (A-type uncertainty) are provided on the right.
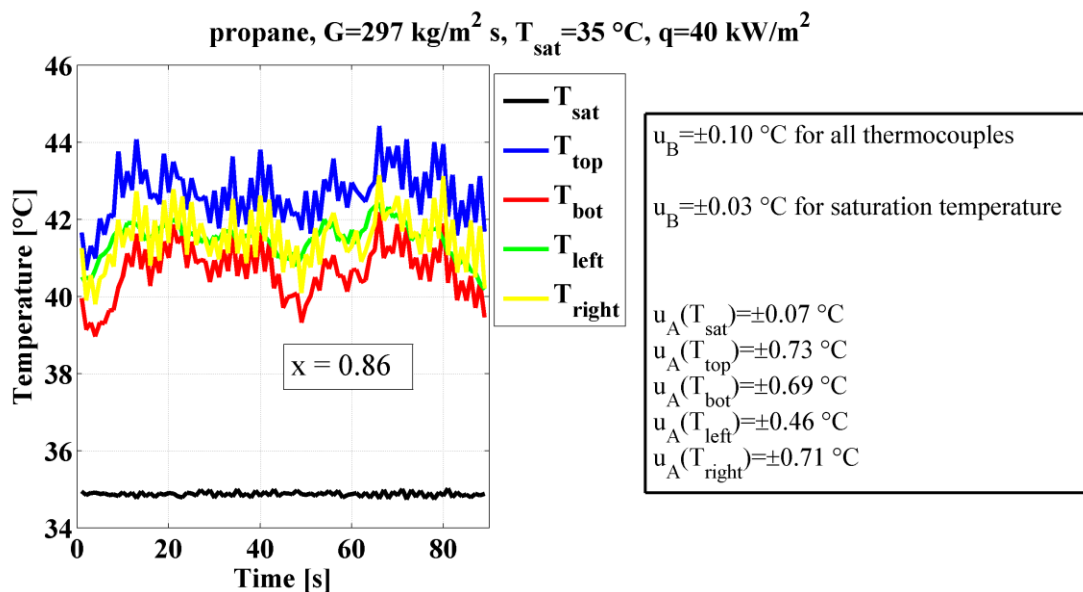
Figure 7.2 Stability analysis performed on the saturation and wall temperatures at a vapor quality of 0.86. The experiment refers to propane at $G = 297$ kg/m^2 s, $q = 40$ kW/m^2 and $T_{sat} = 35$ °C. Instruments accuracy (B-type uncertainty) and observed fluctuations during the experiments (A-type uncertainty) are provided on the right.

Similarly, the time variation of the measured pressure drops is shown in Figure 7.3. The diagram refers to an adiabatic experimental test of propane, at a mass velocity of 298 kg/m^2 s and at a saturation temperature of 25 °C. The blue line corresponds to a vapor quality of 0.08 and the red line to a vapor quality of 0.82 (close to the dry-out occurrence). In case of stable boiling (i.e. low vapor quality), the small fluctuations lead to a A-type uncertainty comparable to the accuracy of the calibrated differential pressure transducer. For a higher vapor quality and close to the dry-out occurrence, instead, the A-type uncertainty is approximately ten time higher (being the 16% of the measured value) and represents the main responsible for the relatively high expanded uncertainty shown in the results diagrams exposed in the following paragraphs.
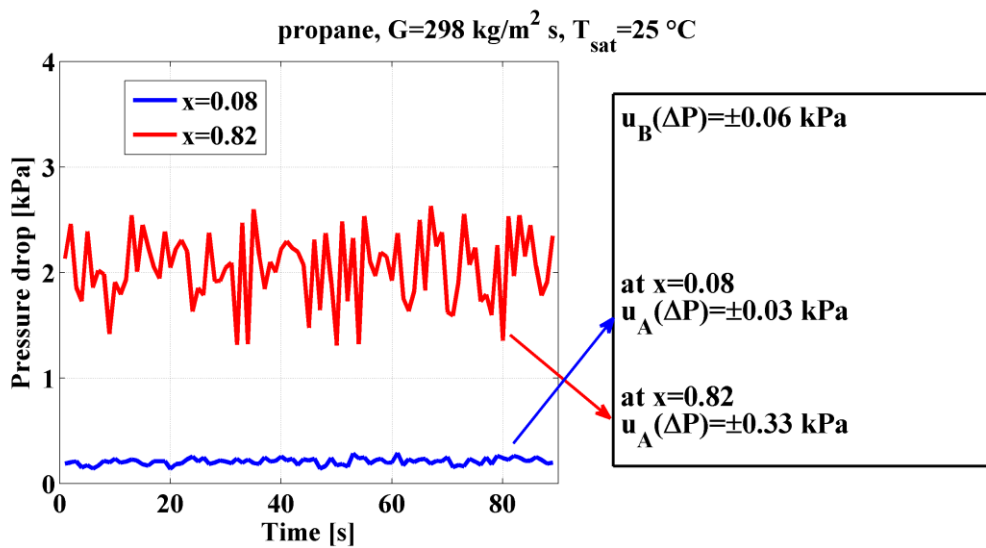
Figure 7.3 Stability analysis performed on the measured pressure drop in case of stable boiling ($x = 0.08$) and close to the occurrence of dry-out ($x = 0.82$). The experiments refers to propane at $G = 298$ kg/m^2 s and $T_{sat} = 25$ °C. Instrument accuracy (B-type uncertainty) and observed fluctuations during the experiments (A-type uncertainty) are provided on the right.

In order to improve the quality of the experimental database, the system was considered stabilized and the data could be recorded only when the expanded uncertainty calculated in real time (including therefore the measurement accuracy and the fluctuations observed during

experiments) of each parameter of interest was inferior to a chosen threshold. The upper limits for acquisition were set to: ±3% for the mass velocity, ±0.2 °C for the wall outer temperature obtained by the T-type thermocouples, ±0.1 °C for the saturation temperature. As shown, for points approaching and beyond the occurrence of dry-out, some fluctuations could be not controlled and therefore tests were taken with higher uncertainties. Data from sensors were recorded with an acquisition frequency of 1.0 Hz and the arithmetic average over 2 minutes was taken as the nominal value of each sample.

7.2 Experimental conditions for flow boiling experiments

The purpose of this experimental campaign was to investigate on the effect of the operative parameters on the pressure drop and mean heat transfer coefficient, which is the heat transfer coefficient averaged over four measurement points on the top, bottom, left and right side of the tube surface. The inner diameter of 6.0 mm was the sole used in this experimental campaign. The imposed mass flux ranged from 150 to 300 kg/m^2 s in case of refrigerant R290 and from 150 to 500 kg/m^2 s in case of refrigerant R134a. With such low mass velocities, the effect of flow stratification could be substantial in some cases and therefore a different heat transfer coefficient on the top and bottom side of the tube were recorded. The saturation temperature ranged from 25 °C to 35 °C in case of refrigerant R290 (thus having reduced pressures from 0.292 to 0.388) and was fixed to 20 °C and 30 °C in case of R134a (thus having reduced pressures of 0.141 and 0.190, respectively). Finally, the heat flux was imposed from 5.0 to 40 kW/m^2 in case of R290 and from 2.5 to 20 kW/m^2 in case of R134a. For each operative condition, the vapor quality was set from the onset of boiling ($x \approx 0.0$) up to the occurrence of dry-out ($x \approx 1.0$).

As a summary, Table 7.1provides all the operative conditions investigated for both R134a and R290.

Table 7.1 Experimental conditions used for the flow boiling heat transfer and pressure drop experiments.

Parameter	Range	
	R290	*R134a*
Saturation temperature T_{sat} [°C]	25 - 35	20; 30
Reduced pressure P_{red}	0.292 - 0.388	0.141; 0.190
Mass flux G [kg/m^2 s]	150 - 300	150 - 500
Heat flux q [kW/m^2]	2.5 - 40	2.5; 10; 20
Tube diameter d [mm]	6.0	
Vapor quality x	0.0 – 1.0	

7.3   Heat transfer coefficient results

The heat transfer coefficient values and the influence of all the operative parameters is shown in this section. The values of the operative parameters and their uncertainty shown in legends and titles are intended to be an average over the represented data. The experimental results will be finally compared with some correlations taken from scientific literature.

7.3.1   Effect of mass flux on heat transfer coefficient

The effect of mass flux on the top, bottom and mean heat transfer coefficient of R134a is shown in Figure 7.4 (a), (b) and (c), respectively. The inlet saturation temperature was fixed to 30 °C, the heat flux was imposed to 10 kW/m^2.and the mass velocity was varied from 152 to 299 kg/m^2 s. The expanded uncertainty of all the operative parameters and of the heat transfer coefficients are also shown. The bottom heat transfer coefficient seems not to be greatly affected by the mass velocity, suggesting that in this case the heat transfer is controlled by nucleate boiling mechanism. The mass flux instead substantially increases the heat transfer coefficient measured at the top. Greater variations are recorded for higher vapor qualities, in which the convective contribution is more accentuated. The resulting average heat transfer coefficient variation with mass velocity is displayed in Figure 7.4 (c). For the

highest mass fluxes of 218 and 299 kg/m^2 s, the mean heat transfer coefficient remains almost the same for the whole range of vapor qualities, whereas at G = 152 kg/m^2 s, a drop at a vapor quality of approximately 0.40 is recorded, suggesting the occurrence of stratification for these operative conditions.
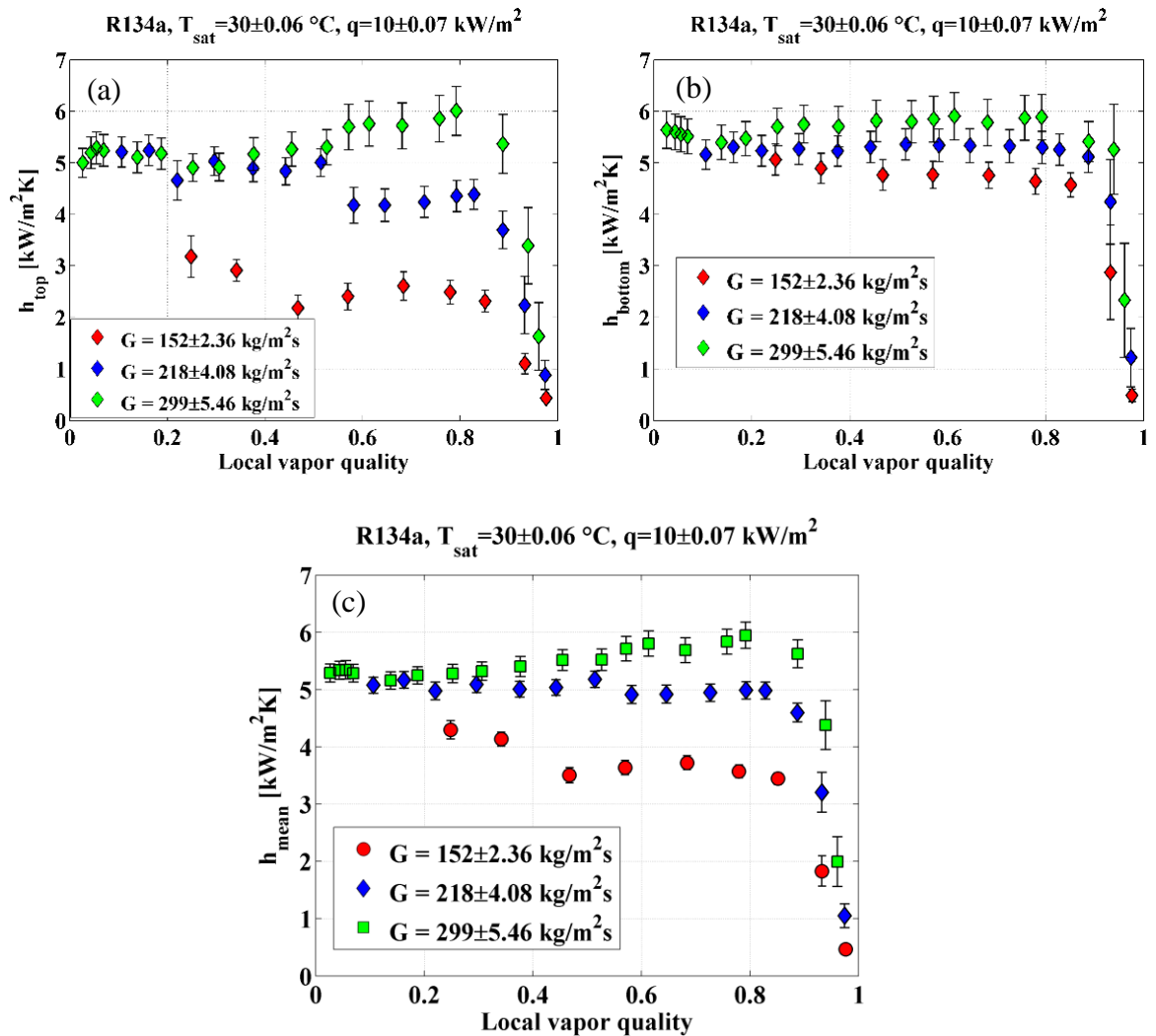
Figure 7.4 Local R134a heat transfer coefficient at different mass velocities, for a saturation temperature of 30 °C and a heat flux of 10 kW/m^2. (a) Top heat transfer coefficient. (b) Bottom heat transfer coefficient. (c) Average heat transfer coefficient over the tube perimeter.

The effect of a different mass velocity is also shown in Figure 7.5 at a higher imposed heat flux (40 kW/m^2) with propane having an average saturation temperature of 35 °C. For such a

high heat flux, the convective contribution seems not to be important, since both top and bottom heat transfer coefficients are almost the same when changing the mass flux from 150 to 296 kg/m^2 s. This assumption is also corroborated by the trends of the local heat transfer coefficients, which are not affected by the increase of vapor quality. Finally, dry-out appears quite early, at a vapor quality approximately equal to 0.75.
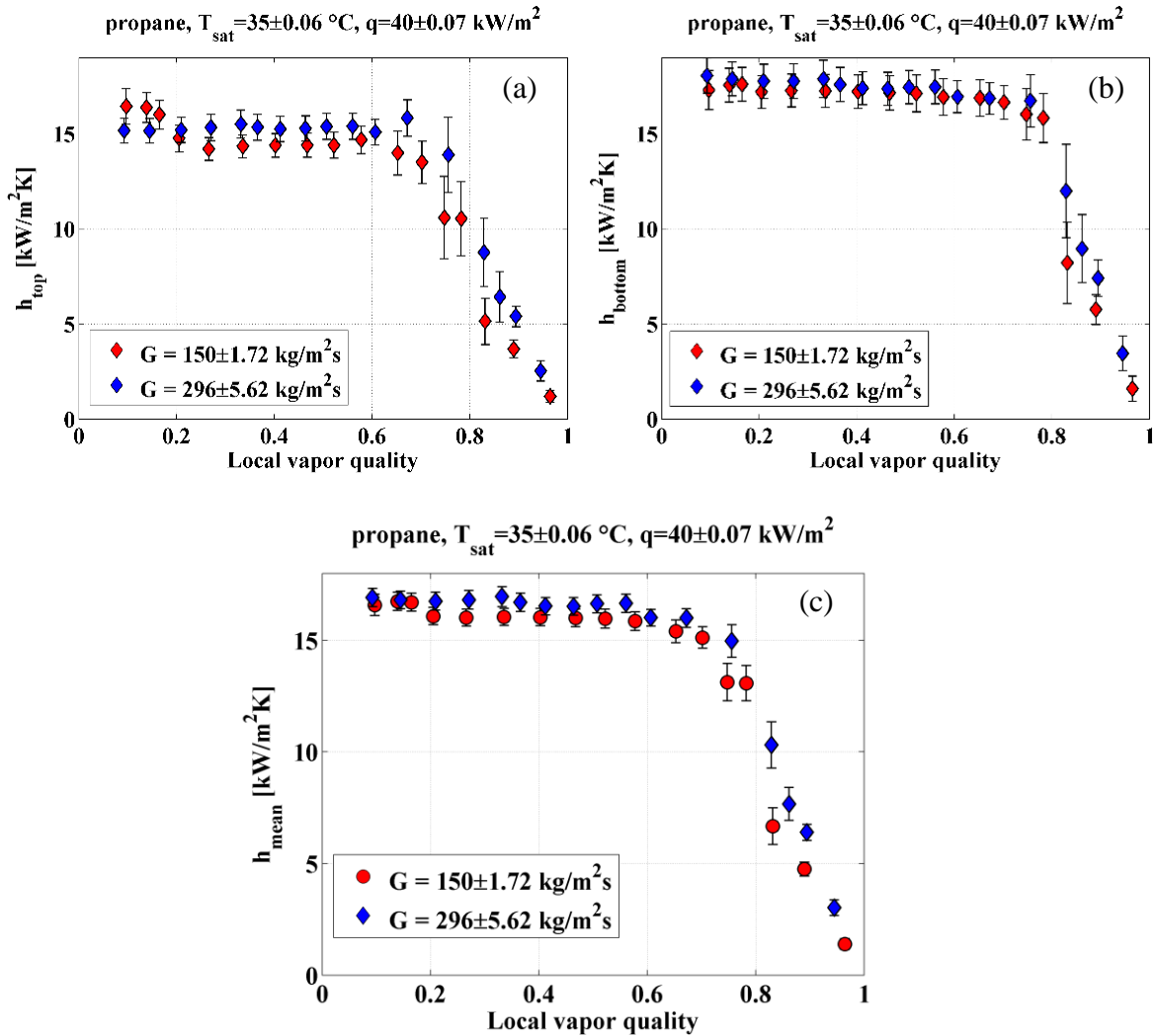
Figure 7.5 Local heat transfer coefficient for propane for different mass velocities, at a saturation temperature of 35 °C and an imposed heat flux of 40 kW/m^2. (a) Top heat transfer coefficient. (b) Bottom heat transfer coefficient. (c) Average heat transfer coefficient over the tube perimeter.

7.3.2   Effect of heat flux on heat transfer coefficient

The effect of heat flux on top, bottom and average heat transfer coefficient of R134a is shown in Figure 7.6 (a), (b) and (c), respectively. The average mass velocity of all the curves is 150 kg/m^2 s, while the inlet saturation temperature is 20 °C. Different heat fluxes of 2.5, 10 and 20 kW/m^2 were imposed. In this case, the heat transfer coefficient at the top (Figure 7.6 (a)) is not greatly influenced by the heat flux at any vapor quality, suggesting that the convective evaporation contribution is the leading heat transfer mechanism. On the contrary, the bottom heat transfer coefficient (Figure 7.6 (b)) is strongly enhanced when with increasing heat flux, indicating a significant nucleative boiling contribution. Specifically, the bottom heat transfer coefficient at a vapor quality of 0.40 passes from approximately 2 kW/m^2 K up to 6 kW/m^2 K when the heat flux is changed from 2.5 to 20 kW/m^2. Finally, the heat transfer coefficient averaged over the whole tube perimeter is displayed in Figure 7.6 (c). The importance of nucleative boiling contribution is evident for heat fluxes of 10 and 20 kW/m^2, in which the mean heat transfer coefficient presents a monotonic drop up to the dry-out condition. For the lowest heat flux of 2.5 kW/m^2, the convective contribution is somehow preserved, observable as a weak heat transfer coefficient increase in the annular flow region up to the occurrence of dry-out.
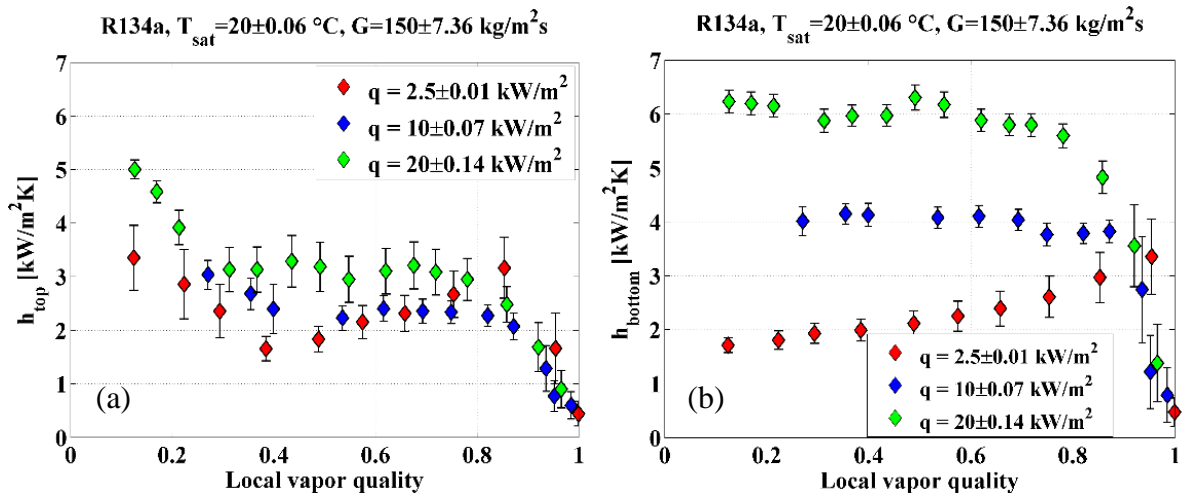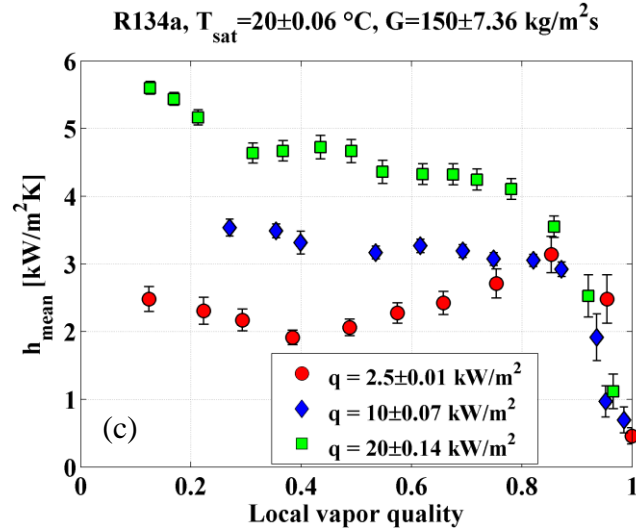
Figure 7.6 Local R134a heat transfer coefficient at different heat fluxes, for a saturation temperature of 20 °C and a mass flux of 150 kg/m² s. (a) Top heat transfer coefficient. (b) Bottom heat transfer coefficient. (c) Average heat transfer coefficient over the tube perimeter.

The effect of heat flux on the top, bottom and mean heat transfer coefficient is also shown for propane in Figure 7.7 (a), (b) and (c), respectively. The saturation temperature was fixed to 25 °C and the average mass flux for all the experiments was 150 kg/m² s. The imposed heat flux was varied from 10 to 40 kW/m². As it can be seen from Figure 7.7 (a) and (b), the bottom heat transfer coefficient is in any case at least 15% higher than that measured on the top surface of the tube. Moreover, differently from R134a, both top and bottom heat transfer coefficients are greatly affected by an increase of heat flux and for all curves there is almost no dependency from the vapor quality, suggesting that nucleate boiling is the controlling heat transfer mechanism. The heat transfer coefficient averaged over the tube perimeter is shown in Figure 7.7 (c): its values passes from approximately 6.0 kW/m² K up to 14 kW/m² K when increasing the imposed heat flux from 10 to 40 kW/m². Finally, the dry-out occurs earlier in case for higher heat fluxes, passing from a vapor quality of 0.85 at $q = 10$ kW/m² to a vapor quality of approximately 0.70 at $q = 40$ kW/m².
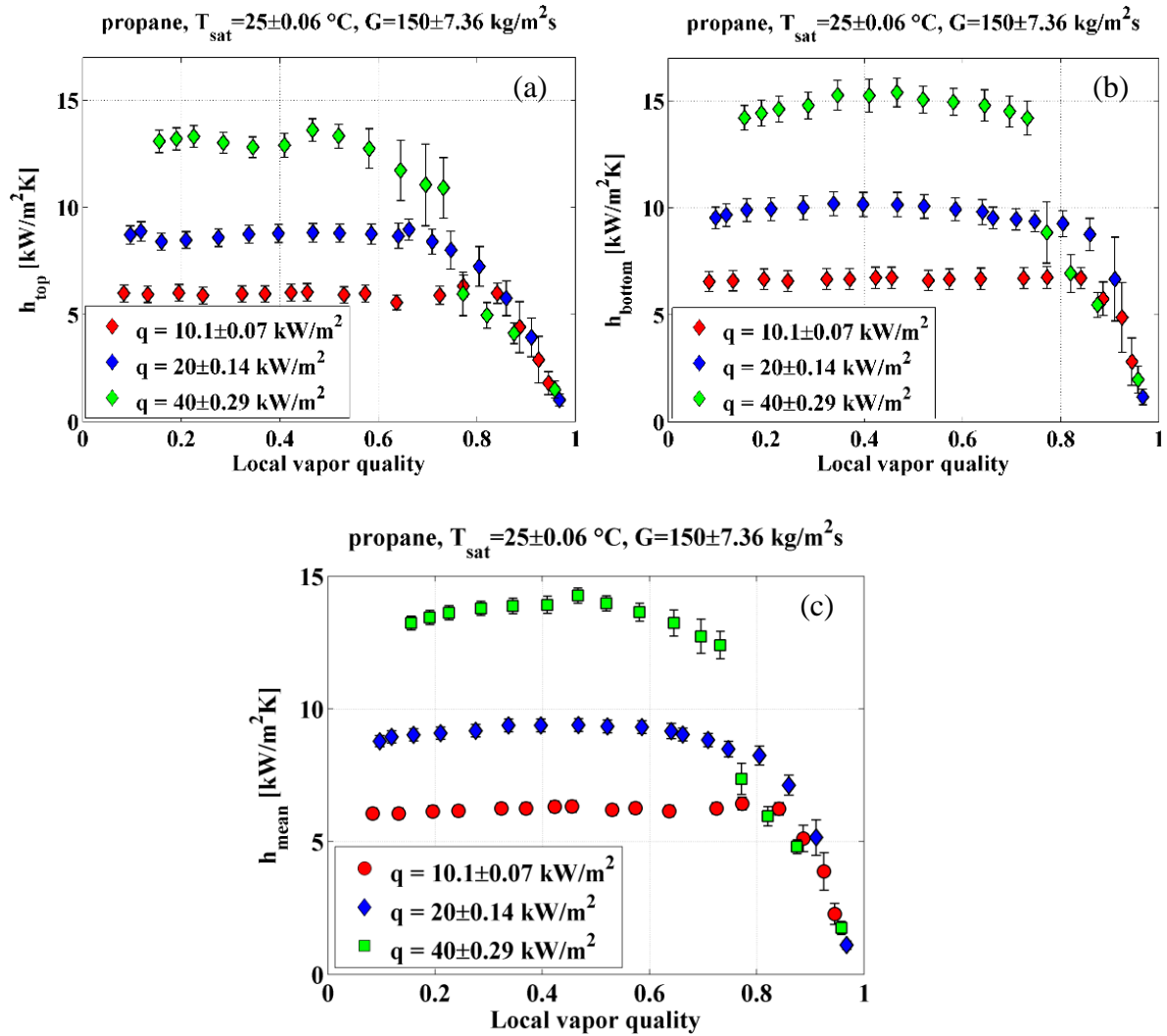
Figure 7.7 Local heat transfer coefficients for propane at different heat fluxes, for a saturation temperature of 25 °C and a mass flux of 150 kg/m² s. (a) Top heat transfer coefficient. (b) Bottom heat transfer coefficient. (c) Average heat transfer coefficient over the tube perimeter.

7.3.3   Effect of saturation temperature on heat transfer coefficient

The effect of saturation temperature on top, bottom and average heat transfer coefficient of R134a is shown in Figure 7.8 (a), (b) and (c), respectively. The average mass and heat fluxes for all curves are 150 kg/m² s and 2.5 kW/m², respectively, whereas the saturation temperature was set to 20 °C and 29.8 °C. In this case, both top and bottom heat transfer coefficient seems not to be greatly influenced by the saturation temperature. In particular, Figure 7.8 (a) and (b) show that the variations are included in the heat transfer coefficients expanded uncertainty. For both the saturation temperatures, the average heat transfer

163

coefficients present an increasing trend with vapor quality and the values are a bit higher (approximately +15%) at 30 °C. In all cases, the dry-out occurrence is anticipated when increasing the saturation temperature.
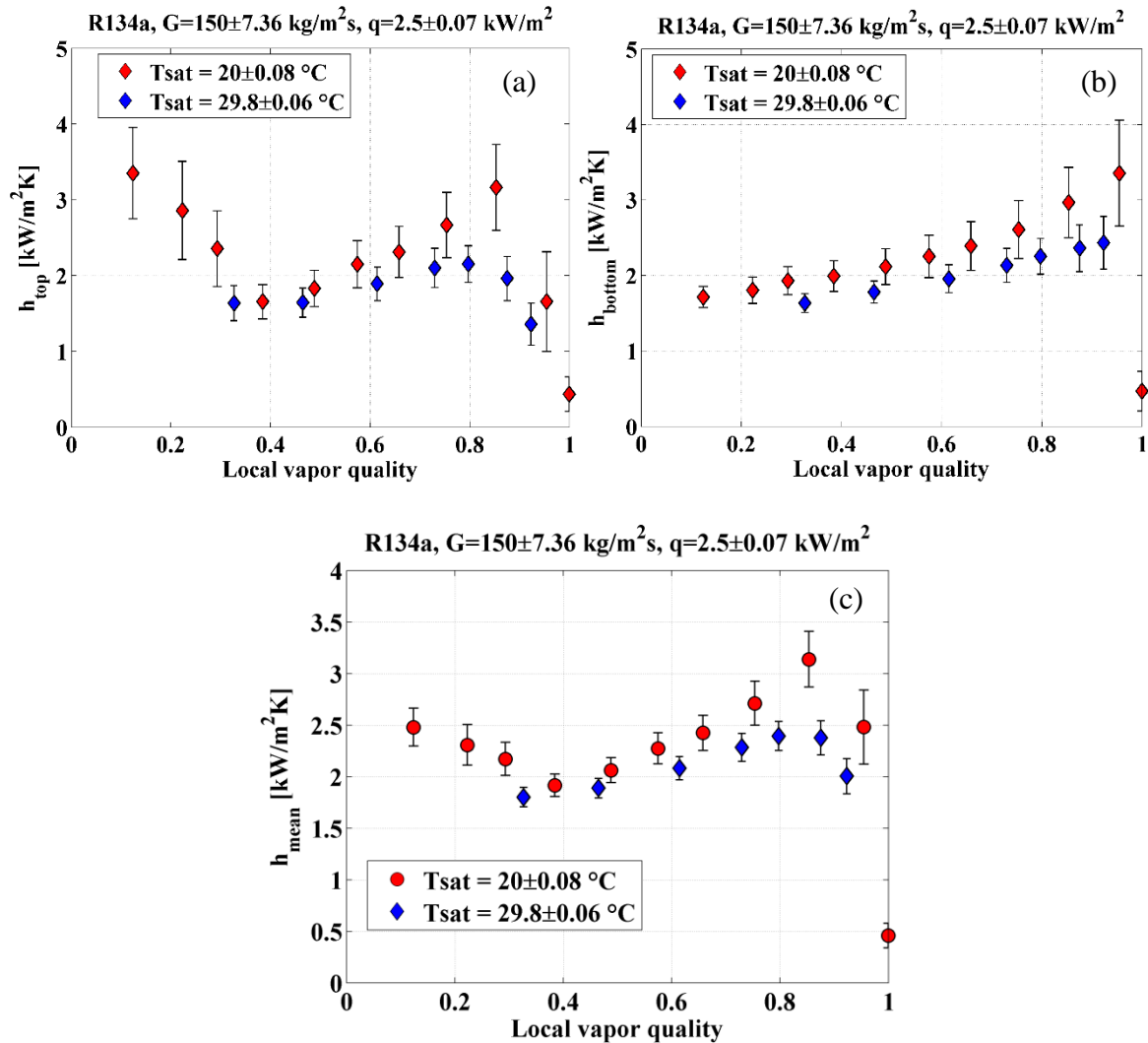
Figure 7.8 Local R134a heat transfer coefficient at different saturation temperature, for a heat flux of 2.5 kW/m^2 and a mass flux of 150 kg/m^2 s. (a) Top heat transfer coefficient. (b) Bottom heat transfer coefficient. (c) Average heat transfer coefficient over the tube perimeter.

The effect of the saturation temperature is also shown for top, bottom and average heat transfer coefficients of propane, in Figure 7.9 (a), (b) and (c), respectively. The average mass flux of all experiments was equal to 150 kg/m^2 s and the heat flux was imposed to 10 kW/m^2.

The saturation temperature was instead varied from 25 to 35 °C. Differently from R134a, the heat transfer coefficient constant trend with vapor quality suggests the dominance of nucleate boiling contribution. Both top and bottom heat transfer coefficients are affected by an increase of the saturation temperature and this behavior reflects on the average heat transfer coefficient which is shown in Figure 7.9 (c), passing from 6 kW/m^2 K up to approximately 7.5 kW/m^2 K. The vapor quality at the occurrence of dry-out, instead, is not greatly affected by saturation temperature and it is approximately equal to 0.85 for these operative conditions.
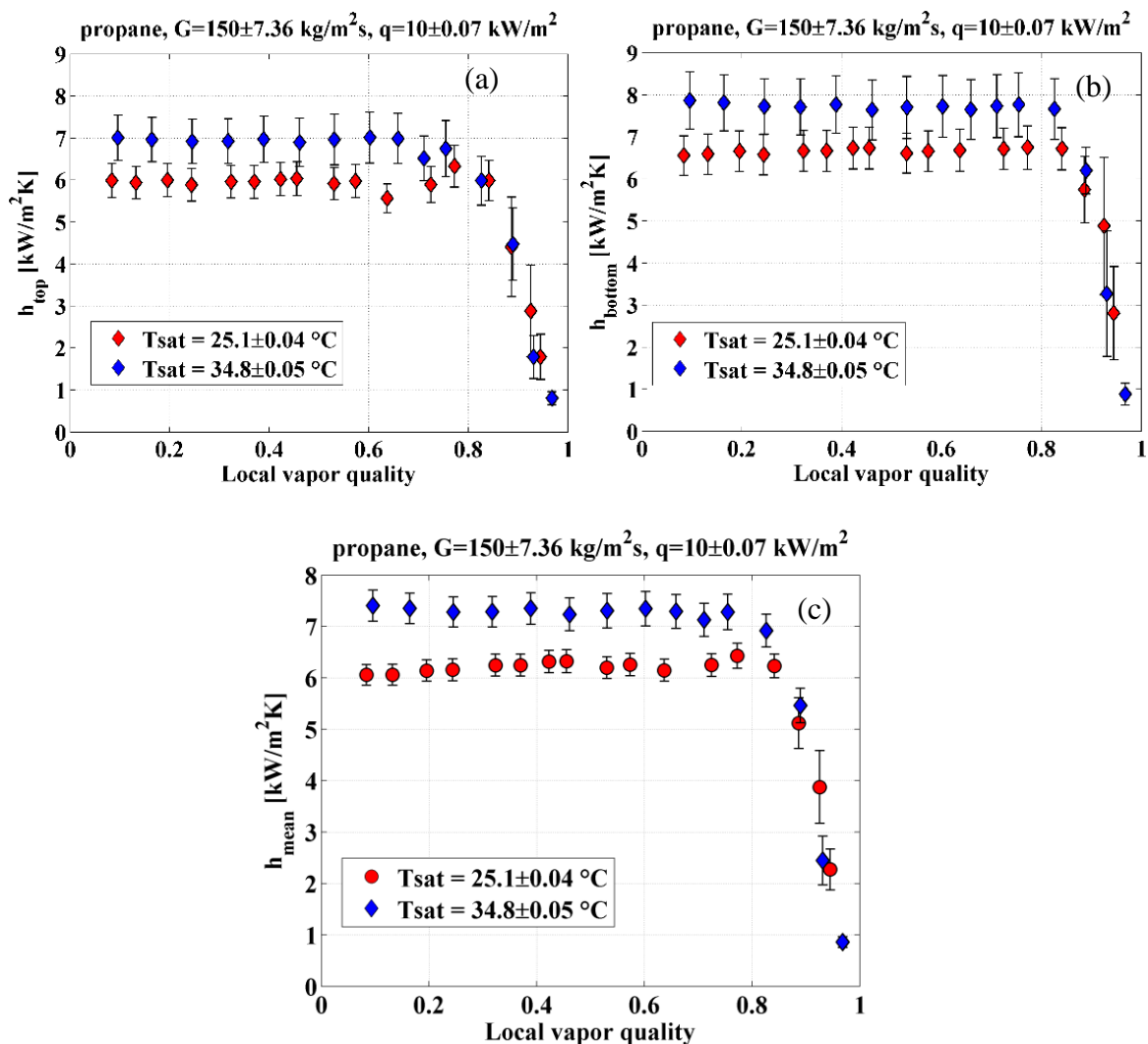
Figure 7.9 Local heat transfer coefficients of propane at different saturation temperature, for a heat flux of 10 kW/m^2 and a mass flux of 150 kg/m^2 s. (a) Top heat transfer coefficient. (b) Bottom heat transfer coefficient. (c) Average heat transfer coefficient over the tube perimeter.

The effect of saturation temperature can be also seen by using the reduced pressure, including therefore both fluids studied. Figure 7.10 shows the mean heat transfer coefficients obtained at an average mass velocity of 150 kg/m^2 s, an imposed heat flux of 20 kW/m^2 and at different reduced pressures. The lowest values of 0.141 and 0.190 represents data of R134a (at 20 and 30 °C saturation temperature) and the last two reduced pressures of 0.292 and 0.388 are instead related to propane (at 25 and 35 °C saturation temperature). All curves display a nucleate boiling dominance, with the vapor quality having almost a negligible effect on the heat transfer coefficient. In these conditions, the reduced pressure has a significant importance in case of R134a, whereas smaller variations of the heat transfer coefficient are found in case of propane. The vapor quality at the occurrence of dry-out goes from 0.75 to 0.90 and it seems to be lower with increasing reduced pressure.
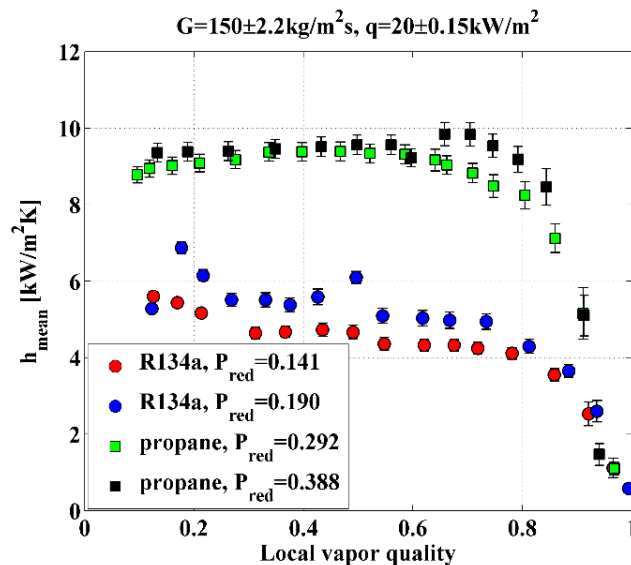
Figure 7.10 Local heat transfer coefficients averaged over the tube perimeter at different reduced pressures, for a mass velocity of 150 kg/m^2 s and a heat flux of 20 kW/m^2.

7.3.4   *Effect of the working fluid on heat transfer coefficient*

Finally, Figure 7.11 (a), (b) and (c) show the top, bottom and average heat transfer coefficients, respectively, obtained at the same operative conditions in term of mass flux (299

kg/m^2 s), heat flux (10 kW/m^2) and saturation temperature (30 °C). The top heat transfer coefficient, in both cases, carries a convective boiling contribution, since the effect of vapor quality is not negligible. This is less highlighted for the bottom heat transfer coefficient, in which only propane shows a weak increase of the heat transfer performance with ongoing evaporation. Both top and bottom heat transfer coefficient of propane are higher than the corresponding values obtained for refrigerant R134a, and this reflects to the average heat transfer coefficients (see Figure 7.11 (c)), in which the difference may reach 30% for high vapor qualities. This behavior can be probably explained by looking at the effect of the reduced pressure shown in the previous subsection. As a matter of fact, propane has a higher reduced pressure when working at the same saturation temperature of 30 °C (0.254 against 0.190 of R134a).

T$_{sat}$**=30±0.06°C, G=300±6.4kg/m²s, q=10±0.06 kW/m²**
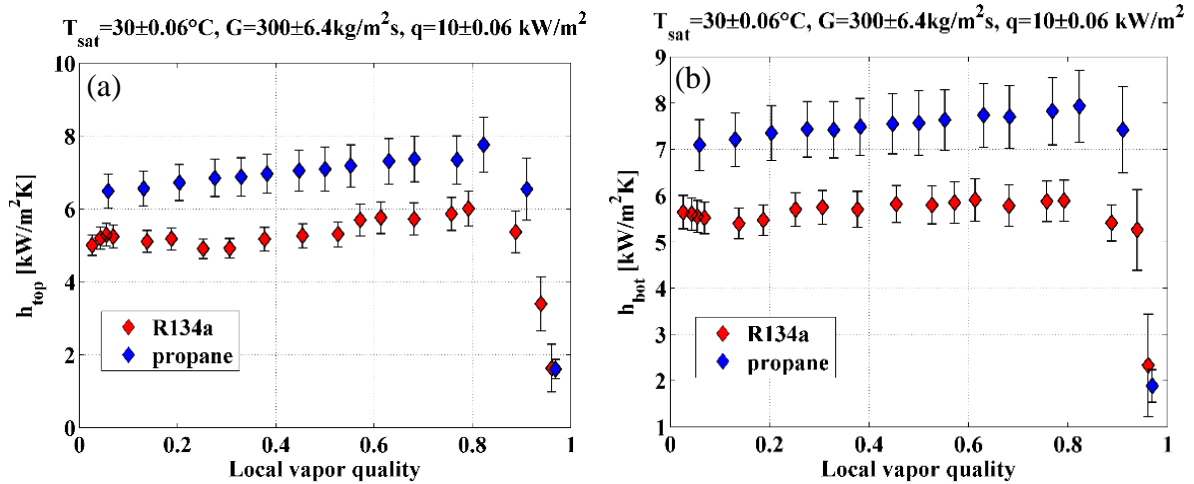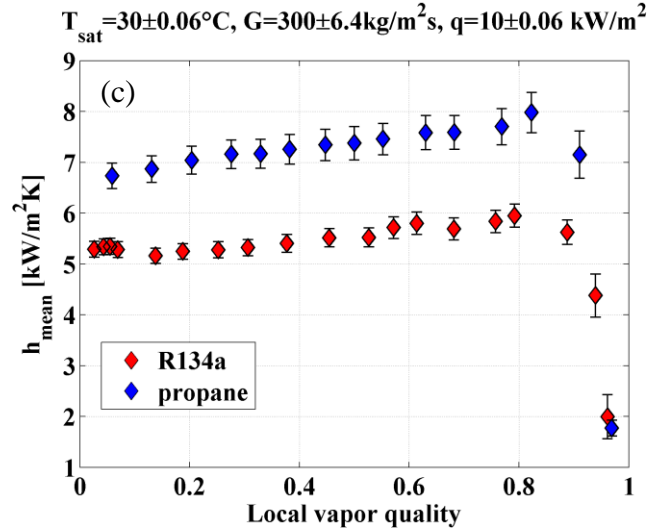
Figure 7.11 Local heat transfer coefficients for R134a and propane, for a heat flux of 10 kW/m², a mass flux of 299 kg/m² s and a saturation temperature of 30 °C. (a) Top heat transfer coefficient. (b) Bottom heat transfer coefficient. (c) Average heat transfer coefficient over the tube perimeter.

7.3.5   *Comparisons with correlations – Heat transfer coefficient*

The experimental data are compared in this section with some of the two-phase heat transfer coefficient correlations exposed in the literature review (see section 3.2.2). Particularly, the correlations of Chen [68], Gungor and Winterton [72], Del Col [60], Bertsch et al. [76] and Wojtan et al. [86] have been used in this thesis.

Figure 7.12 shows the comparison performed with the whole database with the correlations of Bertsch et al. [76] and Wojtan et al. [86], which better fit the experimental data. The prediction method of Bertsch et al. [76] provides a Mean Absolute Error of 55% and a Mean Relative Error of 34%, whereas the correlation of Wojtan et al. [86] provides a lower MAE of 27% and a negative MRE of -19%. For a closer look, Figure 7.13 shows the same comparison by separating three different vapor quality ranges ($x<0.3$, $0.3<x<0.6$, and $x>0.6$). While the correlation of Bertsch et al. [76] works reasonably well at low vapor quality, it strongly overestimates the experimental data approaching the dry-out condition. The prediction method of Wojtan et al. [86], instead, is more balanced for all the ranges of vapor qualities, exposing approximately the same deviations. As a matter of fact, the authors payed particular attention to the identification of the dry-out and mist flow patterns, providing the corresponding heat transfer coefficient equations.

168
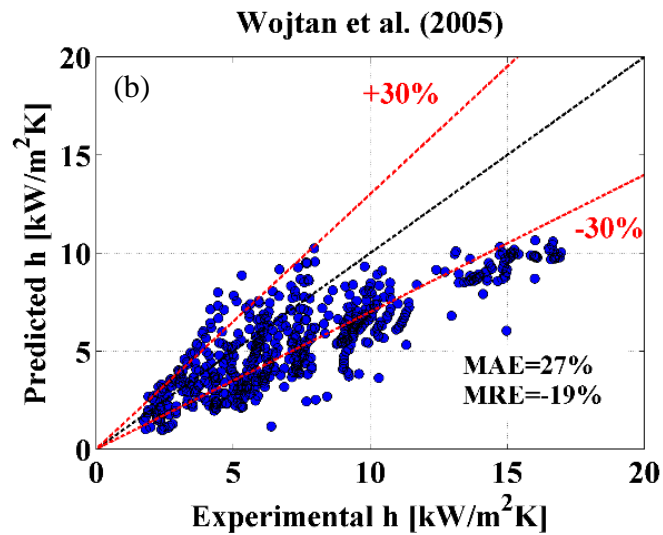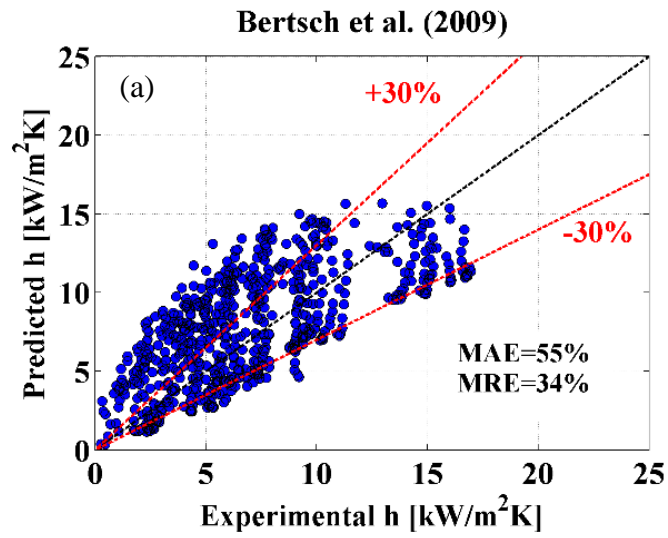
Figure 7.12 Experimental versus predicted heat transfer coefficient for the whole database. Prediction method of (a) Bertsch et al. [76] and (b) Wojtan et al. [86].
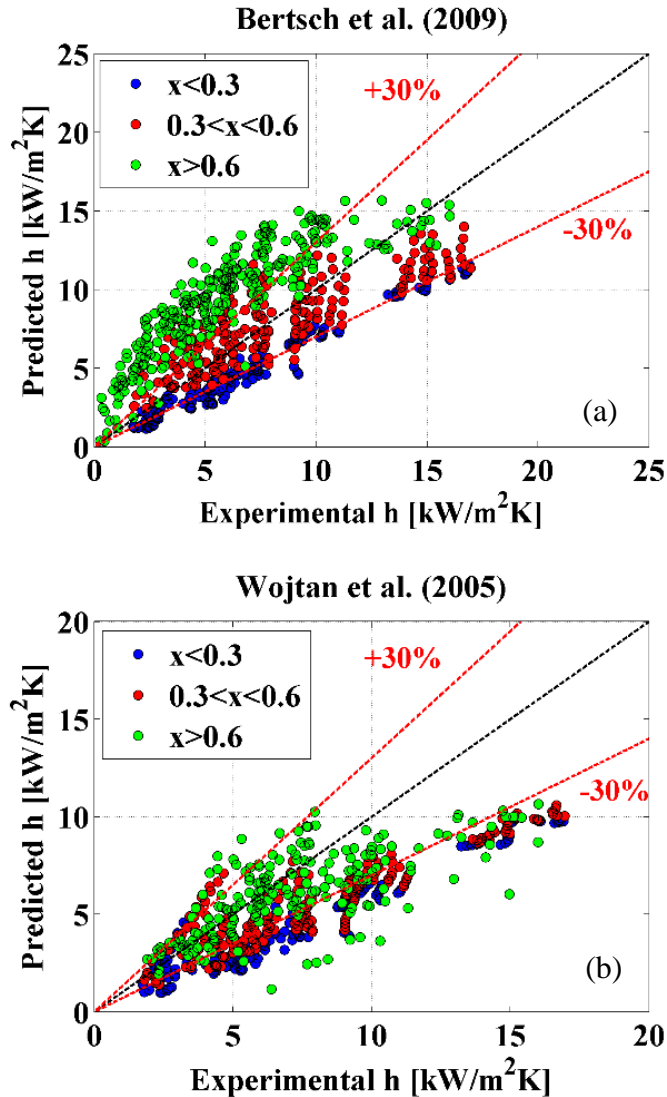
Figure 7.13 Experimental versus predicted heat transfer coefficients. Comparison performed by separating three different vapor quality ranges. Prediction method of (a) Bertsch et al. [76] and (b) Wojtan et al. [86].

The assessment summary is available in Table 7.2. Wojtan et al.[86] better fits the entire database and also the experimental points close to the occurrence of dry-out ($MAE_{x>0.6}$ = 51%), exposing also the lowest standard deviation of 25%. The best relative agreement is found with the modification of the Gungor-Winterton [72] prediction method of Del Col [60] (MRE = 3%). This correlation works also best at low vapor qualities ($MAE_{x<0.6}$ = 20%) and 69% of the experimental data are predicted within a range of ±30%.

Table 7.2 Summary of the assessment performed for the chosen two-phase heat transfer prediction methods. The parameter δ refers to the percentage of data points falling in an error range of ±30%. The MAE has been evaluated for the whole database and also separately for the experimental points with vapor qualities lower and higher than 0.6. The best statistical results related to each parameter are highlighted in bold.

Authors	MAE			MRE	SD	δ
	x < 0.6	x > 0.6	whole			
Wojtan et al. (2005)	34	**51**	**27**	*-19*	**25**	*38*
Bertsch et al. (2009)	29	90	55	34	79	42
Gungor-Winterton (1986)	28	*55*	39	-14	62	47
Del Col (2010)	**20**	*56*	35	**3**	74	**69**
Chen (1966)	41	181	101	40	415	38

7.4   Pressure drop results

The influence of all the operative parameters on the adiabatic frictional pressure gradient is shown in this section. The values of the operative parameters and their uncertainty shown in legends and titles are intended to be an average over the represented data. The experimental results will be finally compared with some correlations taken from scientific literature.

7.4.1   Effect of mass velocity and saturation temperature on frictional pressure gradient

The influence of the mass velocity on the frictional pressure drop of R134 and propane is shown in Figure 7.14 (a) and (b), respectively. For R134a, the average saturation temperature is 30 °C and the mass flux was instead set to 152, 218 and 299 kg/m^2 s. In case of propane, the average saturation temperature is 25 °C and the mass flux was fixed to 149 and 298 kg/m^2 s. The expanded uncertainties of the experimental points are also provided: larger error bands are referred to points close to the occurrence of dry-out, in which the fluctuations of the measured pressure drop was significant. The general trend is a pressure drop rise with vapor quality due to the higher velocity, until a peak is reached. Then, a further increase of vapor quality leads to a partial decrease of the pressure drop. As regards the effect of mass velocity, it leads to a considerable increase of the frictional pressure gradient. This was

expected due to the higher flow velocity and inertia. As explained in the literature review (see section 3.3), these trends are corroborated by all the studies presented.

One point worth noting is the slight change of trend with vapor quality occurring in some operative conditions. As it can be seen from Figure 7.14 (a), for mass velocities of 218 and 299 kg/m^2 s, the pressure drop has a sudden decrease at a vapor quality of approximately 0.55, before going on with the usual trend. The same phenomenon was also observed in case of propane (see Figure 7.14 (b)) at different vapor qualities. As suggested by Revellin and Thome [110], this behavior may correspond to a change in the flow patterns with the transition from wavy annular to smooth annular.
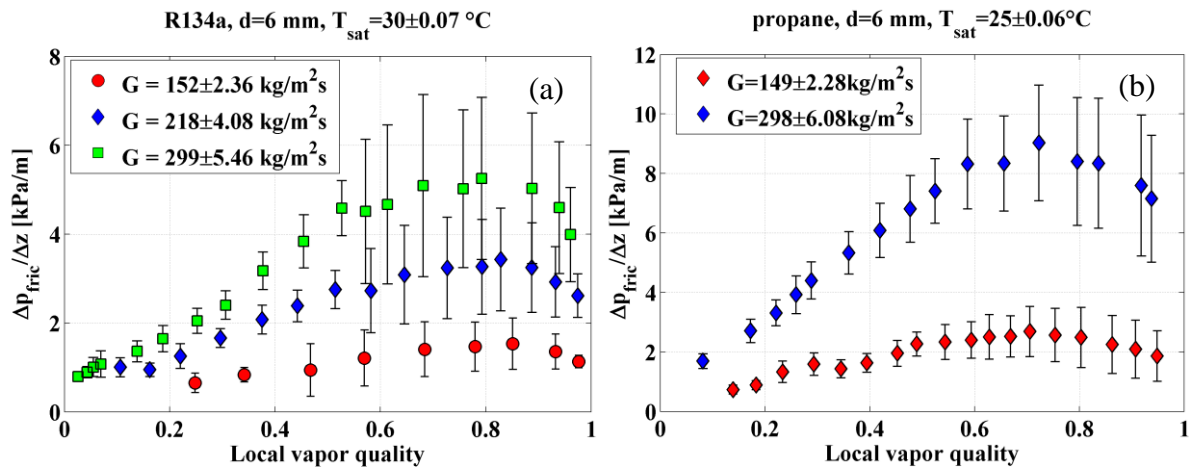
Figure 7.14 Frictional pressure gradient of R134a (a) and propane (b) as a function of the local vapor quality. Effect of mass velocity, with a saturation temperature of: (a) 30 °C and (b) 25 °C.

The effect of the saturation temperature on frictional pressure drop of R134a and propane is instead shown in Figure 7.15 (a) and (b), respectively, in which the R134a mass velocity was fixed to 300 kg/m^2 s and the propane mass flux was 150 kg/m^2 s. When increasing the reduced pressure, the vapor density increases leading to an inferior vapor phase velocity. As a direct consequence, the frictional pressure gradient is reduced. This effect is however not so pointed out in Figure 7.15, since the variation in the reduced pressure is weak (passing from 0.14 to 0.19).
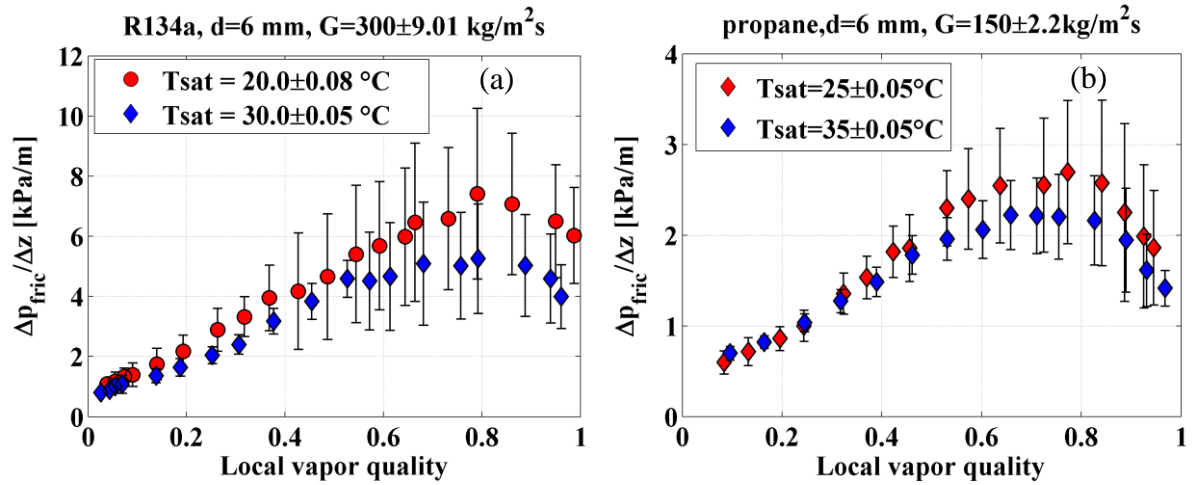
Figure 7.15 Frictional pressure gradient of R134a (a) and propane (b) as a function of the local vapor quality. Effect of saturation temperature, with a mass velocity of: (a) 300 kg/m^2 s and (b) 150 kg/m^2 s.

7.4.2 *Effect of working fluid on frictional pressure gradient*

The frictional pressure gradient for R134a and propane at the same operative conditions is shown in Figure 7.16 including the expanded uncertainties. The average mass flux for all the experimental points is 299 kg/m^2 s and the saturation temperature was fixed to 30 °C. As it can be seen, the measured pressure drop was found to be higher in case of propane, even if, at the same saturation temperature, it exposes a higher reduced pressure (0.254 against 0.190 of R134a). As a matter of fact, at a saturation temperature of 30 °C, propane has a liquid density of 484 kg/m^3, whereas that of R134a is significantly higher (1188 kg/m^3). This difference leads to much higher velocities during the evaporation inside the tube in case of propane and therefore to higher frictional pressure drops.
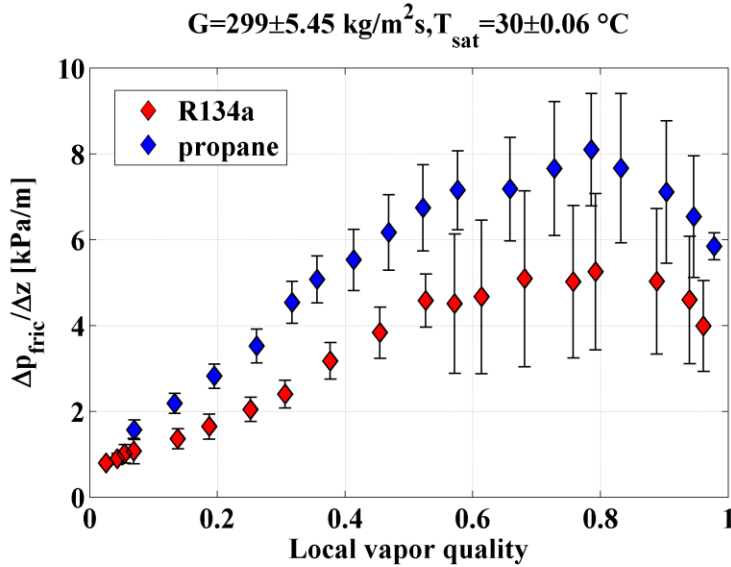
Figure 7.16 Frictional pressure gradient as a function of the local vapor quality, for a mass flux of 299 kg/m² s and a saturation temperature of 30 °C. Effect of the working fluid.

7.4.3   Comparisons with correlations – Pressure drop

The experimental data are compared in this section with some of the two-phase frictional pressure drop correlations exposed in the literature review (see section 3.3.2). Particularly, the separated flow methods of Müller-Steinhagen and Heck [99], Friedel [102] and Zhang and Webb [95] have been used in this thesis.

Figure 7.17 shows the comparison results for the abovementioned correlations. All of them work reasonably well for the entire experimental database. The correlation of Müller-Steinhagen and Heck [99] exposes the lowest standard deviation of 19%, whereas the prediction method of Friedel [102] is the best in terms of mean absolute and relative errors, 17% and -7%, respectively, and manages to capture up to 87% of the experimental data within an error band of ±30%. The correlation of Zhang and Webb [95] is situated in the middle, tending to slightly underestimate the experimental trend, with MAE = 22%, MRE = -15%, SD = 21% and 70% of the data falling into a ±30% error band.
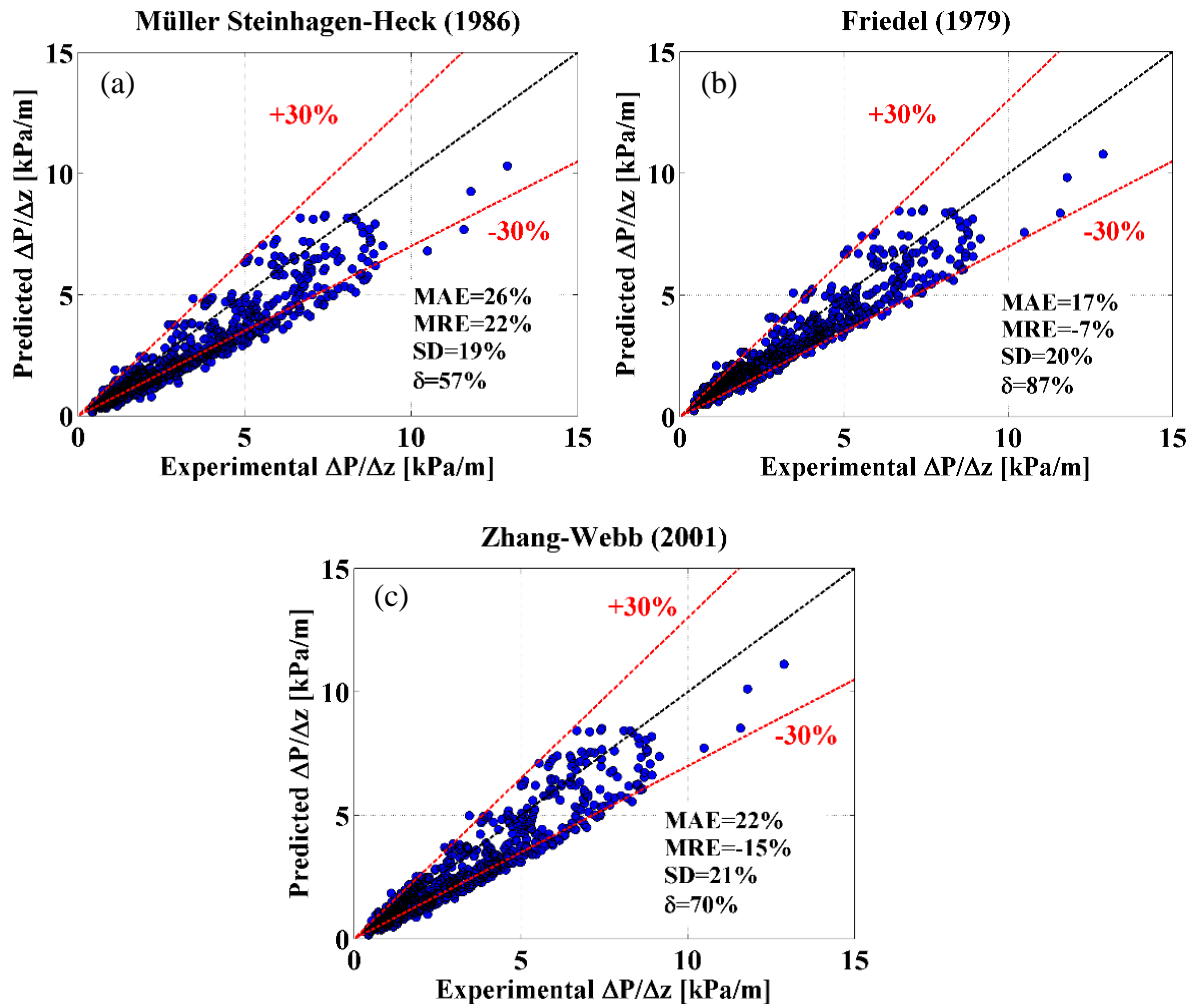
Figure 7.17 Experimental versus predicted frictional pressure drop data. Correlations of:(a) Müller-Steinhagen and Heck [99], (b) Friedel [102] and (c) Zhang and Webb [95].

8 Conclusions

Saturated CHF in an aluminum multi-minichannel heat sink and flow boiling heat transfer and two-phase pressure drop in a single horizontal channel of 6.0 mm internal diameter were studied in this thesis. The main outcomes of this study are summarized here.

8.1 Summary of CHF experimental campaign

A comprehensive literature review on saturated CHF in single channels, minichannels and multi-minichannel heat sink geometries has been performed, showing that:

- The operative definition of critical heat flux during the experiment is not universal: different authors use different criteria to detect the onset of the thermal crisis during their tests.
- The general trends show that CHF is enhanced with increasing mass flux and decreasing the heated length-on-equivalent diameter ratio L_h/D. The effect of saturation temperature is not univocal for all the studies presented, but most of the researchers have detected a CHF decrease when increasing the system pressure.
- Some correlations for saturated CHF are available in literature applicable for different geometries and working conditions. Most of them take into account only the effects of mass velocity, saturation temperature and L_h/D ratio, whereas other prediction methods conceive the influence of the inlet vapor quality and/or the inlet sub-cooling.

A new operative definition of critical heat flux has been provided in this thesis, by considering both the boiling curve minimum slope threshold and the maximum wall superheat that might be tolerated during realistic cooling applications.

A multi-purpose test facility has been set-up for the CHF, using an aluminum multi-minichannel heat sink with rectangular minichannels as test section. No flow stabilizers and orifice inserts were used for this campaign, preserving a design that may easily constructed in the industrial sector. However, as a preliminary analysis, an aluminum slit-orifice was placed in the inlet manifold to check for possible instabilities before the real CHF tests. The boiling

curves behavior, as well as the fluctuations of the mass flow rate and inlet pressure were not significantly affected by the use of the slit orifice insert.

Saturated CHF tests (288 in total) were then obtained by using R134a, R1234yf, R1234ze, R1233zd and R32 as working fluids, with three different L_h/D ratios of 19, 27 and 44, mass fluxes ranging from 145 to 3000 kg/m^2 s and saturation temperatures from 24.7 to 75.5 °C. The experimental results showed that:

- The mass velocity has not a great influence on the first part of the boiling curve, suggesting that the average heat transfer coefficient inside the multi-minichannel heat sink is not affected by a change in the mass flux. On the other hand, CHF increases with mass velocity, but its effect becomes less important for $G > 500$ kg/m^2 s.
- The saturation temperature shifts the first part of the boiling curve towards left, suggesting that the average heat transfer coefficient inside the multi-minichannel heat sink is enhanced with system pressure. In most cases, saturation temperature has instead a weak effect on the experimental CHF, that may be reduced up to a 20% when passing from 25 to 75 °C. However, when the mass flux is higher than 500 kg/m^2 s, instead, the effect of the saturation temperature changes, leading to an enhancement of CHF values, which is higher at higher mass velocities. For refrigerant R1233zd at a mass flux of 2002 kg/m^2 s, for instance, CHF increases of 19% passing from 55 to 65 °C.
- R32 displays the highest CHF experimental values, due to its relatively high latent heat, whereas R1234yf and R1234ze exhibits the lowest CHF values, probably due to their low surface tension and low latent heat at disposal.
- A general reduction of CHF is recorded when increasing the L_h/D ratio, accentuated for low mass velocities. However, in case of higher mass velocities ($G > 500$ kg/m^2 s) the experimental trend is reversed. In case of R134a, for instance, for a mass velocity of 1500 kg/m^2 s, the CHF is higher when increasing L_h/D from 27 to 44, passing from 122 to 175 W/cm^2.

The assessment of existing correlations in open literature has shown that the experimental data are in good agreement with prediction methods that use the Weber number with a non-negligible negative exponent. In this way, the non-linear effect of mass velocity

experimentally observed for $G > 500$ kg/m^2 s can be caught. Particularly, Wojtan et al. [23] correlation is able to fit quite well the data obtained at high mass fluxes, with a calculated *MAE* of 30.8%, whereas the correlation that best fit the experiments performed at low mass velocity is that of Callizo [51], with a calculated *MAE* of 11.1%.

8.2 Summary of the flow boiling experimental campaign

A state-of-the-art review on flow boiling heat transfer and pressure drop for conventional tubes and minichannels has shown that:

- There is not a universal trend of the heat transfer coefficient for all fluids, geometries and operative conditions investigated. Generally, in cases where convective boiling is the dominant mechanism, the heat transfer coefficient is affected by a change of mass velocity and vapor quality, whereas in case the nucleate boiling contribution controls the phenomenon, heat flux and saturation temperature are the most influencing parameters.
- Adiabatic frictional pressure drops increase with increasing mass velocities and also with vapor quality up to a peak value which may occur at the inception of dry-out or mist flow regime, or even before the dry-out occurrence. An increase of saturation temperature, instead, leads to lower values of the measured pressure drop.

The same test facility used for the CHF experiments has been modified by using different sensors and transducers and by changing the test section to a single horizontal stainless steel circular tube, directly heated with Joule effect and with four thermocouples for the measurement of the heat transfer coefficient on the top, bottom, left and right side of the tube surface.

A dedicated *in-situ* calibration of the differential pressure transducer and of the thermocouples for the wall temperature measurement was performed. In this way, the systematic uncertainty was kept reasonably low (± 0.06 kPa and ± 0.10 °C for the differential pressure transducer and the thermocouples, respectively). To improve the quality of the experimental database, the data could be recorded only when the expanded uncertainty calculated in real time (including therefore the measurement accuracy and the fluctuations

observed during experiments) of each parameter of interest was inferior to a chosen threshold.

Different flow boiling tests (524 in total) were performed with refrigerants R134a and propane (R290) and compared to some available prediction methods, by using mass velocities from 150 to 500 kg/m^2 s, saturation temperature from 20 to 35 °C and heat fluxes from 2.5 to 40 kW/m^2. The experimental results showed that:

- In case of R134a at low heat flux of 10 kW/m^2, the bottom heat transfer coefficient seems not to be greatly affected by the mass velocity, suggesting that in this case the heat transfer is controlled by nucleate boiling mechanism. The mass flux instead substantially increases the heat transfer coefficient measured at the top. Greater variations are recorded for higher vapor qualities, in which the convective contribution is more accentuated. For propane at an imposed heat flux of 40 kW/m^2, the mass velocity has substantially a negligible influence on both top and bottom heat transfer coefficient, suggesting that in this case nucleate boiling is the controlling heat transfer mechanism.

- The heat flux has a strong influence on the average heat transfer coefficient, at least in case of low mass velocities. Specifically, for R134a, the heat flux effect is significant only at the bottom, whereas both top and bottom heat transfer coefficients of propane are greatly affected by an increase of the imposed heat flux.

- Saturation temperature has a significant positive effect on heat transfer coefficient, especially in case of propane. A further analysis has shown that, regardless the fluid used, the increase of the reduced pressure leads to higher heat transfer coefficients.

- Most of the correlations chosen to fit the experimental data fail to capture heat transfer coefficients taken at high vapor qualities (x>0.6). Only the prediction method of Wojtan et al. [86], explicitly developed to identify the dry-out and mist flow patterns, exposes a Mean Absolute Error inferior to 55%.

- Pressure drop results confirm the trends shown in literature: the frictional pressure gradient is higher for higher mass velocities and has an increasing trend with vapor quality up to a peak value close to the dry-out occurrence. By increasing saturation

temperature (i.e. the reduced pressure) for both refrigerants, instead, the pressure drop decreases accordingly.

- At the same operative conditions in terms of mass flux and saturation temperature, measured pressure drop of propane are higher than those of R134a, as a direct consequence of the lower propane liquid density, which determines a higher velocity of the flow.

- Good agreements with the experimental pressure drop data are found with the separated flow methods of Müller-Steinhagen and Heck [99], Friedel [102] and Zhang and Webb [95]. The best results are obtained with the prediction method of Friedel [102], which exposes Mean Absolute and Relative Errors of 17% and -7%, respectively.

Nomenclature

Roman

$\dot{Q}$	heat power	[W]
U_x	expanded uncertainty of x	[same of x]
X_{tt}^2	Martinelli parameter	[-]
$\frac{dP}{dz}$	pressure gradient	[Pa/m]
$\dot{m}$	mass flow rate	[kg/s]
s_x	standard deviation of x	[same of x]
u_x	combined uncertainty of x	[same of x]
w_x	type-B uncertainty of x	[same of x]
A	cross section	[m^2]
c	specific heat capacity	[J/kg K]
D	(equivalent) diameter	[m]
d	diameter	[m]
d_h	hydraulic diameter	[m]
E	enhancement factor	[-]
ER$_x$	error of x	[same of x]
f	friction factor	[-]
G	mass flux	[kg/m^2 s]
g	acceleration of gravity	[m/s^2]
h	heat transfer coefficient	[W/m^2 K]
H	height	[m]
i	specific enthalpy	[J/kg]
I	current	[A]
L	length	[m]
M	molecular mass	[kg/kmol]
N	number of channels (CHF experiments)	[-]
n	number of samples	[-]
P	pressure	[Pa]
q	heat flux	[W/m^2]
S	suppression factor	[-]
s	Distance RTD-wall (CHF experiments)	[m]

183

T	temperature	[K]
u	velocity	[m/s]
V	voltage	[V]
W	width	[m]
x	vapor quality	[-]
z	coverage factor	[-]

Greek

Δ	variation	
Φ	two-phase multiplier	[-]
α	void fraction	[-]
δ	liquid film thickness / percentage of data points falling into a ±30% error band	[m] / %
η	fin efficiency	[-]
θ	flow angle	[rad]
λ	thermal conductivity	[W/m K]
μ	viscosity	[Pa s]
ρ	density	[kg/m^3]
σ	surface tension	[N/m]

Subscripts

A	related to the A-type
acc	acceleration
amb	ambient
ave, mean	averaged
b	base
B	related to the B-type
bot	related to the bottom side
C	measurement point for the flow boiling experiments
cb	convective boiling
ch	channel
cr	critical
D	related to the diameter
dry	dry

eff	effective
eq	equivalent
f	fluid
fin	fin
fr	friction
grav	gravitational
h	heated
in	inlet
L	liquid/related to a length
left	related to the left side
lim	limit, threshold
LO	liquid only
loss	loss
LV	liquid-to-vapor
max	maximum
o	outer
out	outlet
pb	pool boiling
preh	preheater
red	reduced
right	related to the right side
RTD	related to the RTD measurement
sat	saturation
sp	single-phase
sub	sub-cooling
th	related to the thermocouple measurement
top	related to the top side
tp	two-phase
V	vapor
VO	vapor only
w, wall	related to wall
wet	wet

Abbreviations

CHF	critical heat flux
DNB	departure from nucleate

	boiling
GWP	global warming potential
HTC	heat transfer coefficient
MAE	mean absolute error
MRE	mean relative error
RSS	root sum square
RTD	resistance temperature detector
SD	standard deviation

Dimensionless numbers

Bd	Bond
Bo	Boiling
Co	Confinement
Fr	Froude
Nu	Nusselt
Pr	Prandtl
Re	Reynolds
We	Weber

List of Figures

List of Tables

Bibliography

[1] United States Semiconductor Industry Association (SIA), European Semiconductor Industry Association (ESIA), The Japan Electronics and Information Technology Industries Association (JEITA). Int. Tech. Roadmap Semic. (2009) http://www.itrs.net/Links.

[2] I. Mudawar, Assessment of high-heat-flux thermal management schemes, IEEE Trans. Compon. Packag. Techn. 24 (2001) 122-141.

[3] A. Royne, C.J. Dey, D.R. Mills, Cooling of photovoltaic cells under concentrated illumination: a critical review, Sol. Energy Mater. Sol. Cells 86 (2005)-451-483.

[4] B. Palm, Heat transfer in microchannels, Microscale Thermophys. Eng. 5 (2001) 155-175.

[5] Regulation (EU) No 517/2014 of the European Parliament and the Council of 16 April 2014 fluorinated greenhouse gases and repealing Regulation (EC) No 842/2006. Off. J. Union.

[6] D. Del Col, M. Bortolato, S. Bortolin, Comprehensive experimental investigation of two-phase heat transfer and pressure drop with propane in a minichannel, Int. J. Refrigeration 47 (2014) 66-84.

[7] R.W. Lockart, R.C. Martinelli, Proposed correlation of data for isothermal two-phase, two-component flow in pipes. Chemical Engineering Progress 45 (1949) 39-48.

[8] Y. Taitel, A. Dukler, A model for predicting flow regime transitions in horizontals and near horizontal gas-liquid flow. AIChE Journal 22 (1976) 47-55.

[9] S. Nukiyama, The maximum and minimum values of heat Q transmitted from metal to boiling water under atmospheric pressure. J. Jpn. Soc. Mech. Eng. 37 (1934) 367–374.

[10] S.G. Kandlikar, J.N. Chung, Multiphase Flow Handbook. CRC press. Taylor and

Francis Group Boiling and Condensation, 2006.

[11] J.G. Collier, J.R. Thome, Convective boiling and condensation, 3rd Edition. Oxford Science Publications.

[12] T.D. Bui, V.K. Dhir, Transition boiling heat transfer on a vertical surface. J. Heat Transfer 107 (1985) 756-763.

[13] Y.Y. Hsu, R.W. Graham, A visual study of two-phase flow in a vertical tube with heat addition. NASA Technical Note D-1564, 1963.

[14] S.G. Kandlikar, D.K. Dhir, Handbook of Phase Change, Taylor and Francis, Ann Arbor (1999).

[15] Y. Katto, General Features of CHF of Forced Convection Boiling in Uniformly Heated Vertical Tubes with Zero Inlet Subcooling. International Journal of Heat and Mass Transfer 23 (1980) 493.

[16] S. Kim, I. Mudawar, Universal approach to predicting saturated flow boiling heat transfer in mini/micro-channels – Part I. Dryout incipience quality, Int. J. Heat Mass Transfer 64 (2013) 1226-1238.

[17] A.E. Bergles, S.G. Kandlikar, On the nature of critical heat flux in microchannels, J. Heat Transfer 127 (2005) 101-107.

[18] M.H. Maqbool, B. Palm, R. Khodabandeh, Experimental investigation of dryout of propane in uniformely heated single vertical mini-channels. Exp Therm Fluid Sci 37 (2012) 121-129.

[19] C. M. Callizo, R. Ali, B. Palm, Dryout incipience and critical heat flux in saturated flow boiling of refrigerants in a vertical uniformly heated microchannel, in: Proceedings of the Sixth International ASME Conference on Nanochannels, Microchannels, and Minichannels, ICNMM2008, Darmstadt Germany, June 23–25, 2008.

[20] R. Ali, B. Palm, Dryout characteristics during flow boiling of R134a in vertical circular minichannels, Int. J. Heat Mass Transfer 54 (2011) 2434–2445.

[21] W. Qu, I. Mudawar, Measurement and correlation of critical heat flux in two-phase micro-channel heat sinks, Int. J. Heat Mass Transfer 47 (2004) 2045-2059.

[22] J. Lee, I. Mudawar, Two-phase flow in high-heat-flux micro-channel heat sink for refrigeration cooling applications: Part II – heat transfer characteristics, Int. J. Heat Mass Transfer 48 (2005) 941-955.

[23] L. Wojtan, R. Revellin, J.R. Thome, Investigation of saturated critical heat flux in a single, uniformly heated microchannel, Exp. Therm. Fluid Sci. 30 (2006) 765-774.

[24] C.L. Ong, J.R. Thome, Macro-to-microchannel transition in two-phase flow: part 2 – flow boiling heat transfer and critical heat flux, Exp. Therm. Fluid Sci. 35 (2011) 873–886.

[25] J.E. Park, J.R. Thome, Critical heat flux in multi-microchannel copper elements with low pressure refrigerants, Int. J. Heat Mass Transfer 53 (2010) 110–122.

[26] A.W. Mauro, J.R. Thome, D. Toto, G.P. Vanoli, Saturated critical heat flux in a multi-microchannel heat sink fed by a split flow system. Exp Therm Fluid Sci 34 (2010) 81-92.

[27] A. Kosar, Y. Peles, Critical heat flux of R-123 in silicon-based microchannels, J. Heat Transfer 129 (2006) 844–851.

[28] T. Saenen, J.R. Thome, Dynamic numerical microchannel evaporator model to investigate parallel channel instabilities, J. Electronic Packaging 138 (2016) 010901.

[29] R. Mastrullo, A.W. Mauro, J.R. Thome, G.P. Vanoli, L. Viscito, Critical heat flux: performance of R1234yf, R1234ze and R134a in an aluminum multiminichannel heat sink at high saturation temperatures, Int. J. Therm. Sci. 106 (2016) 1-17.

[30] G.M. Lazarek, S.H. Black, Evaporative heat transfer, pressure drop and critical heat

flux in a small vertical tube with R-113, Int. J. Heat Mass Transfer 25 (1982) 945-960.

[31] Y. Katto, H. Ohno, An improved version of the generalized correlation of critical heat flux for the forced convective boiling in uniformly heated vertical tubes, Int. J. Heat Mass Transfer 27 (1984) 1641-1648.

[32] A.M. Lezzi, A. Niro, G.P. Beretta, Experimental data on CHF for forced convection water boiling in long horizontal capillary tubes, In: Proceedings of the Tenth International Heat Transfer Conference 7 (1994) 491-496.

[33] H.C. Kim, W. Baek, S.H. Chang, Critical heat flux of water in vertical round tubes at low pressure and low flow conditions, Nuclear Engineering and Design 199 (2000) 49-73.

[34] W.K. Kuan, Experimental study of flow boiling heat transfer and critical heat flux in microchannels, Ph.D. thesis, Rochester Institute of Technology, NY, USA (2006), available at https://ritdml.rit.edu/handle/1850/1887.

[35] C. Tibiriçá, G. Ribatski, J.R. Thome, Saturated flow boiling heat transfer and critical heat flux in small horizontal flattened tubes, Int. J. Heat Mass Transfer 55 (2012) 7873–7883.

[36] Z. Anwar, B. Palm, R. Khodabandeh, Dryout characteristics of natural and synthetic refrigerants in single vertical mini-channels, Exp. Therm. Fluid Sci. 68 (2015) 257-267.

[37] B. Agostini, R. Revellin, J.R. Thome, M. Fabbri, B. Michel, D. Calmi, U. Kloter, High heat flux flow boiling in silicon multi-microchannels – Part III:Saturated critical heat flux of R236fa and two-phase pressure drops,, Int. J. Heat Mass Transfer 51 (2008) 5426-5442.

[38] R. Mastrullo, A.W. Mauro, L. Viscito, Experimental CHF for low-GWP fluids and R134a. Effect of the Lh/D ratio at low and high mass velocities. Int. J. Heat Mass Transfer 109 (2017) 1200-1216.

[39] M.B. Bowers, I. Mudawar, High flux boiling in low rate, low pressure drop mini-channel and micro-channel heat sinks, Int. J. Heat Mass Transfer 37 (1994) 321-332.

[40] R. Yun, Y. Kim, Critical quality prediction for saturated flow boiling of CO2 in horizontal small diameters, Int. J. Heat Mass Transfer 46 (2003) 2527-2535.

[41] W.K. Kuan, S.G. Kandlikar, Experimental study on saturated flow boiling critical heat flux in microchannels, Proc. 4th Int. Conf. on Nanochannels, Microchannels and Minichannels (2006), Limerick, Ireland.

[42] A.P. Roday, T. Borca-Tasçiuc, M.K. Jensen, The critical heat flux condition with water in a uniformly heated microtube, J. Heat Transfer 130 (2008) 012901.

[43] D. Mikielewicz, J. Wajs, M. Gliński, A.R.S. Zrooga, Experimental investigation of dryout of SES 36, R134a, R123 and ethanol in vertical small diameter tubes, Exp. Therm. Fluid Sci. 44 (2013) 556-564.

[44] A. Diani, S. Mancin, L. Rossetto, Flow boiling heat transfer of R1234yf inside a 3.4 mm ID microfin tube. Exp Therm Fluid Sci 66 (2015) 127-136.

[45] Z. Anwar, B. Palm, R. Khodabandeh, Flow boiling heat transfer, pressure drop and dryout characteristics of R1234yf: experimental results and predictions. Exp Therm Fluid Sci 66 (2015) 137-49.

[46] D. Del Col, A. Cavallini, S. Bortolin, M. Matkovic, L. Rossetto, Dry-out flow boiling in a single circular microchannel: Experimentation and Modeling, Proc. ASME Summer Heat Transfer conf. (2008) Jacksonville, USA.

[47] A.P. Roday, M.K. Jensen, Study of the critical heat flux with water and R-123 during flow boiling in microtubes. Part I: Experimental results and discussion of parametric effects, Int. J. Heat and Mass Transfer 52 (2009) 3235-3249.

[48] F. Tanaka, T. Hibiki, K. Mishima, Correlation for flow boiling critical heat flux in thin rectangular channels, J. Heat Transfer 131 (2009) 121003–121007.

[49] Z. Wu, W. Li, A new predictive tool for saturated critical heat flux in micro/mini-channels: effect of the heated length-to-diameter ratio, Int. J. Heat Mass Transfer 54 (2011) 2880–2889.

[50] W. Zhang, T. Hibiki, K. Mishima, Y. Mi, Correlation of critical heat flux for flow boiling of water in mini-channels, Int. J. Heat Mass Transfer 49 (2006) 1058-1072.

[51] C. Martin-Callizo, Flow Boiling Heat Transfer in Single Vertical Channels of Small Diameter, Ph.D. Thesis, Division of Applied Thermodynamics and Refrigeration, Department of Energy Technology, Royal Institute of Technology (KTH), Stockholm, Sweden, 2010., Available online at <http://www.diva-portal.org/smash/get/diva2:359892/FULLTEXT01.pdfunderlying>.

[52] K. Hambraeus, Heat transfer coefficient during two-phase flow boiling of HFC-134a, Int. J. Refrigeration 14 (1991) 357-362.

[53] C. Wang, J. Yu, S. Lin, C. Lu, An experimental study of convective boiling of refrigerants R22 and R410A, Proceedings of ASHRAE Transactions (1998), Toronto, Canada 1144-1150.

[54] N. Kattan, J.R. Thome, D. Favrat, Flow boiling in horizontal tubes: Part 2 - new heat transfer data for five refrigerants, J. Heat Transfer 120 (1998) 148-155.

[55] C. Park, P. Hrnjak, CO2 and R410A flow boiling heat transfer, pressure drop, and flow pattern at low temperatures in a horizontal smooth tube. Int. J. of Refrigeration 30 (2007) 166-178.

[56] S. Bortolin, D. Del Col, L. Rossetto, Flow boiling of R245fa in a single circular minichannel, Heat Transfer Engineering 32 (2011) 1160-1172.

[57] P. Kew, K. Cornwell, Correlations for the prediction of boiling heat transfer in small-diameter channels, App. Th. Eng. 17 (1997) 705-715.

[58] C. Ong, J.R. Thome, Flow boiling heat transfer of R134a, R236fa and R245fa in a

horizontal 1.030 mm circular channel, Exp. Th. Fluid Science 33 (2009) 651-663.

[59] R. Mastrullo, A.W. Mauro, A. Rosato, G.P. Vanoli, Carbon dioxide local heat transfer coefficient during flow boiling in a horizontal circular smooth tube, Int. J. Heat Mass Transfer 52 (2009) 4184-4194.

[60] D. Del Col, Flow boiling of halogenated refrigerants at high saturation temperature in a horizontal smooth tube. Exp. Th. Fluid Science 34 (2010) 234-245.

[61] C.B. Tibiriçá, G. Ribatski, Flow boiling heat transfer of R-134a and R-245fa in a 2.30 mm tube, Int. J. Heat Mass Transfer 53 (2010) 2459-2468.

[62] S. Grauso, R. Mastrullo, A.W. Mauro, J.R. Thome, G.P. Vanoli, Flow pattern map, heat transfer and pressure drops during evaporation of R-1234ze(E) and R134a in a horizontal, circular smooth tube: Experiments and assessment of predictive methods., Int.J. Refrigeration 36 (2013) 478-491.

[63] S. Grauso, R. Mastrullo, A.W. Mauro, G.P. Vanoli, CO2 and propane blends: Experiments and assessment of predictive methods for flow boiling in horizontal tubes, Int. J. Refrigeration 34 (2011) 1028-1039.

[64] S. Grauso, R. Mastrullo, A.W. Mauro, G.P. Vanoli, Flow boiling of R410A and CO2 from low to medium reduced pressures in macro channels: Experiments and assessment of prediction methods, Int. J. Heat Mass Transfer 56 (2013) 107-118.

[65] M.G. Cooper, Flow boiling - the "apparently nucleate" regime, Int J. Heat Mass Transfer 32 (1989) 459-464.

[66] D.S. Jung, M. McLinden, R.Radermacher, D. Didion, A study of flow boiling heat transfer with refrigerant mixtures, Int. J. Heat Mass Transfer 32 (1989) 1751-1764.

[67] R.L. Webb, N.S. Gupte, A critical review of correlations for convective vaporization in tubes and tube banks, Heat Transfer Eng. 13 (1992) 58-81.

[68] J.C. Chen, Correlation for boiling heat transfer to saturated fluids in convective flow.

Ind. eng. Chem. Process Design and Development 5 (1966) 322-329.

[69] H.K. Forster, N. Zuber, Dynamics of vapor bubbles and boiling heat transfer. AIChE Journal 1 (1955), 531-535.

[70] F.W. Dittus, L.M.K. Boelter, Heat transfer in automobile radiators of the tubular type, Univ. Calif. Publ. Eng. 2 (1930) 443–461.

[71] W. Chen, X. Fang, A note on the Chen correlation of saturated flow boiling heat transfer, Int. J. of Refrigeration 48 (2014) 100-104.

[72] K. Gungor, R. Winterton, A general correlation for flow boiling in tubes and annuli, Int. J. Heat Mass Transfer 29 (1986) 351-358.

[73] M. Cooper, Heat flow rates in saturated nucleate pool boiling - wide-ranging examination using reduced properties, Advances in Heat Transfer 16 (1984) 157-239.

[74] S.G. Kandlikar, A general correlation for saturated two-phase flow boiling heat transfer inside horizontal and vertical tubes, J. Heat Transfer 112 (1990) 219-228.

[75] V. Gnielinski, New equations for heat and mass transfer in turbulent pipe and channel flow, Int. Chem. Eng. 16 (1976) 359–368.

[76] S.S. Bertsch, E.A. Groll, S.V. Garimella, A composite heat transfer correlation for saturated flow boiling in small channels, Int. J. Heat Mass Transfer 52 (2009) 2110-2118.

[77] H. Hausen, Darstellung des Warmeruberganges in Rohren durch verallgemeinerte Potenzbeziehungen, Z. VDI Beiheft Verfahrenstechnik 4 (1943).

[78] Z. Liu, R. Winterton, A general correlation for saturated and subcooled flow boiling in tubes and annuli, based on a nucleate pool boiling equation, Int. J. Heat Mass Transfer 34 (1991), 2759-2766.

[79] T. Tran, M. Wambsganss, D. France, Small circular and rectangular channel boiling

with two refrigeratns, Int. J. Multiphase Flow 22 (1996) 485-498.

[80] W. Yu, D. France, M.W. Wambsganss, J.R. Hull, Two-phase pressure drop, boiling heat transfer, and critical heat flux to water in a small-diameter horizontal tube, Int. J. Multiphase Flow 28 (2002) 927-941.

[81] L. Sun, K. Mishima, An evaluation of prediction methods for saturated flow boiling heat transfer in mini-channels, Int. J. Heat Mass Transfer 52 (2009) 5323-5329.

[82] N. Kattan, J.R. Thome, D. Favrat, Flow boiling in horizontal tubes: Part 1 - development of a diabatic two-phase flow pattern map, J. Heat Transfer 120 (1998) 140-147.

[83] J. R. Thome, J. El Hajal, Flow boiling heat transfer to carbon dioxide: general prediction method, Int. J. Refrigeration 27 (2004) 294-301.

[84] S.Z. Rouhani, E. Axelsson, Calculation of the void volume fraction in the subcooled and quality boiling regions, Int. J. Heat Mass Transfer 13 (1970) 383-393.

[85] D. Steiner, Heat transfer to boiling saturated liquids. In: Verein Deutscher Ingenieure (Ed.), VDI-Wärmeatlas (VDI Heat Atlas). VDI-Geseelschaft Verfahrenstechnik und Chemieingenieurswesen (GCV) 1993, Düsseldorf.

[86] L. Wojtan, T. Ursenbacher, J.R. Thome, Investigation of flow boiling in horizontal tubes: Part II - developement of a new heat transfer model for stratified-wavy, dryout and mist flow regimes, Int. J. Heat Mass Transfer 48 (2005) 2970-2985.

[87] J.R. Thome, V. Dupont, A. Jacobi, HEat transfer model for evaporation in microchannels. Part I: presentation of the model, Int. J. Heat Mass Transfer 47 (2004) 3375-3385.

[88] S.W. Churchill, R. Usagi, A general expression for the correlation of rates of transfer and other phenomena, AIChE Journal 18 (1972) 1121-1128.

[89] A.W. Mauro, A. Cioncolini, J.R. Thome, R. Mastrullo, Asymetric annular flow in

horizontal circular macro-channels: Basic modeling of liquid film distribution and heat transfer around the tube perimeter in convective boiling, Int. J. Heat Mass Transfer 77, (2014) 897-905.

[90] A. Cioncolini, J.R. Thome, C. Lombardi, Unified macro-to-microscale method to predict two-phase frictional pressure drops of annular flows, Int. J. Multiphase Flow 35 (2009) 1138-1148.

[91] A. Cioncolini, J.R. Thome, Algebraic turbulence modeling in adiabatic and evaporating annular two-phase flow, Int. J. Heat Fluid Flow 32 (2011) 805–817.

[92] A. Cioncolini, J.R. Thome, Void fraction prediction in annular two-phase flow, Int. J. Multiphase Flow 43 (2012) 72–84.

[93] A. Cioncolini, J.R. Thome, Entrained liquid fraction prediction in adiabatic and evaporating annular two-phase flow, Nucl. Eng. Des. 243 (2012) 200–213.

[94] A. Cioncolini, J.R. Thome, Liquid film circumferential asymmetry prediction in horizontal annular two-phase flow, Int. J. Multiphase Flow 51 (2013) 44–54.

[95] M. Zhang, R.L. Webb, Correlation of two-phase friction for refrigerants in small-diameter tubes, Exp. Th. Fluid Science 25 (2001) 131-139.

[96] J.M. Quiben, J.R. Thome, Flow pattern based two-phase frictional pressure drop model for horizontal tubes. Part I: Diabatic and adiabatic experimental study. Int. J. Heat Fluid Flow 28 (2007) 1049-1059.

[97] M. Ducoulombier, S. Colasson, J. Bonjour, P- Haberschill, Carbon dioxide flow boiling in a single microchannel - Part II: Heat transfer. Exp. Thermal and Fluid Science 35 (2011) 597-611.

[98] C. Kuo, C. Wang, Horizontal flow boiling of R22 and R407C in a 9.52 mm micro-fin tube, Appl. Th. Eng. 16 (1996) 719-731.

[99] H. Müller-Steinhagen, K. Heck, A simple friction pressure drop correlation for two-

phase flow in pipes. Chem. Eng. and Processing: Process Intensification 20 (1986) 297-308.

[100] R. Grönnerud, Investigation of liquid hold-up, flow-resistance and heat transfer in circulation type of evaporators, part IV: two-phase flow resistance in boiling refrigerants. In: Annexe1972-1, Bulletin De l'Institute du Froid (1979).

[101] S.Grauso, R. Mastrullo, A.W. Mauro, G.P. Vanoli, Two-phase adiabatic frictional pressure gradients for R410A and CO2 in a macro channel: Experiments and a simplified predictive method for annular flow from low to medium reduced pressures, Exp. Th. Fluid, Science 52 (2014) 79-87.

[102] L. Friedel, Improved friction pressure drop correlations for horizontal and vertical two-phase pipe flow. Paper E2, European Two Phase Flow Group Meeting. Ispra, Italia (1979).

[103] A.W. Mauro, J.M. Quibén, R. Mastrullo, J.R. Thome, Comparison of experimental pressure drop data for two phase flow to prediction methods using a general model, Int. J. of Refrigeration 30 (2007) 1358-1367.

[104] J.M. Quibén J.R. Thome, Flow pattern based two-phase frictional pressure drop model for horizontal tubes, Part II: New phenomenological model, Int. J. Heat and Fluid Flow 28 (2007) 1060-1072.

[105] D. Del Col, D. Torresin, A. Cavallini, Heat transfer and pressure drop during condensation of the low GWP refrigerant R1234yf, Int. J. Refrigeration 33 (2010) 1307-1318.

[106] A. Cavallini, D. Del Col, M. Matkovic, L. Rossetto, Frictional pressure drop during vapour-liquid flow in minichannels: modeling and experimental evaluation, Int. J. Heat Fluid Flow 30 (2009) 131-139.

[107] M. Padilla, R. Revellin, P. Haberschill, A. Bensafi, J. Bonjour, Flow regimes and two-phase pressure gradient in horizontal straight tubes: Experimental results for HFO-

1234yf, R-134a and R-410A, Exp. Th. Fluid Science 35 (2011) 1113-1126.

[108] R. Revellin, P. Haberschill, Prediction of frictional pressure drop during flow boiling of refrigerants in horizontal tubes: comparison to an experimental database, Int. J. Refrigeration 32 (2009) 487-497.

[109] A. Cavallini, D. Del Col, L. Doretti, M. Matkovic, L. Rossetto, C. Zilio, Two-phase frictional pressure gradient of R-236ea, R-134a and R-410A inside multi-port channels, Exp. Th. Fluid Science 29 (2005) 861-870.

[110] R. Revellin, J.R. Thome, Adiabatic two-phase frictional pressure drops in microchannels, Exp. Th. Fluid Science 31 (2007) 673-685.

[111] C.T. Tibiriçá, J.D. da Silva, G. Ribatski, Experimental investigation of flow boiling pressure drop of R134a in a microscale horizontal smooth tube, J. Th. Sc. Eng. Appl. 3 (2011) 1-8.

[112] C.B. Tibiriçá, G. Ribatski, Two-phase frictional pressure drop and flow boiling heat transfer for R-245fa in a 2.32-mm tube, HEat Tr. Eng. 32 (2011) 1139-1149.

[113] A. Cicchitti, C. Lombardi, M. Silvestri, G. Soldaini, R. Zavarettelli, Two-phase cooling experiments: Pressure drop, heat transfer and burnout measurements, Energia Nucleare 7 (1960) 407-425.

[114] W. McAdams, W. Woods, R. Bryan, Vaporization inside horizontal tubes-ii-benzene-oil-mixtures, Journal of Heat Transfer 64 (1942) 193-200.

[115] A.E. Dukler, M. Wicks, R.. Cleveland, Pressure drop and hold-up in two-phase flow Part A - a comparison of existing correlations and Part B - an approach through similarity analysis, AIChE Journal 10 (1964) 38-43.

[116] D. Chisholm, A theoretical basis for the Lockhart-Martinelli correlation for two-phase flow, Int. J. Heat Mass Transfer 10 (1967) 1767-1778.

[117] K. Mishima, T. Hibiki, Some characteristics of air-water two-phase flow in small

diameter vertical tubes, Int. J. Multiphase Flow 22 (1996) 703-712.

[118] A. Pamitran, K. Choi, J. Oh, P. Hrnjak, Characteristics of two-phase flow pattern transitions and pressure drop of five refrigerants in horizonta circular small tubes, Int. J. Refrigeration 33 (2010) 578-588.

[119] D. Beattie, P. Whalley, A simple two-phase frictional pressure drop calculation method, Int. J. Multiphase Flow 8 (1982) 83-87.

[120] R. Martinelli, D. Nelson, Prediction of pressure drop during forced-circulation boiling of water, J. Heat Transfer 70 (1948) 695-702.

[121] Labview release. Austin, Texas, United States of America. National Instrument.

[122] MATLAB release. Natick, Massachussets, United States, The MathWorks, Inc.

[123] Lemmon E W, Mc M.O. Linden, M.L. Huber, REFPROP NIST Standard Reference Database 23, Version 9.0, 2009.

[124] H.D. Baher, K. Stephan, Heat and Mass Transfer, second ed., Springer, 2006.

[125] R.J. Moffat, Contributions to the theory of a single-sample uncertainty analysis. Transactions of the ASME: Journal of Fluids Engineering 104 (1982) 250–260.

[126] R.J. Moffat, Using uncertainty analysis in the planning of an experiment. Transactions of the ASME: Journal of Fluids Engineering 107 (1985) 173–178.

[127] S.J. Kline, F.A. McClintock, Describing uncertainties in single-sample experiments. Mechanical Engineering 75 (1953) 3–8.

[128] H.W. Coleman, W.G. Steele, Experimentation and Uncertainty Analysis for Engineers, second ed. John Wiley & Sons, New York, 1989.

[129] J.R. Taylor, An Introduction to Error Analysis, second ed. University Science Books, California, 1997.

[130] J.R. Taylor, Incertitudes et analyses des erreurs dans les mesures physiques. Dunod, 2000.

[131] ISO, Guide to the Expression of Uncertainty in Measurement. International Organization for Standardization, Geneva, 1993.

[132] WECC Guidelines for the expression of the uncertainty of measurement in calibrations, Western European Calibration Cooperation, WECC Doc. 19, 1990.

[133] S.M. Kim, I. Mudawar, Review of tho-phase critical flow models and investigation of the relationship between choking, premature CHF, and CHF in micro-channel heat sinks, Int. J. Heat Mass Transfer 87 (2015) 497-511.

[134] R. Mastrullo, A.W. Mauro, A. Rosato, G.P. Vanoli, Carbon dioxide heat transfer coefficients and pressure drops during flow boiling: assessment of predictive methods. Int J Refrig 33 (2010) 1068-85.

[135] R. Revellin, J.R. Thome, A theoretical model for the prediction of the critical heat flux in heated microchannels, Int. J. Heat Mass Transfer 51 (2008) 1216–1225.

[136] Z. Rohuani, E. Axelsson, Calculation of volume void fraction in a subcooled and quality region. International Journal of Heat and Mass Transfer 17 (1970) 383-393.

[137] R.J. da Silva Lima, J.M. Quibén, J.R. Thome, Flow boiling in horizontal smooth tubes: new heat transfer results for R134a at three saturation temperatures, Appl. Th. Eng. 29 (2009) 1289-1298.

[138] C.A. Dorao, O.B. Fernandez, M. Fernandino, Experimental study of horizontal flow boiling heat transfer of R134a at a saturation temperature of 18.6 °C, J. Heat Transfer 139 (2017) 111510.

[139] G.B. Jiang, J.T. Tan, Q.X. Nian, S.C. Tang, W.Q. Tao, Experimental study of boiling heat transfer in smooth/micro-fin tubes of four refrigerants. Int. J. Heat Mass Transfer 98 (2016) 631-642.

[140] D.F.S. Tapia, G. Ribatski, Flow boiling heat transfer of R134a and low GWP refrigerants in a horizontal micro-scale channel. Int. J. Heat Mass Transfer 108 (2017) 2417-2432.

[141] G.P. Celata, M. Cumo, Y. Katto, A. Mariani, Prediction of the critical heat flux in water subcooled flow boiling using a new mechanistic approach. International Journal of Heat and Mass Transfer 42 (1999) 1457-1466.